A Study of Superdeformation in ^{131}Ce and ^{132}Ce

Thesis submitted in accordance with the requirements of
the University of Liverpool for the degree of Doctor in Philosophy

by

Adrian Thomas Semple

Oliver Lodge Laboratory

September 1995

To my mother and father,
who encouraged me in all things.

And to my sister,
who is never forgotten.

This thesis is dedicated to them.

Abstract

High-spin states in ${}^{131}_{58}$Ce and ${}^{132}_{58}$Ce have been studied using the reactions ^{100}Mo(^{36}S,5n) and ^{100}Mo(^{36}S,4n) respectively, at a beam energy of 155 MeV. The Eurogam γ-ray spectrometer was used at the Nuclear Structure Facility, Daresbury, U.K..

Excited superdeformed bands have been observed in these nuclei for the first time. One such band has been observed in ^{131}Ce, whilst two bands have been observed in ^{132}Ce. This brings a total of two superdeformed bands in ^{131}Ce and three superdeformed bands in ^{132}Ce. Possible configurations are proposed in terms of particle-hole excitations from a theoretical analysis based on the cranked shell model with a deformed Woods-Saxon potential.

From relationships between the experimental $\Im^{(2)}$ moments of inertia, and corresponding γ-ray energies, the existence of identical superdeformed bands in the Mass A$\approx$130 region is established for the first time.

ΔI=2 energy staggering is observed in three of the superdeformed bands discussed in this work. This is not only the first observation of this phenomenon in the Mass A$\approx$130 region, but is also the first observation of the effect in a pair of identical bands. The staggering distribution observed in these nuclei also has the unique property of a mid-band disappearance.

Some of the results discussed in this work are reported in [San95] and [Sem95].

Acknowledgements

Oh, boy. I've been writing this thesis for so long now, that I think I've sprained my brain. Please accept my apologies if I've missed you out.

To start things off, a special thanks must go to my supervisor, Dr. Paul Nolan. His help and encouragement throughout my three years as a post-graduate is immeasurable. His sense of timing in coming to find me when I had just 'popped down town' is also quite unique. I would also like to thank Prof. P.J Twin as the head of department for allowing me to pursue this research at Liverpool, probably the best city in the world.

I learned to do things right by doing them wrong at least three times, and would like to express my gratitude to Drs. Con Beausang, Mats Bergström and Sally Forbes for all their help and answers to my really stupid questions. Many thanks to Drs. Dave Cullen and Eddie Paul, and to Anna Wilson for reading this work, setting me straight on a few misconceptions, and for correcting all my spelling misstakes. A round of applause must also go to the computer staff for keeping the system chugging along happily : John Cresswell, Jomar Hønsi, Janet Sampson, and Linda Pratt.

Many thanks to the accelerator crew and engineers at the Nuclear Structure Facility, Daresbury, who kept things running smoothly throughout its time of operation.

Now to the other inhabitants of the second floor, particularly my fellow third years, Sean Clarke and John Smith. In all my years I have never met two more upstanding pillars of society. That's a lie. They made me write it.

Thanks also to (listed in order of appearance in the morning) Duncan Applebe, Sefa Ertürk, Kevin Cann, David Joss, James Cocks, Martin Smith and Roger Allatt.

I also promised I would mention my sister-in-law, Fiona. Thanks for sending me on my way to the sixty-something trees.

Finally, I gratefully acknowledge the financial support provided by the Engineering and Physical Sciences Research Council (EPSRC).

Now unless I'm very much mistaken, that's the bottom of the page coming up at me, so I'll finish off. Many thanks everybody.

Contents

Introduction

The study of deformed nuclei is a subject of considerable interest in nuclear structure physics. During the last ten years, large γ-ray detector arrays have revealed the existence of very deformed nuclei at high angular momenta in three main mass regions; $A \approx 130$, 150, 190.

This thesis concerns the study of large deformation in two isotopes of cerium, ^{131}Ce and ^{132}Ce. The present work is built upon the initial discoveries that ^{131}Ce [Luo87] and ^{132}Ce [Nol85] each contain a single rotational band, which has properties indicative of superdeformed nuclei. The development of the Eurogam γ-ray spectrometer has facilitated an in-depth study of these nuclei to search for new and weaker superdeformed phenomena.

In order to justify the nuclear models used in the interpretation of the data, basic principles of nuclear structure are presented prior to the experimental, analysis, and discussion chapters.

Chapter 1 summarises some fundamental aspects of nuclear structure. In particular, concepts crucial to the study of nuclear rotation are introduced.

Chapter 2 describes the nuclear models which have been used in this work. The liquid-drop model is a first attempt to understand the bulk properties of the nucleus. The treatment of the nucleus in terms of a shell structure is then described by the shell model, and the discussion then progresses to include deformation (the Nilsson Model) and rotation (the cranked shell model). The liquid-drop and shell models are then combined to produce a total energy description of the nucleus. This enables the stability of the nucleus to be described in terms of its deformation, which naturally leads to the prediction of superdeformed nuclei.

Chapter 3 discusses the population of high-spin states and the detection of γ-rays emitted as they decay. Methods of data analysis are then briefly discussed.

Chapter 4 presents the details of the experiment carried out to study ^{131}Ce and ^{132}Ce at high-spin. After a brief description of the characteristics of the data obtained, the superdeformed bands observed in these nuclei are introduced. Various measurements and aspects of these bands are then presented.

Chapter 5 then compares these results with theoretical predictions, and their agreement is discussed. The most probable nuclear structures for the bands are also deduced. Finally, the observation of new fine structures, underlying the gross phenomena, is presented.

Chapter 1

Nuclear Properties and Parameters

1.1 Some Fundamental Properties

In this section, some properties of the nucleus which are essential to the understanding of nuclear structure, and particularly to high spin states of the nucleus, are described.

1.1.1 Nuclear Forces

The nucleus is composed of protons and neutrons. The Coulomb repulsion between protons would prevent the formation of stable nuclei unless some attractive forces existed. The strong nuclear force, shown schematically in Fig. 1.1, is responsible for binding the nucleons together and has a number of important properties.

1. Short range and saturation properties. Nuclear forces do not extend beyond a nucleon's nearest neighbours, and saturate beyond ~ 2 fm. Below this separation they are strongly repulsive. This balancing of attractive and repulsive forces results in nucleons possessing a mean separation.

2. The nuclear force between nucleons is charge independent.

3. The nuclear forces which are responsible for binding nucleons together, are the strongest forces in nature. They are 10^{40} times stronger than the gravitational

forces at nuclear separations.

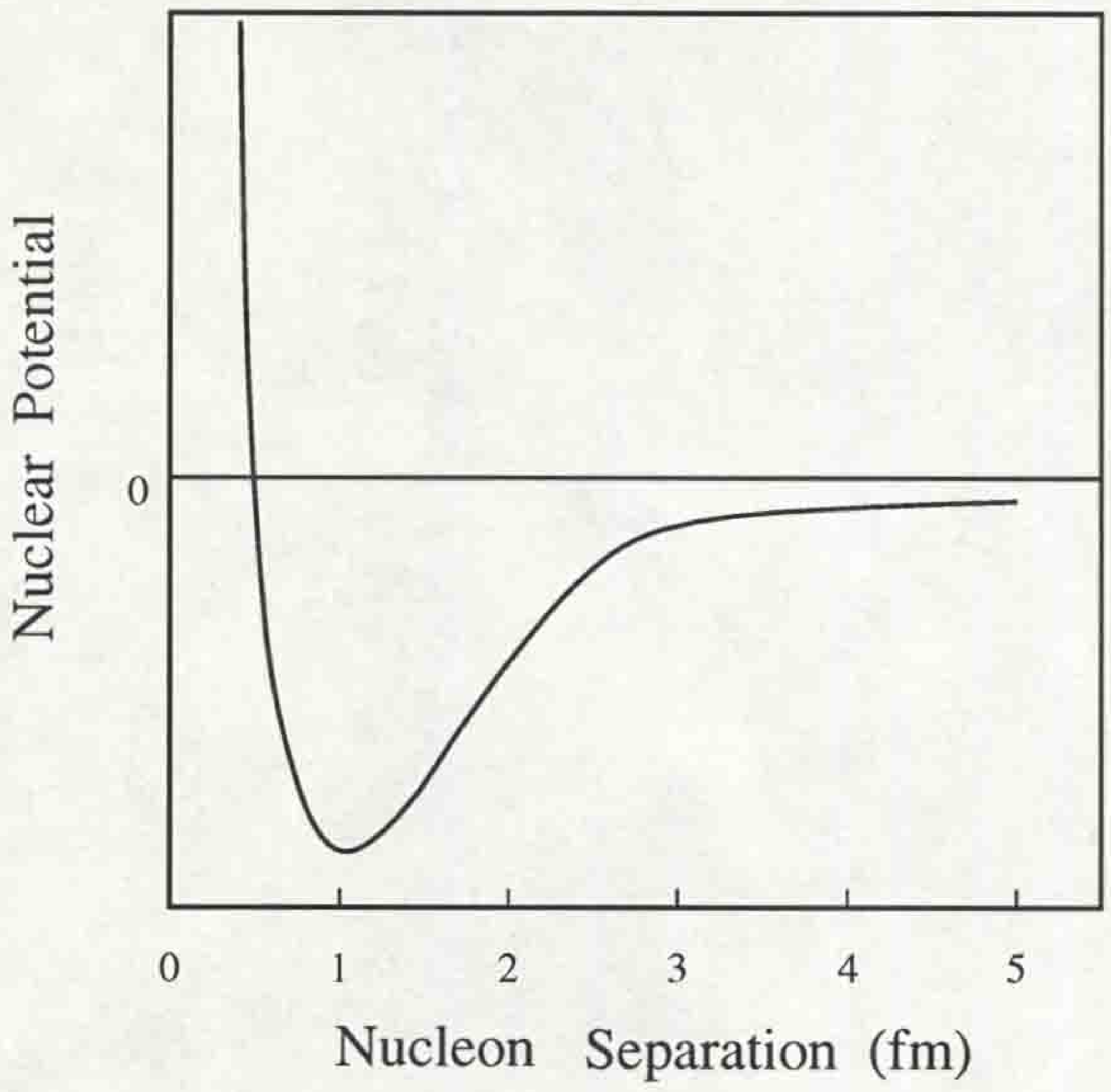

Figure 1.1: Typical Nuclear Potential

1.1.2 Nuclear Size and Density

Although the atomic nucleus is often thought of as a single entity, it is not a solid body with a definite boundary. The 'size' of the nucleus therefore, depends upon the experiment being carried out to measure it. The nuclear size may be described in terms of either nuclear charge (primarily due to protons) or nuclear matter. Electron scattering experiments (such as [Ehr59]) reveal that the central nuclear charge density is nearly the same for all nuclei. Therefore, if the number of nucleons per unit volume is roughly constant, then

$$\frac{A}{\frac{4}{3}\pi R^3} \approx constant \tag{1.1}$$

where R is the mean nuclear radius, and A is the mass number. It follows that

$$R = r_0 A^{\frac{1}{3}} \tag{1.2}$$

where $r_0 \approx 1.2$ fm from experimental measurements.

The radius of a typical nucleus is therefore R $\approx$ 2 x 10^{-15} m. It is perhaps a surprising result that α-particle scattering experiments reveal that the matter radii of nuclei are nearly equal to the charge radii, even though for larger nuclei the number of neutrons is 50% more than the number of protons.

From eqn. 1.1, if R $\approx 10^{-15}$ m, then an estimate of the nuclear matter density is $\rho \sim 10^{18}$ kg m^{-3}.

1.1.3 Nuclear Binding Energy

Measurements of nuclear masses show that the mass of a nucleus is less than the sum of the masses of the constituent protons and neutrons. This 'lost' mass, or mass defect, corresponds to the energy released when individual nucleons fuse to form a single nucleus. The released energy, or binding energy B, of the nucleus is given by

$$B(N,Z) = (Z\,M_p + (A-Z)\,M_n - M_N)c^2 \tag{1.3}$$

for a nucleus of mass M_N, composed of Z protons of mass M_p and (A-Z) neutrons of mass M_n.

Experimental measurements of nuclear masses enable the variation of binding energy per nucleon B/A, with mass number A to be determined. This is shown in Fig. 1.2 (see e.g [Kra88]).

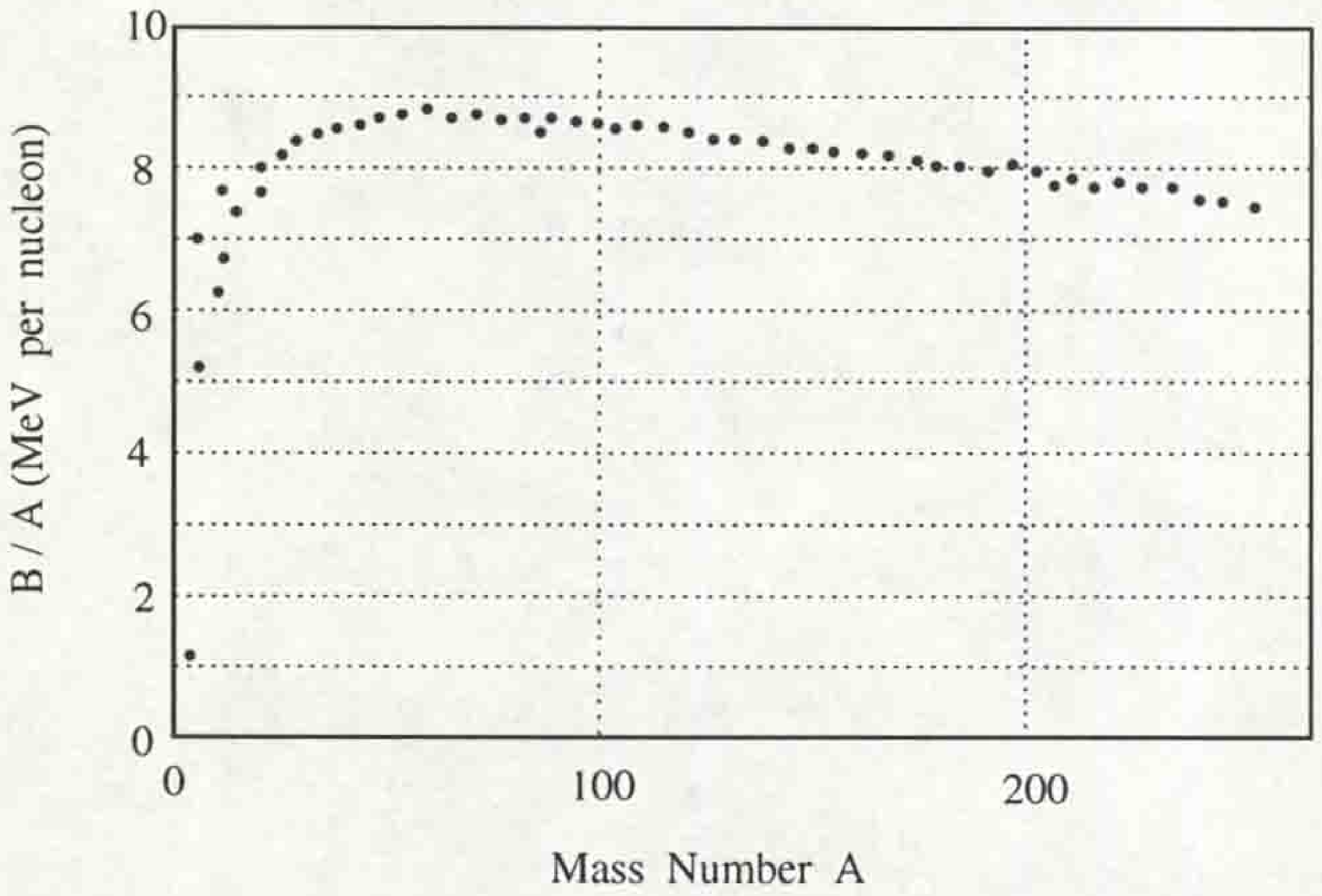

Figure 1.2: Binding Energy per Nucleon as a Function of Mass Number

The average binding energy per nucleon for most nuclei is within 10% of 8 MeV, and reaches a maximum for the nucleus ^{56}Fe. The approximate constancy of B/A is indicative of the staturation properties of the nuclear forces discussed in section 1.1.2.

1.2 Deformation Parameters

The surface of a nucleus can be described by a radius vector R defined in spherical co-ordinates from its centre to a point on its surface

$$R(\theta,\phi) = C(\beta_{\lambda,\mu})R_0\left[1+\sum_{\lambda=0}^{\infty}\sum_{\mu=-\lambda}^{\lambda}\alpha_{\lambda,\mu}Y_{\lambda,\mu}(\theta,\phi)\right] \tag{1.4}$$

where :

- R_0 is the radius of a sphere having the same volume as $R(\theta,\phi)$
- $C(\beta_{\lambda,\mu})$ conserves the volume enclosed by the surface with respect to a sphere of radius R_0
- $Y_{\lambda,\mu}(\theta,\phi)$ are spherical harmonics with coefficients $\alpha_{\lambda,\mu}$
- λ classifies the deformation type : e.g λ=2 represents quadrupole, λ=3 octupole, and λ=4 hexadecapole deformations
- μ is an integer in the range of $-\lambda$ to $+\lambda$

For this study, quadrupole deformation (λ=2) is the most important type of deformation. Under this constraint, the nuclear shape is described in terms of five $\alpha_{\lambda,\mu}$ coefficients (λ=2 and $\mu = -2$ to $+2$). These five coefficients may be reduced to two real independent variables, which give a description of the nucleus with quadrupole deformation : $\alpha_{2,0}$ and $\alpha_{2,2}$.

The parameters $\alpha_{2,0}$ and $\alpha_{2,2}$ may be expressed by another set of parameters, β_2 and γ, which have a more direct physical significance :

$$\alpha_{2,0} = \beta_2 \cos\gamma \tag{1.5}$$

$$\alpha_{2,2} = \frac{1}{\sqrt{2}}\,\beta_2 \sin\gamma \tag{1.6}$$

β_2 is the quadrupole deformation parameter and γ is the triaxiality parameter which describes the nuclear deviation from an axially symmetric shape. Eqn. 1.4 can now be simplified in terms of quadrupole deformation :

$$R(\theta,\phi) = R_0 C(\beta_2)[1 + \beta_2 Y_{20}(\theta,\phi)] \tag{1.7}$$

where $Y_{20}(\theta,\phi)$ is a spherical harmonic of quadrupole order.

The shapes correspond to various (β_2,γ) co-ordinates for λ=2 and are illustrated in Fig. 1.3.

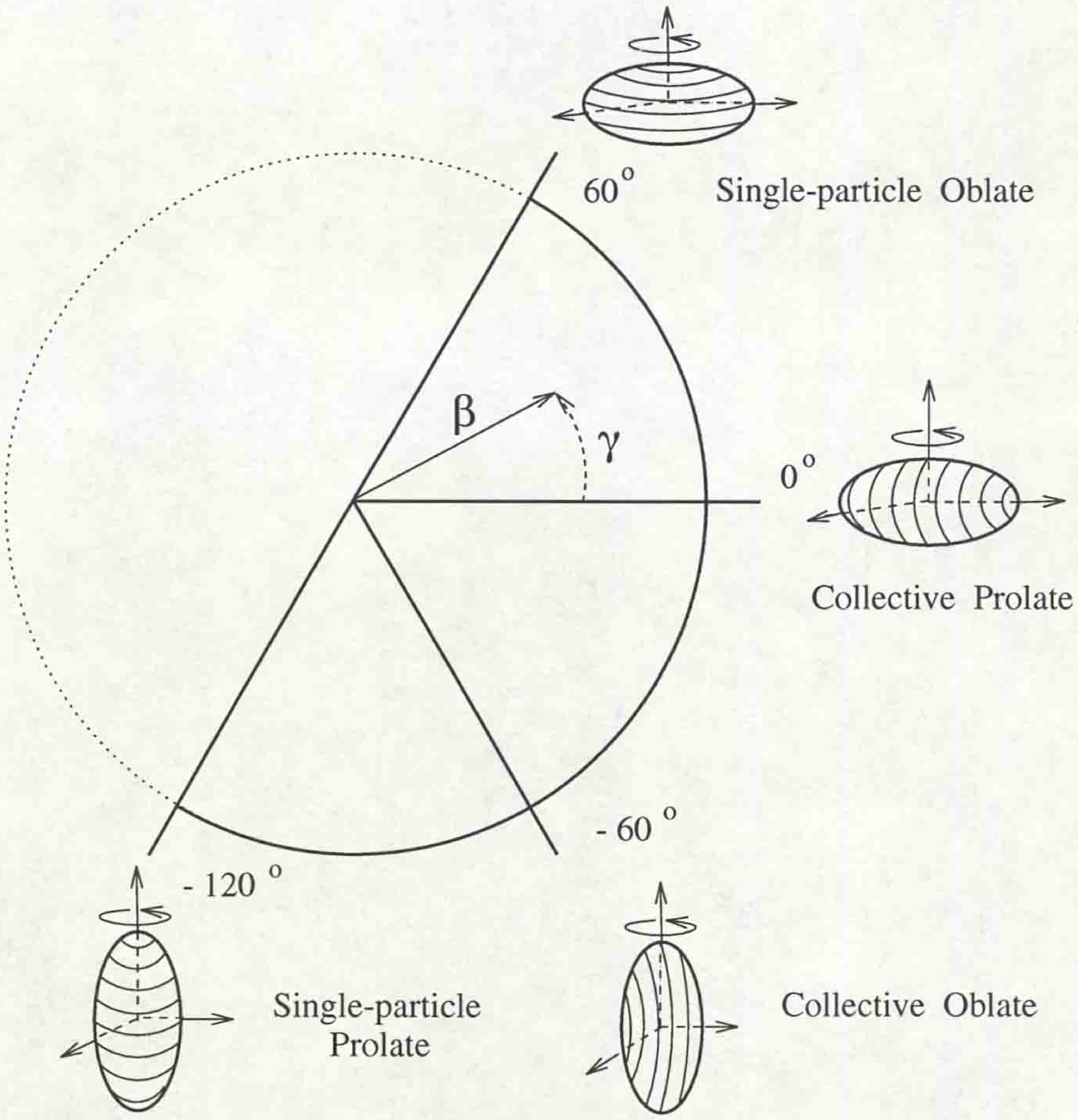

Figure 1.3: Nuclear deformation in terms of β and γ

In the Lund convention for γ [And76, HW53], rotation takes place around the smallest, the intermediate and the largest axes corresponding to the three sectors $0° \leq \gamma \leq 60°$, $-60° \leq \gamma \leq 0°$ and $-120° \leq \gamma \leq -60°$ respectively. The nucleus is described as rotating collectively if its angular momentum is generated by the collective motion of all its nucleons. If the angular momentum is generated by single-particle processes (Sec. 1.3.1) then the nucleus is described as rotating non-collectively.

The maximum collectivity is observed for $-60° \leq \gamma \leq 0°$, whereas non-collective rotation occurs at γ=60° (oblate shape) and γ=–120° (prolate shape) where the rotation axis coincides with the symmetry axis. Usually, only the 0° – 60° sector is required, as this is where the collective-prolate and single-particle oblate structures are defined. These structures rotate about their smallest axis and are thus favoured energetically over those which rotate about their larger axes. The $-120° \leq \gamma \leq 60°$ sector is required when nuclear vibrations occur, since the nucleus may then rotate about any one of its three axes.

The quadrupole deformation parameter β_2 can be defined in terms of the length of the axes :

$$\beta_2 = \frac{4}{3}\sqrt{\frac{\pi}{5}}\frac{\Delta R}{R_0} \tag{1.8}$$

Where ΔR is the difference between the major and minor axes. The type of deformation then depends on the sign of β_2 :

$$\text{Spherical} : \beta_2 = 0$$
$$\text{Prolate deformations} : \beta_2 > 0$$
$$\text{Oblate deformations} : \beta_2 < 0$$

The Nilsson model [Nil69] (sec. 2.3.2) uses a further description of quadrupole deformation, ϵ_2. This is related to β_2 by the simple expression

$$\epsilon_2 \approx \frac{3}{4}\sqrt{\frac{5}{\pi}}\beta_2 \approx 0.95\beta_2 \tag{1.9}$$

1.3 Rotation Parameters

This section describes the parameters and concepts that are used throughout this work to describe superdeformed nuclei at high spin (or high rotational frequencies).

1.3.1 Angular Momentum

Large angular momentum in nuclei may be generated in two ways :

1. By collective rotation of a deformed system.
2. By the alignment of the intrinsic angular momenta of the individual nucleons along the rotation axis.

The total angular momentum **I**, of an axially symmetric deformed nucleus, rotating about an axis which is perpendicular to the symmetry axis, can be decomposed into the collective rotational angular momentum of the core **R**, and the intrinsic angular momentum of the unpaired valence nucleons **J** (paired nucleons couple their angular momenta so that J=|**J**|=0), such that

$$\mathbf{I} = \mathbf{R} + \mathbf{J} \tag{1.10}$$

J can be expressed more explicity as the vector sum of the intrinsic angular momenta of the individual nucleons :

$$\mathbf{J} = \sum_i \mathbf{j}_i \tag{1.11}$$

Fig. 1.4 shows a vector diagram which represents this type of angular momentum coupling. The vectors are represented in the body-fixed intrinsic system, i.e. in a frame of reference in which the nucleus is at rest.

The valence nucleons act more or less independently within the deformed potential created by the core. The magnitude of the nucleon-core coupling determines how ‘free’ the valence nucleons are. For an axially symmetric shape, collective rotation about the symmetry (z) axis is forbidden in quantum mechanics. Collective rotation may therefore only occur about an axis which is perpendicular to the symmetry axis.

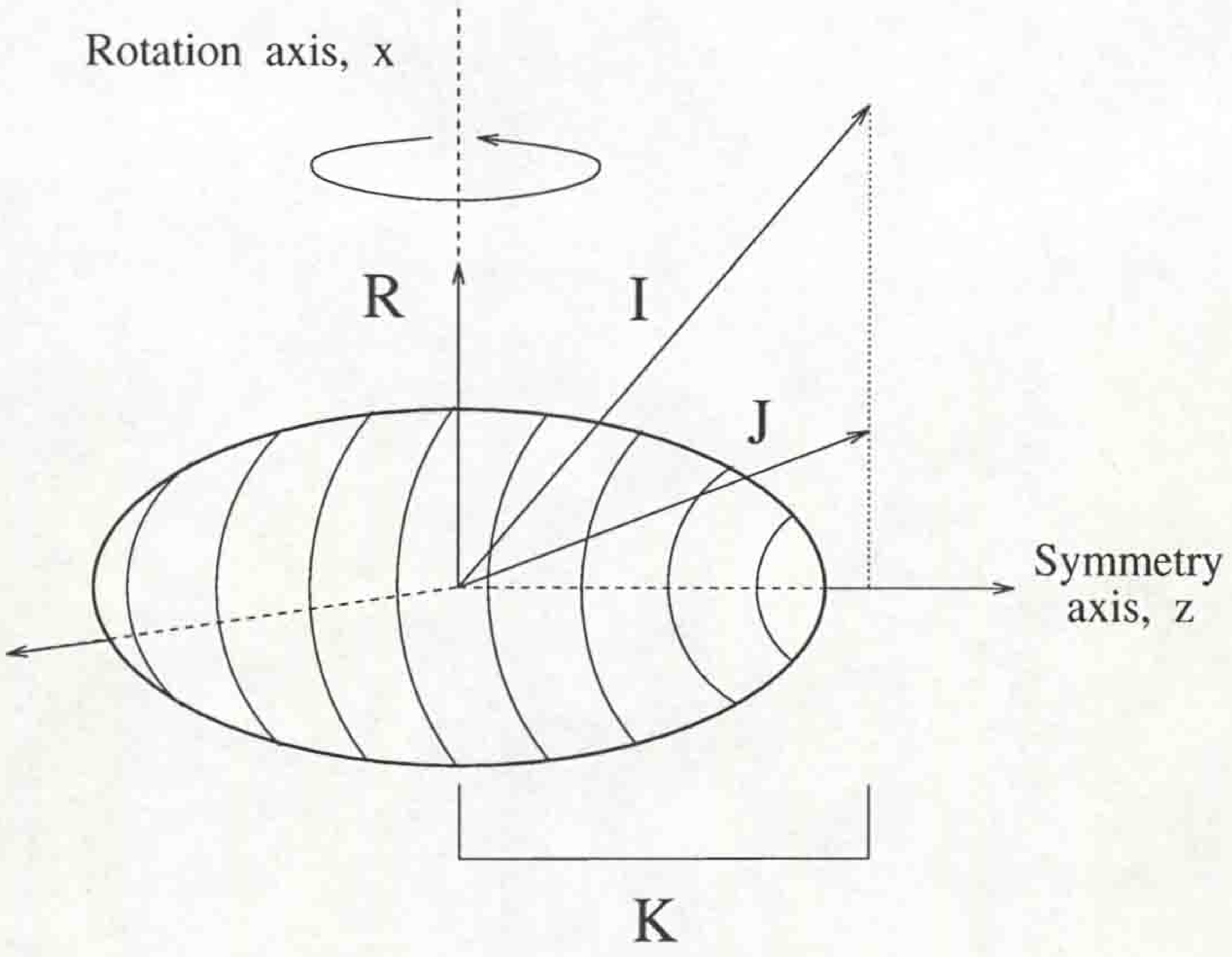

Figure 1.4: Coupling of angular momentum for an axially symmetric deformed nucleus rotating about an axis perpendicular to the symmetry axis

The axial symmetry condition ensures that the projection onto the symmetry axis K is a conserved quantum number in the deformation aligned coupling scheme (Sec. 1.3.7)

$$K = \sum_i \Omega_i \tag{1.12}$$

where Ω is the projection of the intrinsic angular momentum **j** onto the symmetry axis.

1.3.2 Rotational Frequency, $\hbar\omega$

Nuclear rotation is often described as a function of rotational frequency, ω. Classically, the rotational frequency of an object rotating about an axis is defined as

$$\omega = \frac{dE}{dI} \tag{1.13}$$

where E is the total energy of the object, and I is its angular momentum.

The collective rotation of a nucleus can be experimentally observed as a rotational band of states. The rotational frequency of the nucleus rotating about its x-axis (with the component I on the x-axis being I_x) is calculated quantum mechanically by

$$\hbar\omega = \frac{dE}{dI_x} = \frac{E_i - E_f}{I_{xi} - I_{xf}} \tag{1.14}$$

where the subscripts *i* and *f* denote initial and final states respectively. For stretched electric quadrupole transitions (for which ΔI=2) and for high spin (for which $I_x \rightarrow$ I), eqn. 1.14 is conventionally quoted as

$$\hbar\omega \approx \frac{E_\gamma}{2} \tag{1.15}$$

where E_γ is the energy of the γ-ray emitted when the rotational sequence decays from its initial state *i*, to its final state *f* by the emission of a stretched electric quadrupole transition.

1.3.3 Parity, π

The only symmetries that remain for an axially symmetric quadrupole deformed nucleus, rotating about an axis perpendicular to its symmety axis, are the space reflections (parity), and the transformation described by the rotation operator $\hat{R}$ (a rotation of π about the rotation axis). Nuclear states in a rotating nucleus are therefore labelled in terms of the parity of the state and by the quantity signature.

Parity refers to the symmetry under space reflection (reflection through the origin). In one dimension, if the parity operator $\hat{\pi}$ acts on a wavefunction Ψ(x), then for odd parity

$$\hat{\pi}\Psi(x) = \Psi(-x) \tag{1.16}$$

and for even parity

$$\hat{\pi}\Psi(x) = \Psi(x) \tag{1.17}$$

The eigenvalues of $\hat{\pi}$ must therefore be ± 1. Parity describes configurations in terms of positive or negative assignments ($\pi = \pm$), depending upon the effect of the reflection operation on the single-particle wavefunction. The total parity of the nucleus is therefore determined by the product of the parities of all occupied levels.

1.3.4 Signature, α

The signature of a particular state is obtained from a consideration of the rotation operator $\hat{R}$, which acts on the nuclear state u_α (see Sec. 2.4.3 for a more complete description of $\hat{R}$).

$$\hat{R}u_\alpha = exp(-i\pi j_x)u_\alpha \tag{1.18}$$

and the eigenvalues are

$$\hat{R}u_\alpha = exp(-i\pi\alpha)u_\alpha \tag{1.19}$$

which can be related to the angular momentum I, by

$$I = \alpha + 2k \tag{1.20}$$

where k=0,1,2... and

$$\alpha = 0 \text{ or } 1 \text{ for even - A nuclei}$$
$$\alpha = \pm\tfrac{1}{2} \text{ for odd - A nuclei}$$

For a non-rotating deformed nucleus, the nucleon orbits are two-fold degenerate (Sec. 2.3.2) with respect to Ω. For a rotating nucleus this degeneracy is removed (Sec. 2.4.3), and each energy level is split into two energy levels of opposite signature (α=$+\frac{1}{2}$ and α=$-\frac{1}{2}$). These energy levels (now called Routhians as they are energy levels in the rotating frame) are called 'signature partners', and the energy splitting between them is called 'signature splitting'. The degree of splitting is dealt with in Sec. 1.3.7.

1.3.5 Rotational Bands

For the ground state of an even-even nucleus, the nucleons fill each orbital in time-reversed pairs with single-particle angular momentum components $\pm\Omega$. The resulting nuclear ground state is composed of spin and parity (Sec. 1.3.3), $I^\pi = 0^+$. A rotational band may be built upon nuclear states with excitation energy proportional to I(I+1) (eqn. 1.21) with I=0,2,4... .[Here, K=0 because **J**=0. The states with odd angular momentum are excluded and the parity is positive because of the rotational invariance for an axially-symmetric shape (Sec. 2.4.3)].

Excited rotational bands are built up in a similar manner, but in this case the lowest spins for these bands (called the bandhead spin) may have I$\neq 0\hbar$. The bandhead spin is governed by the projection K, of the total angular momentum **I**, of the valence nucleons onto the symmetry axis.

The rotational band of states which have the lowest energy for a given spin is known as the yrast (meaning dizziest) band.

1.3.6 Moments of inertia

The excitation energy E, of the states within a rotational band are given by (see e.g [BV78])

$$E = \frac{\hbar^2}{2\Im^{(0)}}[I(I+1) - K^2] \tag{1.21}$$

where $\Im^{(0)}$ is the static moment of inertia and I is the angular momentum. As discussed in Sec. 1.3.1 angular momentum can be built up by two distinct mechanisms which are spin dependent. Consequently, this moment of inertia is not a constant but is a function of spin. In order to extract more information about the effect of rotation on the nuclear structure, it is instructive to define two more types of moment of inertia. These are related to the first and second derivatives of eqn. 1.21, with appropriate approximations for high spin : I >> K and I $\approx$ I_x, so that K $\rightarrow$ 0. I_x is the projection of the total angular momentum I on the rotational axis, and is defined by

$$I_x = \sqrt{I(I+1) - K^2} \tag{1.22}$$

The kinematic moment of inertia $\Im^{(1)}$ is defined by the first derivative of eqn. 1.21

$$\Im^{(1)} = \hbar^2 I_x \left[\frac{dE}{dI_x}\right]^{-1} = \hbar\frac{I_x}{\omega} \tag{1.23}$$

and the dynamic moment of inertia $\Im^{(2)}$ by the second derivative of eqn. 1.21

$$\Im^{(2)} = \hbar^2 \left[\frac{d^2E}{dI_x^2}\right]^{-1} = \hbar\frac{dI_x}{d\omega} \tag{1.24}$$

The differential part of these definitions have been eliminated using eqn. 1.14.

The quantities $\Im^{(1)}$ and $\Im^{(2)}$ are related by the expression

$$\Im^{(2)} = \Im^{(1)} + \omega \frac{d\Im^{(1)}}{d\omega} \tag{1.25}$$

which for a rigid rotor there is no longer a dependence of $\Im^{(1)}$ on ω, so

$$\Im^{(1)} \approx \Im^{(2)} \approx \Im_{rigid} \tag{1.26}$$

where $\Im_{rigid}$ is the rigid body moment of inertia.

In the experimental measurements of these quantities, the expressions are simplified by a consideration of the stretched electric quadrupole (E2) γ-ray transitions in rotational bands.

The expression for $\Im^{(1)}$ is then

$$\Im^{(1)} = \hbar^2 \frac{(4I-2)}{2E_\gamma} \tag{1.27}$$

and for $\Im^{(2)}$

$$\Im^{(2)} = \frac{4\hbar^2}{\Delta E_\gamma} \tag{1.28}$$

where ΔE_γ is the spacing between consecutive γ-rays of energy E_γ. Because of its relationship to the second derivative, the $\Im^{(2)}$ is very sensitive to changes in internal structure (e.g alignments). Also, it is only dependent on the spacing of the γ-rays and is not dependent on spin (which is not conclusively known for superdeformed bands). The $\Im^{(2)}$ is therefore directly related to experimental data and is used widely in the study of superdeformation such as contained in this work.

1.3.7 Coupling Schemes

The coupling of the angular momentum of a valence nucleon to a deformed, collectively rotating nuclear core may be described in terms of two coupling schemes : the deformation aligned scheme (DAL) and the rotation aligned scheme (RAL). The description of these schemes uses the same vector representation as that discussed previously.

The DAL and RAL schemes represent extreme limits within which all rotational coupling behaviour falls. The text refers to Fig. 1.5.

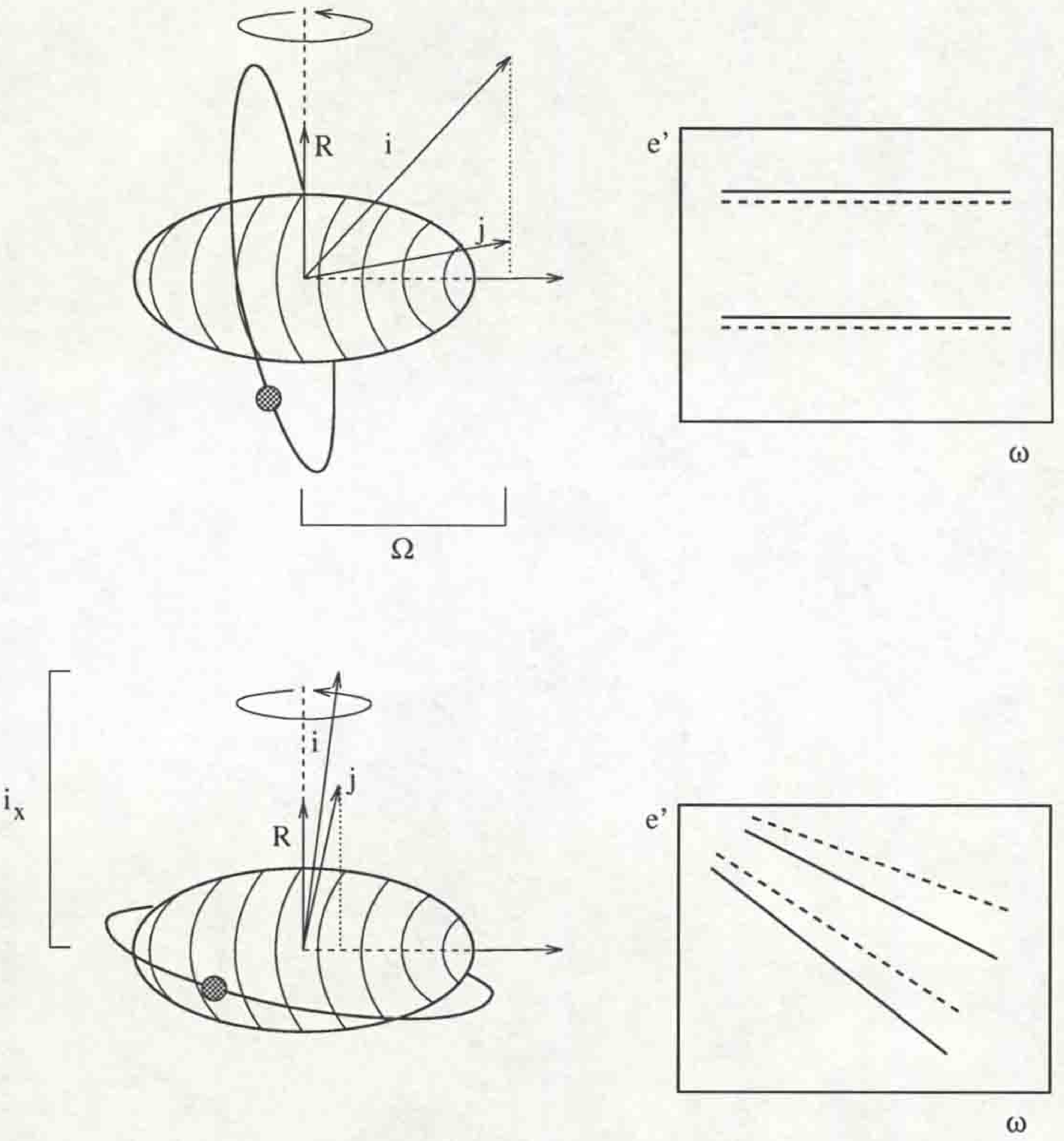

Figure 1.5: (Top) DAL Coupling : The alignment of a valence nucleon's intrinsic angular momentum **j**, with the deformation, and (Bottom) RAL Coupling : The alignment of a valence nucleons intrinsic angular momentum **j**, with the rotation axis. The effect of each coupling on the single-particle Routhian is also shown.

1. Deformation aligned (DAL)

   When there is a large deformation and low rotational frequency, a valence nucleon will follow the core closely and its angular momentum **j**, will be aligned with the deformation, so that **j** precesses about the symmetry axis. In this scheme Ω is a good quantum number. The valence nucleon is strongly coupled to the core, and is unaffected by the Coriolis force : the Coriolis force can do little to align the angular momentum of the valence nucleon with the rotation axis. This results in the Routhians of the signature-partners exhibiting very little signature splitting (alternatively, the -ωj_x term in eqn. 2.33 is small so that modifications to its energy are small). The Routhians are therefore degenerate. See Fig. 1.5 (top).

2. Rotation aligned (RAL)

   When there is a smaller deformation and rapid rotation, the Coriolis force dominates, and aligns the intrinsic angular momentum of the valence nucleon with the axis of rotation so that **j** precesses about the rotation axis. In this scheme Ω is not conserved and is no longer a good quantum number (although it is still used as a label in the asymptotic limit). This results in the nucleon orbit lying in the plane of the symmetry axis. High-**j**, low-Ω orbitals are effected most by the Coriolis force. The valence nucleon becomes almost completely decoupled from the core. The Coriolis force has maximum effect on the energy of such orbitals and the Routhians exhibit a large degree of signature splitting. See Fig. 1.5 (bottom).

1.3.8 Band Crossings

The 'backbend' (so-called because of the shape of the variation of spin with $\hbar\omega$), such as that exhibited by the yrast normal-deformed band in ^{132}Ce (Fig. 1.6), is interpreted as the crossing of two bands built upon different internal configurations. The crossing arises when the Coriolis force becomes large enough to overcome the pairing force between a pair of nucleons, and the nucleons align their angular momentum with the axis of collective rotation.

At the rotational frequency of the backbend, it is energetically favourable to generate angular momentum by such an alignment, and the rate of collective rotation may be reduced. Such pair alignment causes backbending because the aligned configuration has a greater I than the unaligned one at the same ω.

The 'sharpness' of a backbend is dependent on the interaction strength of the band crossing. For weak interaction strengths, a sharp backbend is observed ($\hbar\omega \approx$ 0.35 MeV on Fig. 1.6).

For strong interaction strengths, more smooth changes are observed and occur over several transitions ($\hbar\omega \approx 0.6$ MeV on Fig. 1.6).

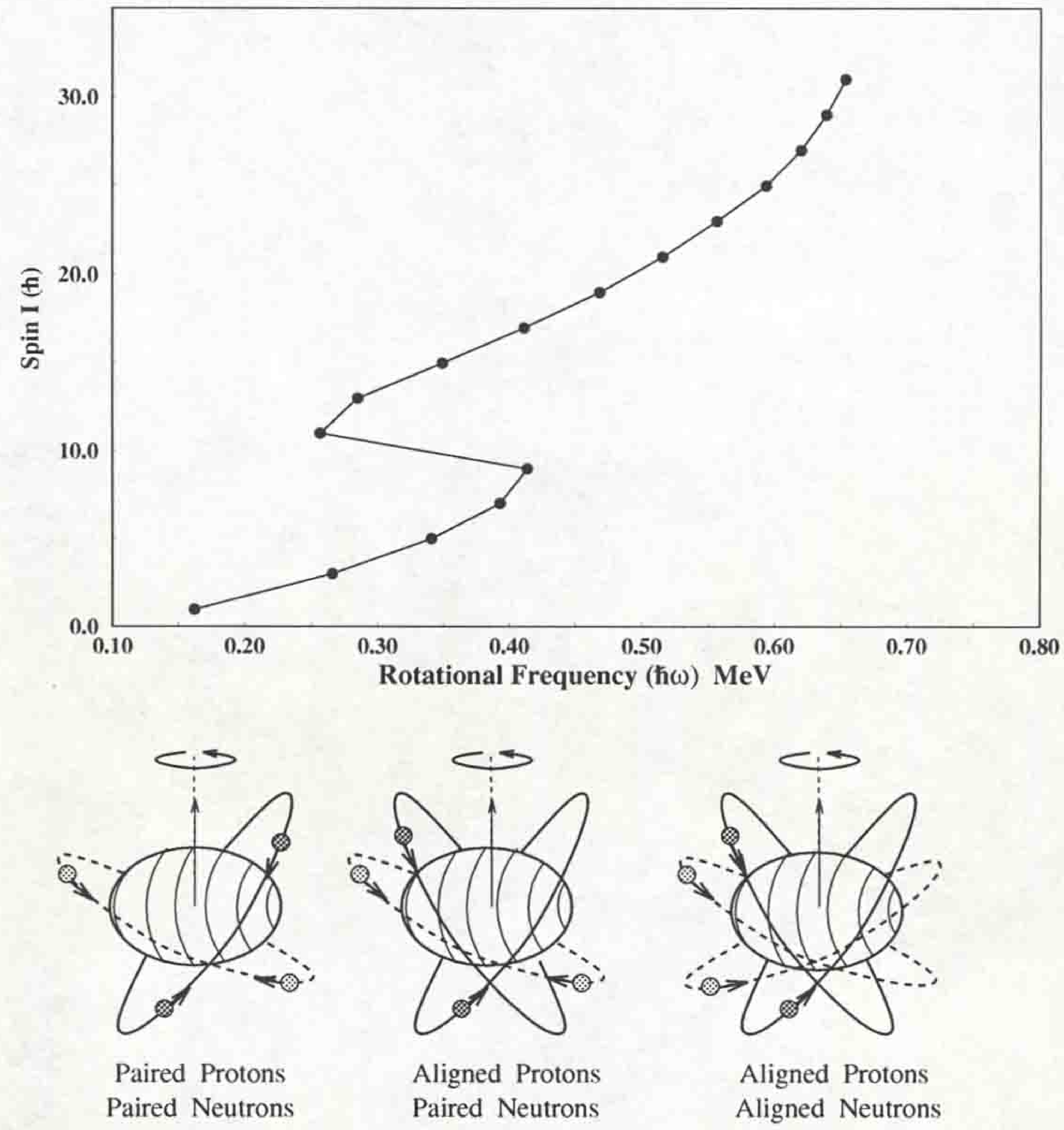

Paired Protons
Paired Neutrons

Aligned Protons
Paired Neutrons

Aligned Protons
Aligned Neutrons

Figure 1.6: Plot of spin I ($\hbar$) v rotational frequency ($\hbar\omega$) for the yrast normal-deformed rotational band in ^{132}Ce, illustrating beckbending. The first backbend is due to a pair of $h_{\frac{11}{2}}$ protons aligning (solid orbits), while the upbend at the end is due to a pair of $h_{\frac{11}{2}}$ neutrons (dashed orbits) aligning.

1.4 Electromagnetic Decay

Excited states of nuclei, decay rapidly to the ground state via the emission of photons of electromagnetic radiation. The photon may be described in terms of multipole moments : a multipole of order L transfers an angular momentum of L$\hbar$. Consider a γ-decay from an initial excited state of angular momentum I_i and parity π_i to a final state I_f and parity π_f. Conservation of angular momentum requires that :

$$\mid I_i - I_f \mid \leq L \leq \mid I_i + I_f \mid \tag{1.29}$$

and so the order (L) of the multipole is restricted. The resulting radiation will be a mixture of possible multipoles, e.g;

L=1 Dipole
L=2 Quadrupole
L=3 Octupole
L=4 Hexadecapole

Whether the emitted radiation is of the electric or magnetic type is determined by the relative parity of the initial and final levels. If there is no change in parity, then the radiation field must have even parity. If there is a change in parity, then the radiation field must have odd parity.

$$\pi(ML) = (-1)^{L+1} \tag{1.30}$$

$$\pi(EL) = (-1)^{L} \tag{1.31}$$

where ML is a magnetic multipole of order L, and EL is an electric multipole of order L. For transitions where more than one multipole is possible, the lowest permitted multipole dominates. So if possible transitions are E2, M3, E4, M5... etc, then the E2 transition would be dominant. The exception to this rule is that the electric order L and magnetic order (L-1) are comparable in strength; e.g E2 and M1 would both be dominant.

Chapter 2

Nuclear Models

2.1 The Liquid-Drop Model

In an attempt to understand the relationship between binding energy and mass number (Fig. 1.2), and also the bulk properties of the nucleus, an analogy can be drawn between the nucleus and a drop of incompressible liquid. This analogy leads to the liquid-drop model, which was the first theoretical model used to describe the nucleus, e.g [RS80].

The liquid-drop model is able to reproduce the following bulk properties of the nucleus :

1. Saturation properties of the nuclear forces (Sec. 1.1.1)
2. Very low compressibility.
3. Well defined surface.

The total energy of the nucleus in the liquid-drop model E_{LD}, is given by the sum of 5 terms [Wei35]:

$$\mathrm{E}_{LD} = \mathrm{E}_{VOL} + \mathrm{E}_{SURF} + \mathrm{E}_{COUL} + \mathrm{E}_{SYM} - \delta\mathrm{A} \tag{2.1}$$

where the first 4 terms represent the volume, surface, Coulomb and so-called symmetry (extra stabilty for N=Z nuclei) contributions to the energy of the nucleus respectively, and the δA term acknowledges the extra stability obtained for paired nucleons.

Such a treatment of the nucleus leads to a rather good agreement of the variation of binding energy per nucleon with mass number (Fig. 1.2). The treatment fails however, for certain nuclei which are observed to have exceptionally stable configurations (e.g $^{4}_{2}$He, $^{16}_{8}$O, $^{88}_{38}$Sr, $^{140}_{58}$Ce...). These nuclei have neutron (N) or proton (Z) numbers corresponding to the magic numbers of

N,Z = 2,8,20,28,50,82 and 126

The extra stability of these 'magic' nuclei reflect the effects of shell structure within the nucleus which have been neglected in the liquid-drop model.

2.2 The Shell Model

2.2.1 Introduction : The Nuclear Mean Field

Soon after the discovery of the neutron in 1932, attempts were made to describe the nucleus in terms of a shell structure in a manner analogous to that for the electrons in an atom. In the atomic case, the potential is supplied by the Coulomb field of the nucleus. The Schrödinger equation is then solved for this potential and the energies (eigenvalues) of the electron orbits are calculated.

There is no equivalent central potential for the nucleus, so in the nuclear shell model, a single nucleon is considered to move in a mean field (or potential) produced by all the other nucleons. Although the form of this average potential should reflect the shape of the nucleus, it cannot be expected to describe all aspects of the nuclear force. Some of the remaining properties are described by residual two body interactions; e.g the pairing force. The shell model Hamiltonian $\hat{H}$ is composed of this average potential $\hat{V}$, plus the sum of the individual kinetic energies of all the independent nucleons $\hat{T}$

$$\hat{H} = \hat{T} + \hat{V} \tag{2.2}$$

$$\hat{H} = \sum_{i=1}^{A} \left[\frac{p_i^2}{2m} + V_i(r) \right] \tag{2.3}$$

$$\hat{H} = \sum_{i=1}^{A} \left[\frac{\hbar^2}{2m} \nabla_i^2 + V_i(r) \right] \tag{2.4}$$

where m and p represent the nucleon mass and momentum respectively, and $V_i(r)$ represents the exact form of the potential well. The existence of definite orbits is then a result of the Pauli Exclusion Principle. Each nucleon exists in a fixed energy state with a set of unique quantum numbers, and no two nucleons can possess the same set of quantum numbers.

The mean-field approximation is a good starting point for the development of a successful nuclear model. By adding various other features such as deformation, spin-orbit interactions and rotation, a more realistic nuclear potential can be obtained. Fig. 2.1 (based on a figure by J.D.Garrett[Gar85]) illustrates the evolution of the nuclear potential from the three-dimensional simple harmonic oscillator (SHO) to the cranked shell model. The three dimensional SHO (Sec. 2.2.2) is the simplest approximation to the nuclear potential. However, not only is it necessary to improve the radial shape (as in the Woods-Saxon potential, Sec. 2.2.3), but a spin-orbit term must also be added (Sec. 2.2.4). Deformation (Sec. 2.3.2) then has dramatic consequences on the nuclear energy levels, and when the nucleus is rotated (Sec. 2.4.3), Coriolis and centrifugal forces acting on the nucleons, further alter the single-particle spectrum.

The remaining part of this chapter will deal with the treatment of the nucleus in terms of a shell structure, and the development of a suitable nuclear potential.

2.2.2 The Harmonic Oscillator Potential

The harmonic oscillator potential is a useful starting point to describe the nucleus, because it describes the prescence of a restoring force that acts to return a system to its equilibrium condition. It is defined as

$$V_{sho}(r) = \frac{m\omega_0^2}{2}(r^2 - R_0^2) \tag{2.5}$$

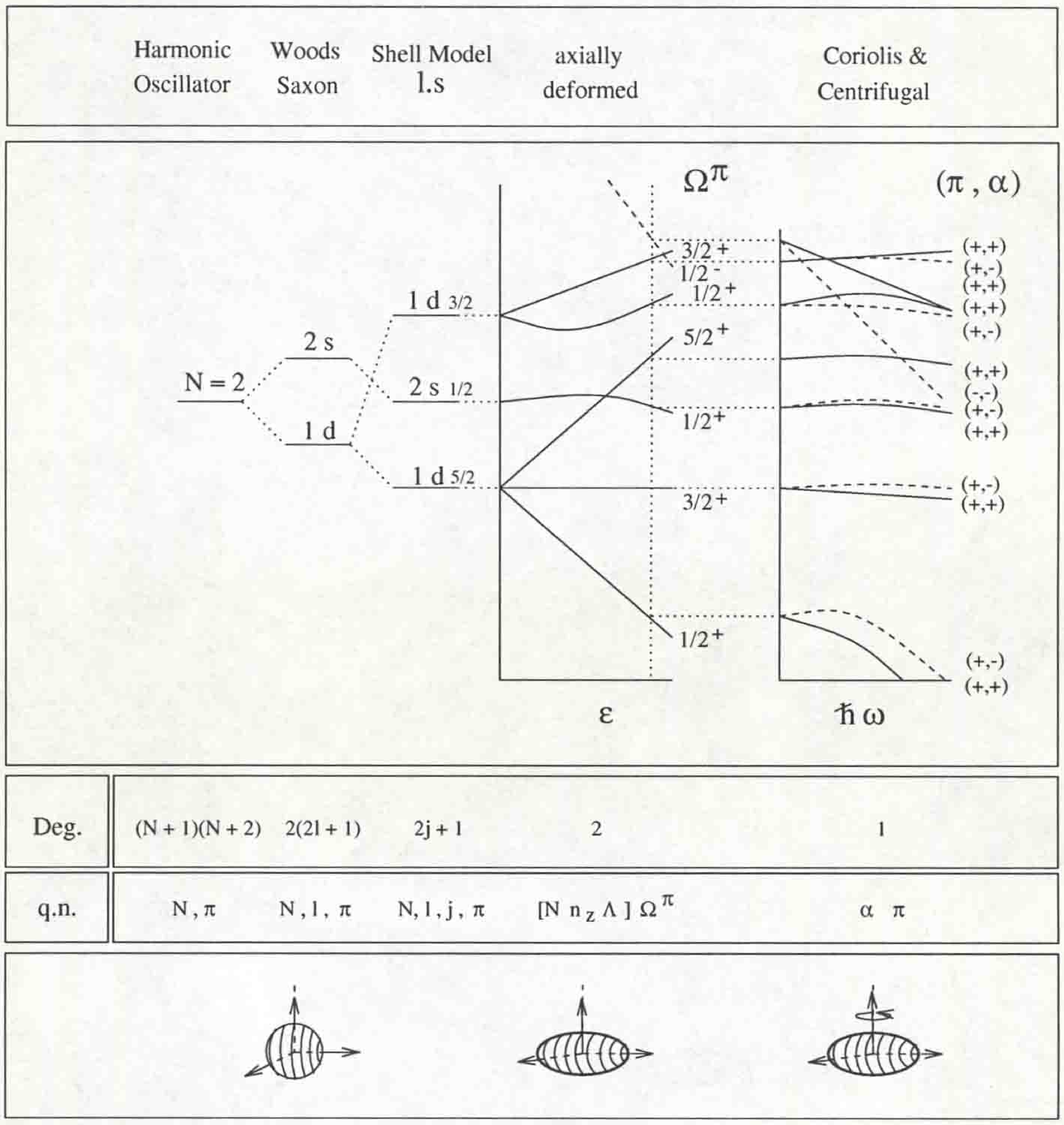

Figure 2.1: The evolution of the nuclear potential. The degeneracy (Deg) and the quantum number (q.n.) labeling is also shown. The 2s level is unaffected by the spin-orbit interaction (because l=0), but is shown reduced in energy for clarity.

and is shown schematically in figure 2.2.

The harmonic oscillator Hamiltonian $\hat{H}_{sho}$ can then be written

$$\hat{H}_{sho} = \frac{-\hbar^2}{2m}\nabla^2 + \frac{m\omega_0^2}{2}(r^2 - R_0^2) \tag{2.6}$$

where ω_0 is the oscillator frequency, R_0 is the nuclear radius and r is the displacement from the centre of the potential. The energy eigenvalues are given by

$$E_{nl} = \hbar\omega_0(N + \frac{3}{2}) = \hbar\omega_0(2n + l + \frac{3}{2}) \tag{2.7}$$

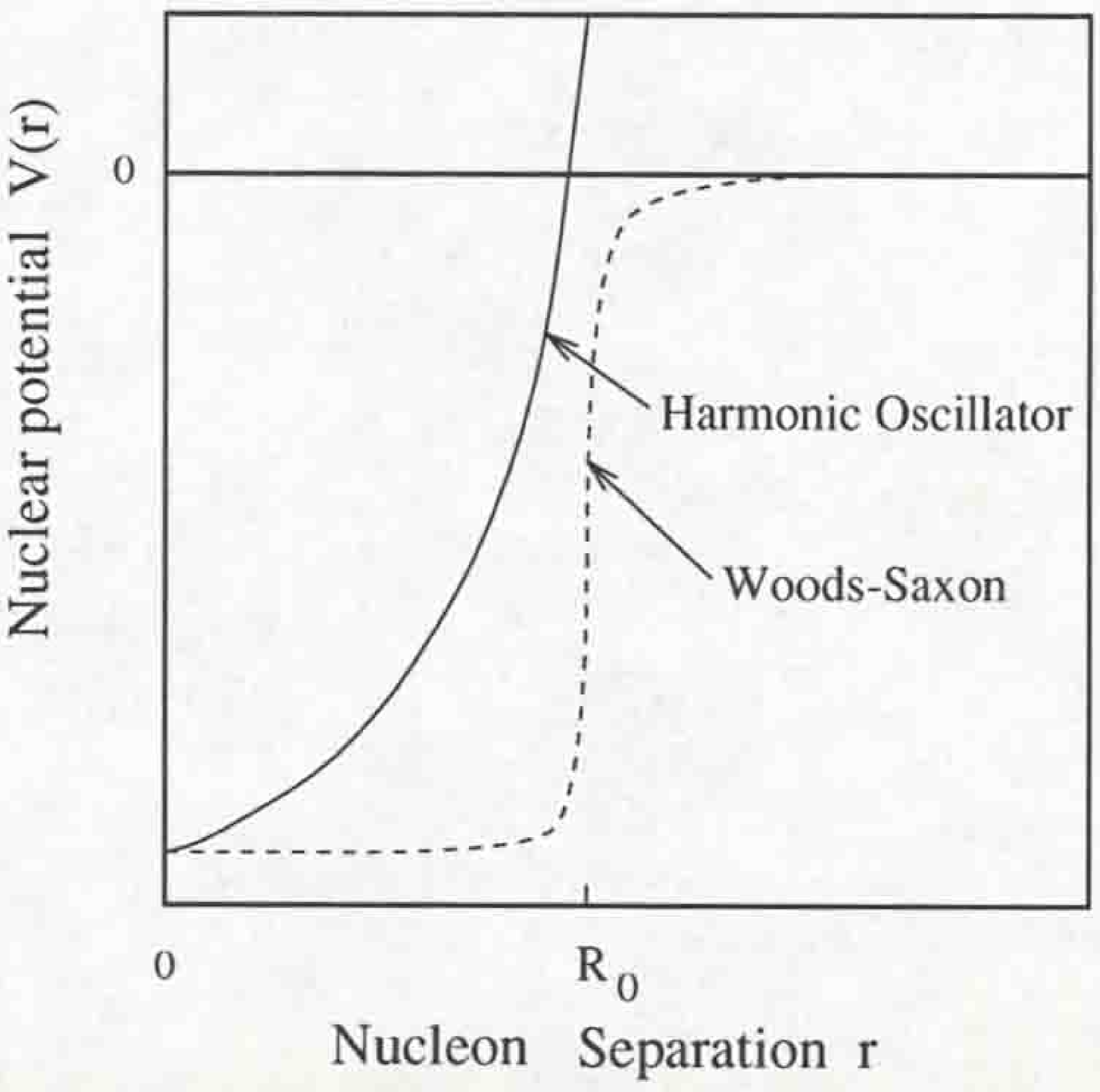

Figure 2.2: The harmonic oscillator and Woods-Saxon potentials. The Nuclear radius R_0 is indicated.

Where N, n and l are the principal, radial and angular momentum quantum numbers respectively. The quantum numbers n and l arise from the spherical harmonics which are required to describe the eigenfunctions. It is clear from the above equation that

1. The energy levels are evenly spaced.

2. All levels in a major shell are degenerate, with a degeneracy $\frac{1}{2}$(N+1)(N+2).

Each oscillator shell only contains states of the same parity, given by

$$\pi = (-1)^N \tag{2.8}$$

Therefore, shells with even N have positive parity and shells with odd N have negative parity. However, for heavier nuclei the shape of the simple harmonic oscillator potential is incorrect; nucleons at the surface of the nucleus should experience a smaller potential than those at the centre - a condition which is not reproduced (the harmonic oscillator potential has infinite values at infinite radii). The next set of modifications (Fig. 2.1) are described by Woods-Saxon potential.

2.2.3 The Woods-Saxon Potential

The degeneracy of the harmonic oscillator is removed by altering its shape to reflect the fact that the nuclear forces have a finite range. So that the condition

$$V(r) \rightarrow 0, r > R_0 \tag{2.9}$$

is met. The Woods-Saxon potential [WS54] reproduces this condition quite well, and is defined by the expression

$$V_{ws}(r) = \frac{-V_0}{1 + exp^{\frac{(r-R_0)}{a}}} \tag{2.10}$$

and is shown in Fig. 2.2. The shape of the potential well is given a flatter bottom and the walls are made steeper. The above expression uses $\mathrm{R}_0 = \mathrm{r}_0\mathrm{A}^{\frac{1}{3}}$ with R_0 the nuclear radius, $\mathrm{r}_0 \approx 1.2$ fm, and *a* gives the surface diffuseness ≈ 0.5 fm. V_0 represents the depth of the potential ~ 50 MeV, which can be adjusted to suit measured separation energies. The nuclear Hamiltonian becomes

$$\hat{H}_{ws} = \frac{-\hbar^2}{2m} \nabla^2 + \frac{-V_0}{1 + exp^{\frac{(r-R_0)}{a}}} \tag{2.11}$$

Although the agreement with the experimentally observed magic numbers is now better, the Woods-Saxon potential still does not reproduce them sufficiently well.

2.2.4 Spin Orbit Coupling

The success of the shell model was really only confirmed by the introduction of a spin orbit term by Haxel, Jensen and Suess [HJS49]. They showed that the inclusion of a spin-orbit interaction term in the nuclear potential could correctly reproduce the experimentally observed magic numbers.

The total angular momentum **j**, of a nucleon is equal to the vector sum of its orbital angular momentum **l**, and its spin angular momentum **s** :

$$\mathrm{j} = \mathrm{l} + \mathrm{s} \tag{2.12}$$

and is illustrated in Fig. 2.3.

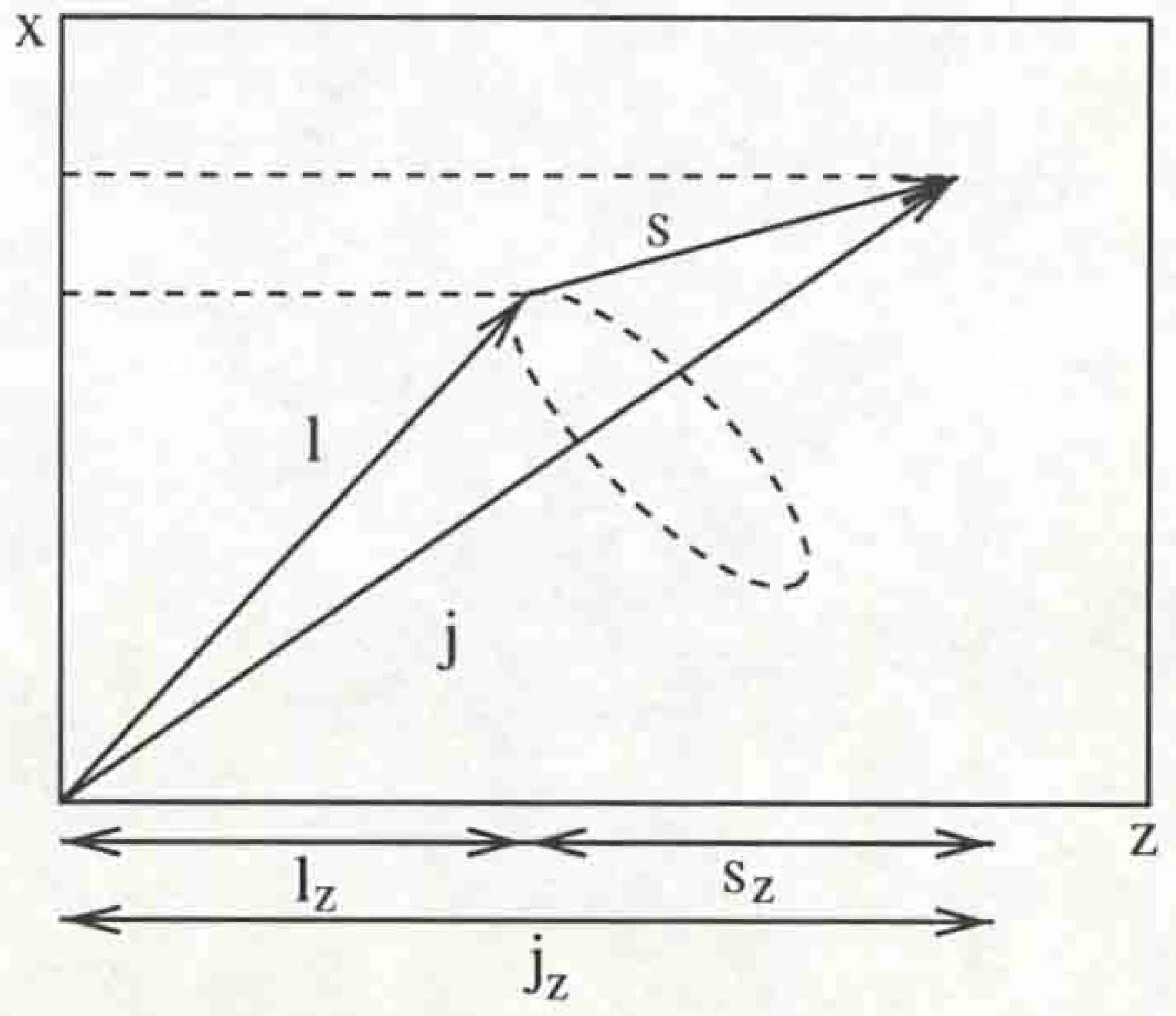

Figure 2.3: Coupling of **l** and **s**. Components on the symmetry axis are shown. Total angular momentum **j** precesses about the symmetry axis. **l** and **s** precess about **j**. l_z and s_z vary. j_z remains fixed.

The spin-orbit coupling is such that it splits the possible energy states into

$$\mathbf{j} = \mathbf{l} - \frac{1}{2} \tag{2.13}$$

and

$$\mathbf{j} = \mathbf{l} + \frac{1}{2} \tag{2.14}$$

such that

$$E_{j=l-\frac{1}{2}} > E_{j=l+\frac{1}{2}} \tag{2.15}$$

i.e. a given l state is split into 2 possible j states, such that the high-j state is lower in energy than the low-j state. This is illustrated for the 1d (N=1, l=2) level in Fig. 2.1.

This is incorporated into the nuclear potential by the spin-orbit potential term $V_{so}(r)$

$$V_{so}(r) = -f(r)\mathbf{l.s} \tag{2.16}$$

where f(r) (a function of r with f(r) $\propto \frac{1}{r}\frac{\delta V(r)}{\delta r}$) controls the strength of the coupling, and **l.s** is the spin-orbit term. The nuclear Hamiltonian now becomes

$$\hat{H} = \hat{T} + \hat{V}_{ws} + \hat{V}_{so} \tag{2.17}$$

$$\hat{H}_{ws} = \frac{-\hbar^2}{2m}\nabla^2 + \frac{-V_0}{1 + exp^{\frac{(r-R_0)}{a}}} - f(r)\mathbf{l.s} \tag{2.18}$$

and correctly reproduces the magic numbers. The inclusion of the spin-orbit (proportional to **l.s**) results in levels being depressed more as l increases. In particular, levels with the highest **j** (**j** = **l** + **s**) are depressed the most by this coupling and generally penetrate into the major oscillator shell below. These depressed states will have opposite parity (see eqn. 2.8) to the states in which they reside, and are called 'intruder orbitals'. They play a particularly important role when the nuclear potential is deformed (Sec. 2.3.2) and when rotation is considered (Sec. 2.4.3).

2.3 Deformation and The Shell Model

2.3.1 Introduction

The shell model considered so far has assumed that the average nuclear field is spherically symmetric. This is not a bad assumption for nuclei which possess a closed shell ('magic nuclei') or are close to a closed shell. However, the experimental evidence of rotational bands and large quadrupole moments indicate the existence of nuclei that possess stable ground state deformation. As a consequence of the non-spherical nuclear shape, an orientation of the nucleus may be specified. In turn, this enables quantum mechanical rotation to be described. Spherical nuclei have already been described by the simple harmonic oscillator potential and the Woods-Saxon potential.

The following section discusses the formulation of a nuclear model to incorporate deformation into the above potentials.

2.3.2 The Nilsson Potential

The deformed average nuclear potential may be described by an anisotropic harmonic oscillator potential. The Nilsson potential is a harmonic oscillator potential modified to take into account the deformation of the nucleus. Nilsson also added further modifications to include a spin-orbit term, and a correction to reflect the flatter potential felt by those nucleons in the centre. The Nilsson potential is defined as

$$V_{osc} = \frac{m}{2}(\omega_x^2 x^2 + \omega_y^2 y^2 + \omega_z^2 z^2) \tag{2.19}$$

where ω_x, ω_y, ω_z are one-dimensional oscillator frequencies in cartesian co-ordinates. The energy difference between major N shells (eqn. 2.7) defines the oscillator frequency ω_0

$$\hbar\omega_0 = 41A^{-\frac{1}{3}} MeV \tag{2.20}$$

which also conserves the volume contained within the nuclear surface :

$$\omega_x \omega_y \omega_z = \omega_0^3 \tag{2.21}$$

The elegance of this potential is in its separation into easily solvable 1-D potentials in x, y and z. The eigenstates are therefore easily calculated and may be characterised by the quantum numbers n_x, n_y and n_z with eigenvalues given by

$$E(n_x, n_y, n_z) = \hbar\omega_x(n_x + \frac{1}{2}) + \hbar\omega_y(n_y + \frac{1}{2}) + \hbar\omega_z(n_z + \frac{1}{2}) \tag{2.22}$$

The deformed simple harmonic oscillator potential may be simplified further by considering only axially-symmetric shapes with the z-axis defined as the symmetry axis:

$$V_{osc} = \frac{m}{2}(\omega_\perp^2(x^2 + y^2) + \omega_z^2 z^2) \tag{2.23}$$

where now $\omega_\perp$ and ω_z are the oscillator frequencies perpendicular and parallel to the symmetry (z) axis.

The deformation is introduced through the parameter ϵ

$$\omega_\perp = \omega_x = \omega_y = \omega_0(\epsilon)(1 + \frac{1}{3}\epsilon) \tag{2.24}$$

$$\omega_z = \omega_0(1 - \frac{2}{3}\epsilon) \tag{2.25}$$

Finally, Nilsson added a spin-orbit term (Sec. 2.2.4) to reproduce the correct magic numbers, and an angular momentum term to flatten the potential. The latter term creates a more realistic 'squarer' potential in order that the nucleons near the surface experience a deeper potential. The Nilsson potential is now defined as

$$V_{nil} = V_{osc} - 2\kappa\hbar\omega_0 \left[\mathbf{l.s} - \mu(l^2 - < l^2 >_N)\right] \tag{2.26}$$

where **l.s** is the spin orbit term and $(l^2 - \langle l^2 \rangle_N)$ is the angular momentum term. κ determines the strength of the spin-orbit interaction and the product $\kappa\mu$ controls the 'squareness' of the potential. The values of κ and μ are chosen so as to reproduce the experimentally observed level sequences.

The effect of this potential on the energy levels depends on the spatial orientation of the orbit. The top half of Fig. 2.4 shows the possible orientation of orbits with j=$\frac{7}{2}$ for prolate and oblate deformations (for clarity, only positive projections are shown).

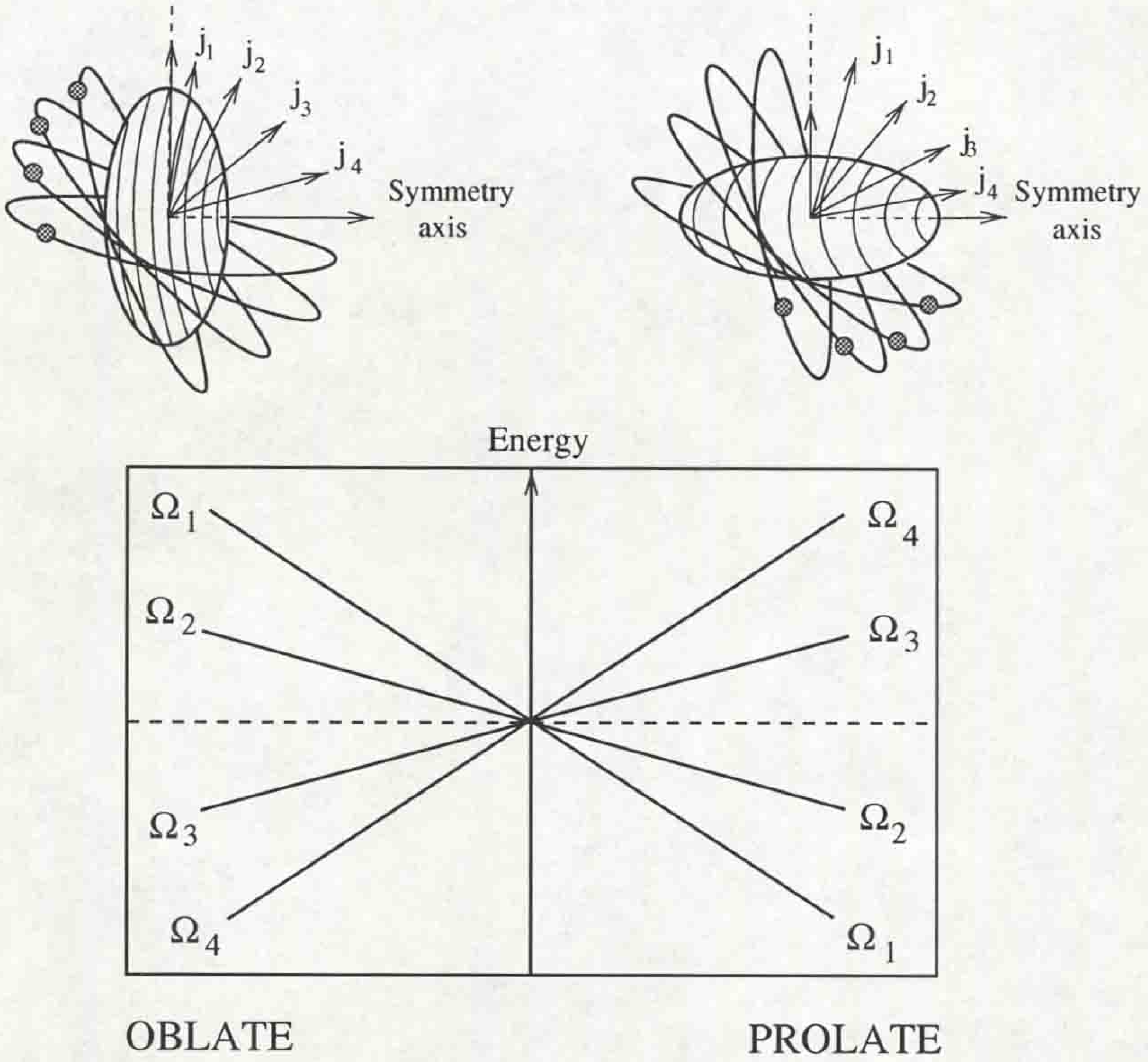

Figure 2.4: The effect of deformation on orbitals depends on the orbits spatial orientation. Ω is the component of the relevant j on the symmetry axis.

A nucleon with j=$\frac{7}{2}$ can have eight possible components of **j** along the symmetry axis : $-\frac{7}{2}$ to $+\frac{7}{2}$. The component of **j** on the symmetry axis is Ω. Because prolate and oblate nuclei have reflection symmetry for either of the two possible directions of the symmetry (z) axis (i.e a rotation of π about an axis perpendicular to z), the components $-\Omega$ and $+\Omega$ are degenerate, so that each Nilsson orbital has a degeneracy of 2. Thus a $j=\frac{7}{2}$ state is split into 4 states with $\Omega=\frac{1}{2}, \frac{3}{2}, \frac{5}{2}, \frac{7}{2}$. The bottom half of Fig. 2.4 shows the effect of deformation (as described by the Nilsson potential) on the various orientations.

For prolate deformation, the low Ω component corresponds to an orbit that interacts closely with the core and is therefore lower in energy (more stable). Conversely, for oblate deformation, the high Ω component is lower in energy. For complete description of orbitals, the Nilsson model uses the following set of quantum numbers.

$$[Nn_z\Lambda]\,\Omega^{\pi} \tag{2.27}$$

where

N = Principal quantum number

n_z = number of oscillator quanta along the axis of symmetry

Λ = Component of orbital angular momentum (**l**) on symmetry axis

Ω = Component of total angular momentum (**j**) on symmetry axis

π = Parity of state = $(-1)^N$

Fig. 2.5 shows the components of **l**, **s** and **j** which are used to identify the Nilsson orbitals.

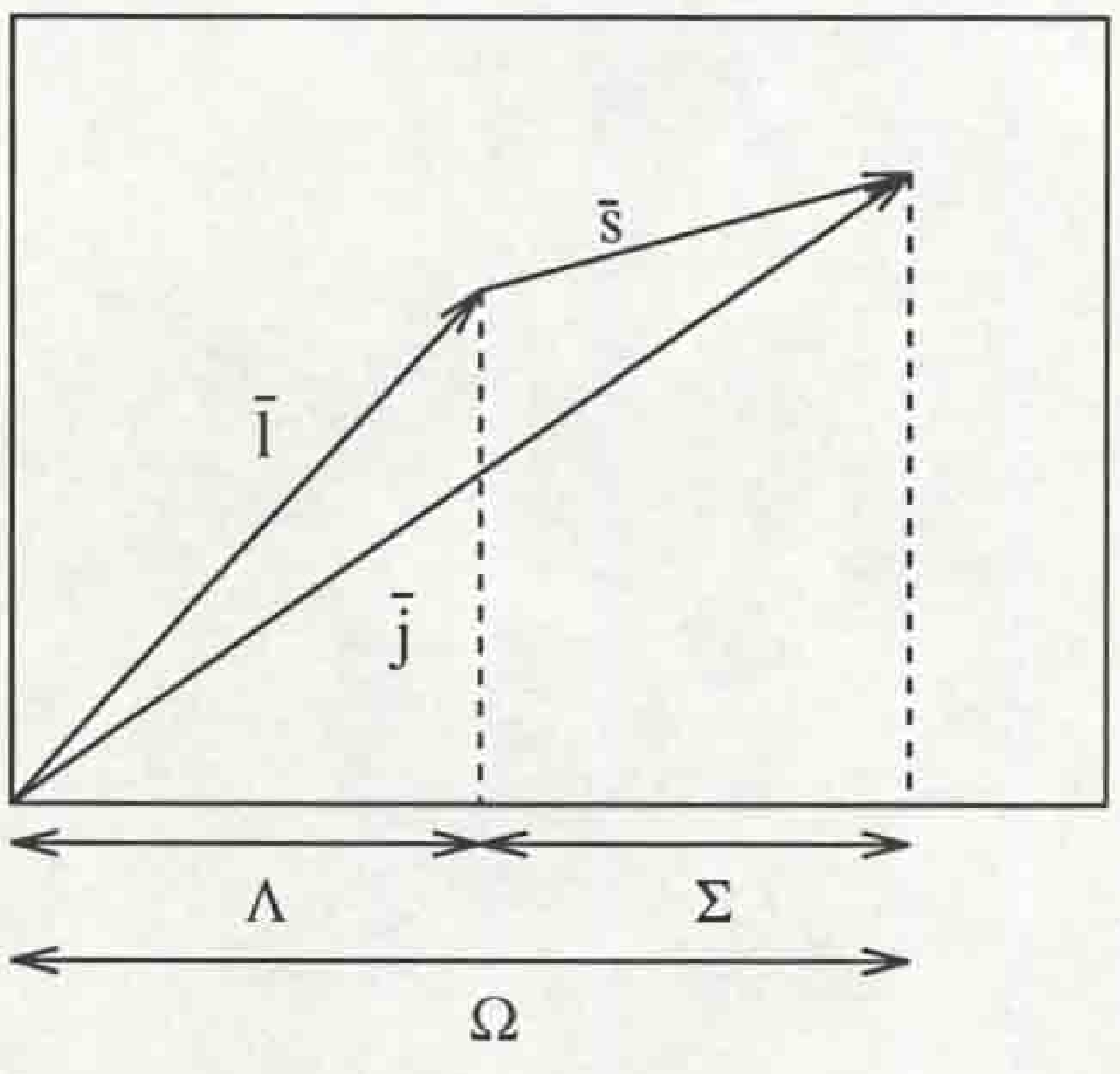

Figure 2.5: Coupling of l and s. Components on the symmetry axis (z) are also shown. These components are used to describe states in the Nilsson model.

It is clear that $\Omega = \Lambda + \Sigma$, where $\Sigma = \pm\frac{1}{2}$ represents the spin of the nucleon in the level. Although the Nilsson potential is relatively successful, the deformed Woods-Saxon potential is a more accurate representation of the nuclear potential, and is therefore more realistic for high-spin calculations. In view of this fact, single-particle diagrams used in this work employ a deformed Woods-Saxon potential. Before proceeding to outline some characteristic features of Nilsson diagrams (whether using a Nilsson potential or a deformed Woods-Saxon potential), the deformed Woods-Saxon potential will be discussed.

2.3.3 The Deformed Woods-Saxon Potential

The motivation behind the development of a deformed Woods-Saxon potential came from the results of the Nilsson Model. The $l^2 - <l^2>_N$ term of eqn. 2.19 was originally only l^2, and was changed by Nilsson because it had the effect of lowering the energy of the high-j orbitals too much in comparison with experimental data. Due to an abscence of an l^2 term in the deformed Woods-Saxon potential, this effect is not present. J. Dudek and T. Werner [DW78] defined the deformed Woods-Saxon potential such that

$$V_{dws}(r,\beta) = \frac{V_0}{1 + exp^{\frac{dist_\Sigma(r,\beta)}{a}}} \tag{2.28}$$

where the dist_Σ(r,β) term is a function of the distance r from the surface Σ of a nucleus with deformation β. As with the spherical Woods-Saxon potential, the complete hamiltonian is described by

$$\hat{H} = \hat{T} + \hat{V}_{dws} + \hat{V}_{so} \tag{2.29}$$

Finally, the above parameters are adjusted in much the same way as with the Nilsson potential in order to reproduce the experimentally determined magic numbers.

2.3.4 Characteristics of Nilsson Diagrams

Fig. 2.6 shows calculated single-particle neutron levels in a deformed Woods-Saxon (W-S) potential.

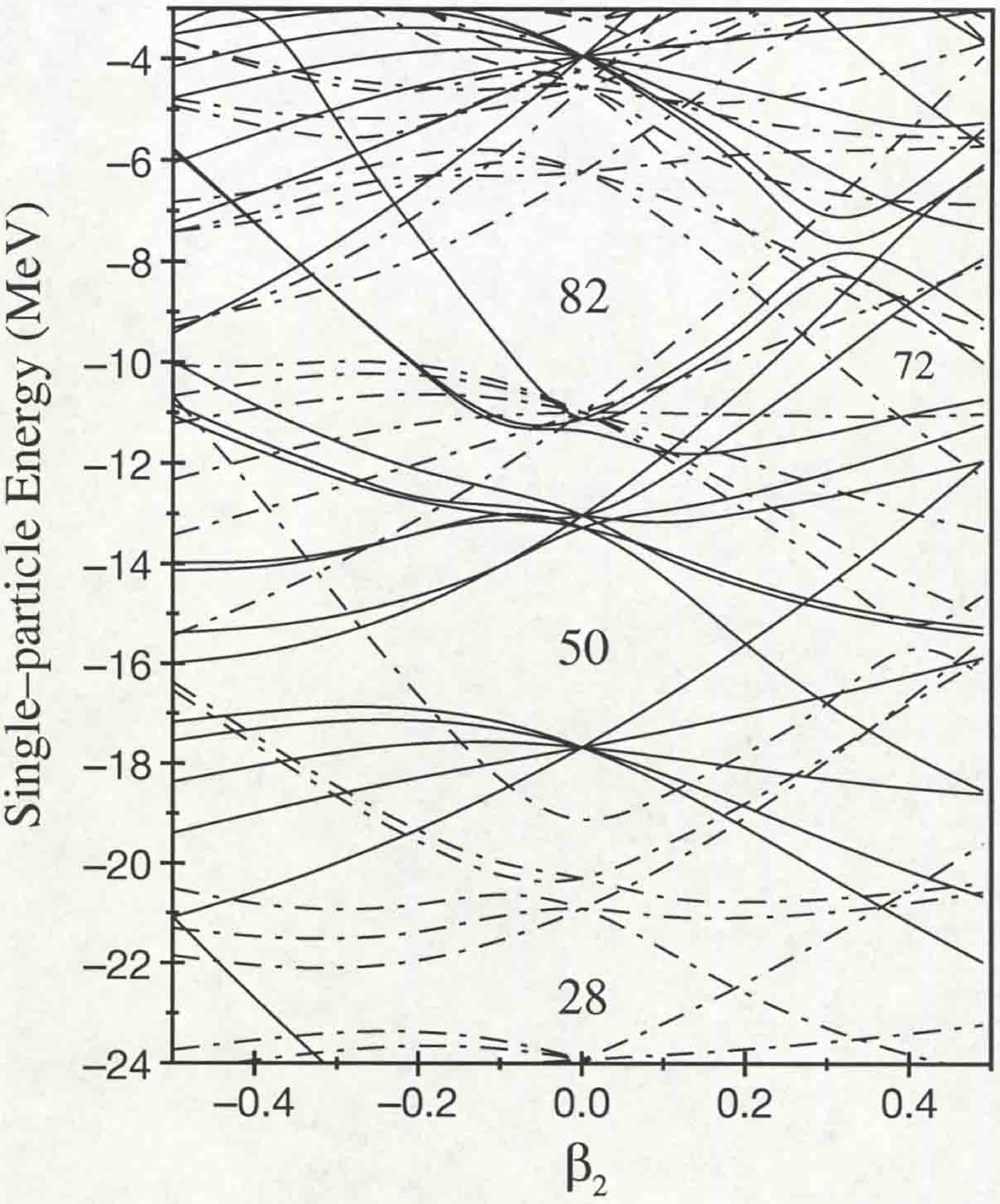

Figure 2.6: Single-particle neutron levels in the deformed Woods-Saxon potential. The magic numbers appear at zero deformation where there are large shell gaps. New shell gaps appear at other deformations. In particular a shell gap appears for N=72 at $\beta_2 \approx 0.4$.

Such diagrams have characteristic features irrespective of whether a Nilsson or deformed W-S potential was used in the calculation :

1. The empirically observed magic numbers appear as regions of low level density in the energy levels at zero deformation.

2. As the potential becomes more deformed, these shell-gaps disappear rapidly, and at certain deformations new gaps can appear which help create stable nuclear shapes at these deformations.

3. The Pauli principle forbids any two levels having the same quantum numbers to

cross. Levels with the same Ω and π therefore interact, and in doing so exchange their properties and trajectories. The remaining good quantum numbers are Ω and π, the other asymptotic quantum numbers act as little more than labels.

4. Orbitals with high j (such as $h_{\frac{11}{2}}$ and $i_{\frac{13}{2}}$) are forced down into the oscillator shell below because of the spin-orbit interaction. These orbitals then reside in a level density of opposite parity and do not interact. This means that their trajectories are unperturbed and this has led to them being called intruder states.

5. Levels with low Ω (high j_x) are lowered in energy for positive (prolate) deformations.

6. Levels with high Ω (low j_x) are lowered in energy for oblate shapes. This makes the generation of angular momentum by single-particle excitation more efficient for oblate shapes when the Fermi surface lies at the bottom of a major shell.

2.4 Nuclear Models of Rotation

2.4.1 Introduction

The study of superdeformation at high spin requires the consideration of single-particle levels in an axially deformed rotating nuclear potential. Fig. 2.1 has already shown the dramatic effect that rotation has upon the s-d levels (l=0 and l=2, respectively), and the following section describes the addition of rotation into the nuclear shell model. To begin with however, a brief consideration of the rotating liquid drop yields some interesting results.

2.4.2 The Rotating Liquid Drop

The analogy between the nucleus and a liquid drop was outlined in Sec. 2.1, but no consideration was given to rotation. The classical mechanics of a 'liquid drop nucleus' reveal that it will possess a spherical shape at rest. However, if the drop is rotated, it is likely to deform. Cohen, Plasil and Swiatecki [CPS74] considered the destructive effects of the centrifugal force on the spherical liquid drop. From their work it is possible to predict the possible angular momentum versus the mass number A for a nucleus, as shown in Fig. 2.7.

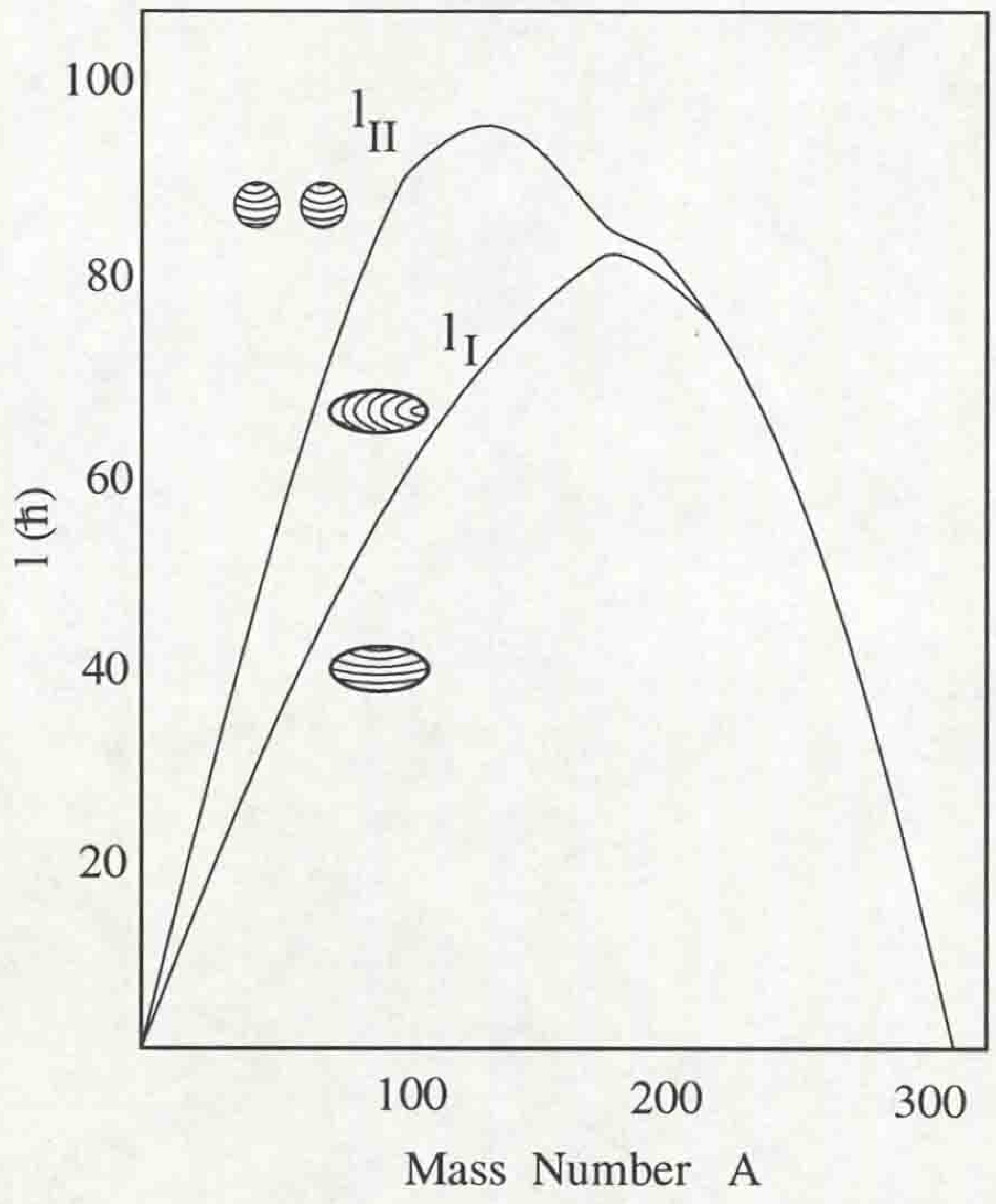

Figure 2.7: Critical angular momenta of the rotation of a liquid drop. Beyond l_I elongated triaxial shapes are possible which fission if l is increased beyond l_{II}

The two critical points are :

- l_I : below l_I, the liquid drop acquires an oblate shape because of the effects of the centrifugal force. Above l_I, the nucleus may lose its stability and describe a series of triaxial shapes (rotating about their smallest axes) leading to rather elongated or superdeformed shapes.
- l_{II} : angular momenta above l_{II} leads to fission. This curve decreases in I for heavier nuclei (A>100) as a consequence of the increased Coulomb repulsion.

Predictions for the majority of heavy nuclei (A≤200, Fig. 2.7) indicate the existence of prolate superdeformed shapes (through a series of elongated triaxial shapes) at high spin, before the system becomes unstable with respect to nuclear fission. However, the superdeformed shapes are not stable, and the predictions need to be modified and refined by the necessary shell structure which is required to stabilise these shapes in the total energy description of the nucleus.

2.4.3 The Cranked Shell Model

The cranked shell model [Ing54] considers particle motion in a rotating potential generated by the collective motion of the nucleus. The single-particle motion is coupled to the collective rotation by the Coriolis and centrifugal forces which modify the energy levels.

For a nucleus rotating about an axis (x) perpendicular to the symmetry axis (z), the transformation from the lab frame to the rotating frame is achieved by means of a rotation operator $\hat{R}$:

$$\hat{R} = exp\left[\frac{-i\omega t j_x}{\hbar}\right] \tag{2.30}$$

The wavefunction of the nucleon in the rotating frame is then

$$\Psi_{lab} = \hat{R}\Psi_{rot} = exp\left[\frac{-i\omega t j_x}{\hbar}\right]\Psi_{rot} \tag{2.31}$$

and the Schrödinger equation in the rotating frame is

$$\hat{H}_{lab}\Psi_{lab} = i\hbar\frac{\delta\Psi_{lab}}{\delta t} \tag{2.32}$$

Differentiation of eq. 2.31 and substitution into eq. 2.32 yields :

$$\hat{H}_{rot} = \hat{H}_{lab} - \omega j_x \tag{2.33}$$

So the effect of the rotation on the single particle Hamiltonian $\hat{H}$ is to add a term $-\omega j_x$ which contains the effects of the centrifugal and Coriolis forces. The Coriolis force modifies the nucleon orbitals by rearranging them in such a way as to align their angular momentum with the rotation axis. The centrifugal force on the other hand, tends to force the nucleons as far as possible from the axis of rotation. Since the Coriolis term (-ωj$_x$) has a different sign depending on whether the nucleon is moving in the direction of, or counter to, the rotation of the nucleus (See Fig. 2.8), for $\hbar\omega > 0$ MeV, time reversal symmetry is broken.

The Hamiltonian corresponding to the laboratory system, $\hat{H}_{lab}$ is supplied as one of the deformed single-particle examples previously considered (Nilsson Hamiltonian or the deformed Woods-Saxon potential). The eigenvalues of the single-particle cranking Hamiltonian are known as single-particle Routhians e', and are defined as

$$e' =< u \mid \hat{H}_{rot} \mid u > \tag{2.34}$$

with

$$e' =< u \mid \hat{H}_{rot} \mid u >=< u \mid \hat{H}_{lab} \mid u > -\omega < u \mid \hat{j}_x \mid u > \tag{2.35}$$

So that

$$e' = e - \omega j_x \tag{2.36}$$

where u represents the eigenstates of the Cranking Hamiltonian.

The total energy E of the system, is represented by the sum of the energies of all occupied orbits plus the contributions from the -ωj$_x$ terms.

Fig. 2.9 shows calculations of theoretical neutron Routhians for ^{132}Ce as a function of rotational frequency, $\hbar\omega$. There are several important features of these single-particle Routhians which are worth pointing out because they are crucial to the understanding of many experimental results.

1. The usual Nilsson levels are observed at $\hbar\omega$= 0 MeV. Each level at $\hbar\omega$= 0 MeV is two-fold degenerate with respect to time reversal symmetry, since the nucleons are paired together. The levels may be labelled at $\hbar\omega$= 0 MeV by the asymptotic Nilsson quantum numbers $[Nn_z\Lambda]\,\Omega^{\pi}$.

2. The two signatures from the same Nilsson level at $\hbar\omega$= 0 MeV, may or may not be split significantly as $\hbar\omega$ increases, depending on how the orbit is coupled to the core (RAL or DAL), (See Fig. 1.5). The effects of the Coriolis and centrifugal forces (-ωj$_x$) are strongest on the most highly-alignable, high-j, low-Ω orbitals.

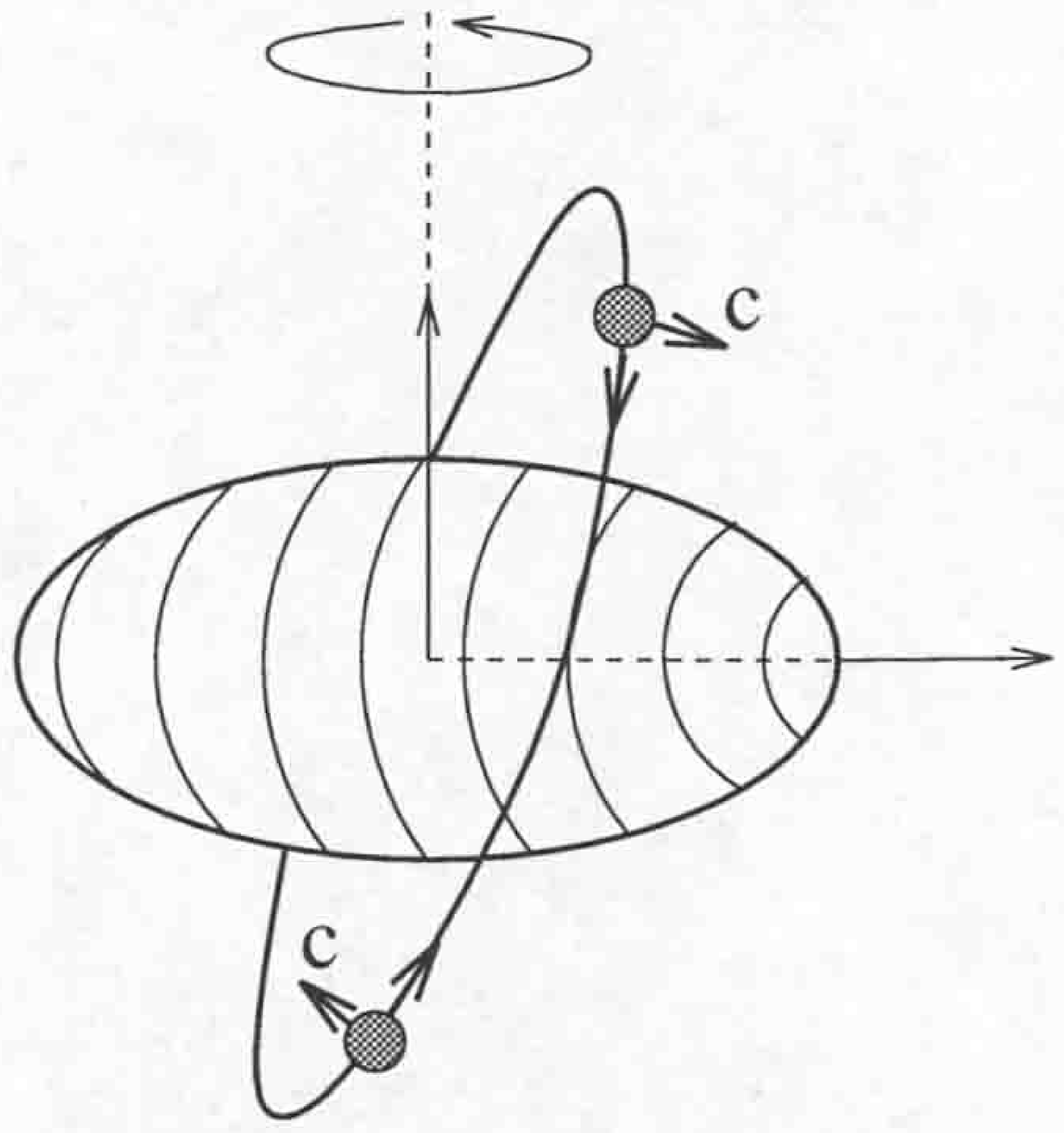

Figure 2.8: Nucleons moving in time-reversed orbits with velocity **v** in a rotating prolate deformed nucleus with angular velocity ω, are subject to the Coriolis force **c**. This force acts in different directions depending on whether the nucleon is moving in the direction of, or counter to, the rotation of the nucleus. The direction of the Coriolis force may be determined from **c** = -2m(ω x **v**)

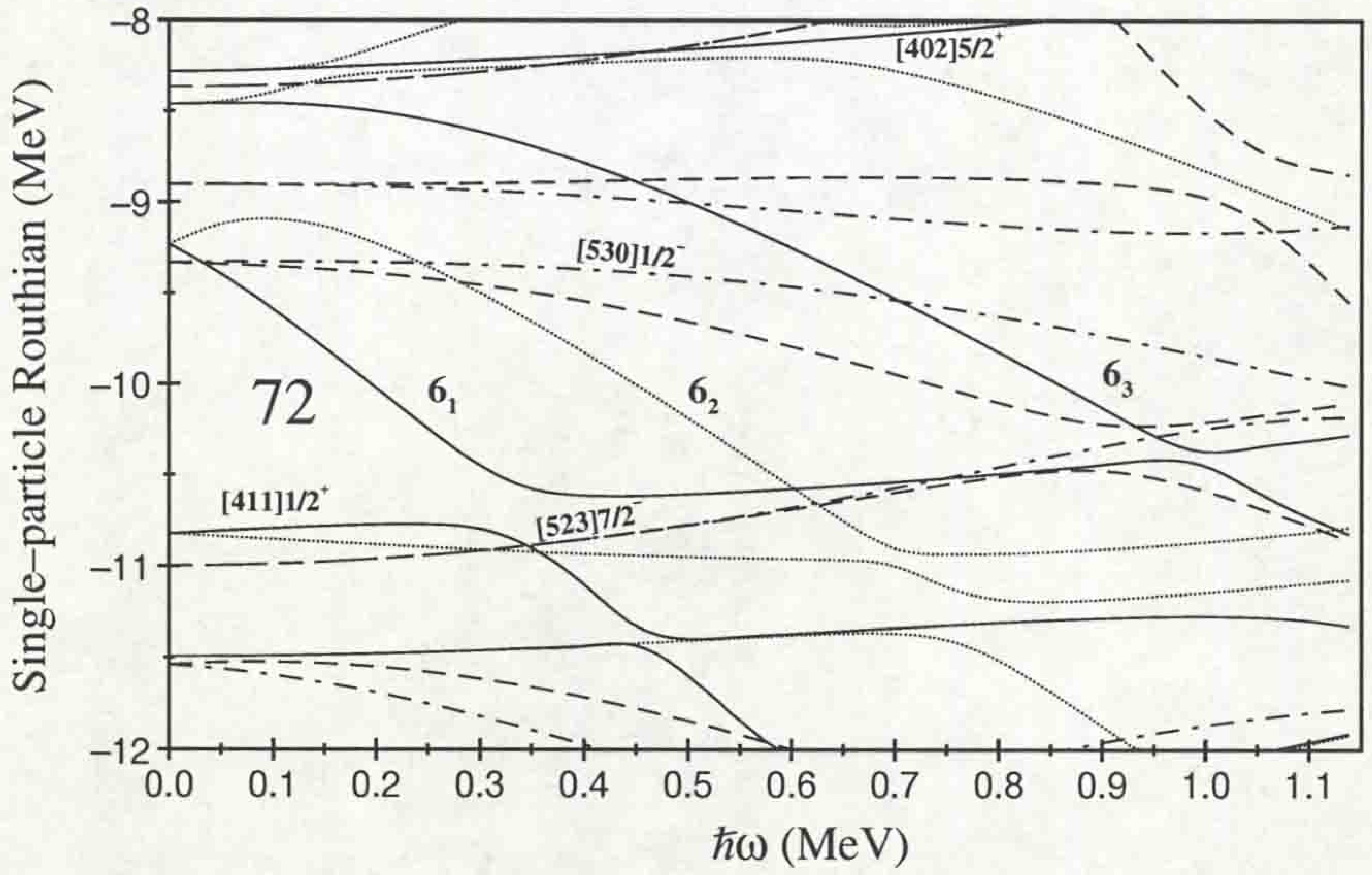

Figure 2.9: Single-particle neutron routhians calculated for ^{132}Ce at β_2 = 0.43, γ=0°. Some important orbitals are labelled by their asymptotic Nilsson quantum numbers. Other labels such as 6_1 etc, indicates the first intruder orbital of the N=6 shell. More correctly, each orbital should be referred to by its parity and signature (π, α) : solid line = (+,+1/2), dotted line = (+,-1/2), dot-dash line = (-,+1/2), dashed line = (-,-1/2).

3. As $\hbar\omega$ increases, a given orbit trajectory may meet another of the same (π, α) with which it will mix. Since nucleons are fermions, the trajectories may not actually cross because this would lead to both nucleons sharing the same energy state with the same quantum numbers. Instead, the levels 'repel' each other and interchange their characters (quantum numbers). Such crossings often result in large changes in experimentally deduced moments of inertia. Consequently, their description in terms of the Nilsson quantum numbers becomes invalid. At frequencies above $\hbar\omega$= 0 MeV, the levels are only correctly labelled by consideration of the possible parities (+ or -) and signatures (+ or -) in the from of (π, α).

The total energy E, of the system is represented by the sum of the energies of all occupied orbits plus the contributions from the $-\omega j_x$ terms.

$$E = \sum_u e'_u + \omega \sum_u < u \mid j_x \mid u > \tag{2.37}$$

A major advantage of the cranked shell model is that it can describe collective angular momentum as a sum of single-particle angular momenta and may therefore be used to describe collective as well as single-particle rotation. The total angular momentum projection on the rotational axis is thus given by

$$I_x = \sum_u < u \mid j_x \mid u > \approx I \tag{2.38}$$

since for high spin, $I_x \rightarrow I$.

Single-particle routhians such as those of Fig. 2.9 illustrate that some orbitals are very sensitive to changes in angular velocity ω. Eqn. 2.35 implies that

$$\frac{de'}{d\omega} = - < u \mid j_x \mid u > = i_x \tag{2.39}$$

So the slope of the single-particle routhian is directly related to the rotational alignment (i_x) of the orbital. Since the high-j, low-Ω orbitals (e.g the $i_{13/2}$ orbitals in Fig. 2.9, labelled as 6_1 indicating the first (1) intruder orbital of the N=6 shell) possess the largest slopes, then these orbitals are the most strongly alignable.

2.4.4 Pairing

In the preceding section, the effect of collective rotation on single-particle orbits was discussed. It was shown that at $\hbar\omega = 0$ MeV, the nucleons are paired and share time-reversed orbits. As $\hbar\omega$ increases, the Coriolis and centrifugal inertial forces gradually remove this symmetry. However, there was no consideration of the short range attractive forces that exist between the paired nucleons. The existence of these forces resist the removal of such pair correlations, and has considerable experimental evidence.

1. All even-even nuclei have ground state spins of $I=0\hbar$, indicating that the nucleons are arranged in such a way that their angular momenta cancel out. The ground state spins of odd-A nuclei are determined solely by the spin of the last nucleon.
2. The energy spacing between the ground state and the first non-rotational excited state in even-even nuclei is consistently greater than 1 MeV. In odd - A nuclei the spacing is much reduced.
3. Nuclear moments of inertia derived from rotational bands are consistently $\approx$ 30% of the rigid body value, indicating the existence of pair correlations.
4. The binding energy of an odd - even nucleus is always found to be smaller than the mean binding energy of the two neighbouring even - even nuclei; an indication of complete pairing in the even A nuclei.

A somewhat classical picture of paired nucleons is shown in Fig. 2.10. The nucleons can be considered as occupying time-reversed orbits; interacting twice per orbit and subsequently being scattered into a different pair of time-reversed states. In the deformed nucleus, where the degenerate components of j are split, this scattering results in the occupation of levels of different energies and the Fermi surface is 'smeared' out. This smearing removes the sharply defined division between particle and hole states which is present when there are no pairing correlations. In the vicinity

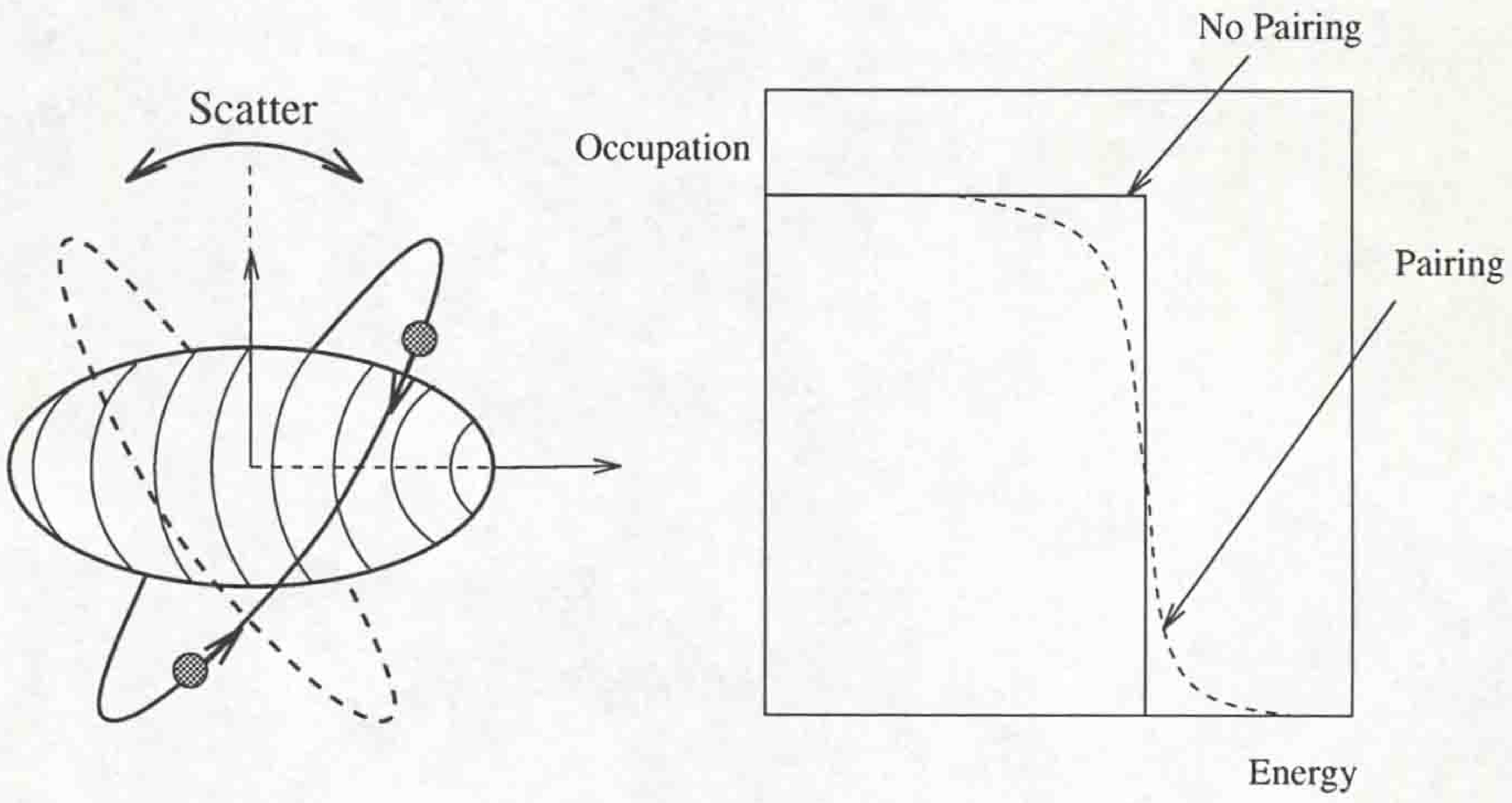

Figure 2.10: Nucleons occupying time-reversed orbits interact twice per orbit and scatter into a different pair of time-reversed states. This scattering into other orbits smears out the Fermi surface.

of the smeared Fermi level it is more appropriate to discuss excited states in terms of their particle and hole occupation probabilities. For this reason, the concept of quasiparticles is introduced.

2.4.5 Quasiparticles

Quasiparticles are fictitious mathematical constructions, and are neither particles nor holes, but are linear combinations of particle and hole wavefunctions. The particle-hole character of the quasiparticle is explicitly expressed in the eqn. 2.40

$$U_j^2 + V_j^2 = 1 \tag{2.40}$$

where U$_j$ is the particle and V$_j$ is the hole probability amplitudes. The total probability of the state being a hole, particle or a mixture of both must be unity. The quasipaticle approach is known as the Hartree-Fock-Bogolybov (HFB) formalism, and has been discussed in many publications (e.g [Goo76, BF79, BMR73, BT73, Cas82]). It is assumed that the nucleus has an axial symmetric shape, such as shown in Fig. 1.4. The rotational axis and collective rotation are dealt with using the HFB hamiltonian:

$$\hat{H}_{qp} = \hat{H}_{sp} - \Delta(P^{+} + P^{-}) - \lambda\hat{N} \tag{2.41}$$

$\hat{H}_{sp}$ is the single particle hamiltonian as defined in eq. 2.33. Δ (P^{+}+P^{-}) represents the pairing correlations where P^{+} and P^{-} are total creation and annihilation operators for the nucleus and Δ is the pairing gap. This pairing term is a two body operator because of the nature of quasiparticle calculations. The calculations simultaneously describe both the particle and hole states; if a rearrangement is made in the occupation of the particle states, the equivalent rearrangement must be made amongst the hole states. i.e. when a quasiparticle is created in state E, a quasiparticle must be annihilated in the corresponding hole state E′.

The quantity λ is referred to as the Fermi energy as it represents the increase in energy with particle number N. λ determines the expectation value of the particle number operator $\hat{N}$. Quasiparticles are analogous to Cooper pairs (electron pairs) used to describe super conductivity in the Bardeen Cooper Schreiffer (BCS) theory ([BCS57, BM58]). BCS treatment can be used to obtain an expression for the excitation energies e_ν, of the quasiparticles with respect to the Fermi level λ : the Fermi level being a common reference energy for the particle and hole states.

$$e_\nu = \sqrt{(e'_\nu - \lambda)^2 + \Delta^2} \tag{2.42}$$

where e'_ν is the single-particle energy of the state and Δ is the pairing gap.

Cranked shell model calculations involving quasiparticles are usually presented as diagrams of the Routhian (e_ν) as a function of rotational frequency ($\hbar\omega$).

Fig. 2.11 is an example of such calculations performed for the parameters appropriate for the yrast superdeformed band in ^{132}Ce (Sec. 5.2). There are several features worth discussing.

1. As with the cranked shell model, the Nilsson labels are not fully adequate for specifying the energy (quasiparticle) states of a rotating nucleus. Although the Nilsson labels may still be used at $\hbar\omega = 0$ MeV, quasiparticle states are labelled using parity and signature in the form (π,α).

2. The quasiparticle diagrams are constructed relative to a reference configuration. This reference configuration (also called the 'vacuum') is represented by all

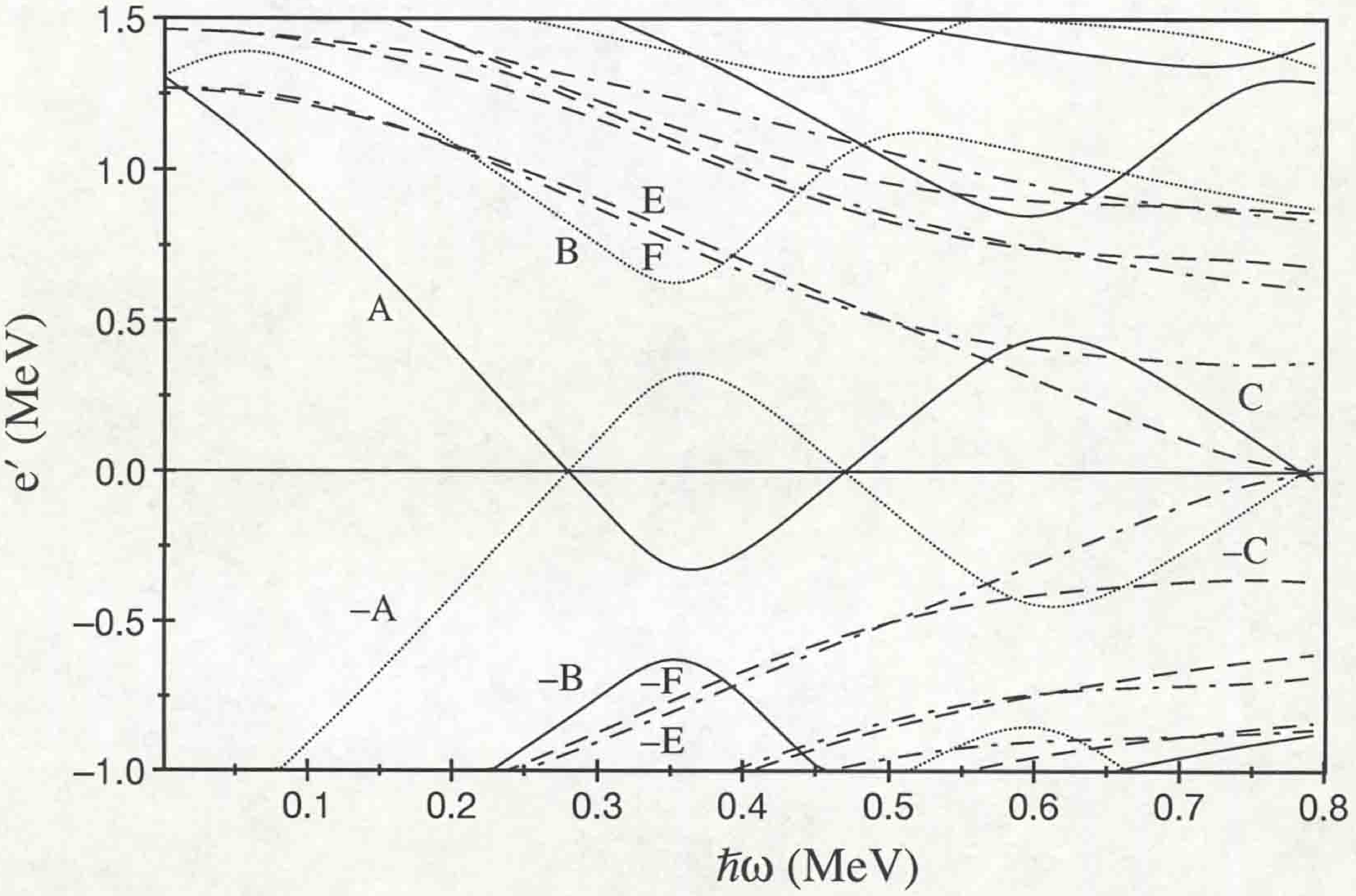

Figure 2.11: Quasineutron calculations for ^{132}Ce at $\beta_2 = 0.43$, γ=0°. Each orbital is referred to by its parity and signature (π, α) : Solid lines = (+,+1/2), dotted lines = (+,-1/2), dot-dash lines = (-,+1/2), dashed lines = (-,-1/2). Additional labels A,B,C,D are used to identify the first four high-j intruder levels above the Fermi surface. The levels of opposite parity are labelled E,F,G... . Conjugate partners are labelled -A,-B,-C...

negative energy levels filled. The excitation energy with respect to this vacuum is the sum of the energies of the occupied physical states.

3. If a level is occupied, then the conjugate level is free. The conjugate level is the reflection of the level through $e'_\nu = 0$ MeV, resulting also in a change of signature ($\alpha \rightarrow -\alpha$).

4. A quasiparticle excitation occurs when a level at e'_ν is occupied, freeing its conjugate partner. This results in a change of energy : an excitation.

5. Quasiparticle trajectories with the same (π,α) do not cross, but approach each other and interchange character. The frequency at which this occurs is referred to as the crossing frequency, and represents a band crossing (the crossing of two

bands built upon different configurations).

6. For a crossing to take place between a level A and the level B (the AB crossing), both of the quasiparticle trajectories must be unoccupied. If one of the trajectories is occupied, it is said to 'block' the crossing.

As an example of the interpretation of band crossings, consider the AB neutron crossing on Fig. 2.11. The energy required to break a pair of quasineutrons is represented by the energy gap at $\hbar\omega$=0 MeV. When the nucleus is rotated, the Coriolis and centrifugal effects (Sec. 2.4.3) decrease the energy of the high-j, low-Ω orbits (A and B), bringing them closer to the Fermi surface. When it is energetically favourable to do so, quasiparticles from the core may be excited into orbits above the Fermi surface. For orbits A and B, this will correspond to the point where the sum of the energies of the orbits become zero, i.e.

$$e'_\nu(A) + e'_\nu(B) = 0 \tag{2.43}$$

This excitation therefore corresponds to the scattering of a pair of quasineutrons from some orbits in the core into a pair of $i_{13/2}$ quasineutron orbits. Beyond the crossing frequency, the configuration based upon an aligned pair of $i_{13/2}$ quasineutrons becomes yrast. This constitutes a sudden change in the structure of the nucleus, and its effects can be observed in the $\Im^{(2)}$ moment of inertia (to be discussed in Sec. 5.3).

This AB crossing is important in this work as its effects are dramatically observed in the yrast superdeformed band in ^{132}Ce. The quasiparticle approach is particularly useful in predicting such band crossings, but as with its no-pairing single-particle counterpart, the slope of the quasiparticle routhians also represent the rotational alignment of the orbitals.

2.4.6 The Strutinsky Shell Correction & Total Rothian Surfaces (TRS).

Two approaches have been discussed to model the nucleus in the preceding sections. The liquid-drop model is a collective model which recognises the existence of strong interactions between nucleons, but has no features that reflect the nuclear shell structure. In the opposite situation, the shell model is an independent particle model in which it is assumed that individual nucleons have little interaction with each other. The disadvantage of the shell model is that the sum of the single-particle energies do not agree with the total energy estimates of the liquid-drop model.

The Strutinsky procedure [Str66, Str67] is a method which combines both collective and single-particle approaches, and results in a total energy description of the nucleus that can be used to predict regions of stability in terms of deformation. In effect, the Strutinsky shell-correction superimposes the single-particle energy oscillations onto the total energy from the liquid drop.

The energy of the shell model U, can be divided into two parts: $\bar{U}$ and δU.

1. $\bar{U}$ is a contribution that represents a smooth density of states.
2. δU (called the shell correction) is an oscillatory contribution that describes the uneven level density distribution; i.e. the bunching of energy levels into shells.

The shell correction δU, can be expressed thus :

$$\delta U = U - \bar{U} \tag{2.44}$$

The shell model energy U, and the smooth contribution $\bar{U}$, are simply obtained by summing all occupied energy levels. U is dependent upon an oscillatory level density function, whilst $\bar{U}$ is dependent on a 'smeared' (or averaged) level density function. The total energy of the nucleus W, can be determined by combining the shell correction with the liquid drop energy U_{LD} :

$$W = U_{LD} + \delta U \tag{2.45}$$

Stable nuclear deformations may be found by obtaining the minimum values of W from Eqn. 2.45. For magic nuclei (Sec. 2.1) stable deformations will correspond to spherical shapes. However, at some deformations, areas of low level density in the shell structure may result in a minimum W, which is lower than that obtained by the nucleus when it is spherical. In this situation, the nucleus will exhibit stable ground state deformation. More importantly, minima in the total energy may exist at very large deformations in addition to the ground state miminum. The Strutinsky procedure can be generalised to include additional rotational energy [And76] by;

1. including a rotational term in the liquid drop model energy, $U_{LD} \rightarrow U_{RLD}$.
2. calculating U and $\bar{U}$ using level density functions that incorporate the effects of rotation upon the energy levels : i.e. the energy levels become Routhians. This produces a new shell effect term, $\delta U \rightarrow \delta U_I$.

The total energy at a given spin W_I, is thus determined by

$$W_I = U_{RLD} + \delta U_I \tag{2.46}$$

The total energy of the nucleus as defined by eqn. 2.46, can no longer be expressed in terms of merely deformation, because spin is no longer a constant. It is usually displayed in the form of a contour plot or 'Total Routhian Surface' (TRS), parameterised by the deformation β_2 and γ; with the contours denoting the energy. Fig. 2.12 shows various segments of the β_2-γ plane; each segment representing a different frequency.

2.5 Introducing Superdeformation (SD)

It was shown in Sec. 2.2.2 that the harmonic oscillator potential was a useful starting point in an attempt to describe the nucleus. It was unsuccessful however, because it failed to reproduce the magic numbers obtained from experimental evidence. However, this simple nuclear potential still provides an insight into the origins of stable deformed nuclear shapes. When the nuclear potential is deformed, a new set of shell gaps appear at deformations given by the integer ratios of nuclear axes 3:2, 2:1 and 3:1 (see Fig. 2.13).

With the more realistic Woods-Saxon potential, the regular shell closure structure of the harmonic oscillator is lost, but the strong shell gaps of 1:1, 3:2, 2:1 and 3:1 are

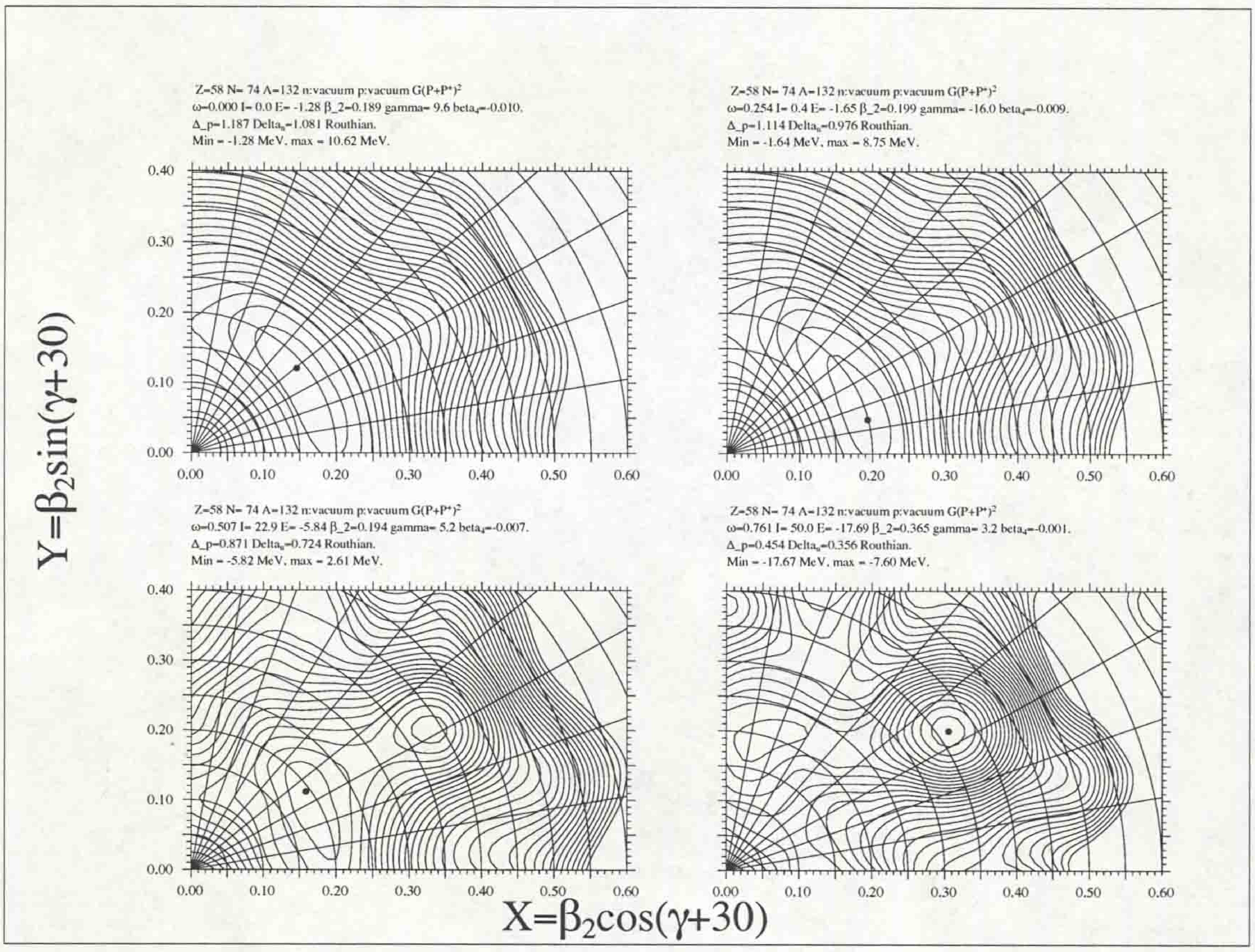

Figure 2.12: Total Routhian Surfaces for ^{132}Ce, parameterised by the deformation β_2 and γ. The development of the prolate superdeformed minimum $\beta_2 \approx 0.4$ can be seen above I=22 $\hbar$ (bottom left). A hyperdeformed minimum ($\beta_2 \approx 0.7$) is also observed to be developing in the top right hand corner at I=50 $\hbar$ (bottom right).

still produced. Fig. 2.6 in Sec. 2.3.4 shows the new shell gaps at $\beta_2 \approx 0.4$ (3:2 axis ratio), which for N=72 is partly responsible (see Sec. 5.3) for the stabilisation of the superdeformed bands in ^{131,132}Ce, detailed in this work.

The TRS calculations for ^{132}Ce (shown in Fig. 2.12), indicate that at low spin, the minimum energy that the nucleus can achieve results in a deformation of $\beta_2 \approx 0.2$ (i.e. not spherical even in it's ground state). At higher spins however, this minimum soon becomes shallower, and this is accompanied by the development of a new minimum at a higher deformation of $\beta_2 \approx 0.4$ (now more prolate in shape). Nuclei that are observed to decay via states in these second minima are known as 'superdeformed'

(SD) nuclei.

The first superdeformed nuclei to be observed were the fission isomeric nuclei such as ^{240}Pu [Pol62, SW72, Met80]. Their deformation is due to electrostatic stress : it is primarily a result of the Coulomb repulsion due to the abundance of protons (shell effects also help to stabilise the deformation). These heavy nuclei were observed to decay from excited states with anomalously short half-lives when compared with the half-lives of spontaneous fission from nuclear ground states (Fig. 2.14).

The first observed superdeformed nuclei populated at high spin were ^{132}Ce [Nol85, Kir87] and later ^{152}Dy [Twi86]. The deformation of these nuclei is a result of the centrifugal force which is present due to the high-spin collective rotation.

There are now known to be three main mass regions were superdeformed nuclei at high spin may be produced : A $\approx$ 130,150 and 190 (the recent first observation of superdeformed nuclei in the Mass A $\approx$ 80 region [Bak95] is omitted in the following discussion). Superdeformed properties specific to the three main mass regions will now be outlined, but the yrast superdeformed band in ^{132}Ce will be used to illustrate their more general properties.

2.5.1 The Mass 130 region & Typical SD properties

Superdeformed nuclei in the Mass 130 region are a consequence of the shell gaps which occur for both protons (Z=58) and neutrons (N=72) at nuclear deformations corresponding to $\beta_2 \approx 0.4$ (Fig. 2.15). However, calculations of the potential energy of the ^{132}Ce nucleus, similar to those described in Sec. 2.4.6 (See Fig. 2.16, based on a figure in [Be85]) indicate that the superdeformed minimum only becomes yrast at high angular momentum (I $\approx 45\hbar$). The single-particle energies in this region are not affected too much by the rotation however, and the low level densities required for the stability of the superdeformed nuclei remain (Fig. 2.15). Detailed spectroscopy of the yrast superdeformed band in ^{132}Ce indicates that it posesses an intensity of $\approx$5% that of the total fusion cross section for the ^{132}Ce reaction channel (Sec. 4.7.3). This high intensity is not typical of superdeformed bands in this or any other mass region:

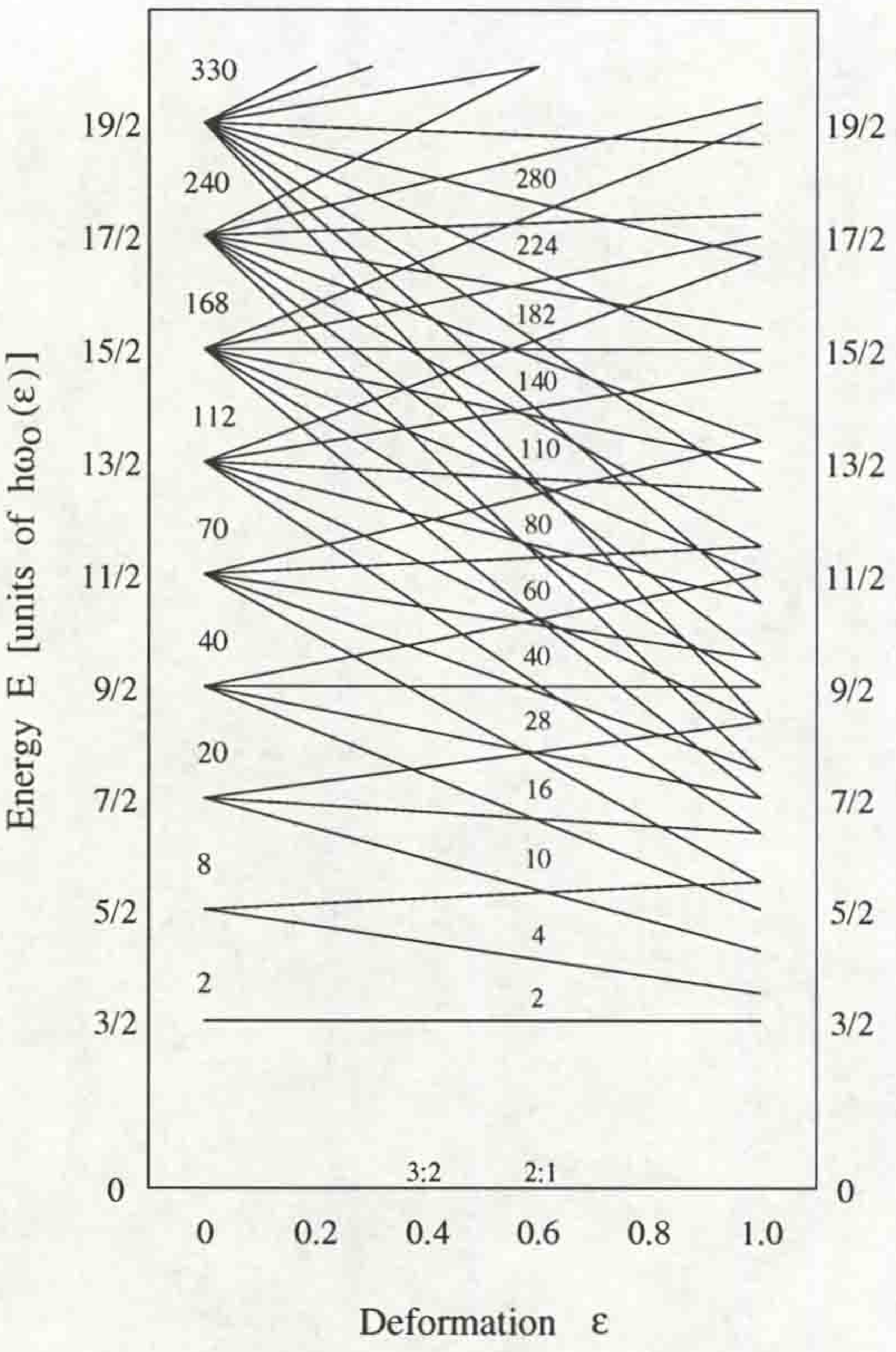

Figure 2.13: Harmonic Oscillator energy levels plotted as a function of deformation. Only levels originating from those shown at ϵ=0 are shown, but already the development of new shell gaps at particular deformations are evident.

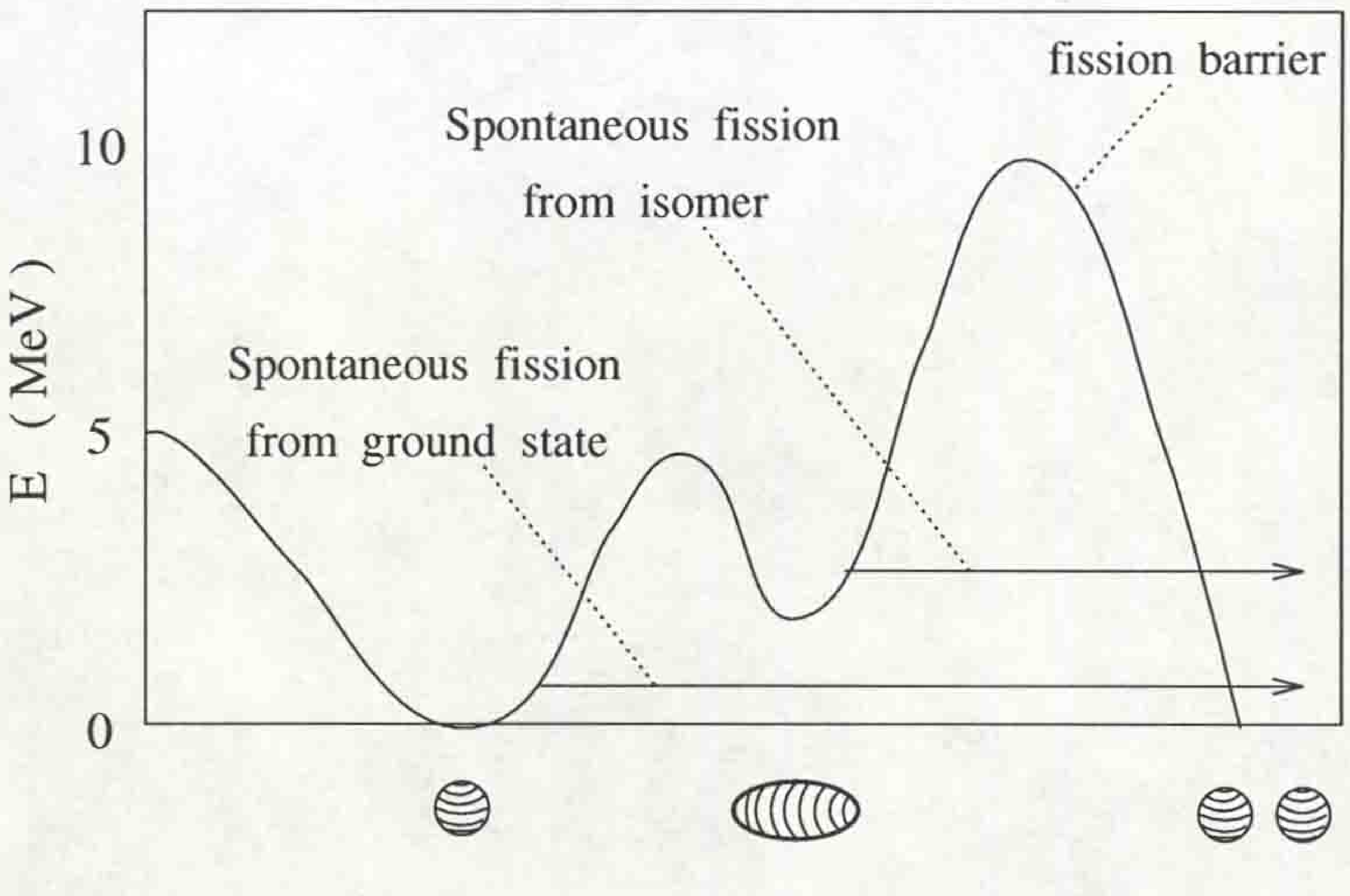

Figure 2.14: A schematic plot illustrating the fission barrier in the total energy surface versus deformation for the fission isomer ^{236}U.

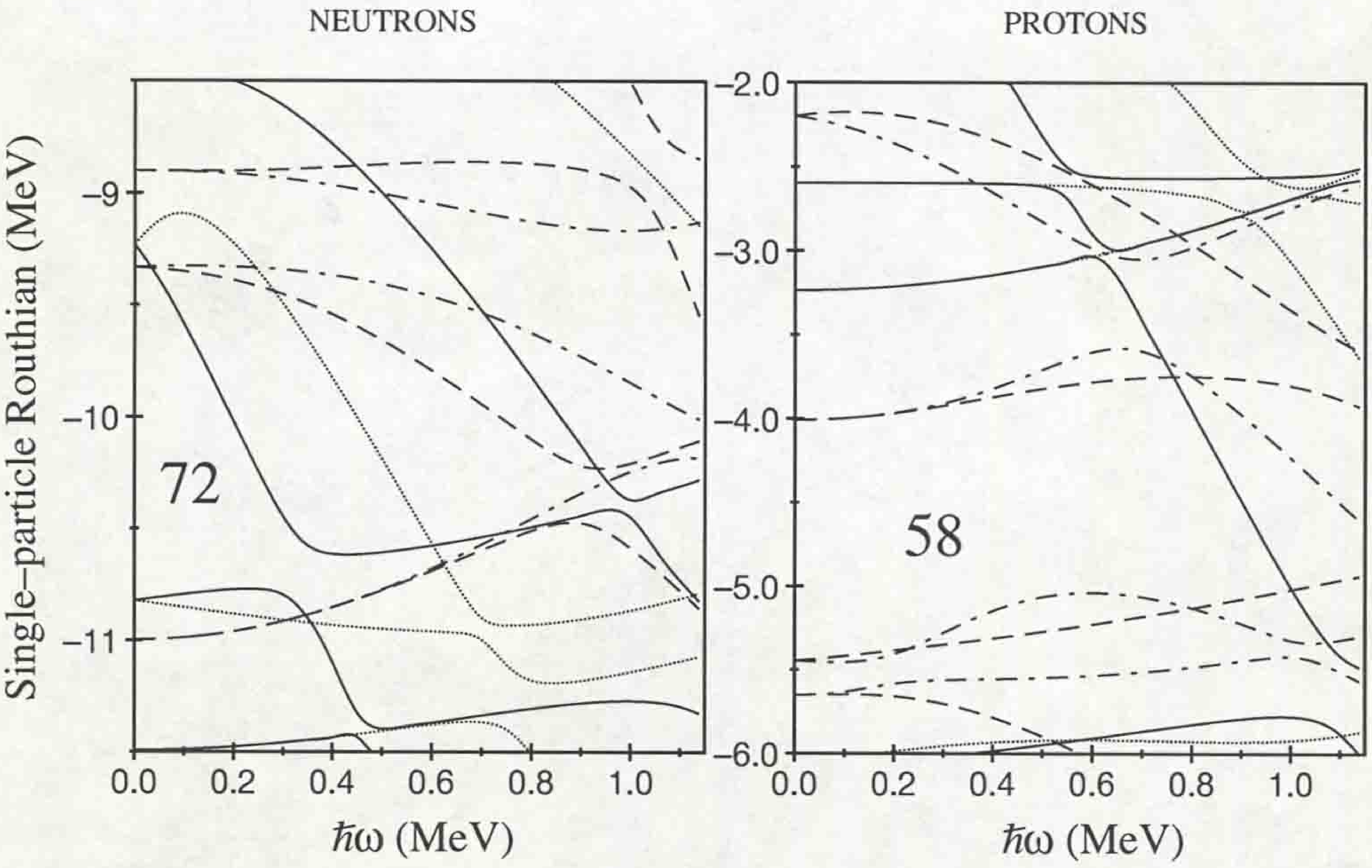

Figure 2.15: Neutron and proton single-particle routhians calculated for the yrast superdeformed band in ^{132}Ce ($\beta_2 = 0.43$). The low energy level densities for N>72 and Z=58 are responsible for stabilising the superdeformed shape.

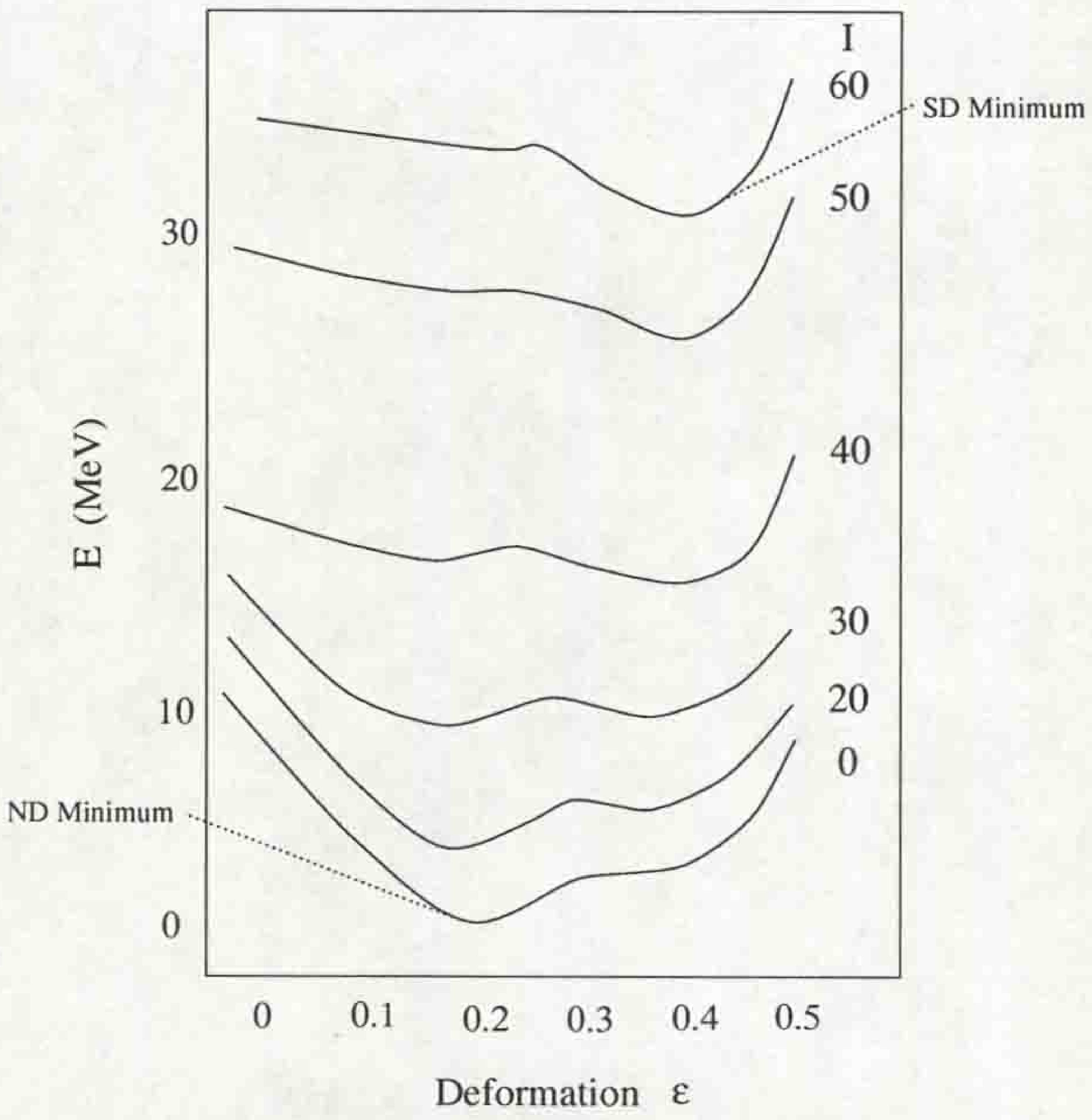

Figure 2.16: Potential energy surface versus quadrupole deformation for ^{132}Ce at constant spins. The secondary potential energy minimum becomes yrast only at higher spins (I ≈ 45-50ℏ).

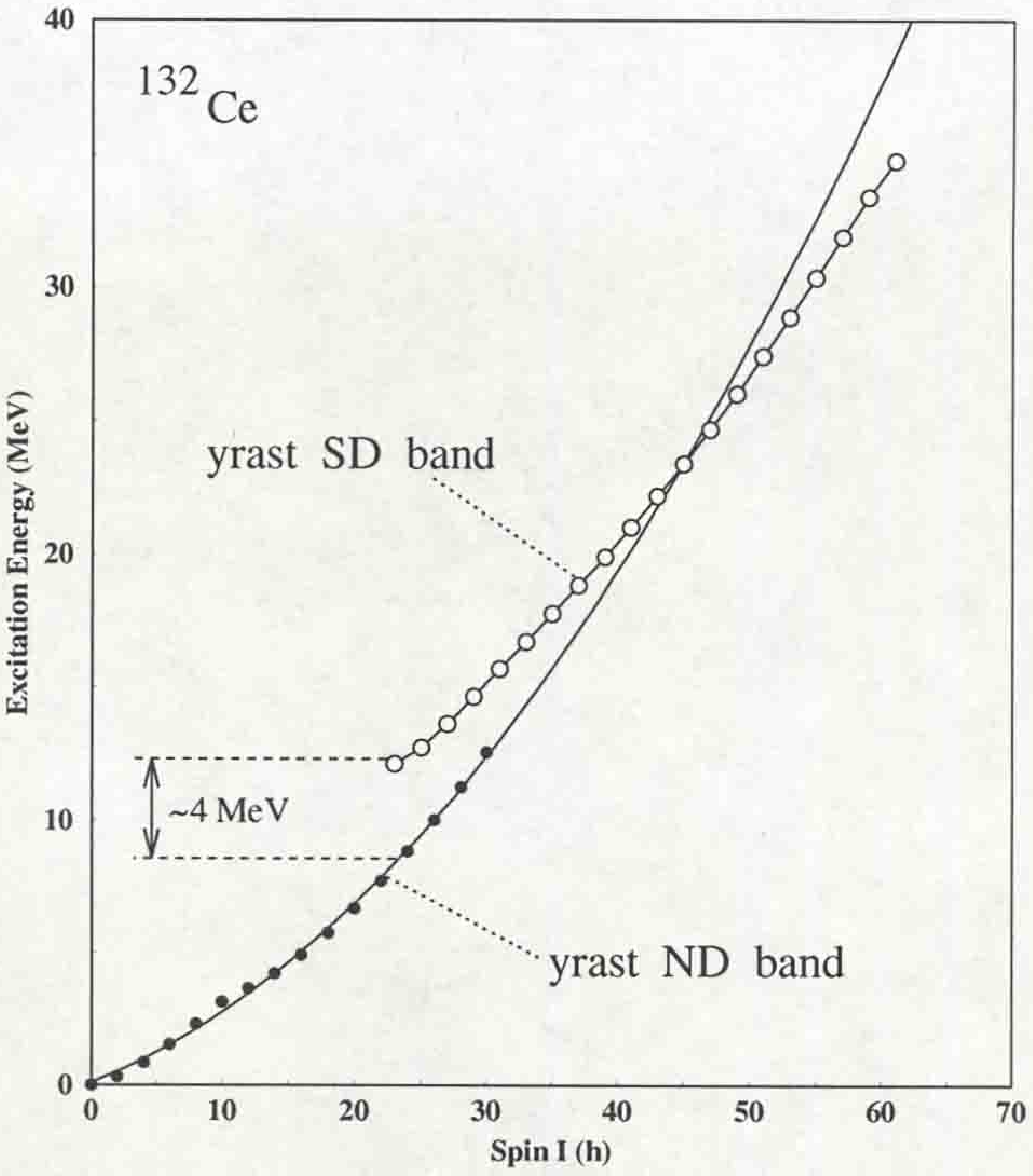

Figure 2.17: Excitation energy as a function of spin for ^{132}Ce yrast SD band. Calculations suggest that the SD band becomes yrast at spin I ≈ $45\hbar$ where it crosses an extrapolation of the ND yrast band. This indicates that the band depopulates at an excitation energy approximately 4 MeV above the ND yrast states.

most have intensities of ≈1% that of their respective reaction channels.

A plot of excitation energy versus spin for ^{132}Ce yrast SD band is shown in Fig. 2.17. The figure assumes that the spins of the SD band are known: they have been deduced from observations of where the band feeds into the normal deformed states, and are probably accurate to $\pm 2\hbar$ (Sec. 4.8).

Calculations the type of Fig. 2.16 indicate the SD band becomes yrast at spin I ≈ $45\hbar$, where it crosses an extrapolation of the normal-deformed yrast line (the normal deformed yrast band extends to spins of I ≈ $30\hbar$). It can be seen from the figure that the superdeformed band is expected to de-excite at an excitation energy of ≈ 4 MeV above the normal-deformed states. At the time of writing, no discrete linking transitions between superdeformed and normal deformed states have been observed, although it is believed that such a decay will proceed via ≈ 2-4 transitions.

The quadrupole deformation of the yrast SD band in ^{132}Ce has been determined from mean lifetime experiments to be $\beta_2 \approx 0.43$ [Kir87] which corresponds to a 3:2 axis ratio (a typical deformation for the Mass 130 region).

2.5.2 The Mass 150 region

Superdeformed nuclei in this mass region have many similar properties to those outlined above in the mass 130 region. Large shell gaps occur for both protons (Z=66) and neutrons (N=86). These shell gaps are in particular responsible for the stabilisation of the superdeformed band in the doubly magic (for these prolate deformations) nucleus ^{152}Dy. Lifetime measurements on ^{152}Dy yrast SD band yielded a quadrupole deformation of $\beta_2 \approx 0.66$ [Ben87]. Typical deformations in this mass region are $\beta_2 \approx 0.6$, corresponding to a 2:1 axis ratio.

2.5.3 The Mass 190 region

Superdeformed nuclei in this mass region are stabilised by the Z=80 proton gap and the N=112 neutron gap. The Coulomb potential of these nuclei is large in comparison with nuclei of the A $\approx$ 130 and A $\approx$ 150 regions. This results in the reduction of the fission barrier. The reduced fission barrier in turn restricts the maximum rotational frequency to which the superdeformed bands extend. Typical maximum rotational frequencies are $^{192}\mathrm{Hg} : \hbar\omega \approx 0.4$ MeV, in comparison with $^{132}\mathrm{Ce} : \hbar\omega \approx 1.0$ MeV and $^{152}\mathrm{Dy} : \hbar\omega \approx 0.75$ MeV. At the other extreme, the increased Coulomb potential assists the rotational energy in stabilising the superdeformed shape. Hence, superdeformed bands in the A $\approx$ 190 region extend to low rotational frequencies; $\hbar\omega \approx 0.1$ MeV. A typical minimum rotational frequency in the A $\approx$ 130 and A $\approx$ 150 region is $\hbar\omega \approx 0.3$ MeV.

Lifetime measurements of the superdeformed bands [HW92] indicate that these nuclei have quadrupole deformations of $\beta_2 \approx 0.45$, implying an axis ratio of 1:1.65.

2.6 Other Superdeformed Phenomena

2.6.1 Excited Superdeformed Bands

The superdeformed band in ^{132}Ce as discussed in Sec. 2.5.1, is built upon its lowest energy configuration and is therefore termed yrast. However, it is possible that other superdeformed bands may exist in the same nucleus which are built upon excited configurations. These bands are therefore produced by exciting a neutron and/or a proton into a higher energy level, thus altering its single-particle configuration and producing a new rotational band.

The observation of excited bands gives information about the single-particle levels near the Fermi surface, and this can be used to test theoretical predictions.

2.6.2 Identical Superdeformed Bands

With the discovery of excited superdeformed bands came a new and intriguing phenomenon. It was observed that superdeformed bands in one nucleus (e.g. mass A) could sometimes have an identical $\Im^{(2)}$ moment of inertia to superdeformed bands in a neighbouring nucleus (e.g. mass A+1).

A similar $\Im^{(2)}$ implies a similar spacing of transition energies with a band (eqn. 1.28). It is generally observed therefore, that identical bands have transition energies that lie within a few keV of one of the following

1. **The 'Zero Point Energies'** The transition energies of the band in nucleus A, and the band in nucleus A+1, are identical. These bands are also termed **'directly degenerate bands'**.

2. **The 'Quarter-Point Energies'** The transition energies of the band in A are larger than those in A+1 by 25% of the transition energy spacing in A.

3. **The 'Half-Way Point Energies'** The transition energies of the band in A are larger than those in A+1 by 50% of the transition energy spacing in A.

4. **The 'Three-Quarter Point Energies'** The transition energies of the band in A are larger than those in A+1 by 75% of the transition energy spacing in A. This condition is therefore equivalent to the Quarter-Point energies.

Because the $\Im^{(2)}$ is so sensitive to changes in internal structure (because of its relationship to the second derivative of eqn. 1.21) similar $\Im^{(2)}$'s imply similar internal configurations for the superdeformed bands.

The curvature of single-particle routhians (such as those shown in Fig. 2.9) are a measure of their contribution to the $\Im^{(2)}$ of a band : flat orbitals contribute least, strongly curving orbitals contribute most. It is thought therefore, that if the excited band in nucleus A is identical to the yrast band in nucleus A+1, then the differences in single-particle configurations between the two bands must be in an orbital which has a small contribution to the $\Im^{(2)}$: i.e. a flat orbital. This is discussed in Sec. 5.7.

However, it is unclear why there should be a direct or indirect relationship between the transition energies of two superdeformed bands.

2.6.3 ΔI=2 Staggering

The third generation of detector arrays have made it possible to measure with a high degree of accuracy energy states that are only weakly populated. This has revealed unexpected fine structures underlying the previously observed gross phenomena. Perhaps the most striking of these is the discovery of staggering in the $\Im^{(2)}$ moment of inertia. This staggering, or bifurcation (Sec. 5.8.1), is observed to occur in only a select few of the known superdeformed bands. The first reported case of bifurcation was in the SD yrast band of ^{149}Gd [Fli93], where it was observed that successive energy levels separated by spins of $2\hbar$ were perturbed by minute amounts (typically $\sim$ 50 eV) in opposite directions. The effect is such that a rotational band which is built upon states with spin I and separated by ΔI=2, is split into two ΔI=4 sequences. A similar case was reported in three superdeformed bands of ^{194}Hg [Ced94] where a phase change (the regular pattern of oscillations is interrupted) was observed. Prior to this work, these were the only reported cases of this new phenomenon.

2.6.4 Summary

Superdeformation has become a widely investigated area of nuclear physics. Its major appeal is that it provides a stringent test under extreme conditions of the nuclear models presented in this chapter. Because superdeformation is a result of both single-particle effects and collective structure, it is not observed in all nuclei, but is restricted to certain mass regions. Overviews of these mass regions ($A \approx 130$, $A \approx 150$ and $A \approx 190$) can be found on Refs. [Nol93, Twi93, Sha92].

Chapter 3

Experimental Details

3.1 Populating High-Spin States

The nuclei studied in this work were produced at high spin in a heavy-ion fusion-evaporation reaction. The idea that two nuclei may fuse to form an excited compound nucleus was first was proposed by Niels Bohr in 1936 [Boh36]. He suggested that a projectile nucleus could be captured by a target nucleus providing that the kinetic energy of the projectile was sufficient to overcome the Coulomb repulsion of the target nucleus. The kinetic energy of the incident nucleus is then converted to excitation energy, and is shared equally among the constituent nucleons of the newly-formed compound nucleus. Bohr assumed that the formation time of a compound nucleus was much shorter than the time required for thermodynamic equilibrium to be reached, and so the subsequent decay of the nucleus would be independent of its formation process.

3.2 Formation & Decay of Compound Nuclei at High Spin

The principle of a heavy-ion fusion-evaporation reaction involves accelerating a beam of heavy ions. These are used to bombard target nuclei with which they will fuse and produce compound nuclei. Ideally, the production of high-spin states arises when the impact parameter is small enough to ensure the complete fusion of the target and beam nuclei, but also large enough to ensure the transfer of large amounts of angular momentum. Fig. 3.1 illustrates the formation and decay of the compound nucleus for the ^{100}Mo(^{36}S,4n)^{132}Ce fusion-evaporation reaction. There are six main stages to the process:

1. Preformation.

   The ^{36}S nuclei are accelerated to an energy which is sufficient to overcome the Coulomb barrier of the ^{100}Mo nuclei.

2. Formation of the compound nucleus.

   10^{-22} seconds later, the target and projectile nuclei fuse to form a highly excited, rapidly rotating compound nuclear system.

3. Particle (neutron) Emission.

   Within 10^{-19} seconds after preformation, the newly formed compound nucleus has completed a single revolution and the emission of neutrons carries away large amounts of energy (typically equal to atleast their separation energy of 8-10 MeV) but very little angular momentum. By the time the fourth neutron has been emitted, the compound nucleus has rotated about 1000 times.

4. Statistical (cooling) γ-ray emission.

   The compound nucleus has now only existed for about 10^{-15} seconds. The ejection of neutrons has removed about 40 MeV of energy, but when the excitation energy falls below the energy threshold for particle emission, the de-excitation proceeds by a cascade of γ-rays. At this stage, the compound nucleus is still highly excited. The 'statistical' γ-ray emissions remove large amounts of energy but very little spin.

5. Quadrupole (Slowing Down) γ-ray emission.

   The compound nucleus has now existed for approximately 10^{-12} seconds, and has rotated about 10^4 times. Electric quadrupole cascades now dissipate the angular momentum, indicative of collective rotation. As the γ-ray emission proceeds, the cascade becomes sufficiently concentrated such that discrete transitions, and specific decay sequences can be established.

6. Ground State.

   After only a nanosecond since preformation, and 100 billion (10^{11}) rotations later, the compound nucleus reaches its stable ground state. In this short time the compound nucleus has completed a number of rotations which is only one order of magnitude less than the number of rotations the earth has performed since its creation.

Compound nucleus formation is often conveniently illustrated on a diagram of excitation energy E, plotted against the spin of the system I, as shown in Fig. 3.2. For clarity, the formation of the compound system illustrated is not at high enough spin for superdeformation; this would be much further over to the right hand side. A more technical discussion of compound nucleus de-excitation can be found in Refs. [New69] and [Hil79]. The γ-ray sequences of near-yrast, high-spin states, form the basis of the spectroscopy of nuclei in the prescence of strong Coriolis and centrifugal forces. In the following section, methods used for the detection of such γ-rays will be discussed, but first a few practical considerations for the production of compound nuclei will be outlined.

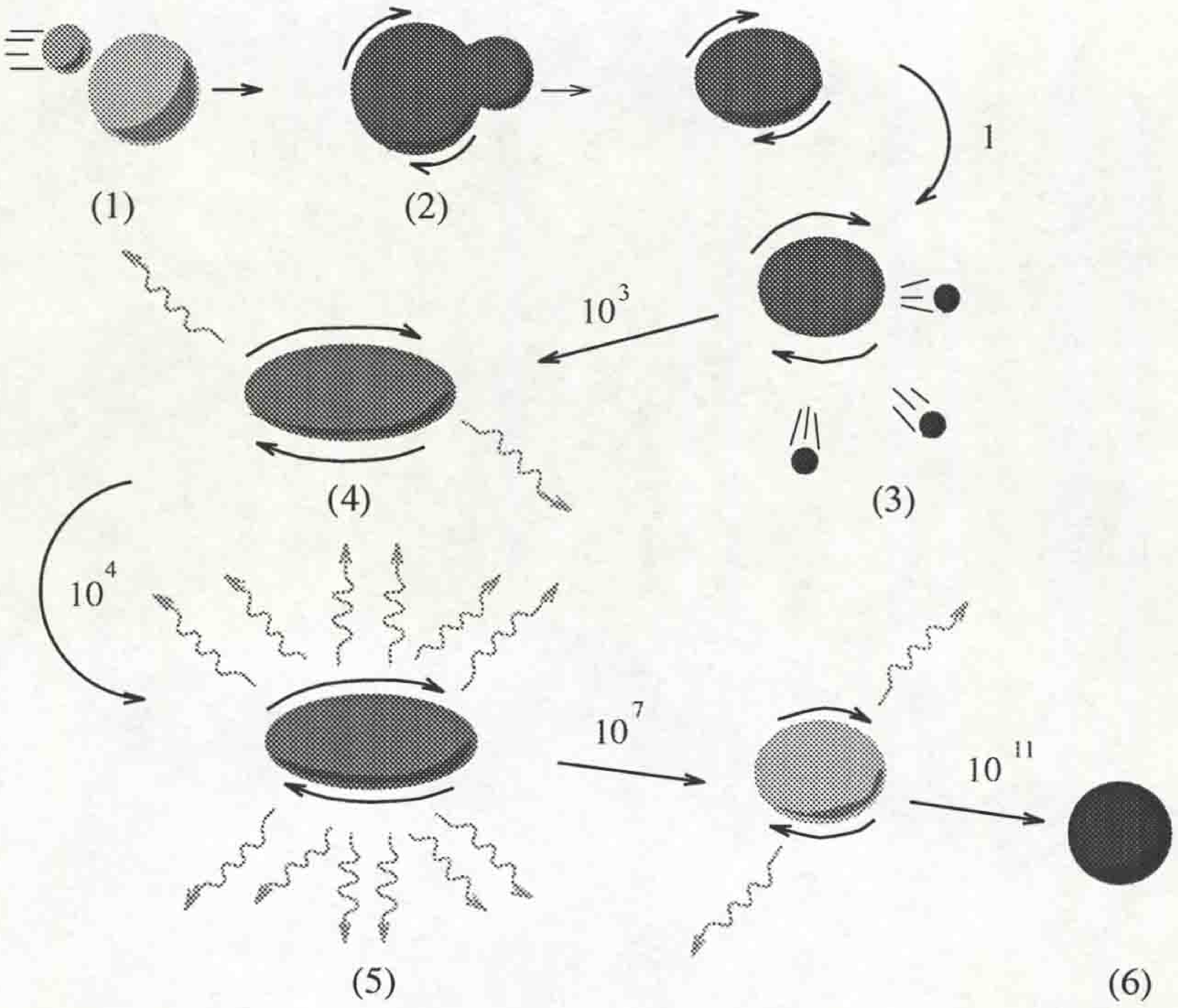

Figure 3.1: The lifetime of a superdeformed nucleus. The number of rotations completed by each stage are shown above the arrows. The numbers in brackets refer to stages in the text.

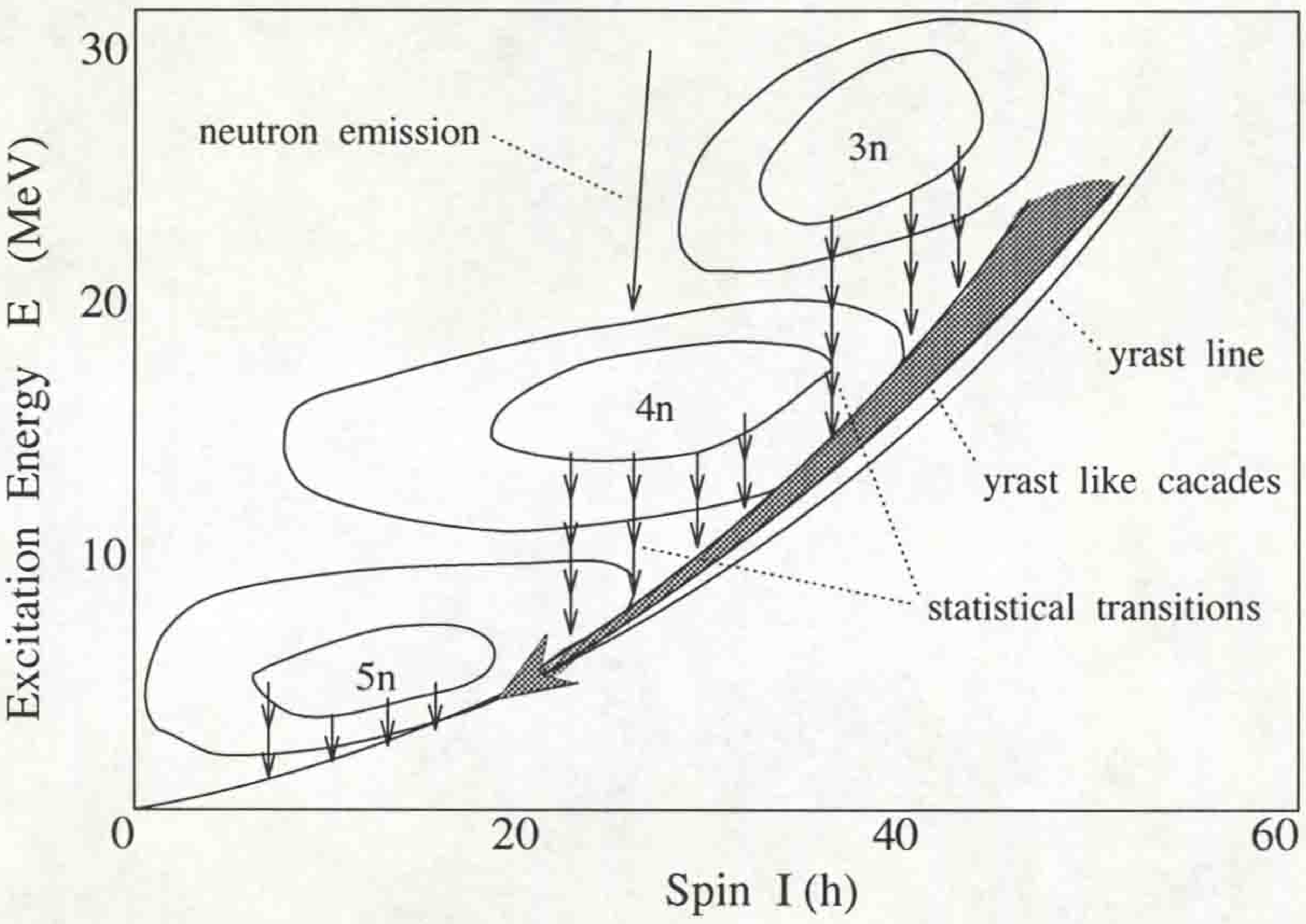

Figure 3.2: Schematic figure illustrating phases of gamma-ray emission. The contours of the 3n-5n entry regions, which are the start of the gamma-ray decay sequences, are also shown.

3.3 Heavy-Ion Beam Production

In order to populate the high-spin states necessary for the study of superdeformation, the incident projectile nucleus must have sufficient kinetic energy to overcome the Coulomb repulsion of the target nucleus. To this end, the ^{36}S beam required for the experiment was provided by a tandem Van de Graaff accelerator [Lil82] situated at the Daresbury Nuclear Structure Facility (NSF).

A caesium sputter source is used to produce negative ions (from a sputter target or 'pill') which are attracted towards the positively charged centre terminal. At this point, the negatively charged ions pass through a carbon foil (or nitrogen gas) where electrons are stripped from the ions (as a consequence of the high velocity of the ion through the medium), leaving highly charged positive ions. Repulsion from the positively charged centre terminal accelerates the ions to the beam energy required.

A dipole analysing magnet diverts a single charge state (and therefore energy) along the beam line where quadrupole magnets are used to focus the heavy-ion beam onto the target.

3.4 Target Requirements

Targets generally consist of self-supporting foils (fragile targets are often backed with a suitable backing for support) and are approximately 1 cm^2 in size. The target material should be isotopically enriched to purity levels in excess of 95% to ensure that the possibilty of unwanted contaminant reactions is minimised. The material should also have a high melting point ($\approx$500K) to ensure good target consistency throughout the experiment.

The thickness of the target is a compromise between high statistics and good energy resolution :

- Thick targets ($\geq$ 1 mg cm^{-2}) provide a high possibility of interactions between projectile and target nuclei.

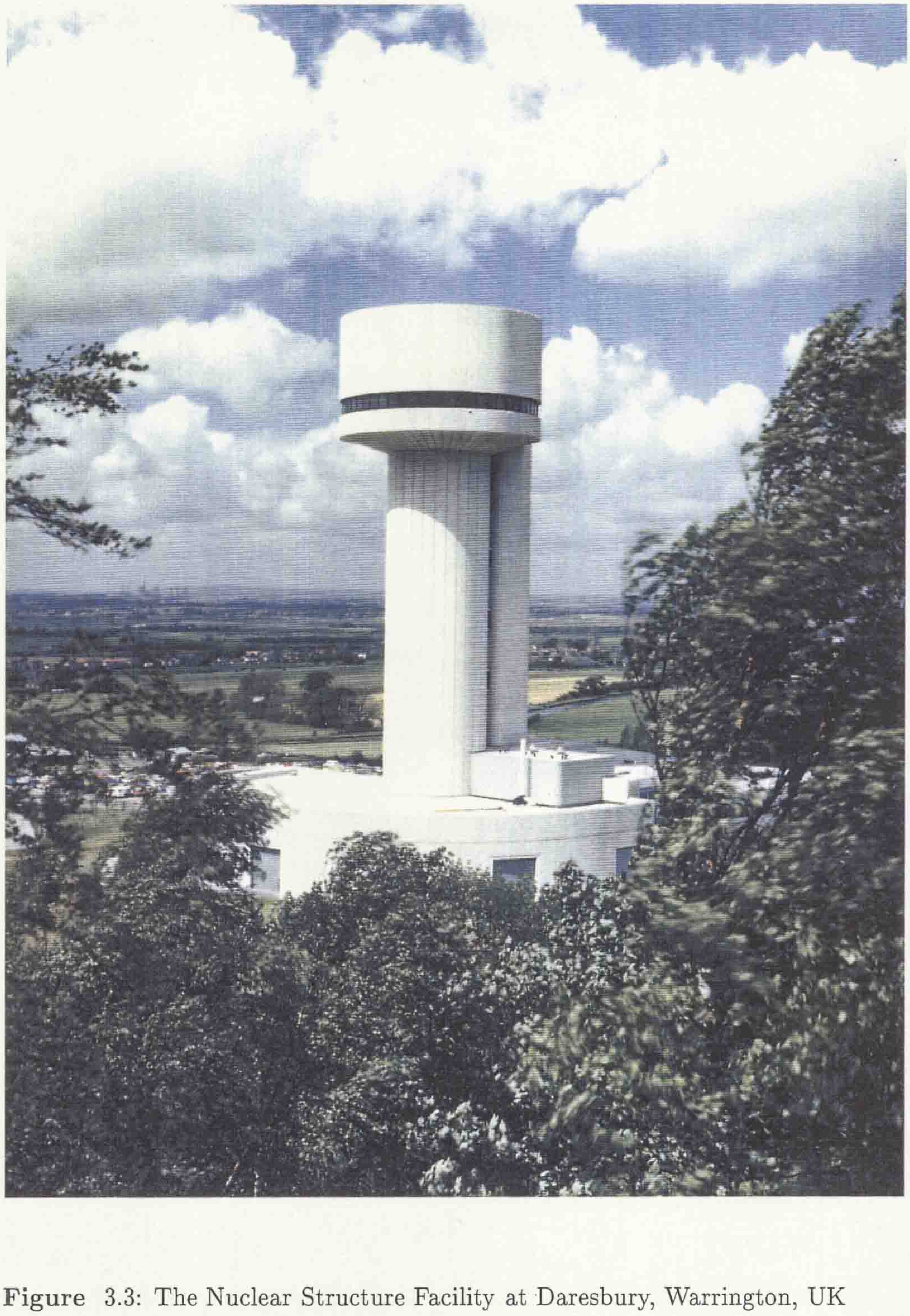

Figure 3.3: The Nuclear Structure Facility at Daresbury, Warrington, UK

- Thick targets cause poorer resolution. This is a consequence of the variation in the recoil velocity as the compound nuclei slow down within the target.

Consideration of these effects results in a typical optimum target thickness of ≈ 500 μg cm^{-2}.

3.5 The Experimental Detection of γ-Radiation.

The detection of γ-rays that are emitted from the de-excitation of nuclear states is achieved by measuring the interaction of the γ-ray with the detector material. There are three main interaction processes through which γ-rays deposit energy in matter : the photoelectric effect, Compton scattering and pair production.

3.5.1 The Photoelectric Effect

For γ-ray energies $E_\gamma < 200$ keV, the dominant interaction process is photoelectric absorption. It involves the complete transfer of the photon energy E_γ, to a bound atomic electron. The electron (now correctly called a photoelectron) is ejected from its atomic orbital with a kinetic energy KE_{pe} given by

$$KE_{pe} = E_\gamma - BE_e \tag{3.1}$$

where BE_e is the binding energy of the atomic electron. The vacancy the photoelectron leaves in the orbitals is rapidly filled by another electron from a higher energy shell. The subsequent cascade results in the emission of X-rays which themselves are absorbed, and the absorption process of the original γ-ray is completed.

The probability of Photoelectric absorption (τ) is found to vary with the atomic number (Z) of the detector material such that $\tau \propto Z^5$ (approximately). Thus, high-Z materials (e.g. lead) are used as shielding against X-rays and γ-rays.

3.5.2 Compton Scattering

Compton scattering is said to occur when an incident γ-ray scatters off an atomic electron of the surrounding material. During the scattering process, some of the energy of the incident γ-ray is transferred to the atomic electron (now a recoil electron, Fig. 3.4).

The energy of the scattered photon may be determined (as a consequence of energy and momentum conservation laws) :

$$E'_\gamma = \frac{E_\gamma}{1 + \frac{E_\gamma}{m_o c^2}(1 - cos\theta)} \tag{3.2}$$

where E'_γ and E_γ are the energies of the incident and scattered photons respectively, θ is the angle that the scattered photon makes to the direction of the incident photon, and $m_o c^2$ is the rest mass of the electron.

Clearly from eqn. 3.2, the maximum energy given to the electron results when the photon is scattered backwards ($\theta = 180°$). Compton scattering is important for intermediate γ-ray energies, but its effects decrease steadily at higher energies. For γ-ray energies relevant to this work, Compton scattering is the most probable interaction. However, the total γ-ray energy is not absorbed by a single interaction, but requires multiple scatters if the total energy is to detected. It is possible however, for a scattered γ-ray to escape from the detector material, in which case only a fraction of the total energy will be detected.

Compton scattering therefore results in the detection of a range of γ-ray energies; from zero to a maximum called the Compton edge (corresponding to $\theta = 180°$), and it is this continuum which produces the main background events in the γ-ray spectra.

3.5.3 Pair Production

For this process to occur, the incident γ-ray photon must have an energy (E_γ) which is greater than the sum of the rest masses of a positron and an electron ($2m_o c^2$). The process is important for high energies only (>1.022 MeV). The incident photon

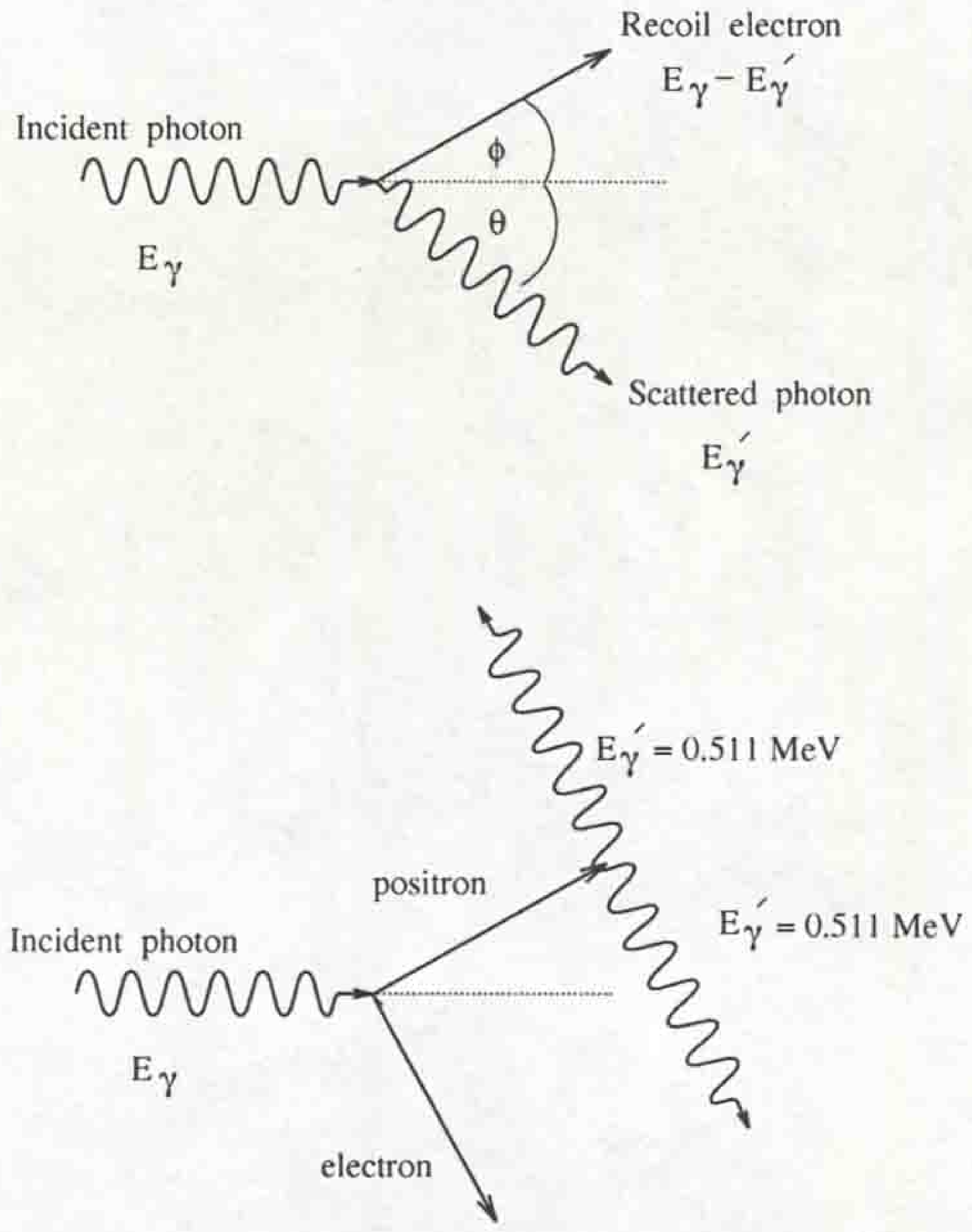

Figure 3.4: (Top) Compton scattering and (Bottom) Pair production for an incident γ-ray in a detector material.

will disappear, and will be accompanied by the creation of an electron-positron pair (Fig. 3.4). The kinetic energy shared between the pair is

$$KE_{pair} = E_\gamma - 2m_oc^2 \tag{3.3}$$

which is lost rapidly as they slow down in the detector. When the positron has slowed down to an energy comparable to that of an atomic electron, further annihilation (with an electron) takes place with the production of 2 photons of equal energies (0.511 MeV) emitted back to back. The energy deposited in the material will depend on whether one or both, of these photons escape from the detector.

- If one photon escapes, the detector will record an energy of E_γ - 0.511 MeV, which results in the 'single-escape peak'; i.e. all of the energy of the incident γ-ray has been absorbed except for the energy of a single annihilation photon which has escaped from the detector.

- If two photons escape, an energy of E_γ - 1.022 MeV will be recorded corresponding to the 'double-escape peak'.

If neither photon escapes, then the full energy of the γ-ray will be deposited in the detector.

3.5.4 Attenuation Coefficients

The total effect of the three photon interaction mechanisms can be described by the total linear attenuation coefficient μ_{total}. Each process is assigned its own coefficient μ which describes the attenuation of γ-rays by the process; so that

$$\mu_{total} = \mu_{PE} + \mu_{CS} + \mu_{PP} \tag{3.4}$$

The intensity I of a mono-energetic beam of γ-rays a distance x into the detector material can be described by

$$I = I_0 exp\left[-\mu_{total} x\right] \tag{3.5}$$

where I_0 is the incident beam intensity.

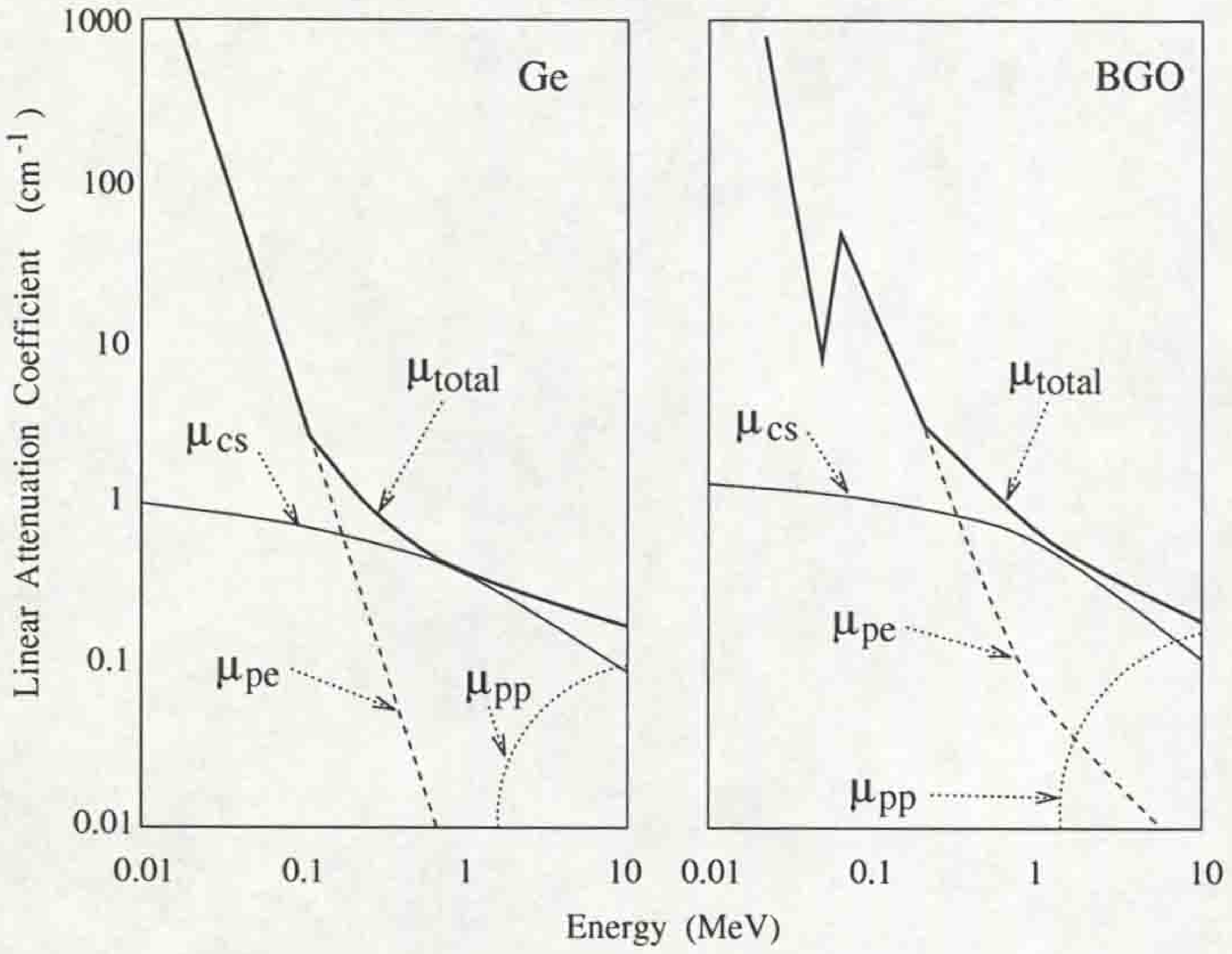

Figure 3.5: The linear attenuation coefficients for photoelectric absorption, Compton scattering and pair production, plotted as a function of γ-ray energy (MeV) for germanium and BGO.

Fig. 3.5 compares the attenuation coefficients for germanium and BGO crystals which have been used as detectors in this work. The figure illustrates the energy ranges over which the different processes dominate, and confirms that Compton scattering is the dominant process for the γ-rays studied in this work (100 keV to 2 MeV).

3.6 Semiconductor Detectors

3.6.1 General Properties

The atoms in a crystalline solid are so close together that their valence electrons constitute a single system of electrons common to the entire crystal. In place of precisely defined energy levels of an individual atom, the entire crystal possesses an energy band, formed when the energy levels of the constituent atoms overlap. The electrons then have a continuous distribution of permitted energies.

The valence band corresponds to electrons which are bound within the crystal, while the conduction band represents electrons which are free to migrate through the crystal. The size of the energy gap between the two bands determines whether the material is classified as a semiconductor (gap $\approx$ 1 eV) or an insulator (gap $\geq$ 5 eV). For an intrinsic semiconductor (or an insulator) the valence band is completely full, and in the abscence of thermal excitation, the conduction band is completely empty.

When a γ-ray passes through a semiconductor, many electron-hole pairs are created along its path. Physically, this process simply represents the excitation of an electron that is normally part of a covalent bond, such that it can leave the specific bonding site ('creating' a hole) and drift through the crystal. The energy expended by the incident γ-ray in producing a single electron-hole pair is called the ionization energy ϵ. This quantity is experimentally observed to be largely independent of the energy of the incident radiation. This allows the interpretation of the number of electron-hole pairs produced in terms of the incident energy of the γ-ray.

In order to achieve an efficient collection of charge carriers from any semiconductor detector, it is necessary to create a large electric field across the crystal. Even in the absence of ionizing radiation however, all detectors show some finite conductivity, and therefore a leakage current will be observed, which will be a significant source of noise. However, the leakage current can be reduced to a sufficiently low value to allow the detection of the added current pulse created by the electron-hole pairs produced along the track of the ionizing γ-ray. This is achieved by placing p- and n-type semiconductors (semiconductors doped to produce either excess positive or excess negative charge respectively) in direct contact, forming a p-n junction. When n-type and p-type semiconductors are combined in this way, a migration of charge carriers occurs that results in a region empty of charge carriers in the vicinity of the interface of the two materials. This depletion region constitutes an active volume where radiation will interact and will result in its detection. The depletion region can be extended further to create a larger active volume by the application of a large reverse bias across the junction.

Natural purity germanium will stand a depletion region of no more than about 2 or 3 mm before electrical breakdown occurs and a current flows. Much greater thicknesses are required for the detectors intended for γ-ray spectroscopy because γ-radiation is very penetrating. Hence to maximise the absorption, a larger depletion layer is required for γ-ray detectors. The thickness of the depletion layer d, is given by [Kno89]

$$d = \left[\frac{2\epsilon V}{eN}\right]^{\frac{1}{2}} \tag{3.6}$$

where V is the reverse bias voltage, N is the net impurity concentration in the bulk semiconductor material, ϵ is the ionization energy, and e is the electron charge. At a given applied voltage therefore, the depletion layer can only be increased by decreasing the value of N through reductions in the net impurity concentration. One approach to reducing net impurity concentrations, is to create a compensated material in which the existing impurities are balanced by an equal concentration of dopant atoms of the opposite type. Germanium with lithium dopants (Ge(Li)) has been used for some time but has now been superseded by the development of high-purity germanium (HPGe) crystals.

3.6.2 High-Purity Germanium Detectors

Techniques for producing high-purity germanium (HPGe) crystals can achieve impurity levels as low as 10^9 atoms/cm^3. If the remaining low-level impurities are acceptors (such as aluminium) the electrical properties of the crystal is mildly p type. Alternatively, if donor impurities remain, the crystal is n-type.

HPGe crystals have the advantage that their purity is not affected by temperature, whereas lithium-drifted germanium crystals need to be cooled during storage and operation to prevent the thermal migration of the dopant atoms and degradation of the impurity compensation. Although HPGe crystals can be stored without cooling, it is necessary to cool them to liquid nitrogen temperatures during use because of the relatively small energy band gap of germanium, ≈ 0.67 eV. Cooling inhibits the thermal excitation of electrons across the band gap, and so reduces thermal noise to an acceptable level.

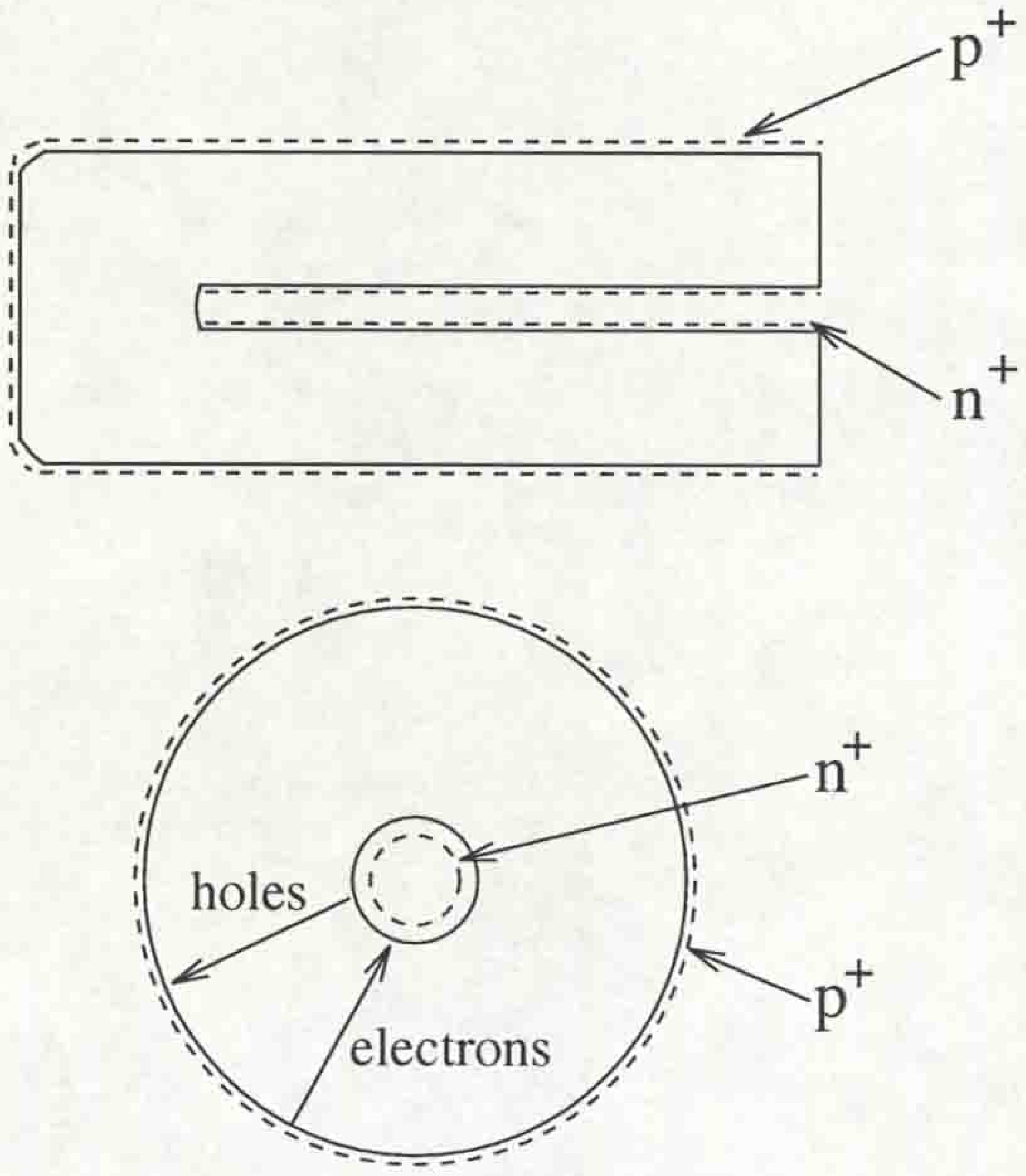

Figure 3.6: Cross-section through (Top) the axis and (Bottom) perpendicular to the axis, of an n-type bulletized coaxial germanium detector crystal.

Gamma-ray spectroscopy requires that detectors have as large an active volume as possible. For this reason, detectors used in the Eurogam array (Sec. 3.11) are constructed in a 'bulletized coaxial' configuration. In this configuration, part of the central core of the germanium crystal is removed and the electrical contacts are extended over the inner and outer surfaces (Fig. 3.6).

Because the crystal can be made long in the axial direction, the active volume can be as much as 400 cm^3 (a more straight-forward planar crystal design has a typical active volume of 30 cm^3). The application of a reverse bias (typically $\sim$ 3500 V) across a HPGe crystal produces a depleted region which extends further into the crystal as the voltage is increased. The voltage also sets up an electric field within the crystal which is increased so as to rapidly sweep the charge carriers out to the terminals. This reduces the probability of charge-carrier recombination before reaching the terminals. On reaching the terminals, the charge carriers are collected and produce an electrical current.

The dominant advantage of HPGe detectors lies in the fact that the ionization energy is relatively small, being $\sim$ 3 eV. The number of electron-hole pairs produced for a given energy deposited in the detector is therefore large, and this has two beneficial effects on the attainable energy resolution :

- The statistical fluctuation in the number of carriers per pulse is reduced.
- The greater amount of charge per pulse leads to a better signal/noise ratio.

The germanium detector energy resolution is therefore very good; the full width at half maximum (FWHM) $\approx$ 2 keV for a 1.33 MeV γ-ray emitted from a ^{60}Co source. Germanium detectors are prone to radiation damage caused by the fast neutrons emitted from heavy-ion fusion-evaporation reactions. The neutrons produce trapping sites in the crystal lattice which leads to poor charge collection and hence a low energy tail on the photopeak (a variable amount of charge is lost per pulse).

3.7 Inorganic Scintillator Detectors

It was stated in Sec. 3.6.1 that electrons in a crystalline solid have available only discrete bands of energy; the valence and conduction bands. Absorption of energy can result in the excitation of an electron from the valence band into the conduction band. These electrons can then decay back to the valence band with the emission of a photon. Scintillation materials are chosen so that the emitted radiation lies in the visible region of the electromagnetic spectrum. A photomultiplier tube collects these photons where they excite photoelectrons at a photocathode. These are then amplified by a factor of 10^6 to produce an adequate current pulse for measurement.

3.7.1 Bismuth Germanate (BGO)

Bismuth germanate ($Bi_4Ge_3O_{12}$ commonly abbreviated to BGO) is a pure inorganic scintillator that does not require the prescence of impurities to promote the scintillation process. The photon emission is associated with an optical transition of the Bi^{3+} ion that is a major constituent of the crystal. The shift in the frequency of light between that of the absorbed γ-ray and that of the emitted photon is large, so that BGO is transparent to its own scintillation light. However, the light yield from BGO is relatively low (10 - 20% that of NaI(Tl), another common scintillator) and its cost is relatively high (2-3 times that of NaI(Tl)). Despite this, because of BGO's high density (7.3 g/cm^3) and the high atomic number of its bismuth component (Z=83), BGO has an excellent stopping power for γ-rays : 6 cm of BGO is required to absorb a 1 MeV γ-ray, while it requires 14 cm of NaI(Tl) to absorb a γ-ray of the same energy.

The use of BGO therefore enables detectors in an array to be more closely packed than if NaI(Tl) was used (as used in the TESSA 2 array [Twi83]), and is of primary interest when the need for high γ-ray counting efficiency outweighs considerations of energy resolution.

3.8 Compton Suppression

An ideal γ-ray spectrometer detecting γ-rays emitted from a ^{60}Co source, would display two prominent photopeaks (1173 keV and 1333 keV) in the form of an energy

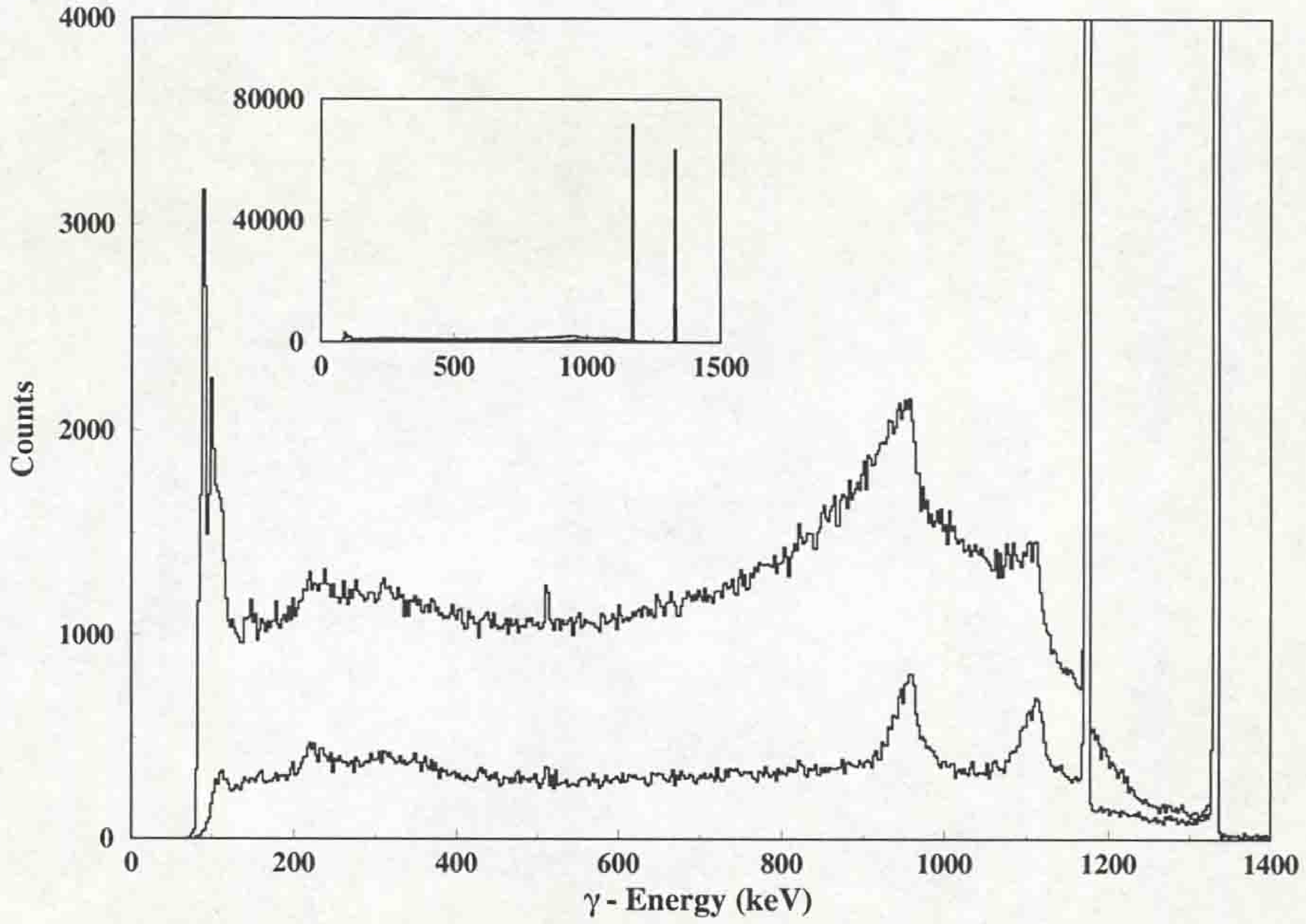

Figure 3.7: The γ-ray spectra of a ^{60}Co source from a Eurogam detector. The top spectrum is unsuppressed, while the bottom spectrum is suppressed (Sec. 3.9). The inset shows the size of the Compton background relative to the 1173 keV and 1333 keV photopeaks.

spectrum. In reality however, γ-ray spectra from germanium detectors have large continuous backgrounds, called the Compton continuum (Fig. 3.7). This is primarily generated by γ-rays that undergo one or more scatterings in the detector, followed by the escape of the scattered photon. There are a number of prominent features of Fig. 3.7.

1. X-ray peaks (100 keV) generated by photoelectric absorption in the surroundings.

2. Broad peaks (250 keV) due to backwards scattering following Compton scattering outside the detector.

3. The annihilation peak (511 keV) arising from the detection of an annihilation photon from pair production in the detector surroundings.

4. 'Compton Edges' at 950 keV and 1100 keV, corresponding to the 1173 keV and the 1333 keV ^{60}Co peaks, respectively. They are the result of back-scatterings

of the γ-rays over a range of angles. The upper limit of each peak corresponds to a back-scatter of 180°.

The Compton continuum can obscure low intensity peaks from other γ-rays, and so it is necessary to reduce this unwanted effect. This is achieved by the use of suppression shields.

3.9 Escape Suppressed Spectrometers

It was shown in Sec. 3.6.2 that the energy resolution for a HPGe detector is very good. However Sec. 3.8 showed that many of the γ-rays entering such a detector will be scattered, and will not deposit their full energy. These γ-rays contribute to the Compton background.

The principle of the escape suppressed spectrometer (ESS) is to surround the HPGe detector with a suppression shield composed of a scintillator. The γ-rays scattered out of the Ge detector will then be detected by the suppression shield. A coincidence event, where a γ-ray is detected simultaneously in the shield and the Ge detector, signifies an unwanted event and is rejected electronically.

The vetoing of Compton-scattered events greatly improves the peak to total ratio (defined as the ratio of the number of counts in the photopeak to the number of counts in the spectrum above 100 keV) from $\sim$20% for a typical Ge detector to $\sim$60% [Bea92] for an escape suppressed spectrometer. The effectiveness of this is shown in Fig. 3.7 where there is a significant reduction in the Compton continuum. A schematic figure of the escape suppressed spectrometer used in Eurogam Phase I (Sec. 3.11) is shown in Fig. 3.8 (based on a figure in [Nol94]).

The germanium detectors are the type detailed in Sec. 3.6.2 and are $\approx$70 mm in diameter and $\approx$75 mm in length. To achieve better packing in the array, the detectors are tapered over their front 3 cm, and for the reasons outlined in Sec. 3.7.1, the scintillator used in the Eurogam shields is BGO. Each shield consists of ten optically isolated BGO segments, each fitted with a photomultiplier tube. Beausang

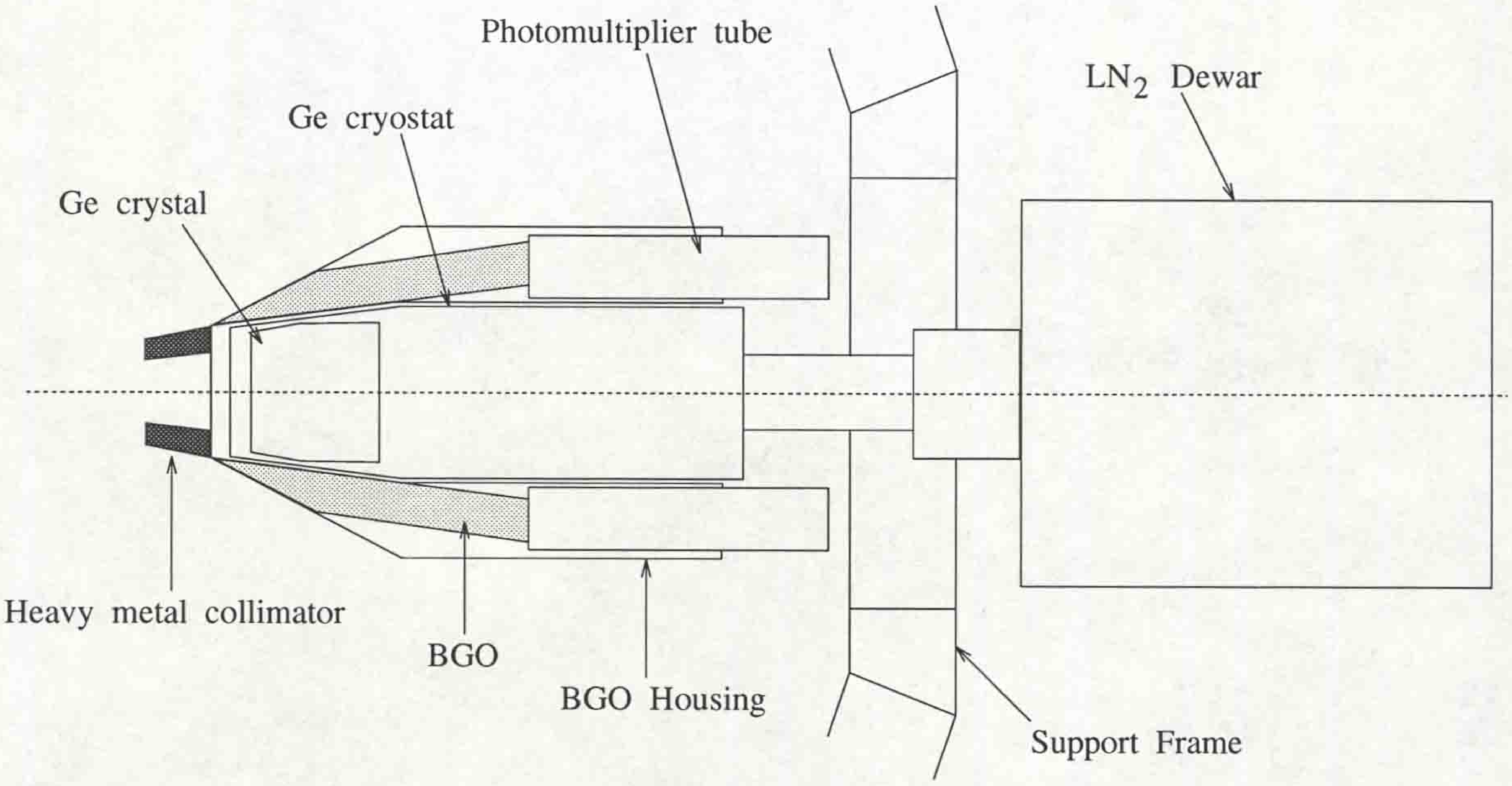

Figure 3.8: A schematic drawing of the escape-suppressed spectrometer used in Eurogam Phase I. The target would be at the end of the dashed line ~ 19 cm away from the front of the detector.

et al. [Bea92] discuss this in more detail.

3.10 Gamma-ray Detector Arrays

High spin γ-ray spectroscopy often involves the study of nuclei which emit a shower of γ-rays during their decay. For example, the yrast superdeformed band in ^{132}Ce consists of a cascade of $\sim$20 γ-rays. In order to determine the relationship between such events, γ-ray coincidence detection information is required. This is achieved by increasing the number of detectors to form an array.

Table. 3.1 illustrates how dramatically the number of possible double (γ-γ), triple (γ-γ-γ) and quadruple (γ-γ-γ-γ) coincidence events rises as the number of detectors is increased. The actual number of detected coincidence events will of course, depend upon the efficiency of the detectors, but the table does illustrate the motivation behind the building of arrays. Fig. 3.9 shows how the observational limit of γ-ray transitions has been successively improved as more advanced detector arrays have been built.

The first generation of γ-ray arrays used segmented shells of NaI scintillators, and although they collected most of the reaction γ-rays, they were limited in the study of discrete spectroscopy by the poor resolution of the NaI.

The second generation of arrays began with a small number of Ge detectors with resolutions ~30 times better than the NaI arrays (See Fig. 3.9). The first of these was an early version of the TESSA array (Sec. 3.10.1) which was capable of probing γ-ray sequences at the 0.1 - 1% population level.

The third generation of arrays (e.g Eurogam, Sec. 3.11) take advantage of the increase in sensitivity that can be achieved with the use of higher-fold coincidences, and can probe to below the 0.01% population level.

Detectors	γ-γ	γ-γ-γ	γ-γ-γ-γ
1	-	-	-
2	1	-	-
3	3	1	-
16	120	560	1,820
70	2,415	54,740	916,895

Table 3.1: Possible γ-ray detector coincidences increase rapidly as the number of detectors is increased. The values are obtained by calculating the number of possible combinations of the fold from the number of detectors.

3.10.1 TESSA 3

TESSA is an acronym for Total Energy Suppression Shield Array and proved to be significant step forward in the field of nuclear structure physics [Twi83]. It is mentioned briefly here because it was with this array that the first superdeformed bands were observed in ^{132}Ce [Nol85, Kir87] and ^{152}Dy [Twi86]. The array consists of 16 ESS's, arranged in 2 rings of 6 spectrometers at ±19° to the horizontal plane. The

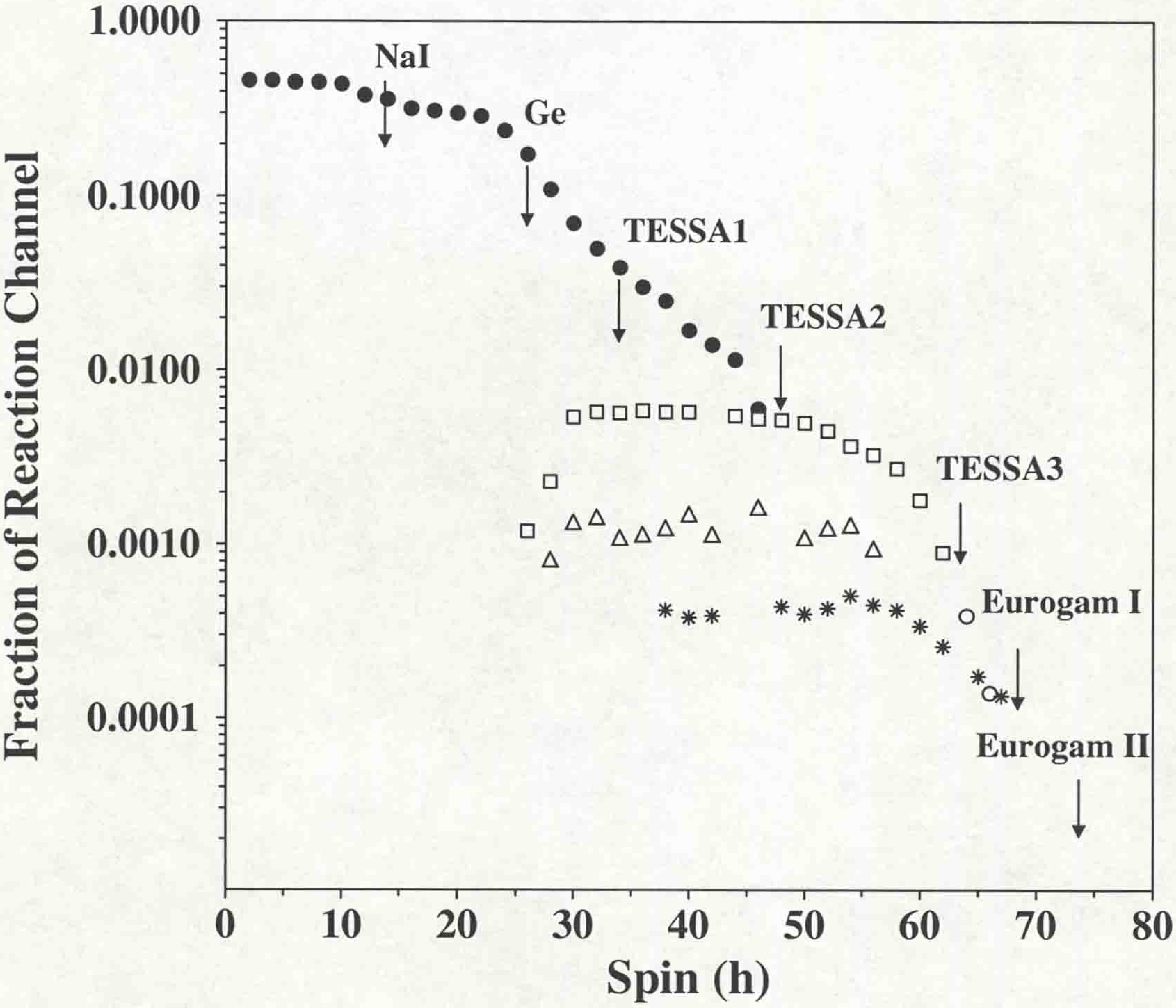

Figure 3.9: The observable limit of γ-ray transitions as a fraction of the reaction channel for NaI detectors, Ge detectors, and the arrays TESSA1, TESSA2, TESSA3 and Eurogam phase 1 are indicated. Also shown is the predicted range for Eurogam phase 2. Symbols are : ($\bullet$) the discrete lines in ^{160}Er measured by NaI detectors, Ge detectors, TESSA1 and TESSA 2 ; ($\Box$) yrast SD band in ^{152}Dy measured by TESSA 3 ; (Δ) first excited SD band in ^{151}Tb measured by TESSA3 ; ($\circ$) additional γ-rays in ^{152}Dy yrast band and excited SD band in ^{152}Dy (*) both measured by Eurogam phase 1. Diagram courtesy of [Cla95] from [Twi93] remaining 4 detectors are in the horizontal plane. At the centre of the arrangement is an inner ball of BGO detectors, capable of giving an indication of the fold (total number of γ-rays detected in an event) and the sum energy (total energy of those γ-rays), its role being to allow reaction channel selection.

3.11 Eurogam

The purpose of building Eurogam was to obtain an array with as large a detection efficiency as was practically and economically feasible. This was obtained by a tighter packing of the germanium detectors than used in the previous γ-ray arrays. The design was based on an array of 12 regular pentagons. Each pentagon contained 5 germanium detectors, one at each corner of the pentagon (a detector slightly further back in the centre of the pentagon face was omitted for phase I). A complete array based on this geometry would have consisted of 71 Ge detectors, with the central hole of one of the pentagons being occupied by the beam line. For Phase I of the Eurogam project, the array was installed next to the recoil mass separator (RMS) [Jam88], which was used in some experiments to supply a level of mass selection in coincidence with the γ-ray events. Consequently, because of the presence of the RMS, it was not possible to mount detectors at forward angles in the array. This resulted in a total of 45 detectors for Phase I which subtended angles relative to the beam axis given in Table. 3.2.

Number of Detectors	5	10	10	5	5	10
Angle	157.6	133.6	107.9	94.2	85.8	72.1

Table 3.2: The numbers of detectors at particular angles (relative to the beam axis) in the Eurogam Phase I array.

In between the Ge detectors were the crystals of BGO which formed the suppression shields. There were 10 crystals in the shields around the Ge detectors in the corners of the main pentagon. The detectors were positioned ≈19 cm away from the target position ($\approx$20.5 cm to the face of the Ge crystal) and the total solid angle covered by the array was $\approx$23% of 4π. This resulted in a total photopeak efficiency of 5.6% for 1.3 MeV γ-rays, which was a dramatic improvement on the previous generation arrays (c.f $\sim$0.5% for TESSA 3).

3.12 Eurogam Electronics & Data Acquisition

3.12.1 Introduction

The previous generation of detector arrays (such as TESSA3) used conventional NIM electronics, where only one function was performed by each electronic module. With the advent of the third generation of detector arrays (Eurogam [Nol92, Nol94], Gammasphere [Lee94] etc) it was necessary to design new integrated electronics and data acquisition systems which could handle the large increase in detector elements, as well as the higher data rates.

The new electronics had to fulfil the following criteria :

1. The large number of detectors in the array require more electronics than previous generation arrays, and therefore the electronics needed to be reliable.
2. The integration of each detector signal processing into a single module. This minimises cable connections.
3. Software control of all adjustable parameters such as thresholds, signal delays etc.
4. Fast data transfer buses to handle the vast quantities of events per second.
5. Modularity of hardware and software to allow a continuous upgrading of equipment.

The basic working principle of the electronics and data acquisition system is the detection and recording of γ-ray coincidence events that have occured within a small time

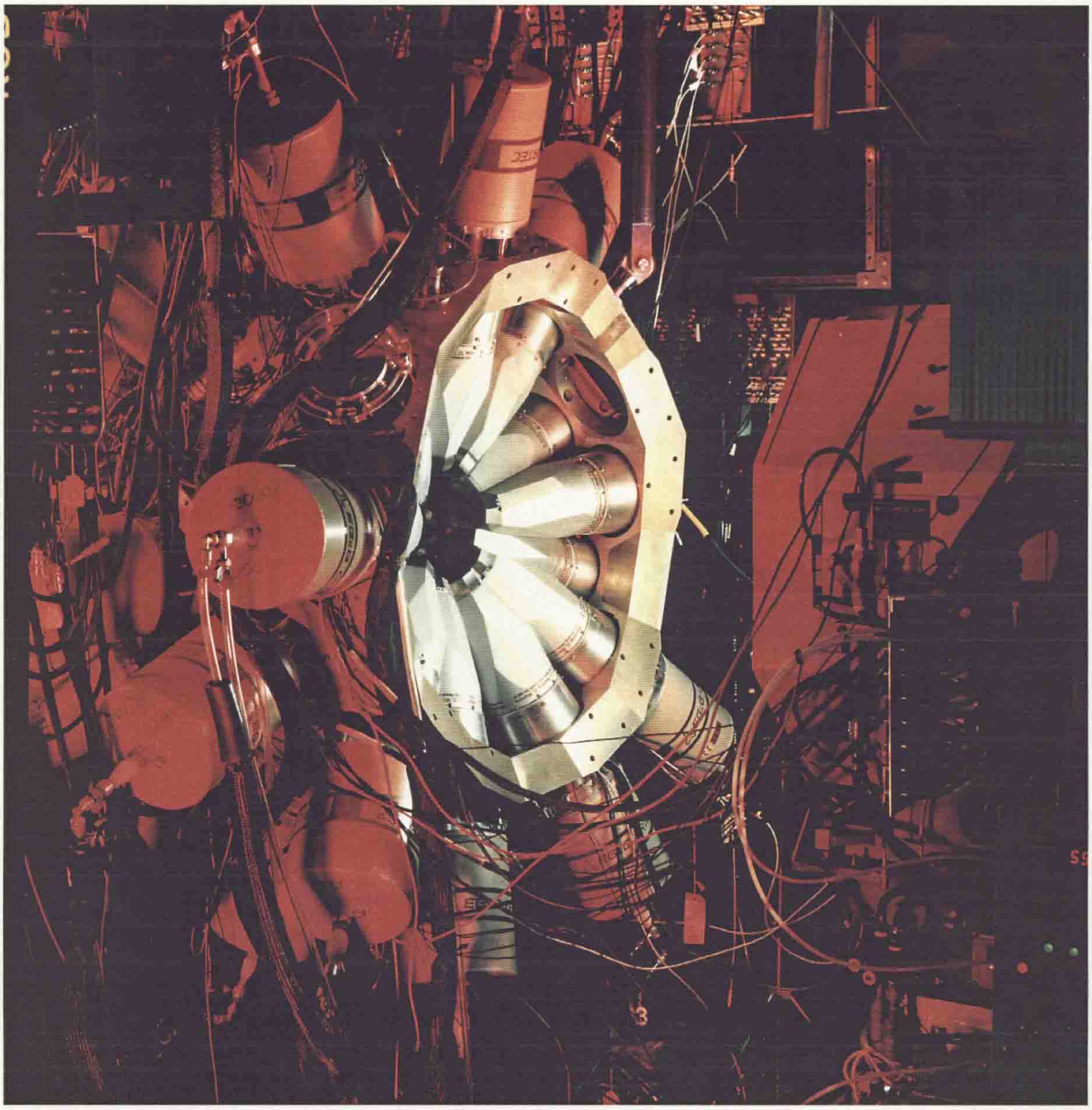

Figure 3.10: The Eurogam Phase I array. The germanium detectors and liquid nitrogen dewar vessels are visible. No detectors are placed at forward angles because of the presence of the RMS (not visible). Courtesy of Daresbury Laboratory.

window (typically ~100 ns). It is within these criteria that the Eurogam electronics system filters the data.

3.12.2 Architecture of the system

The electronics and data acquisition system of the Eurogam array is based on the VME-VXI industry standard data bus. The VXI format is an extension of the VME (VXI : VME eXtended for Instrumentation) format specifically designed for instrumentation tasks. The format was used because its large card size and electrical environment (power supplies and shielding) enables both analogue and digital processing stages of several detectors to be housed on one card. The general architecture of the Eurogam system is shown in Fig. 3.11.

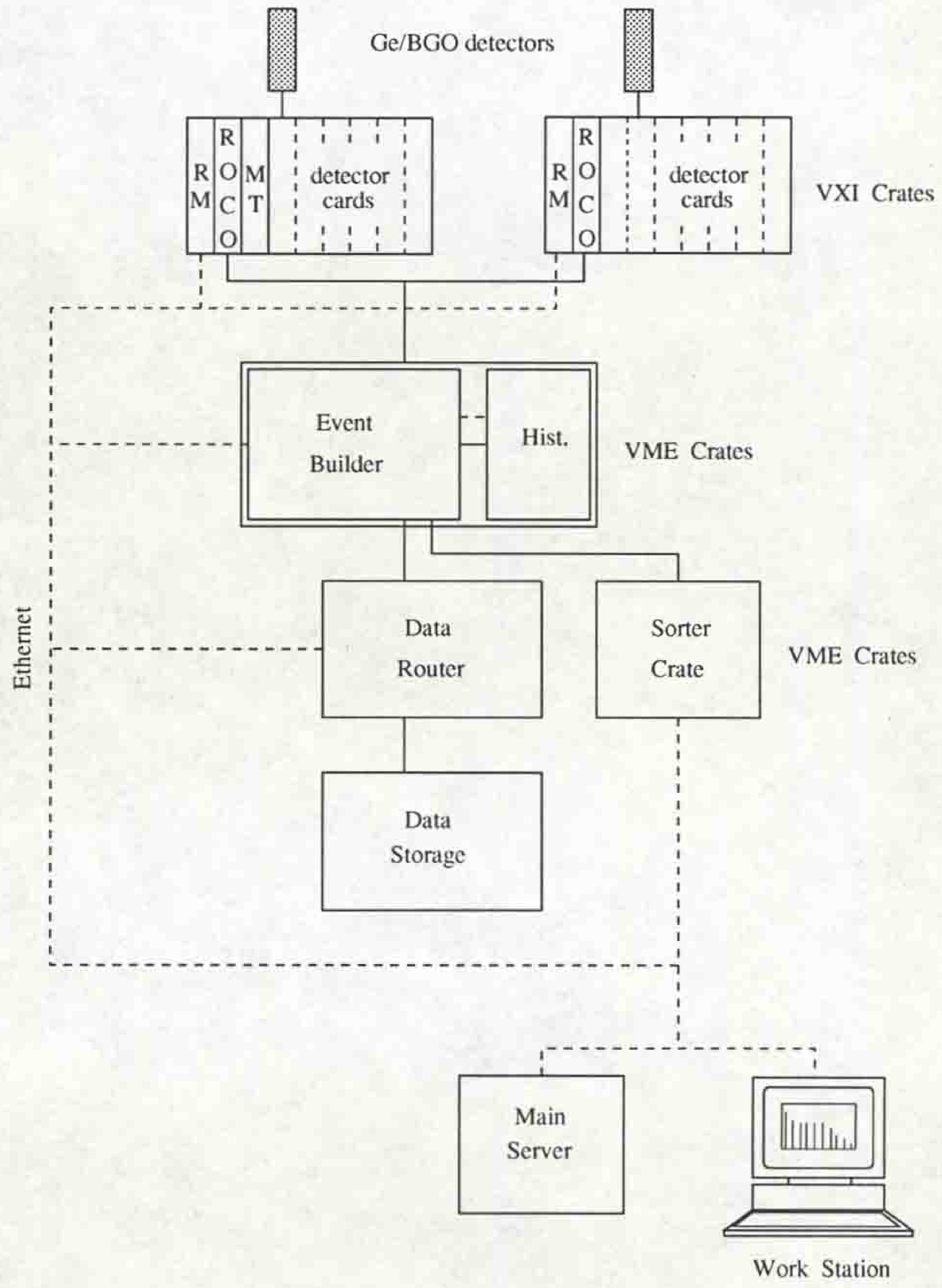

Figure 3.11: The architecture of the Eurogam data-acquisition system.

It is divided into modules :

VXI Crates/Cards. Two VXI crates had space to accommodate ten pairs of VXI cards. One card contained all of the analogue and digital circuitry for either 6 germanium detectors or 60 BGO channels. This meant that each detector module (i.e. one of the 12 pentagons making up the array) could be housed on a single card.
In addition to the detector cards, each crate had a central processing unit (also termed the resource manager, RM), and a Readout Controller Card (ROCO) which organised event data from all the cards in the crate. One of the crates also held the master trigger (MT) module.

VME Crates. Data processed and filtered by the VXI crates were then passed onto the VME crates. These held the event builder card (EB) which constructed the events according to a software routine that was supplied by the user. The VME crate also housed the histogrammer unit. This unit built spectra for each detector, providing a facility for on-line analysis.

Data Router. Processed data from the event builder was then transferred to the data router where events were prepared for storage.

Data Storage. Output from the data router was then written to Exabyte tapes, which have a 5 GByte capacity and can write data at a rate of 400 Kb/s.

Sorter Crate. A sorter crate was also available for online construction of matrices.

Excluding the data storage interface, the entire system was situated in the target area. It was connected by an optical-fibre link to workstations in the control room, where the majority of electronic parameters were set and controlled.

3.12.3 High Voltage Supplies

High voltage supply cards were required for both BGO and Ge detectors. The BGO detectors required 2.5 kV supplies while the Ge detectors required low noise 5 kV supplies. The Ge high voltages could be individually shutdown by a hardware link should there have been an abnormal rise in temperature of the Ge crystal. Computer control of the High voltage cards could be performed through VME connection to the ethernet network of Fig. 3.11.

3.12.4 Ge Signal Processing With VXI Electronics

The VXI electronics are capable of processing γ-ray energy and timing information on a single card. The inputs of these VXI cards come directly from the detectors, where a receiver divides the signal for energy and time measurements.

The energy signal is divided into high (0-20 MeV) and low (0-4 MeV) energy parts by a rebinning process. The analogue voltage signal is then converted into a digital pulse by Analogue to Digital Converters (ADC's).

Timing signals are important to correctly process γ-γ coincidence events. Electronic trigger signals are used to monitor the start and end of events, and also as consistency checks. The most important of these signals are generated by the 'master trigger' module (Fig. 3.11) in the VXI crates. The 'fast trigger' is generally the response to a Ge multiplicity signal in which the multiplicity has exceeded a user-defined threshold. Only after a further trigger, the 'slow trigger' is produced, will the information be available for readout to the readout controller (ROCO).

3.12.5 BGO Signal Processing

The signals from the ten BGO crystals in a suppression shield are combined in a sum amplifier so that there is only one energy output per shield. Timing signals are also processed and fed to the associated Ge card in order to perform Compton Suppression.

3.12.6 Data Handling & Readout

When readout from the last detector module participating in an event is complete, the ROCO module is instructed that the event has finished. Several events are stored in a First In First Out (FIFO) module of each ROCO card.
From the FIFO, the data are transferred to the Histogrammer and the Event Builder (Fig. 3.11) :

- The Histogrammer. The Histogrammer unit enables the viewing of data in real time, as it is collected. The unit samples ('spies') the data before it reaches the Event Builder.
- The Event Builder. The primary function of the Event Builder is to transform each event into a format suitable for storing. The unit may also be used for other functions such as Compton Suppression.

The data are then passed through the Data Router (events are further prepared for storage) and finally onto Exabyte tapes.

3.13 Methods of Data Analysis

3.13.1 γ-γ Matrices

The γ-rays emitted during a nuclear reaction are detected by the array and stored to tape as fold 2 or greater γ-γ coincidences. Each event is stored as data words. These contain the γ-ray energies simultaneously detected by two or more Ge detectors and the identification of these detectors. However, the γ-ray energies recorded by each Ge detector will not only depend on variations in the amplifier gains, but also on Doppler shifts of the γ-ray energies. These effects need to be corrected for by 'gainmatching' and by employing a 'v/c correction' for the Doppler shifts. This is dealt with in Sec. 4.3.

Computer software may then be used to process the data into a form suitable for analysis. This process is referred to as 'sorting'.

If an event consists of two γ-rays detected in coincidence (energies $E_{\gamma1}$ and $E_{\gamma2}$), then this is termed a γ-γ coincidence. The information is sorted by incrementing a two dimensional (2D) matrix, $E_{\gamma1}$ versus $E_{\gamma2}$, at the positions ($E_{\gamma1}$,$E_{\gamma2}$) and ($E_{\gamma2}$,$E_{\gamma1}$).

If the event contains three γ-rays ($E_{\gamma1}$,$E_{\gamma2}$,$E_{\gamma3}$) then this corresponds to three γ-γ coincidences : ($E_{\gamma1}$,$E_{\gamma2}$), ($E_{\gamma1}$,$E_{\gamma3}$), ($E_{\gamma2}$,$E_{\gamma3}$). Each pair is incremented into the matrix twice; i.e. the matrix is incremented six times.

This procedure results in a two dimensional symmetrised matrix (symmetrical about its 'main diagonal') with γ-ray energy along both the x and y axes.

3.13.2 Gates

Sections of γ-γ matrices may be projected out into one dimensional (1D) spectrum by selecting narrow regions of energy on the x-axis. The corresponding 1D spectra consists of all γ-rays in coincidence with the energy on the x-axis, and is projected onto the y-axis. This procedure is referred to as the setting of a 'gate'.

For example, when a gate is set on the energy of a transition in a superdeformed band, the projected spectrum will consist of all the the other transitions in the band, and everything else in coincidence with it.

3.13.3 Gated γ-γ Matrices

In addition to γ-γ matrices, gated γ-γ matrices may also be produced. The gated matrices are constructed by having a gating condition within the sort program itself. The number of gates demanded in the program results in the selecting of triples (1 gate demanded), quadruples (2 gates demanded) or quintuples (3 gates demanded) events.

For example, in order to analyse triple events, the data was sorted requiring that a single γ-ray event on tape (which must consist of atleast three γ-rays) is one of a number of selected gates. This is the setting of a gate because only those γ-rays in coincidence with the gate will be incremented into the matrix. Once this condition is satisfied the remaining two or more γ-rays are unpacked into γ-γ coincidences,

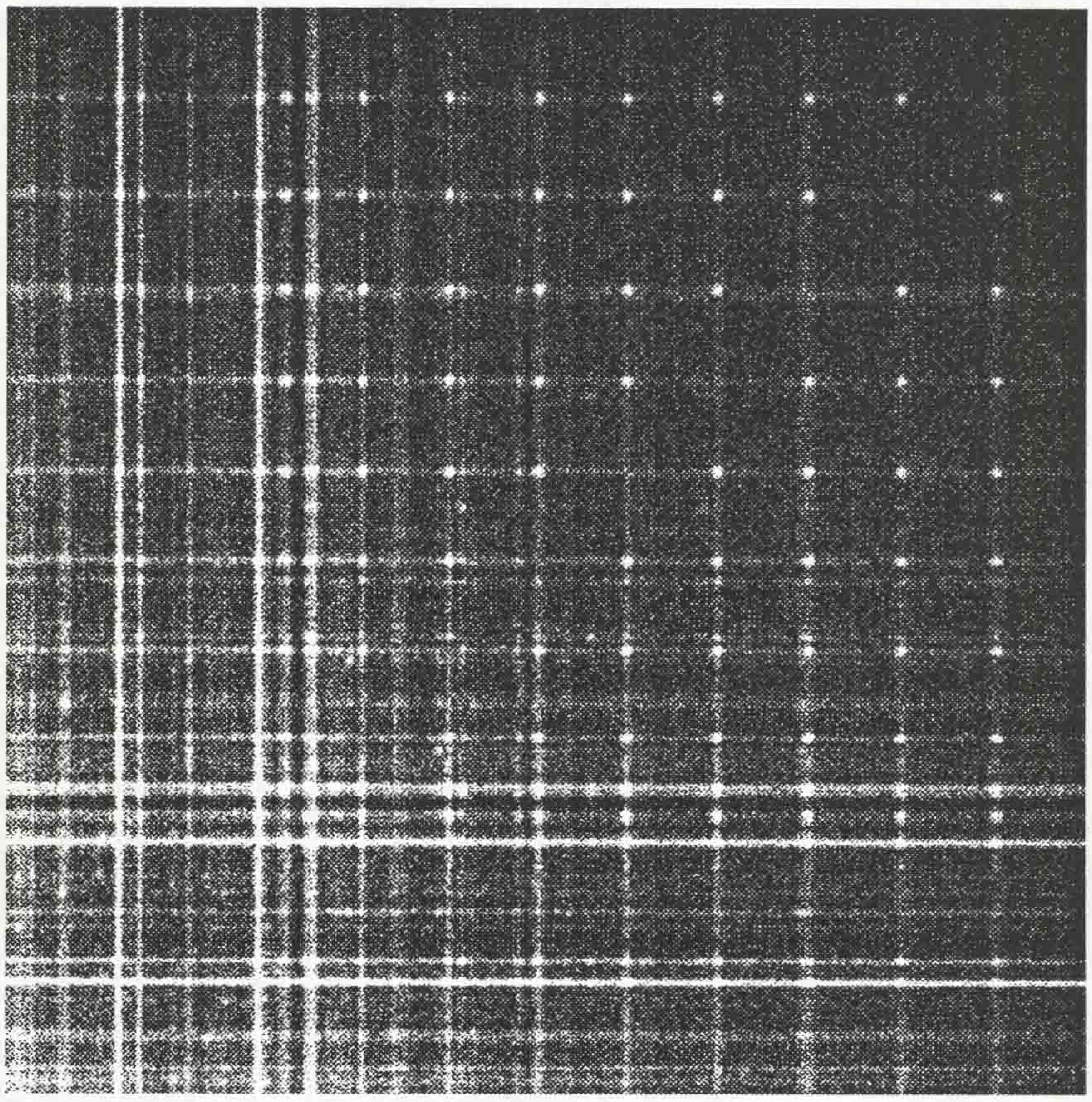

Figure 3.12: Plan view of a two dimensional double gated γ-γ matrix (quadruples coincidences) produced for the ^{132}Ce yrast superdeformed band. The energy range on both axes is 600 keV to 1500 keV. At low energy, the normal-deformed structures are complex. At higher energies, the regular structure of the superdeformed band is clearly evident.

and stored in the matrix. The procedure of gating on this matrix then provides the final stage in the selection of triple events. Fig. 3.12 shows a section of the 2D quadruples matrix produced by all γ-γ coincidences for the ^{132}Ce yrast superdeformed band. Each dot in the figure represents a coincidence between two γ-rays detected at those energies. The more intense the dot, the more coincidences were detected. The complicated pattern corresponding to normal-deformed transitions (lower energies, lower left) is in contrast to the regularly spaced pattern of the superdeformed band (higher energies, upper right).

3.13.4 Background Subtraction

Projected γ-ray spectra produced by gating contain not only true photopeak-photopeak coincidences, but also photopeak-background coincidences. These photopeak-background coincidences result from unsuppressed Compton scattered events, unresolved continuum γ-rays, and random coincidences due to uncorrelated events.

The background is generally removed by subtracting a normalised fraction of a suitable background gate from the gated spectrum. A suitable background can be generated in a number of ways, but two general types of background have been employed in this analysis :

1. The subtraction of a fraction of the total projection.
2. The setting of a number of gates near to the required gate, and by subtracting the normalised average of the background level obtained from these.

The most useful is dependent on the individual spectrum, the statistics and the degree of contamination.

Chapter 4

Results

4.1 Previous Studies of ^{131}Ce and ^{132}Ce

At low spin, the nuclei ^{131}Ce and ^{132}Ce are soft, deformed ($\beta_2 \approx 0.2$), prolate rotors. The normal-deformed structures of ^{131}Ce [Pal91, Mul93] and ^{132}Ce [War68, Deh74, Hus77, Kir87b] have been extensively studied, and there is good agreement between their experimental behaviours and cranked-shell model predictions.

As long ago as 1982, the yrast states of ^{132}Ce were predicted [Abe82, Ben85] to have a more deformed shape ($\beta_2 \approx 0.4$) at higher spins. To investigate the high-spin structure of ^{132}Ce, Nolan *et al.* [Nol85] populated the nucleus by the reaction ^{100}Mo(^{36}S,4n)^{132}Ce at a beam of energy of 150 MeV.

The predicted shape change at high spin was confirmed, and the existence of 'a rotational band in ^{132}Ce with a high moment of inertia' [Nol85] was reported. The superdeformed nature of ^{132}Ce was verified with the first lifetime measurements of the states within the superdeformed second minimum [Kir87], and was reported to be $\beta_2 \approx 0.43$. The yrast superdeformed band was also extended in spin to beyond $50\hbar$ in this analysis.

A superdeformed band extending to $40\hbar$ was then discovered in ^{131}Ce [Luo87] with an intensity of 5% relative to the main reaction channel. This population intensity is the same as that of the ^{132}Ce yrast superdeformed band. The deformation was subsequently measured [He90] to be $\beta_2 \approx 0.35$.

Superdeformation has now been observed in other nuclei in the mass A $\approx$ 130 region; namely the Sm, Nd, Pr and La isotopes.

Excited superdeformed bands have been observed in other mass regions, and in view of the relatively high population intensities of the superdeformed bands in ^{131,132}Ce, it was surprising that no excited bands had been observed in these nuclei. The aim of the studies presented in this work was three-fold:

- To investigate more fully the known superdeformed bands in ^{131,132}Ce, facilitated by the third generation of γ-ray detector arrays.
- To search for excited superdeformed bands in ^{131,132}Ce.
- To search for 'identical bands' in ^{131,132}Ce. Prior to this work, there were no such bands in the mass A $\approx$ 130 region.

4.2 The Experiment

To investigate superdeformation in ^{131,132}Ce, an experiment was performed using the Eurogam Phase I γ-ray spectrometer (Sec. 3.11). The array was equipped with 41 high-purity Compton suppressed germanium detectors. A 155 MeV beam of ^{36}S was provided by the tandem Van de Graaff accelerator at the Nuclear Structure Facility, Daresbury, and was used to bombard a self supporting ^{100}Mo target of thickness 625 μg cm^{-2}. This reaction produced approximately 40% ^{131}Ce and 50% ^{132}Ce by the 5n and 4n reaction channels, respectively. Only events with unsuppressed fold ≥ 7 were recorded and this resulted in a total of 3.5 x 10^9 suppressed γ-γ coincidence events being collected (after unfolding the high fold events, Sec. 4.4.1).

4.3 Gainmatching & v/c Correction

Before analysis of the data can begin, each detector has to be corrected for its different amplifier gain and for the Doppler shifts of the γ-rays. Prior to (and/or after) each experiment, a calibration source (typically ^{152}Eu or ^{56}Co) is placed in the array, and data recorded. These data are then sorted into individual spectra for each detector, and linear gain corrections are applied to align each of the detector gains. The use of a thin target in the experiment studied in this work, ensured that the recoiling ^{132}Ce nuclei travel through the smallest possible distance inside the target material. The γ-rays will therefore be emitted from recoiling nuclei travelling in a vacuum with constant recoil velocity.

For a nucleus travelling at these recoil velocities, the emitted γ-rays are subject to Doppler shifts:

$$E'_\gamma = E_\gamma(1 + v/c \; cos \; \theta) \tag{4.1}$$

where E'_γ is the energy of the γ-ray detected from a moving source, E_γ is the energy of the γ-ray emitted, v is the recoil velocity, c is the speed of light and θ is the angle between the recoil direction and the detector.

Eurogam has detectors at six different angles (Table 3.2, Sec. 3.11), and so the measured energy of the γ-ray detected will be different depending on the detectors' position in the array. Fig. 4.1 shows the $2^+ \rightarrow 0^+$ transition (325 keV) in ^{132}Ce for one detector at each of the angles. The peak is shifted relative to its 'absolute' value depending on the sign of cos θ in eqn. 4.1. A value of v/c for the reaction may therefore be obtained by plotting E'_γ versus cos θ for each detector, as shown in Fig. 4.2 for the 325 keV transition. The intercept on the y-axis when cos $\theta = 0$ gives the value of E_γ. The gradient divided by E_γ then gives the value of v/c. This process was repeated for several peaks in the total projection, and an average value of v/c was calculted :

$$v/c = 0.0218 \pm 0.0001 \tag{4.2}$$

The error is the standard error on the mean. The linear gain coefficients for each detector are then corrected for v/c by dividing each coefficient by (1+v/c cos θ) in accordance with eqn. 4.1.

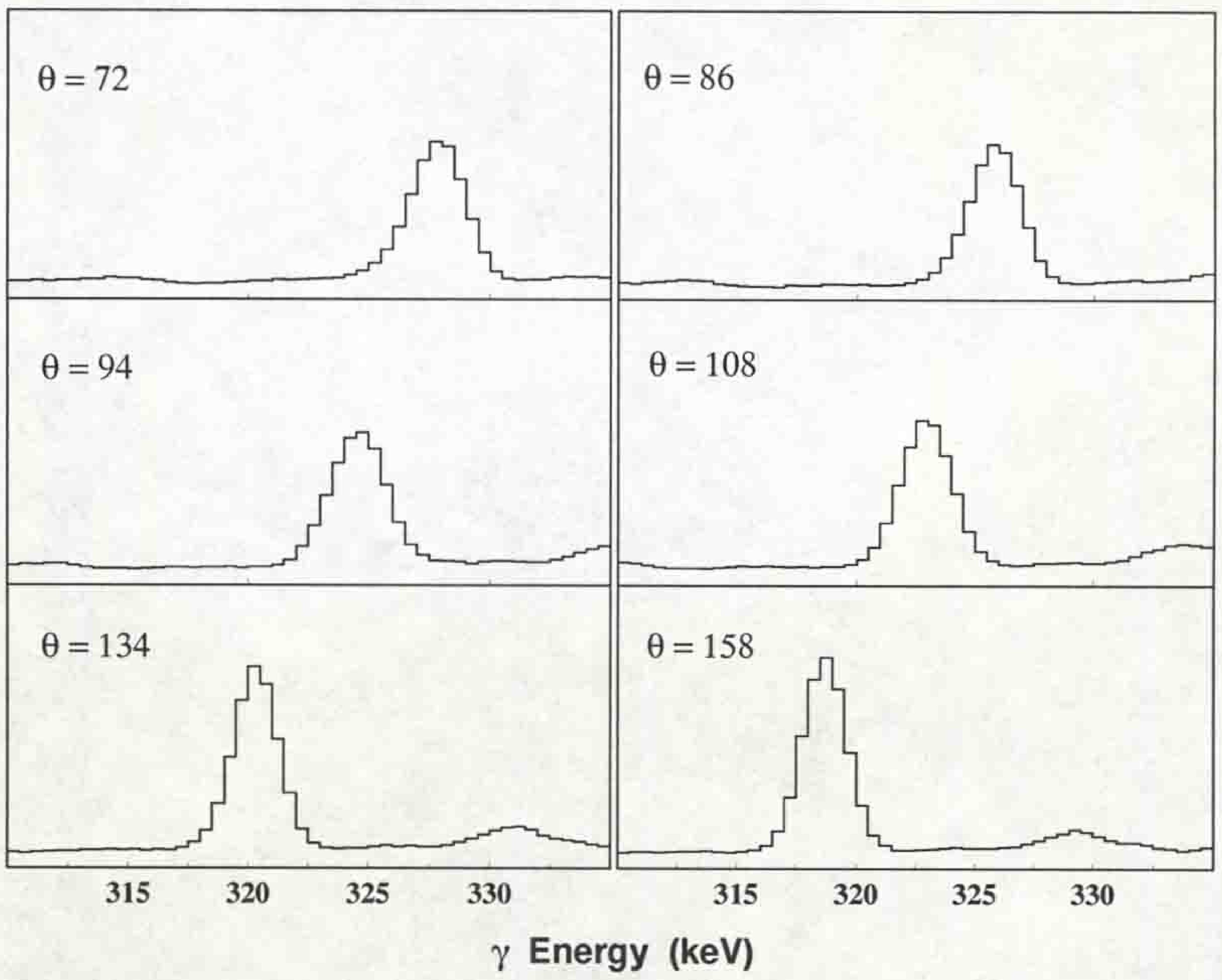

Figure 4.1: The 325 keV transition in ^{132}Ce, as detected by detectors at the six angles in Eurogam Phase I. The peak position is Doppler shifted relative to its absolute value depending on the detector angle.

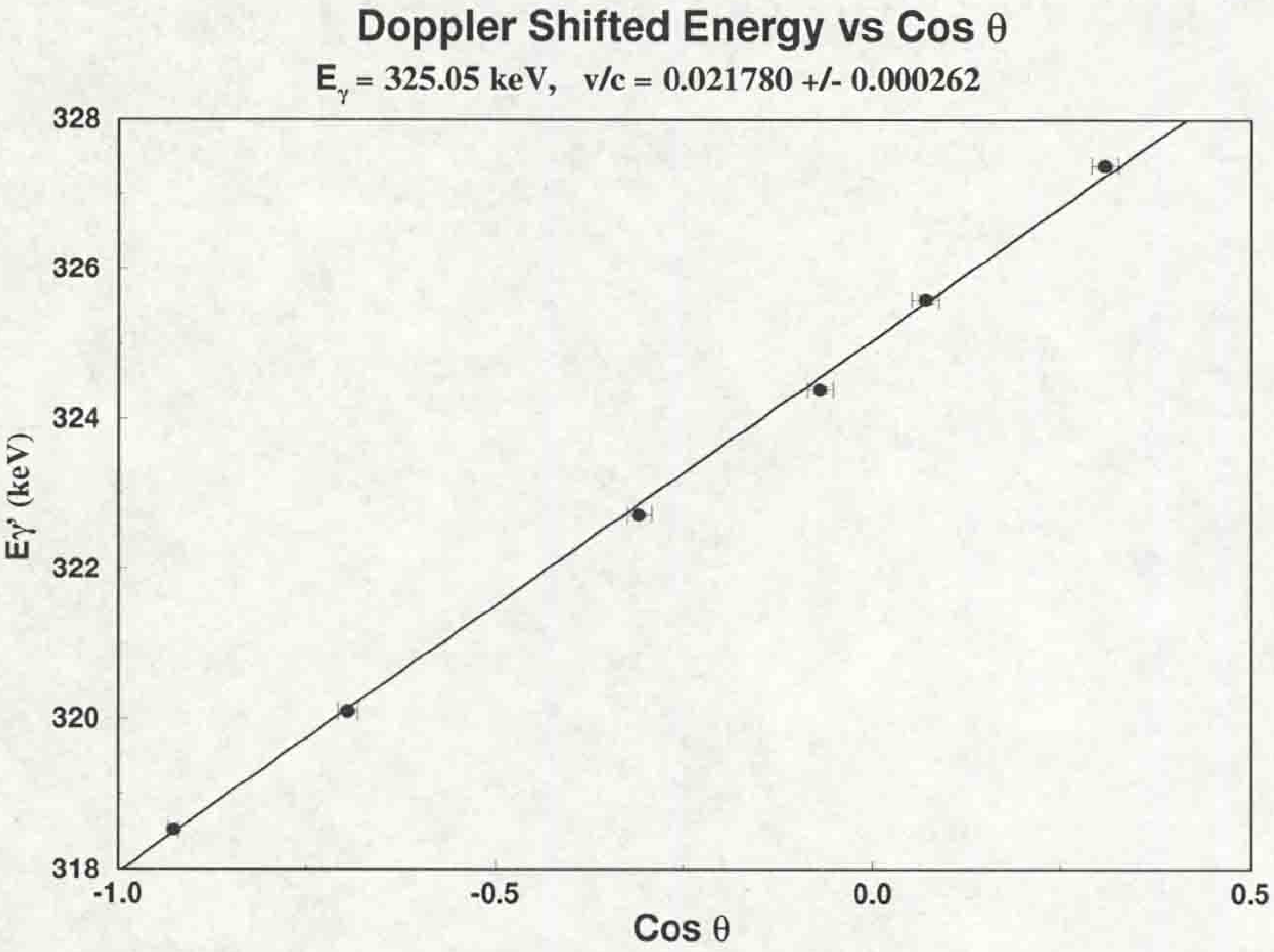

Figure 4.2: Graph of measured peak position versus cos θ for the 325 keV transition in ^{132}Ce.

4.4 Characteristics of the Data

4.4.1 Unfolding the Data

The number of γ-rays detected in coincidence by two or more detectors is referred to as the 'fold'. The mastergate required that only unsuppressed fold ≥ 7 were recorded to tape. The graph labelled 'raw fold' in Fig. 4.3 shows the suppressed fold distribution for the experiment studied in this work, illustrating that triple and quadruple suppressed γ-events dominate the data. Each event may also be 'unpacked' into lower fold events as discussed in Sec. 3.13.1 (for example, a triple event may be unpacked into 3 doubles events). When the data from the higher folds is unpacked into lower folds, the statistics for a particular fold is increased dramatically. The graph labelled 'unpacked fold' of Fig. 4.3 illustrates this effect, where unpacked doubles and triples events now dominate. The graph also shows the acquired statistics for the experiment: approximately 3.5×10^9 doubles, 3.4×10^9 triples and 2.0×10^9 quadruple events were recorded.

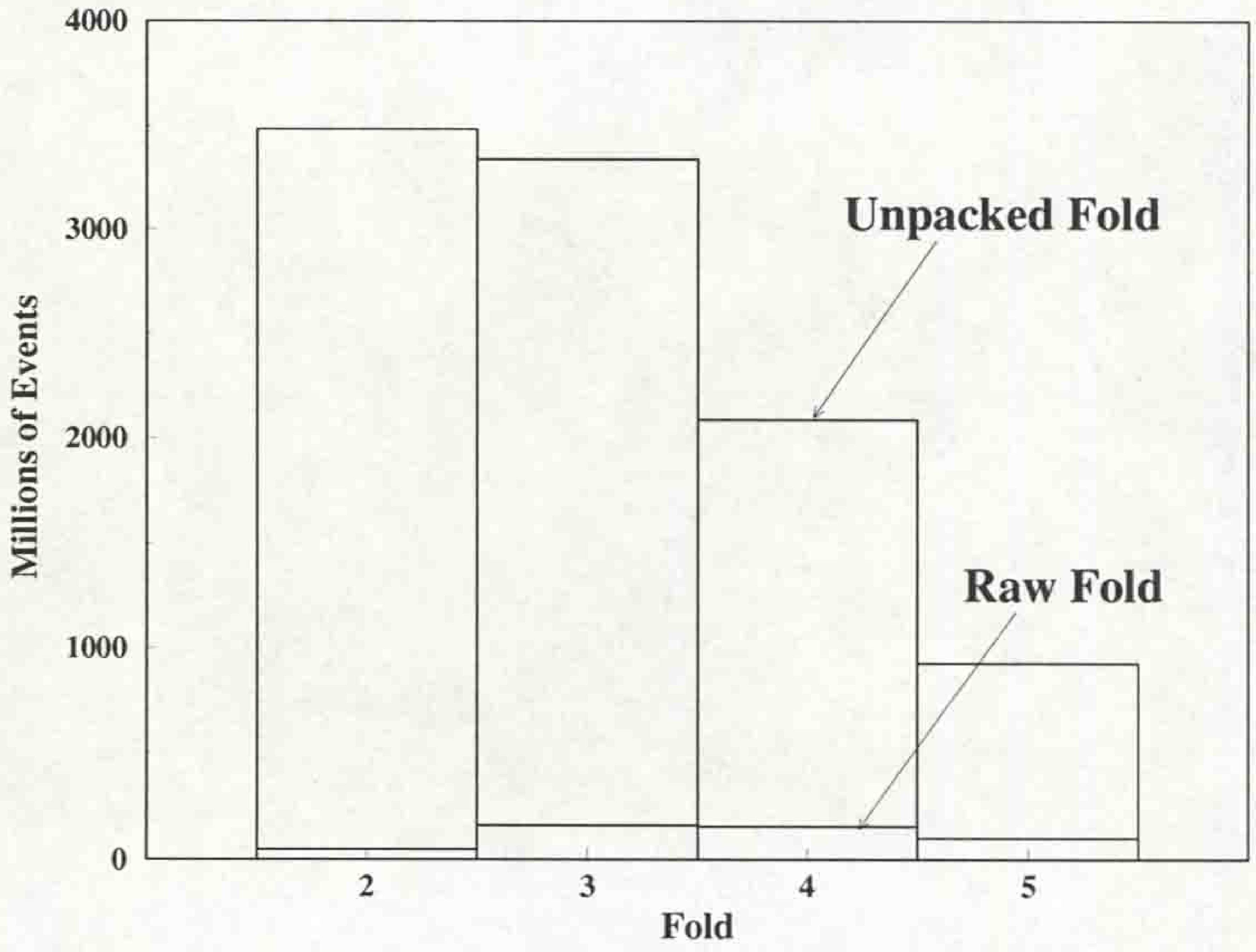

Figure 4.3: ^{132}Ce fold distribution for events in the range $2 \leq$ suppressed fold ≤ 5. The number of events for a particular fold (raw fold) is increased dramatically by unpacking higher fold events (unpacked fold).

4.4.2 The Use of Higher-Fold Data

The selection of increasingly higher fold data when sorting on superdeformed bands, results in a dramatic decrease in contamination. However, the previous section showed that beyond fold three, the number of events for a particular fold, decreases rapidly. Therefore, as higher-fold events are selected, the statistics in the band also decrease rapidly.

Fig. 4.4 shows spectra obtained for the yrast superdeformed band in ^{132}Ce. Each spectrum has been produced by summing gates at each uncontaminated transition energy in the band. Higher-fold spectra have been created by setting one or more gates in the sort, as discussed in Sec. 3.13.3.

As the fold increases, the contaminants are reduced, but the number of counts on the y-axis can be seen to decrease as the data is successively filtered into higher folds. By the stage that quintuples events are selected, the spectrum is exhibiting a large degree of statistical fluctuation. A compromise must therefore be reached in the choice of fold to be analysed in order to maximise statistics but minimise contamination.

The example used here to illustrate this effect is a relatively intense and uncontaminated superdeformed band. Other bands observed in this work are a fifth of this intensity (Sec. 4.7.3), and so anything above triples events are inadequate in the analysis of these bands.

4.5 The Efficiency Measurement of the Eurogam Array

The measurement of the γ-ray intensity of the members of a rotational band, where all the decay paths are known, allows the relative efficiency of the array over the energy range covered by the rotational band to be deduced.

If the array's efficiency was not energy dependant, a gate set at the top of the band would result in every transition below the gate being of equal intensity (provid-

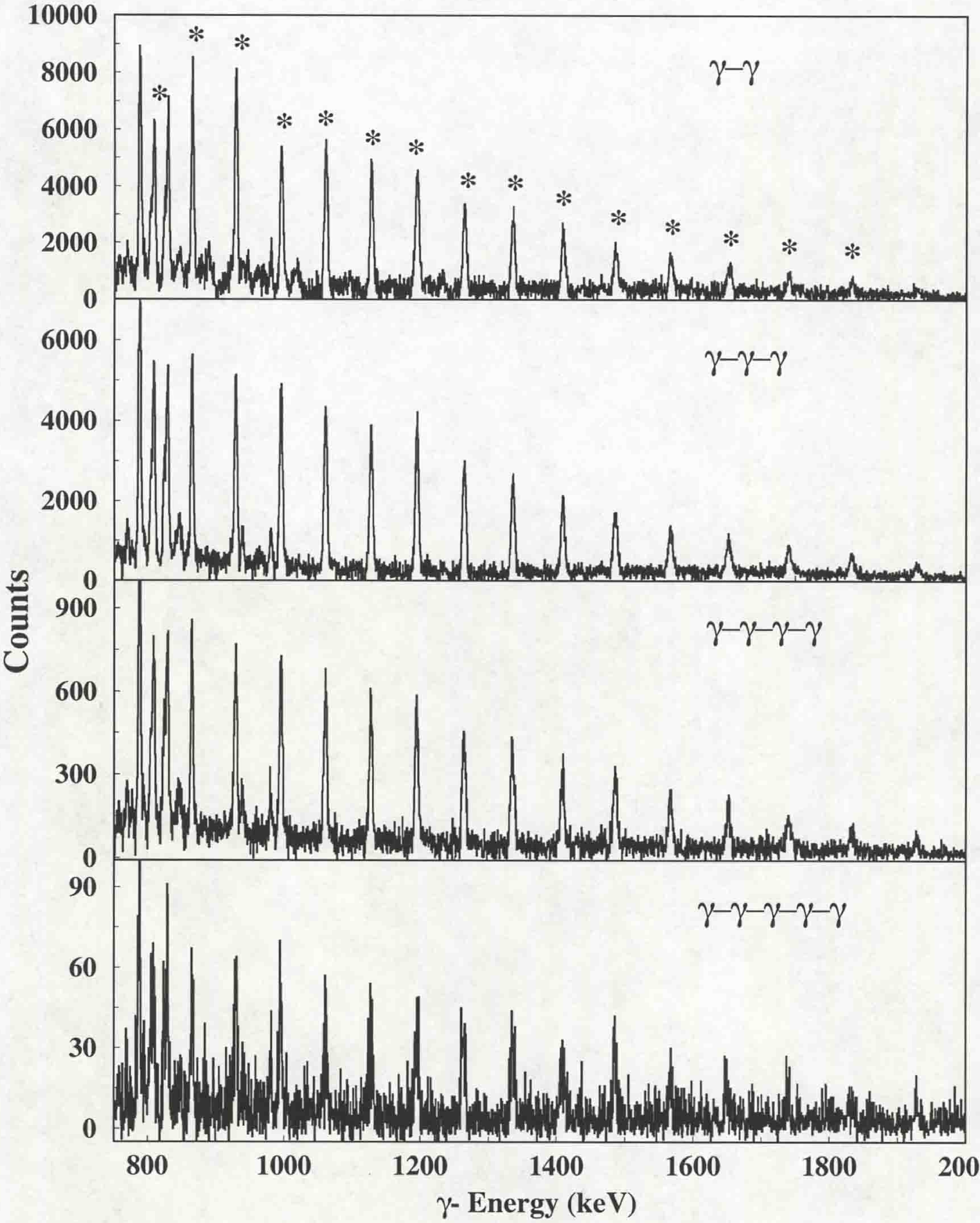

Figure 4.4: ^{132}Ce band 1 obtained with doubles (γ-γ), triples (γ-γ-γ), quadruples (γ-γ-γ-γ) and quintuples (γ-γ-γ-γ-γ) coincidence events. Transitions used in the gating process are indicated (*).

ing there is no decay out of the band). However, Fig. 4.5, which is an efficiency measurement for the ^{132}Ce coincidence data (and source data), indicates that the measured intensity I_{meas} is dependent upon the energy E_γ, of the incident radiation.

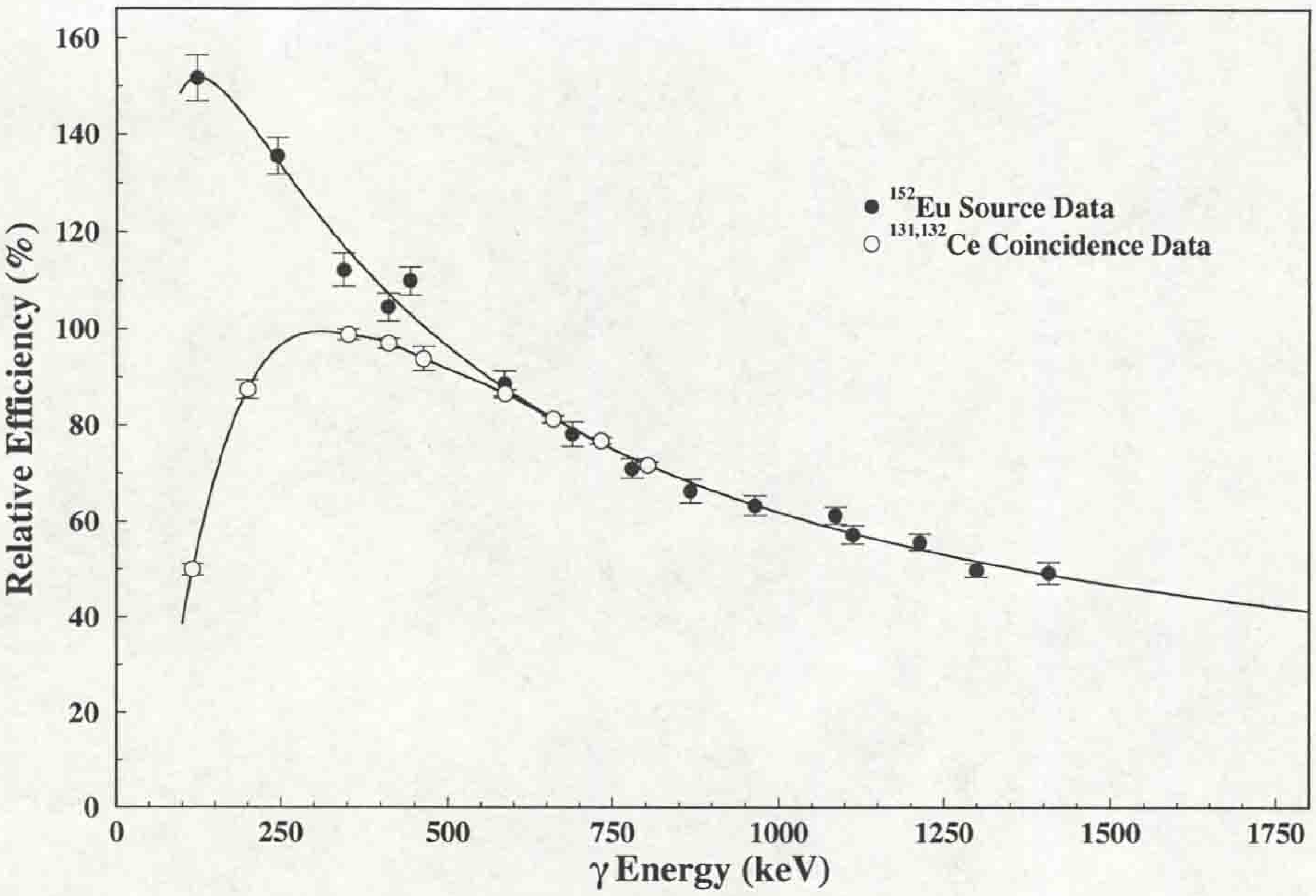

Figure 4.5: Efficiency curve for the Eurogam Phase I detector array. Source and coincidence data measurements are presented.

Above ~400 keV, it is approximated as

$$I_{meas} \approx I_{true} E_\gamma^{-\alpha} \tag{4.3}$$

where I_{true} is the true intensity of the γ-ray. The value of α may be obtained by plotting a suitable graph such that

$$\log I_{meas} \approx -\alpha \ \log \ E_\gamma + \log \ I_{true} \tag{4.4}$$

α is the gradient, and is measured to be 0.59±0.05.

At low energies the efficiency falls off rapidly principally because low energy γ-rays are stopped in the front of the Ge crystal where charge collection is poor. The electronic processing for low energy γ-rays is also less reliable than for energies above ~ 300 keV. Consequently, coincidences between γ-rays are reduced, and this results in the ^{132}Ce coincidence data having a lower efficiency at low energy than ^{152}Eu source data. Nevertheless, all intensities measured in this work are above $\approx$ 600 keV, at which energy the approximation given in eqn. 4.3 is valid.

4.6 Observation of the Superdeformed Bands

4.6.1 Previously Discovered Superdeformed Bands

Prior to this work, the nuclei ^{131}Ce and ^{132}Ce were known each to contain a single superdeformed band ([Luo87] and [Nol85], respectively). Spectra for these two bands as observed in this work (obtained from quadruple coincidence events) are presented in Fig. 4.6. Both bands are assumed to be the yrast superdeformed band of their respective nuclei.

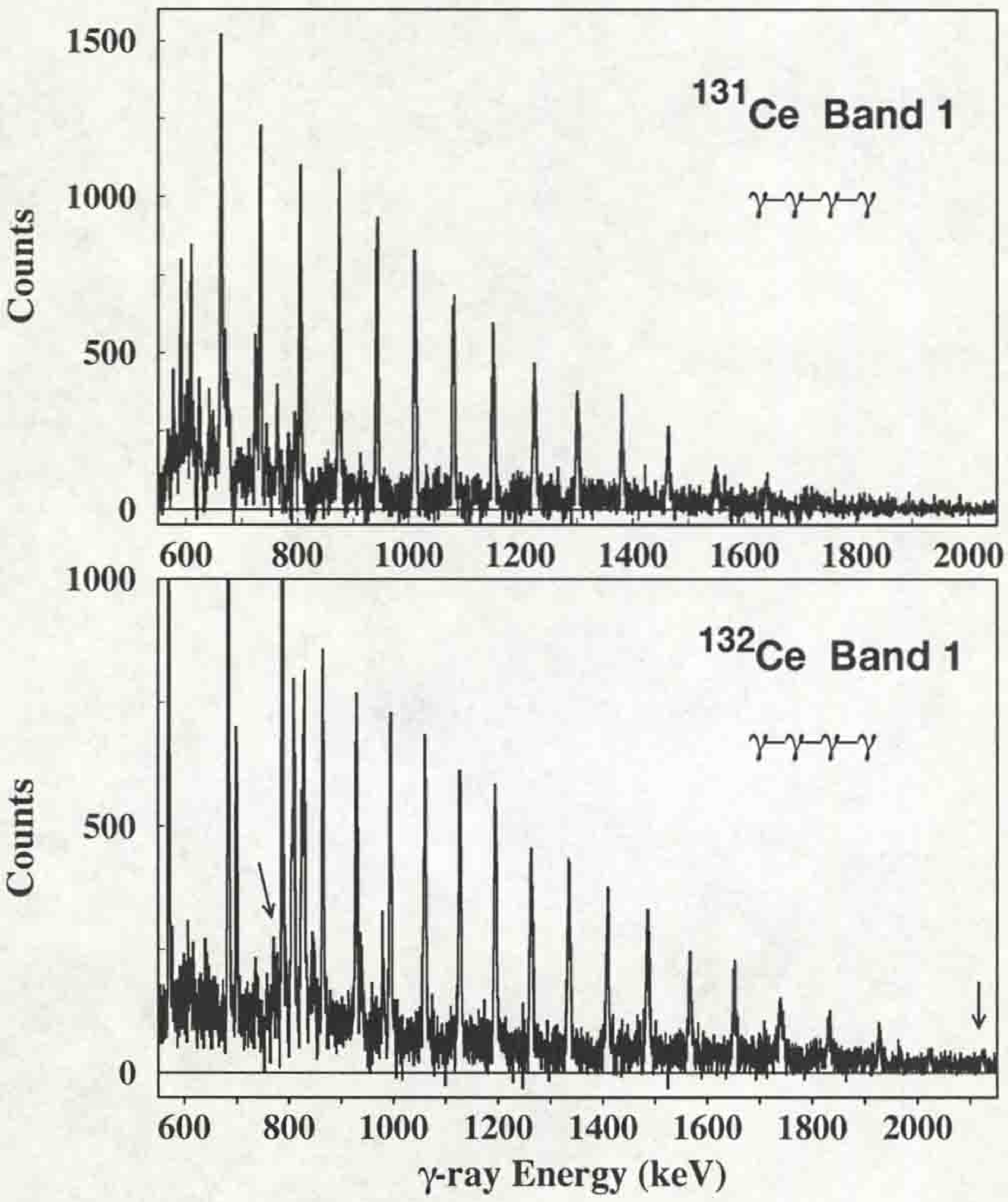

Figure 4.6: Spectra for ^{131}Ce band 1 and ^{132}Ce band 1, obtained from quadruple coincidences. New transitions are indicated with an arrow.

The yrast band in ^{132}Ce (^{132}Ce band 1) has been extended towards higher spins by an additional transition (2119 keV). The band has also been extended at low spins by a single transition at 769 keV. No new transitions have been observed in the yrast band in ^{131}Ce (^{131}Ce band 1).

4.6.2 New Superdeformed Bands

Three new superdeformed bands have been observed in this work. One band has been assigned to ^{131}Ce (^{131}Ce band 2) and two to ^{132}Ce (^{132}Ce band 2 and ^{132}Ce band 3). These bands lie at the detection limit of the Eurogam Phase I spectrometer, and are populated with considerably less intensity than the yrast bands (Sec. 4.7.3). Fig. 4.7 shows triples spectra for each of the new bands.

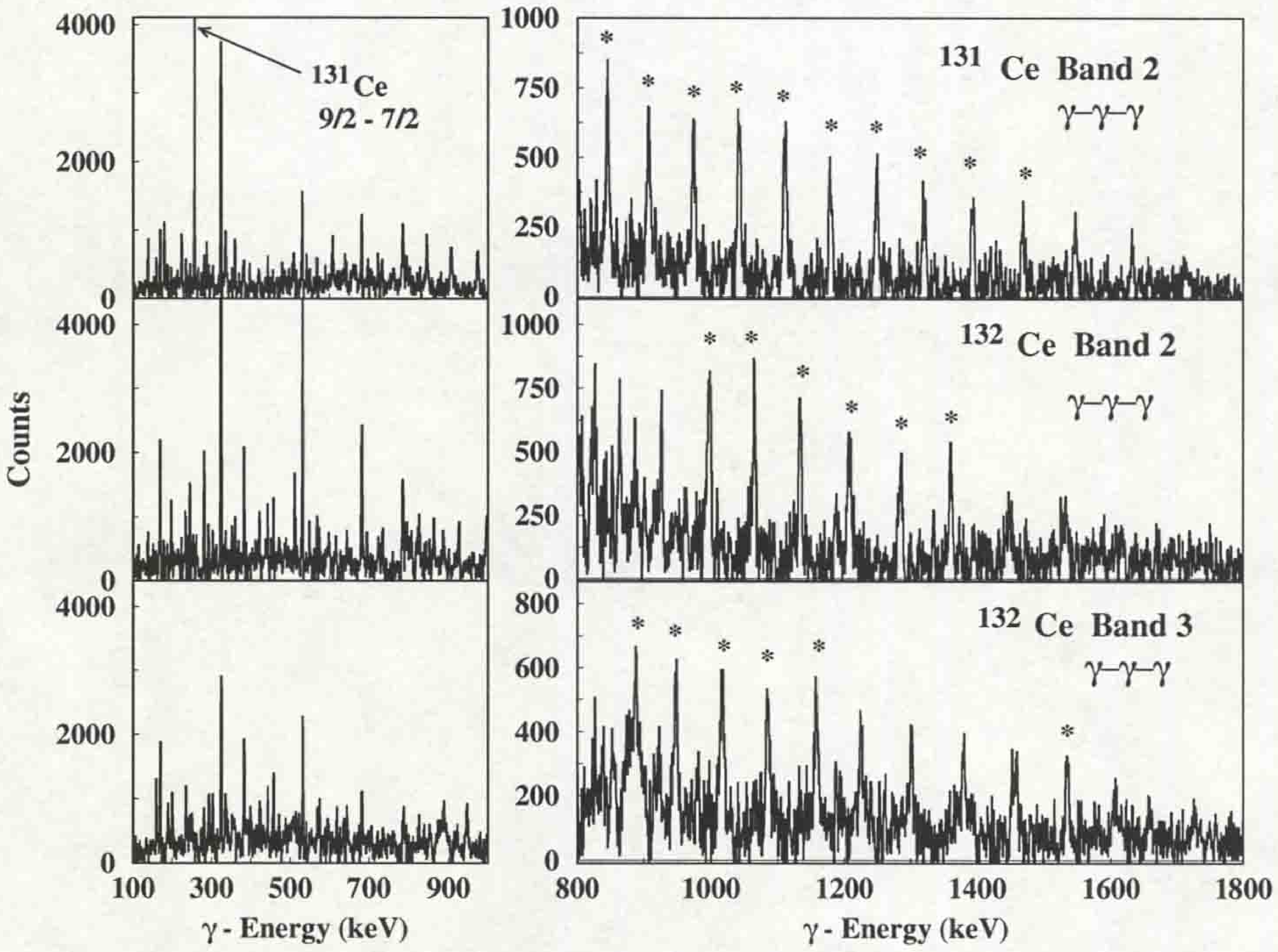

Figure 4.7: Spectra for ^{131}Ce band 2, ^{132}Ce band 2 and ^{132}Ce band 3, obtained from triple coincidences. Gated transitions are indicated (*). The $9/2 \rightarrow 7/2$ transition in ^{131}Ce is also indicated. The transition is absent in the bands in ^{132}Ce.

Their low population intensity meant that analysis of fold four events (or higher) was impossible. There were also very few uncontaminated γ-ray transitions in the superdeformed bands and in some cases, only a few transition remained to sort with. This had a detrimental effect on the statistics. These bands represent the first observation of excited superdeformed bands in the mass A $\approx$ 130 region.

4.7 Experimentally-Measured Quantities

4.7.1 Transition Energy Measurements

The energies of the transitions within the bands were assigned in the conventional way by fitting Gaussian lineshapes to the superdeformed peaks shown in Fig. 4.6 and Fig. 4.7. The spectra were calibrated to 0.5 keV/channel using a ^{152}Eu source as discussed in Sec. 4.3. Due to the large statistics obtained and the large number of data points available with the ^{152}Eu source, the error due to the calibration was found to be minimal. The error on the transition energies is therefore a combination of two separate factors:

1. **The statistical uncertainty,** δ $\delta=\sigma/\sqrt{N}$, where σ is the standard deviation of the peak (obtained from the Full Width at Half Maximum (FWHM) by FWHM $= 2.35\sigma$) and N is the total number of counts in the peak.

2. **The inherent uncertainty in the background** There are changes in the centroid of the peak due to the chosen background. An estimate for this error was obtained by fitting the peaks with several different (but 'reasonable') backgrounds.

The final error on the transition energy is then obtained by adding these contributions in quadrature. The transition energies, along with their corresponding uncertainties are presented in table. 4.1. The uncertainties for ^{131}Ce band 1 and ^{132}Ce band 1 are considerably smaller than for the other bands. This reflects the lower population intensity for the excited bands relative to the yrast bands. Within a band, the uncertainties are relatively small at lower energies, but increase at higher energies.

^{131}Ce Band 1 (keV)	^{131}Ce Band 2 (keV)	^{132}Ce Band 1 (keV)	^{132}Ce Band 2 (keV)	^{132}Ce Band 3 (keV)
590.73(05)				
661.99(05)				
732.52(05)		769.61(10)		
804.27(05)		808.55(05)		
873.95(05)	846.80(10)	864.85(05)	864.79(10)	889.97(10)
942.93(05)	908.07(10)	928.80(05)	927.84(10)	948.89(10)
1011.33(05)	975.52(10)	994.63(05)	999.61(10)	1018.26(10)
1080.48(06)	1043.13(10)	1060.32(05)	1067.19(11)	1086.78(10)
1151.28(06)	1112.24(11)	1127.27(06)	1136.29(11)	1159.26(12)
1225.00(06)	1181.28(12)	1194.72(06)	1209.69(11)	1227.62(12)
1301.38(06)	1250.71(12)	1263.63(06)	1287.13(13)	1305.52(12)
1381.11(08)	1322.04(12)	1334.56(07)	1362.42(13)	1382.76(13)
1464.06(08)	1396.22(15)	1408.34(09)	1451.69(15)	1461.79(16)
1549.89(10)	1470.66(15)	1485.67(10)	1536.49(15)	1538.16(16)
1640.26(12)	1551.81(20)	1566.70(10)	1617.04(18)	1608.58(20)
1731.50(15)	1634.80(22)	1651.49(12)	1691.01(24)	1661.52(20)
(1822.00)	1723.02(30)	1740.29(14)		1729.23(23)
		1832.64(17)		
		1926.50(17)		
		2023.50(20)		
		2119.00(25)		
		(2201.00)		

Table 4.1: γ-ray transition energies for the five superdeformed bands in ^{131}Ce and ^{132}Ce. Tentative transitions are shown in brackets.

This reflects the effects of Doppler broadening and reduced detector efficiency which makes the transitions more difficult to resolve at higher energies.

In addition to the transitions of the superdeformed bands, other transitions are observed that are in coincidence with them. These other transitions represent the decay path of the superdeformed states into the normal-deformed states. Observation of these transitions enable the conclusive assignment of the band to a particular nucleus.

4.7.2 Relative Intensity Measurements

Relative intensity measurements describe the intensity distribution of the superdeformed band relative to its maximum intensity. It has already been discussed that superdeformed bands have low population intensities. In order to produce a spectrum with sufficiently pronounced SD band members, gated γ-γ matrices are required.

Only gates which incorporate the most strongly populated and least contaminated band members are used in the sorting process. The γ-ray peaks were then fitted with Gaussian lineshapes (as discussed in Sec. 4.7.1) and their intensities measured.

The intensities obtained by this procedure must now be corrected for both the efficiency of the Eurogam array (Sec. 4.5), and the efficiencies of the combination of gating conditions. Relative intensity distributions of superdeformed bands have some characteristic features :

1. **Feeding Region.** The region over which the intensity is observed to rise gradually from the highest transition (going from high to low energies). This region corresponds to the population (or feeding) of the superdeformed band.

2. **Plateau Region.** Generally, the feeding of superdeformed bands ceases at some stage, and a region of constant intensity is observed.

3. **Rapid Depopulation Region.** Below the plateau energy region, the intensity drops rapidly over one or two transitions corresponding to a rapid depopulation of the superdeformed band.

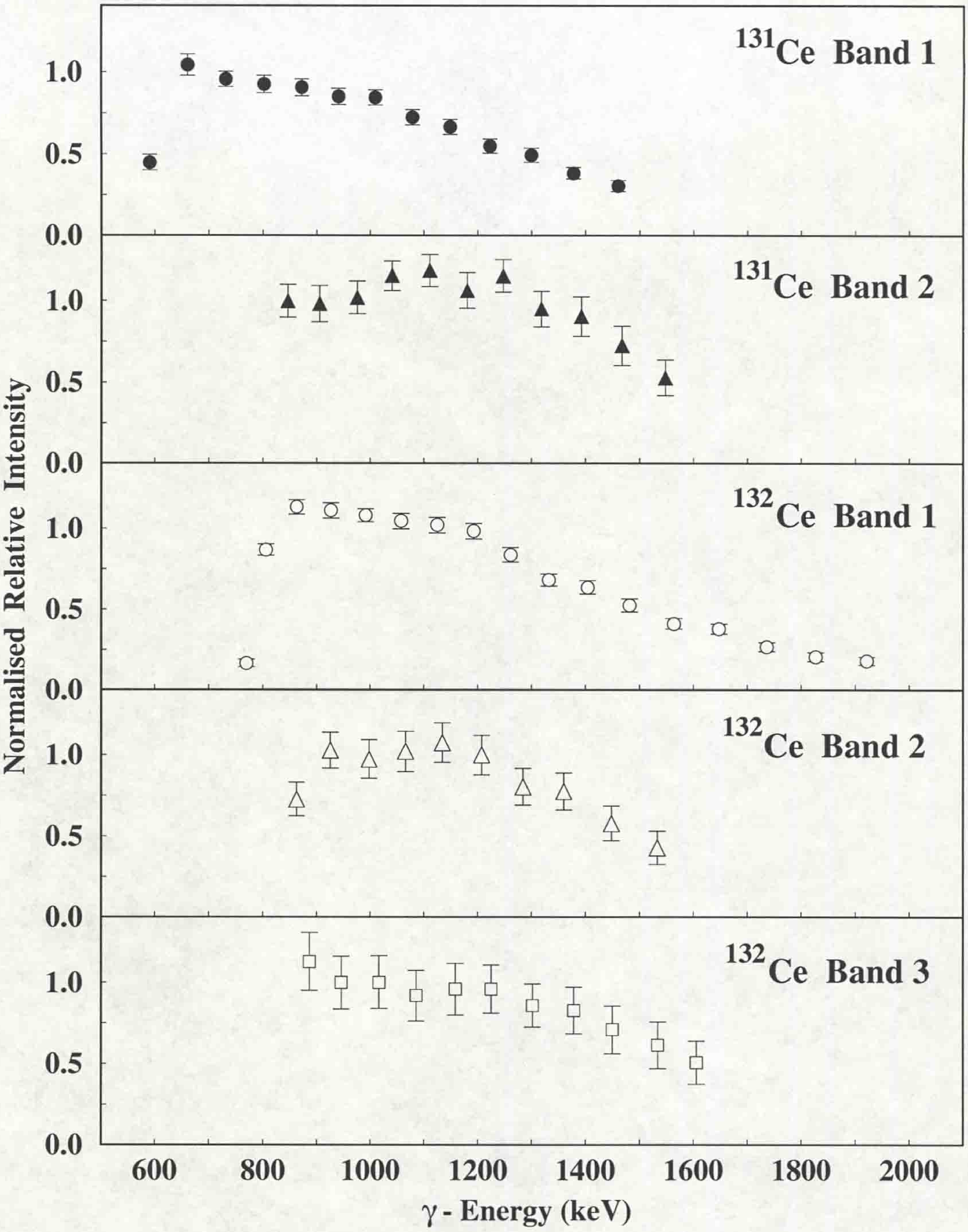

Figure 4.8: Relative intensity measurements for the superdeformed bands in ^{131}Ce and ^{132}Ce, normailsed to the 100% transition(s) in each band.

The relative intensity distributions for the cerium bands discussed in this work are illustrated in Fig. 4.8. It is evident from the figure that ^{131}Ce Band 1 and ^{132}Ce Band 1 both have the characteristic intensity distribution described above. However, the excited bands have two features which distinguish them from the yrast bands.

1. The feeding region occurs over only $\sim$4 transitions (c.f $\sim$8 for the yrast bands), while the plateau region extends over $\sim$8 transitions (c.f $\sim$5 for the yrast bands). This is indicative of the excited bands having a higher excitation energy than the yrast bands.

2. There is no depopulation observed of ^{131}Ce Band 2 and ^{132}Ce Band 3 (^{132}Ce Band 2 shows an indication of depopulation). However, the depopulation is expected to occur over 1 or 2 transitions only, and as these bands are considerably weaker than the yrast bands, it is possible that these transitions are below the observable limit for the array.

4.7.3 Absolute Intensity Measurement

The absolute intensity of a superdeformed band is a measure of the population of the band relative to a reference. This reference is usually the transition depopulating to the ground state of the nucleus, or is often the intensity of the yrast superdeformed band in the nucleus.

The former method involves comparing the intensity of a transition in the 100% intensity region of the SD band with the total intensity flow of the respective reaction channel. The latter method requires that similar gating conditions are used for both bands being compared (i.e. the same number of gates are set on transitions in the 100% intensity region). A direct comparison of intensities may then be made to determine the intensities of the weaker bands.

The results are summarised in Table. 4.2

Superdeformed Band	Intensity Relative to Reaction Channel	Intensity Relative to SD Band 1 in nucleus
^{131}Ce band 1	5.0±0.2%	100±4%
^{131}Ce band 2	1.1±0.3%	22±6%
^{132}Ce band 1	5.0±0.2%	100±4%
^{132}Ce band 2	1.0±0.3%	20±6%
^{132}Ce band 3	0.9±0.3%	18±6%

Table 4.2: Absolute population intensities for the five superdeformed bands in ^{131}Ce and ^{132}Ce.

4.8 Spin Assignments and the Decay of the Bands

It was shown in Sec. 2.5.1 that the bandhead of ^{132}Ce Band 1 is believed to lie ≈ 4 MeV above the yrast line, and is therefore in a region of very high level density. It is possible to trace the intensity of a superdeformed band as it is slowly collected into the yrast sequence. This is achieved by gating on the SD band and by measuring the intensities of all transition peaks in the spectrum. After correcting for array efficiency, a complete decay path of the band may be established. Fig. 4.9 shows the decay of ^{132}Ce Band 1. The population intensity of each normal-deformed state by the superdeformed band has been obtained by subtracting away the intensity of the previous level.

It can be seen that the intensity of the SD band depopulates through the yrast normal-deformed states at spins $14\hbar$ to $20\hbar$.

Although no discrete linking transitions have been observed between the superdeformed and normal-deformed states, it is thought that the decay may occur by a series of up to four statistical transitions, carrying a total spin of $\approx 4\hbar$. From the figure, the average feeding out spin of the superdeformed band is approximately $20\hbar$, and the average feeding in spin to the normal-deformed states is approximately $16\hbar$. This suggests that the linking transitions do indeed carry about $4\hbar$. Based upon this

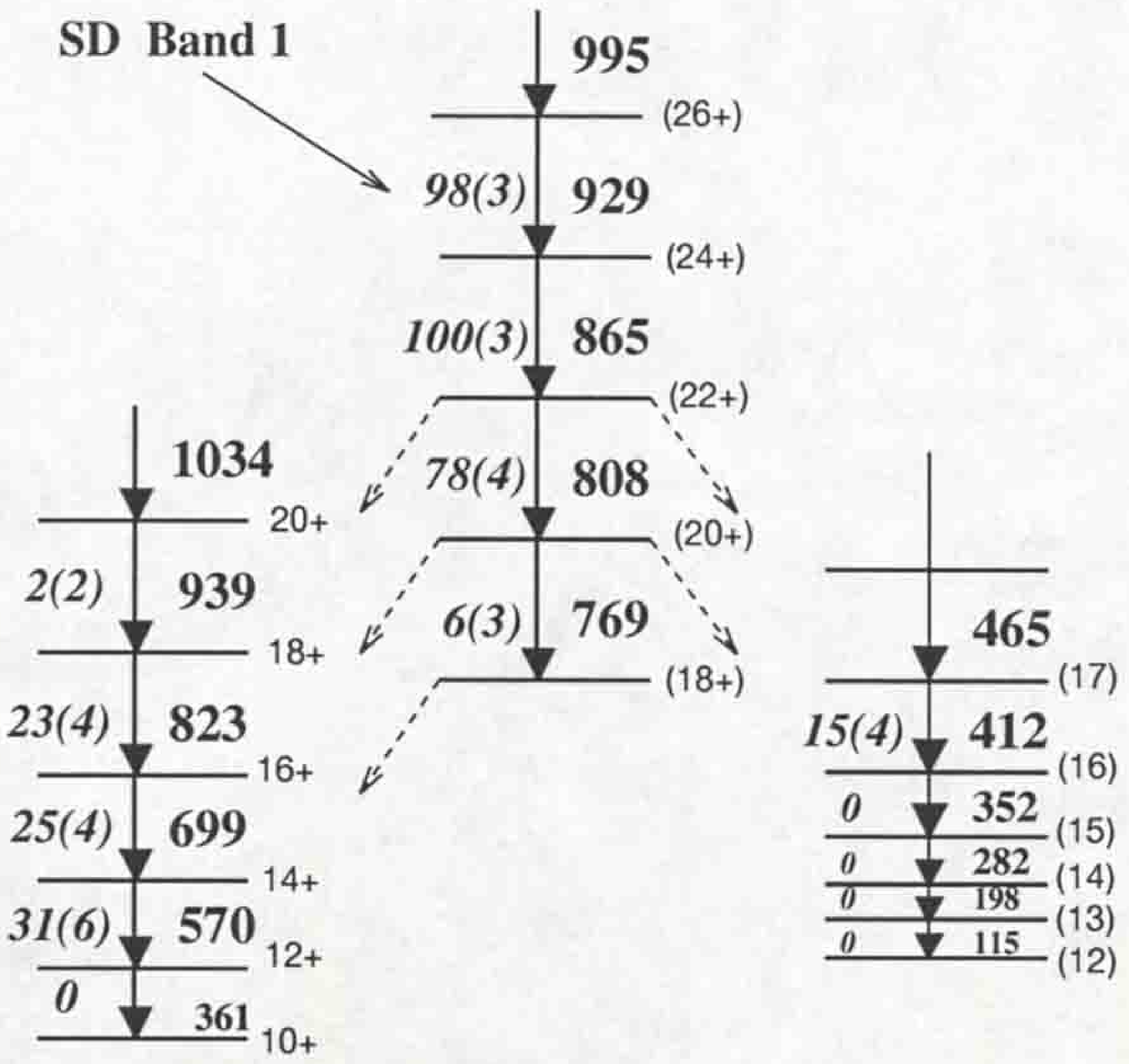

Figure 4.9: The decay of ^{132}Ce Band 1 into the normal deformed states. The partial decay scheme shown is from previous studies [Kir87b]. The numbers on the right of the rotational bands are the transition energies (keV), while those on the left represent the population intensity (%) of the transitions from the superdeformed band. The spins and parities of the normal-deformed states, and the proposed spins and parities for the superdeformed band are shown also shown.

approach, it is reasonable to assign a spin of $\approx 18\hbar$ to the bandhead of ^{132}Ce Band 1.

It should be noted however, that these are only estimates, and that spin values of superdeformed bands should always have an error of at least $\pm 2\hbar$ assigned to them. A similar treatment was also given to the other SD bands discussed in this work which enabled their spin assignments to be made. The proposed spins for the superdeformed bands are presented in the level schemes of Fig. 4.10. The parities of the bands are obtained from a consideration of their deduced nuclear structures and are discussed in Sec. 5.4 and Sec. 5.5.

4.9 Angular Correlation Measurements

It was discussed in Sec. 1.4 that a γ-ray emitted in a rotational band carries with it an angular momentum $L\hbar$, where L is the multipolarity of the γ-ray. States populated

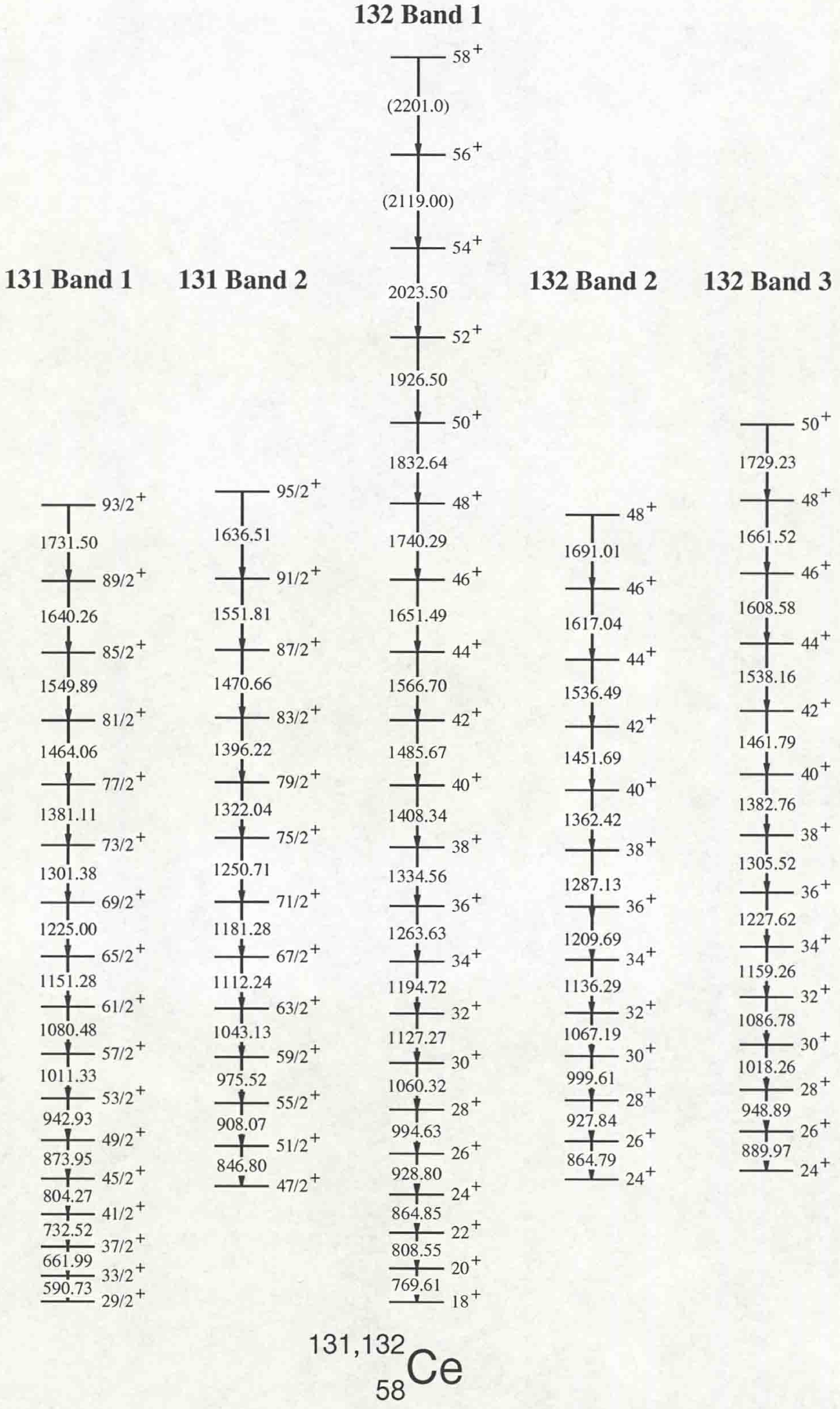

Figure 4.10: The decay schemes for the five superdeformed bands discussed in this work. The spin assignments are tentative, and are based on evidence of feeding to the normal-deformed states. The parities are based on deduced nuclear configurations.

by compound nucleus reactions, such as used in this work, have their spins orientated perpendicular to the beam axis. When the decay of these states results in the emission of a γ-ray, the probability of the angle at which the γ-ray is emitted, depends upon its multipolarity. Angular correlation measurements therefore involve the intensity measurement of a transition at two different angles, and the calculation of the ratio of these intensities. Due to the unique spatial emission probabilities of each multipole, quadrupoles and dipoles will each have distinct angular correlation ratios.

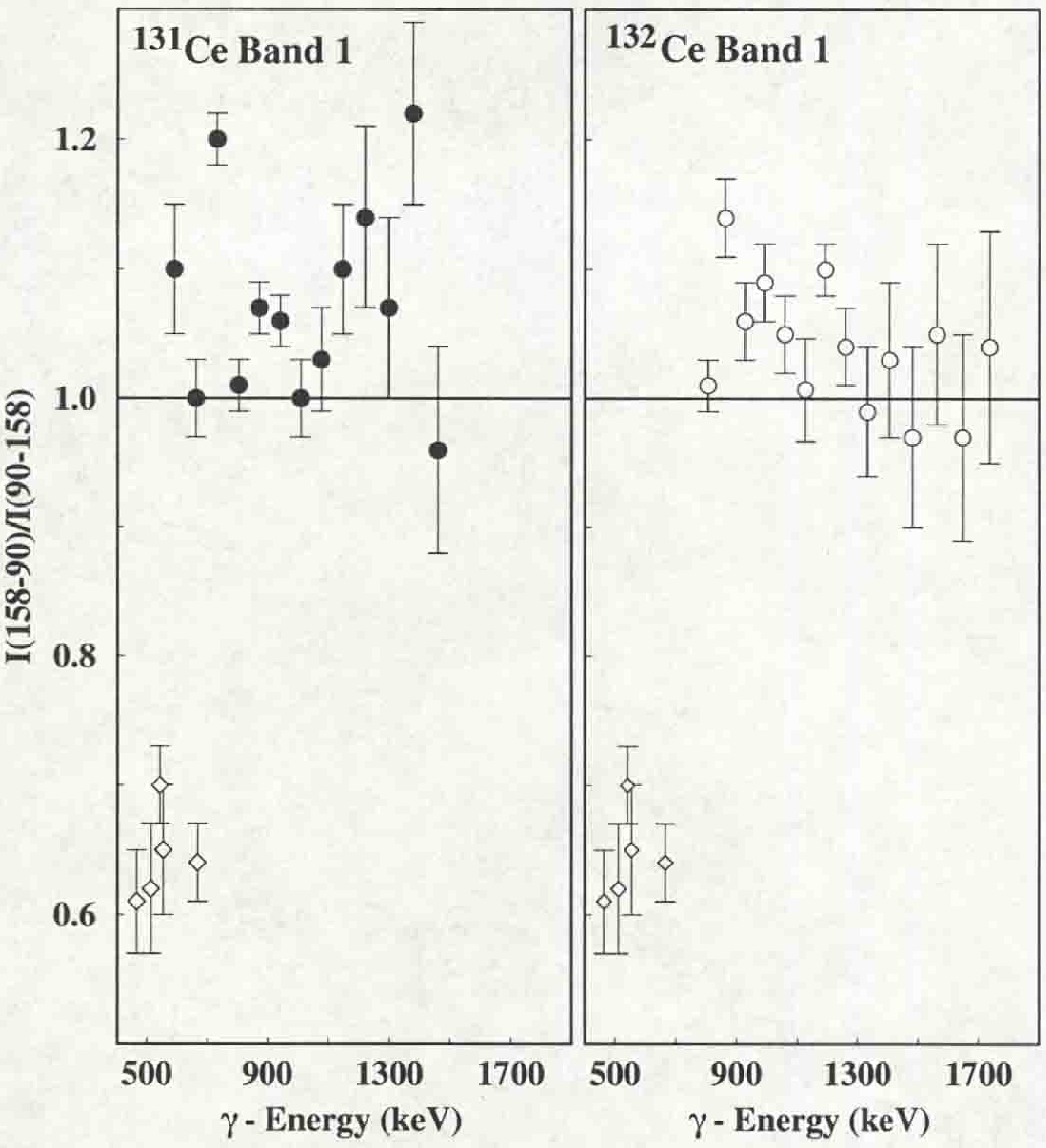

Figure 4.11: Angular correlation measurements for ^{131}Ce Band 1 and ^{132}Ce Band 1. The results are consistent with known stretched electric quadrupole transitions. Known dipole transitions (diamond) are included for comparison.

A γ-γ matrix was produced in a similar manner to that described in Sec. 3.13.1. The matrix corresponded to γ-γ coincidences between a detector at 158° and a detector at 90°. By gating on all uncontaminated transitions in the superdeformed band on the 90° axis of the matrix, the intensities of the transitions detected at 158° could be measured. Conversely, gating on the 158° axis enabled intensities to be measured on the 90° axis.

The angular correlation ratio R is defined as

$$R = \frac{I(158^\circ - 90^\circ)}{I(90^\circ - 158^\circ)} \tag{4.5}$$

where I(158°–90°) = Intensity of γ-ray at 158° when gating on 90° and I(90°–158°) = Intensity of γ-ray at 90° when gating on 158°.

In this work, known transitions have been calibrated such that $R \geq 1$ corresponds to quadrupole transitions, and $0.5 \leq R \leq 1$ corresponds to dipole transitions. Because of intensity considerations, these measurements are only feasible with ^{131}Ce Band 1 and ^{132}Ce Band 1. The results are shown in Fig. 4.11. It is clear that the γ-rays emitted in these superdeformed bands are consisitent with stretched quadrupole assignments.

4.10 The Dynamic Moment of Inertia

Angular momentum in rotating nuclei is generated either by collective rotation or by the alignment of single-particle angular momentum along the rotation axis. Because the moment of inertia for nuclei is related to the experimentally measured γ-ray energies, the competition between the two modes of angular momentum generation can be studied.

The dynamic moment of inertia $\Im^{(2)}$, was shown in Sec. 1.3.6 to be related purely to the spacing of consecutive transitions within the superdeformed bands. Also, because of its relationship to the second derivative of eqn. 1.21, it is extremely sensitive to changes in the structure of the nucleus, and this provides a powerful means of understanding nuclear phenomena. Fig. 4.12 shows the experimental $\Im^{(2)}$ moment of inertia as a function of rotational frequency for the superdeformed bands in ^{131,132}Ce. Due to the fact that the γ-ray transition energies are known to a high degree of accuracy (Sec. 4.7.1), the uncertainties in the $\Im^{(2)}$ values are unobservable on this scale.

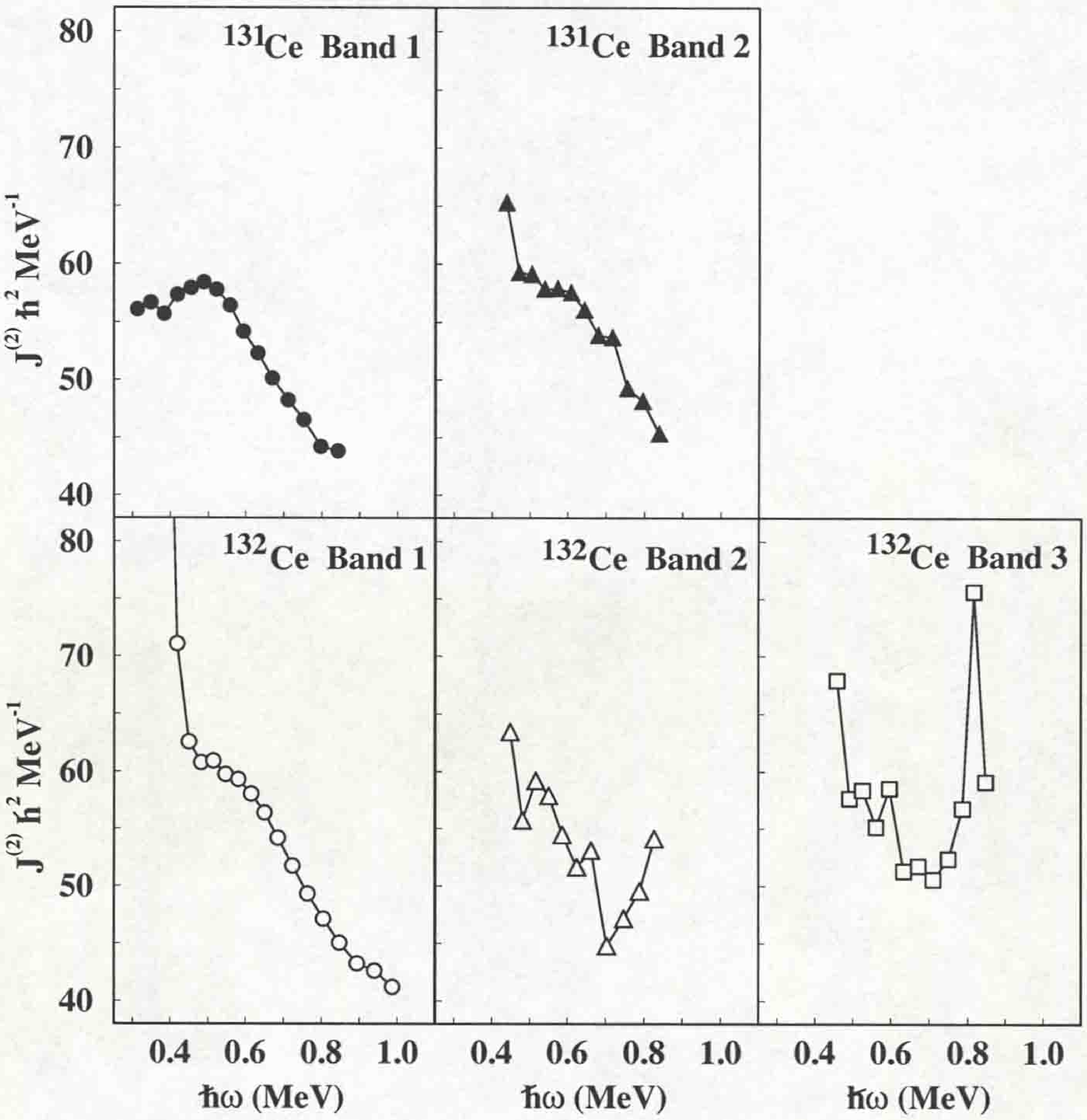

Figure 4.12: The dynamic moment of inertia ($\Im^{(2)}$) for the five superdeformed bands discussed in this work.

The details of the $\Im^{(2)}$ for each band will be discussed in the following chapter, but it is worthwhile pointing out the more prominent features at this stage.

1. ^{131}Ce Band 1 is the only band observed to depopulate at a rotational frequency of $\hbar\omega \approx 0.3$ MeV. The other bands show a distinct upbend at $\hbar\omega \approx 0.4$ MeV.

2. All the bands show a characteristic decrease in the $\Im^{(2)}$ as a function of rotational frequency.

3. ^{132}Ce Band 1 and ^{131}Ce Band 2 have slightly higher $\Im^{(2)}$'s than the other bands.

4. ^{132}Ce Band 2 and ^{132}Ce Band 3 show large increases in the $\Im^{(2)}$ at higher

rotational frequencies.

Such characteristics enable more precise deductions about nuclear structure to be made. However, it will be shown in chapter 5 that there are many problems and anomolies associated with these bands, and conclusive nuclear orbital configurations are difficult to assign.

4.11 Summary of Experimental Results

Table. 4.3 summarises the important experimental evidence obtained from the study of superdeformation in ^{131,132}Ce. This information will be used in the following chapter in an attempt to deduce the nuclear structure for these nuclei.

	^{131}Ce Band 1	^{131}Ce Band 2	^{132}Ce Band 1	^{132}Ce Band 2	^{132}Ce Band 3
Population Intensity (% of reaction channel)	5.0±0.2	1.1±0.3	5.0±0.2	1.0±0.3	0.9±0.3
Feeding Region, $\hbar\omega$ (MeV)	0.5-0.85	0.65-0.8	0.6-0.85	0.6-0.75	0.6-0.8
Depopulation Frequency, $\hbar\omega$ (MeV)	0.3	0.4	0.4	0.4	0.4
Estimated Spin at depopulation ($\hbar$)	16.5	24.5	22	26	24
Maximum observed Frequency, $\hbar\omega$ (MeV)	0.85	0.85	1.00	0.85	0.85
Mean $\Im^{(2)}$ at $\hbar\omega$=0.6 MeV	53	57	57	53	53
Frequency of major Band Crossings, $\hbar\omega$ (MeV)	0.5	0.4	0.4	0.4 0.7-0.9	0.4 0.7-0.9

Table 4.3: Summary of experimental results for the five superdeformed bands in ^{131}Ce and ^{132}Ce.

Chapter 5

Discussion

5.1 Introduction

The previous chapter detailed the experimental results that have been obtained from a single experiment in the study of superdeformation in ^{131}Ce and ^{132}Ce. In this chapter, an attempt will be made to assign a nuclear configuration to each band based upon predictions from the theoretical cranked shell model. However, it will soon become apparent that there are many anomolies in this mass region, and a complete understanding of these bands is difficult. It will also be shown that these bands have 'identical' relationships which represent the first observation of this phenomenon in the A$\approx$130 mass region. Finally, new fine structures in some of these bands will be discussed; structures which currently have no widely accepted theoretical explanation.

5.2 Theoretical Cranked Shell Model Calculations

Theoretical cranked shell model calculations have been performed for the superdeformed bands in ^{131}Ce and ^{132}Ce. These calculations enable possible configurations for the bands to be established. However, such theoretical calculations require the use of deformation parameters. In the case of ^{131}Ce Band 1 and ^{132}Ce Band 1 the quadrupole deformation parameter β_2, has been measured. This parameter has the greatest effect on the orbitals and is therefore the most crucial. The deformations for the excited bands in these nuclei, although not measured, are expected to be $\beta_2 \approx 0.4$, as these bands will be shown to have similar nucleon configurations to ^{132}Ce Band 1.

Two other parameters were required for these calculations; a second deformation parameter β_4, and the triaxiality parameter γ. β_4 was estimated from TRS calculations as discussed in Sec. 2.4.6, while γ was set to 0° to reflect prolate deformation.

For quasiparticle calculations, pairing interactions must be taken into account. In these calculations, the pairing strength is calculated at zero frequency and is modelled to decrease with increasing rotational frequency such that the pairing has fallen by 50% at $\hbar\omega \approx 0.7$ MeV (for details see [Wys88]).

5.3 Interpretation of the $\Im^{(2)}$ Dynamic Moment of Inertia

A direct comparison of theory with experimental data for any superdeformed band is difficult to make, since the absolute energy for such bands is not known (the transitions to the normal-deformed states have not been observed, Sec. 4.8). Also, the experimental spin assignments are tentative, and are probably only accurate to $\pm 2\hbar$ (Sec. 4.8). A detailed consideration of the dynamic moment of inertia $\Im^{(2)}$, is therefore very valuable, as it is dependent on neither of these unknown quantities.

TRS calculations performed by R.Wyss *et al* [Wys88] (of the type described in Sec. 2.4.6) show that the appearance of large deformations in ^{132}Ce is directly associated with the alignment of $i_{13/2}$ neutrons, which have a very strong polarizing effect on the nuclear core. At low rotational frequencies and 'normal' deformations ($\beta_2 \approx 0.2$) the $i_{13/2}$ levels lie high (in excitation energy) above the Fermi surface.

However, the energy of these levels decrease rapidly with increasing deformation (Sec. 2.3.2) and rotational frequency. The single-particle Routhian diagrams of Fig. 5.1 show that at $\beta_2 = 0.4$, which is a representative deformation for the superdeformed bands in these nuclei, $i_{13/2}$ single-particle levels are present in the immediate

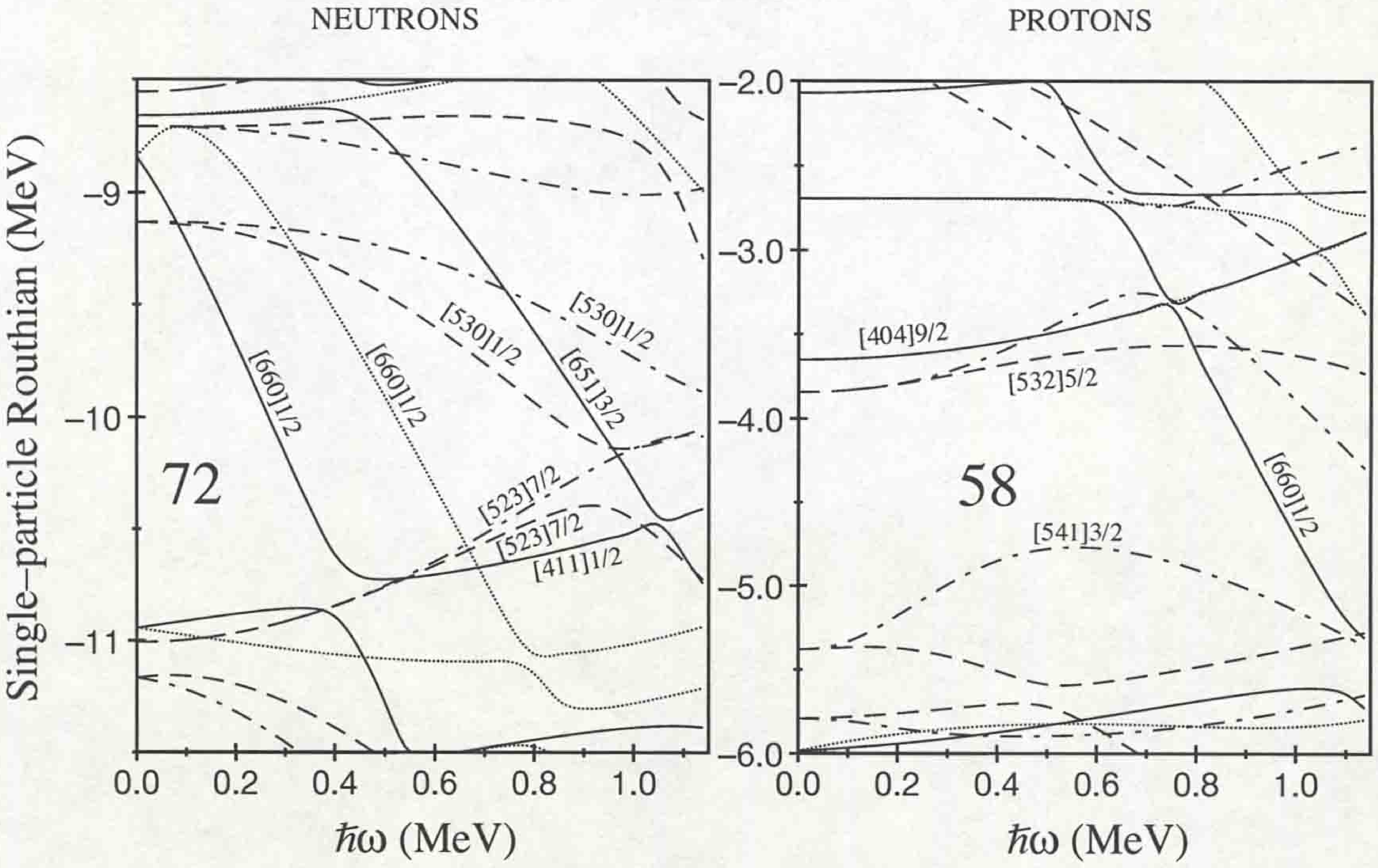

Figure 5.1: Single-particle calculations for $\beta_2 = 0.4$, β_4=0, γ=0°. The N=6 $i_{13/2}$ intruder orbitals ([660]$1/2^+$) are close to the Fermi surface at this deformation. Each orbital is referred to by its parity and signature (π, α) : Solid lines = (+,+1/2), dotted lines = (+,–1/2), dot–dash lines = (–,+1/2), dashed lines = (–,–1/2).

vicinity of the Fermi surface even at low frequencies for N>72.

However, for the superdeformed shape to be stable, the shell structure for both protons and neutrons at large deformation must be energetically favourable compared with the one at normal deformation. The proton single-particle level diagram (Fig. 5.1) shows that from this point of view, proton number Z=58 is particularly favourable. On the other hand, the shell structure at Z=58, N=72 is still not strong enough alone to keep the deformed nucleus stable. It is the interplay between the polarizing force of the $i_{13/2}$ intruder orbital and the shell structure that makes ^{132}Ce Band 1 yrast at medium spin.

The quasiparticle calculations for neutrons (Fig. 5.2) indicate an $i_{13/2}$ neutron alignment occurs at $\hbar\omega \approx 0.4$ MeV. However, similar calculations for protons (Fig. 5.3) indicate an alignment of $h_{11/2}$ protons at a similar frequency ($\hbar\omega \approx 0.4$ MeV). Further

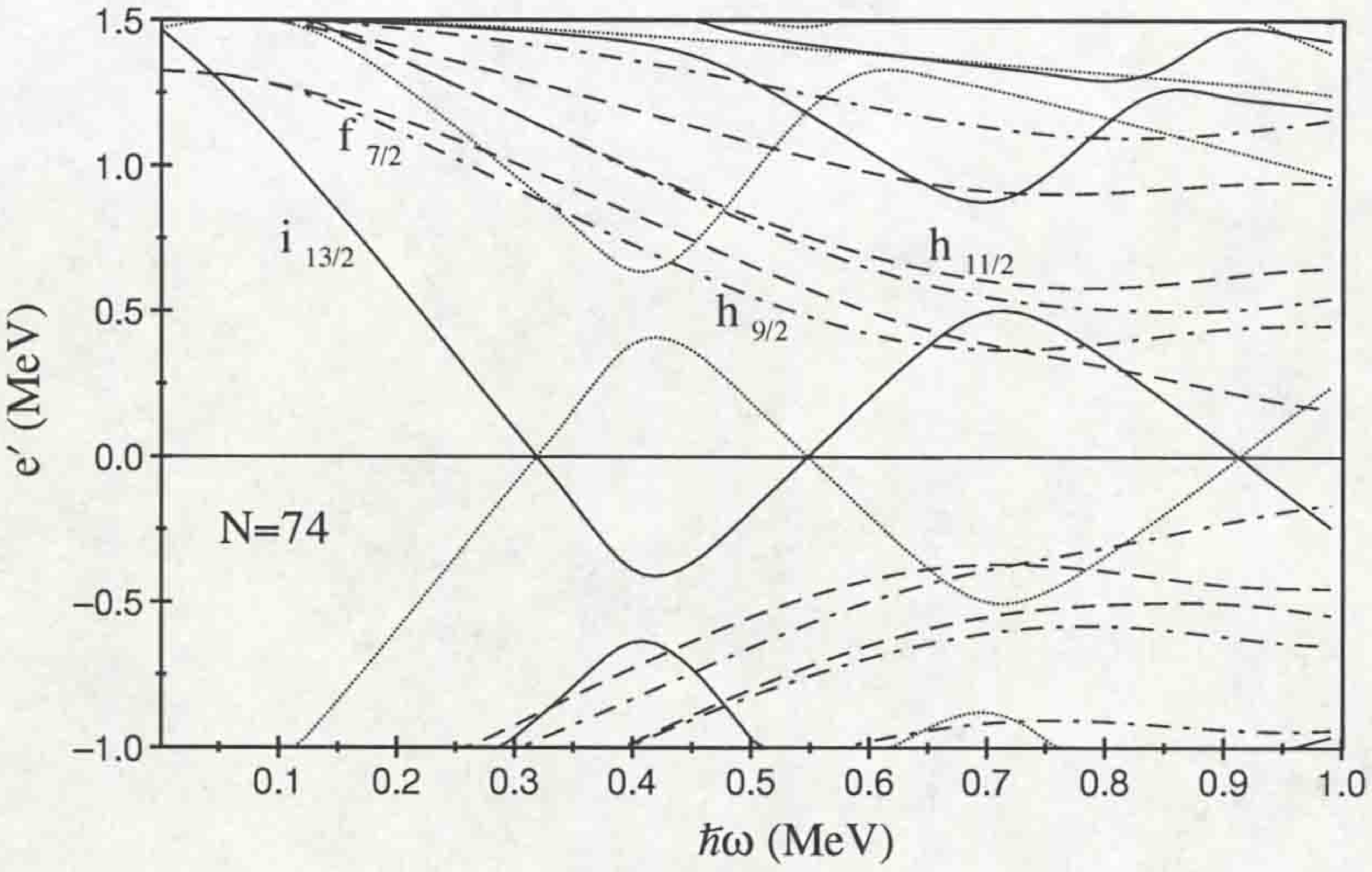

Figure 5.2: Quasineutron calculations for β_2 = 0.4, β_4=0, γ=0°. The orbital labelled $f_{7/2}$ at low frequency becomes highly mixed with an $h_{9/2}$ orbital at higher frequencies, and therefore changes its character. Alignments of $i_{13/2}$ neutron occur at $\hbar\omega\approx$ 0.4 MeV, while more gradual alignments of $h_{9/2}$ and $h_{11/2}$ neutrons occur at $\hbar\omega\approx$ 0.4-1.0 MeV. Each orbital is referred to by its parity and signature (π, α) : Solid lines = (+,+1/2), dotted lines = (+,–1/2), dot–dash lines = (–,+1/2), dashed lines = (–,–1/2).

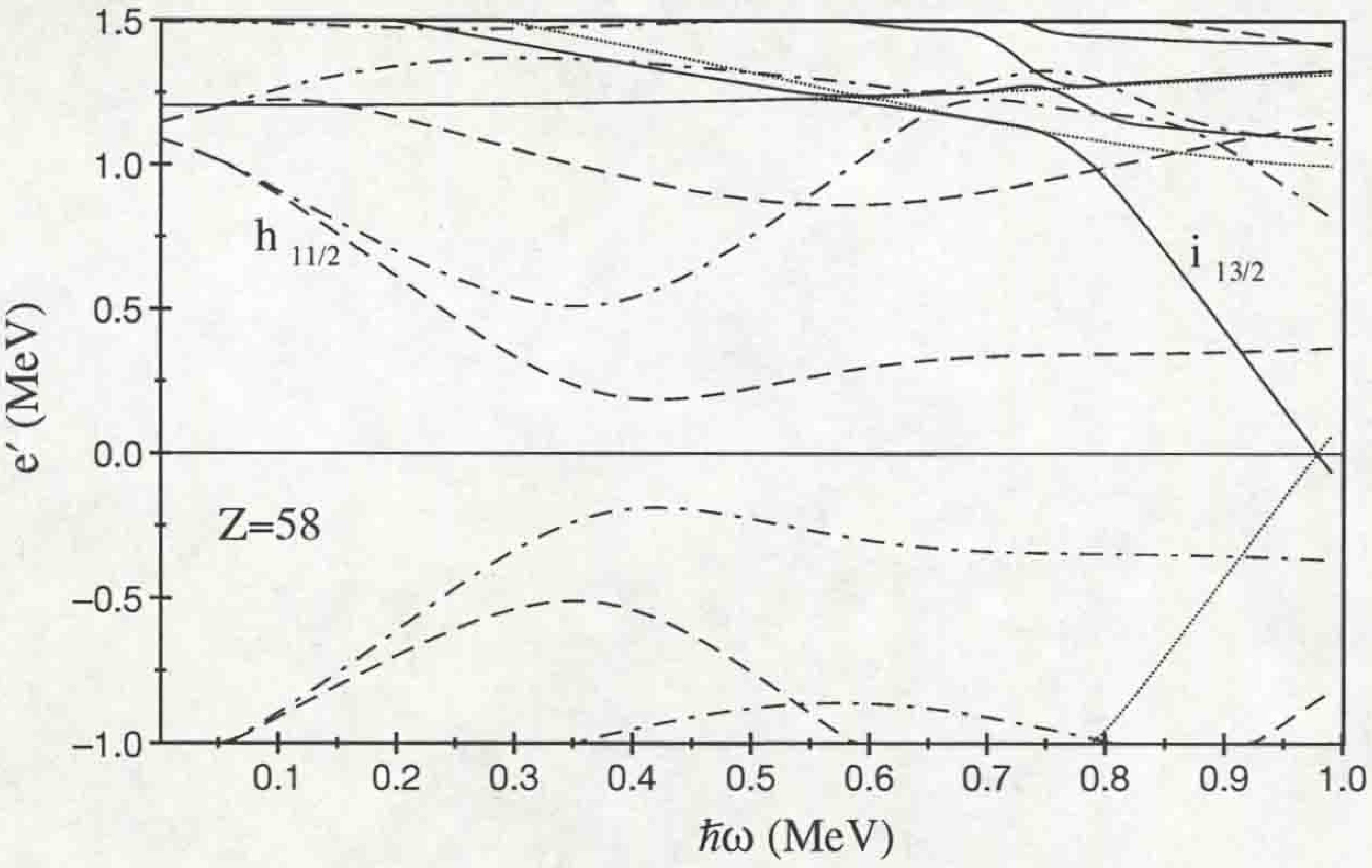

Figure 5.3: Quasiproton calculations for β_2 = 0.4, β_4=0, γ=0°. Alignment of $h_{11/2}$ protons occur at $\hbar\omega\approx$ 0.4 MeV. This alignment is more gradual than the $i_{13/2}$ neutron alignment at the same frequency. Each orbital is referred to by its parity and signature (π, α) : Solid lines = (+,+1/2), dotted lines = (+,–1/2), dot–dash lines = (–,+1/2), dashed lines = (–,–1/2).

gradual alignments of $h_{9/2}$ and $h_{11/2}$ neutrons are also indicated to occur in the region $\hbar\omega$=0.4-1.0 MeV (Fig. 5.2).

R.Wyss *et al.* [Wys88] were also able to calculate a theoretical $\Im^{(2)}$ moment of inertia for ^{132}Ce Band 1 by considering neutron and proton alignment contributions separately. Fig. 5.4 illustrates that the major features of the frequency dependence of the $\Im^{(2)}$, is a combined effect of gradual proton ($h_{11/2}$) and neutron ($i_{13/2}$, $h_{9/2}$+$h_{11/2}$) alignment processes. These alignments may be clearly seen in Fig. 5.2 and Fig. 5.3.

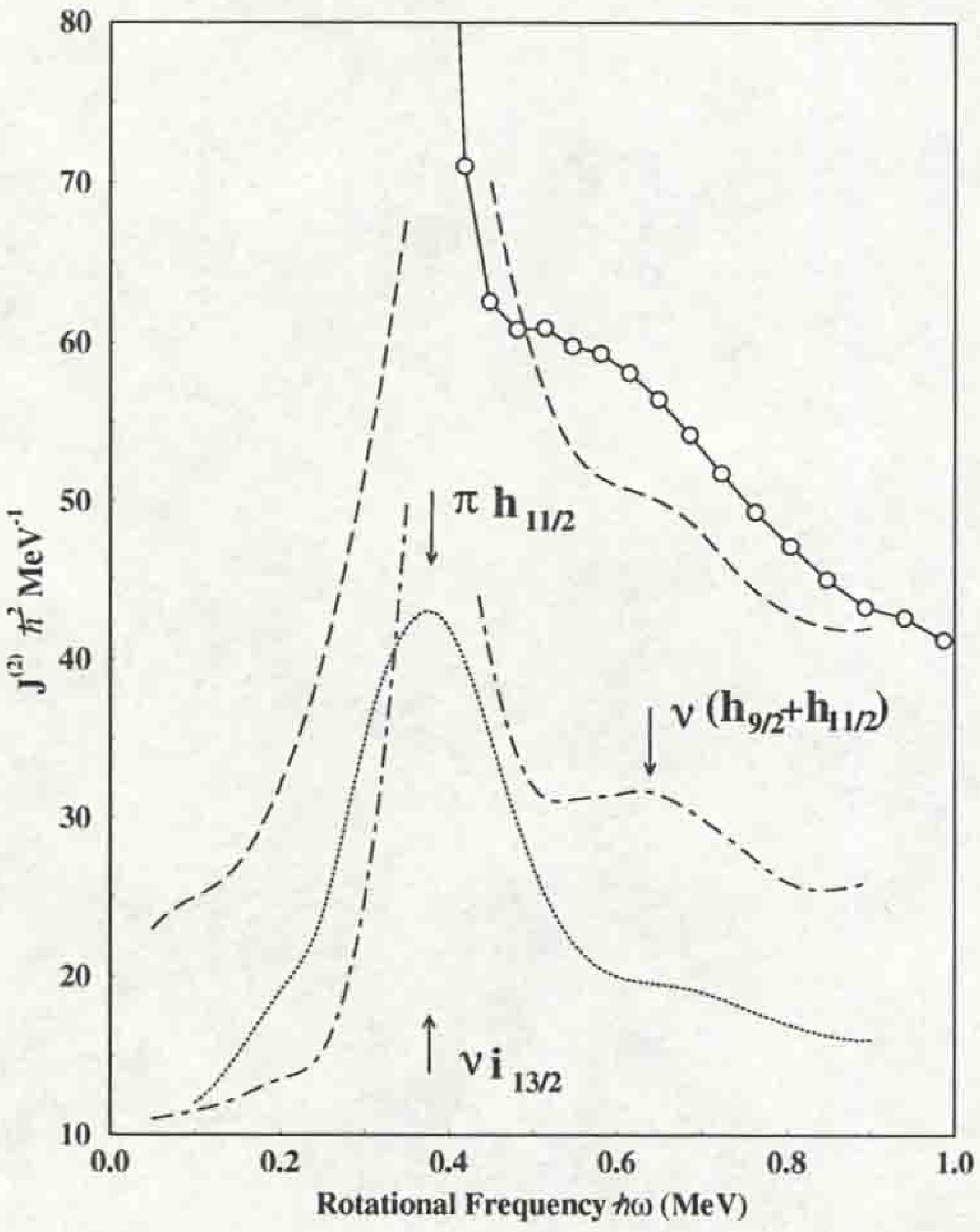

Figure 5.4: Experimental (circles) and calculated (dashed lines) $\Im^{(2)}$ moment of inertia as a function of rotational frequency for ^{132}Ce Band 1. Partial contribution to $\Im^{(2)}$ from protons (dotted lines) and neutrons (dot-dashed lines) are also shown. The peaks in the $\Im^{(2)}$ are caused by the alignment of particular quasiparticles as indicated. Calculations from [Wys88].

A consideration of the other bands, and the remaining features of the $\Im^{(2)}$, may now be built upon these principles. The experimental $\Im^{(2)}$ moment of inertia as a function of rotational frequency for the superdeformed bands in ^{131,132}Ce was shown in Fig. 4.12. It is reproduced in Fig. 5.5 for convenience.

The experimental $\Im^{(2)}$ values for the odd-N ^{131}Ce Band 1 has a well defined max-

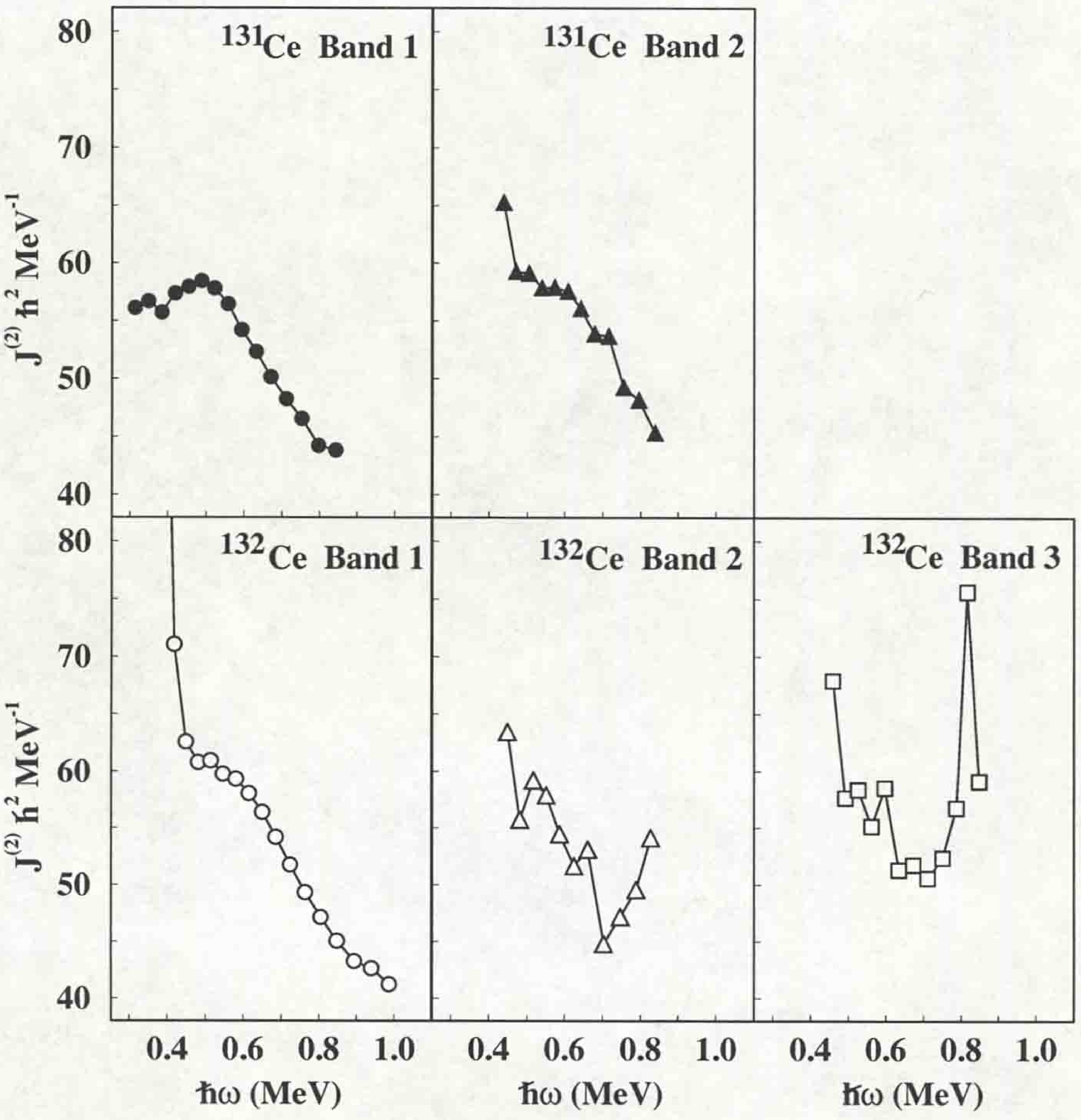

Figure 5.5: The experimental dynamic moment of inertia ($\Im^{(2)}$) for the five superdeformed bands discussed in this work.

imum at $\hbar\omega\approx$0.4 MeV. ^{131}Ce Band 1 and ^{132}Ce Band 1 are expected to have the same proton configurations, so that the $h_{11/2}$ proton alignment will occur in both bands. The $\Im^{(2)}$ for ^{131}Ce Band 1 therefore confirms the expected $\Im^{(2)}$ contribution from the protons shown in Fig. 5.4 and reproduces the $h_{11/2}$ proton alignment convincingly. However, the sharp upbend in the $\Im^{(2)}$ for ^{132}Ce Band 1 is clearly lacking for ^{131}Ce Band 1, suggesting that the $i_{13/2}$ neutron alignment is absent in this band. It is therefore concluded that in the frequency region where ^{131}Ce Band 1 is observed, only 1 $i_{13/2}$ neutron orbital is occupied ('blocking' the $i_{13/2}$ neutron alignment), and that the 74th neutron in ^{132}Ce Band 1 occupies the second $i_{13/2}$ neutron orbital above $\hbar\omega\approx$0.4 MeV.

The differences between the experimental $\Im^{(2)}$ moments of inertia for ^{131}Ce Band 1 and ^{132}Ce Band 1, and their deduced high-N intruder orbital occupation, enables a crucial step to be made in deducing a nuclear structure for the excited bands. Any band exhibiting the sharp upbend in the $\Im^{(2)}$ at $\hbar\omega \approx 0.4$ MeV probably has both $i_{13/2}$ neutron orbitals occupied in the observed frequency region of the band. Since all excited bands show the effect, this is expected to be the case for ^{131}Ce Band 2, ^{132}Ce Band 2 and ^{132}Ce Band 3.

The single-particle routhians for protons (Fig. 5.1) indicate the large shell gap at Z=58, as mentioned earlier. This shell gap exists for the entire frequency range of the excited bands, and makes neutron excitations more likely than proton excitations. It is therefore expected that all the bands have the same proton configurations. The last two protons in all the nuclei discussed in this work occupy a pair of $h_{11/2}$ proton orbitals. The basis of the following discussion will therefore centre on possible neutron configurations for the bands.

5.4 The Yrast Superdeformed Band Neutron Configurations

5.4.1 ^{131}Ce Band 1

Single-particle routhians for ^{131}Ce Band 1 are shown in Fig. 5.6. The quadrupole deformation parameter was set to β_2=0.35 in accordance with its measured value [He90]. The relative intensity distribution for this band (Fig. 4.8 and Table. 4.3) indicates that the feeding occurs in the frequency region $\hbar\omega \approx 0.5$–0.85 MeV. Filling the neutron orbitals up in this frequency range means that the last neutron (N=73) occupies the [523]7/2$^-$ (α=+1/2) orbital, leaving the [660]1/2$^+$ (α=–1/2) neutron orbital empty. This confirms the deduced $i_{13/2}$ neutron orbital occupation discussed in the preceding section. In the high–N notation [Ben88] this configuration is labelled as $\pi 5^4 \nu 6^1$ ($\pi N^n \nu N^m$: n and m specify the n'th and m'th lowest occupied N states of the intruder subshell for protons and neutrons respectively).

5.4.2 ^{132}Ce Band 1

The corresponding theoretical cranked shell predictions for ^{132}Ce Band 1 are shown in Fig. 5.7. The quadrupole deformation parameter was set at β_2=0.43 in accordance with its measured value [Kir87]. Filling up neutron orbitals in the feeding region for this band ($\hbar\omega\approx$ 0.6–0.85, Table. 4.3) results in the last (N=74) neutron occupying the second $i_{13/2}$ neutron orbital; [660]1/2$^+$ (α=–1/2). This configuration is labelled as $\pi 5^4 \nu 6^2$ in the high–N notation. The structures proposed here for ^{131}Ce Band 1 and ^{132}Ce Band 1 are consistent with experimental evidence :

1. The quadrupole deformation of ^{132}Ce Band 1 is larger than that of ^{131}Ce Band 1. This is due to the prolate driving effects of the second highly sloping $i_{13/2}$ neutron orbital occupied in ^{132}Ce Band 1.
2. An upbend in the $\Im^{(2)}$ is observed in ^{132}Ce Band 1 (Fig. 5.5) at the predicted frequency of the $i_{13/2}$ neutron alignment (Fig. 5.2). This is due to the occupation of both $i_{13/2}$ neutron orbitals in ^{132}Ce Band 1. This alignment is blocked for ^{131}Ce Band 1 as it contains a single $i_{13/2}$ neutron.

These structures also agree with those originally proposed in [Luo87] and [Kir87].

5.5 The Excited Superdeformed Band Neutron Configurations

Excited superdeformed bands are produced by the excitation of one or more nucleons into higher energy orbitals (Sec. 2.6.1). However, the single-particle routhians calculated for ^{131}Ce Band 1 (Fig. 5.6) and ^{132}Ce Band 1 (Fig. 5.7) indicate that there are many orbitals just below and above the Fermi Surface for each nucleus. This makes the number of possible excitations very large. In fact, if only the most likely excitations are considered (where the energy difference between the orbitals are relatively

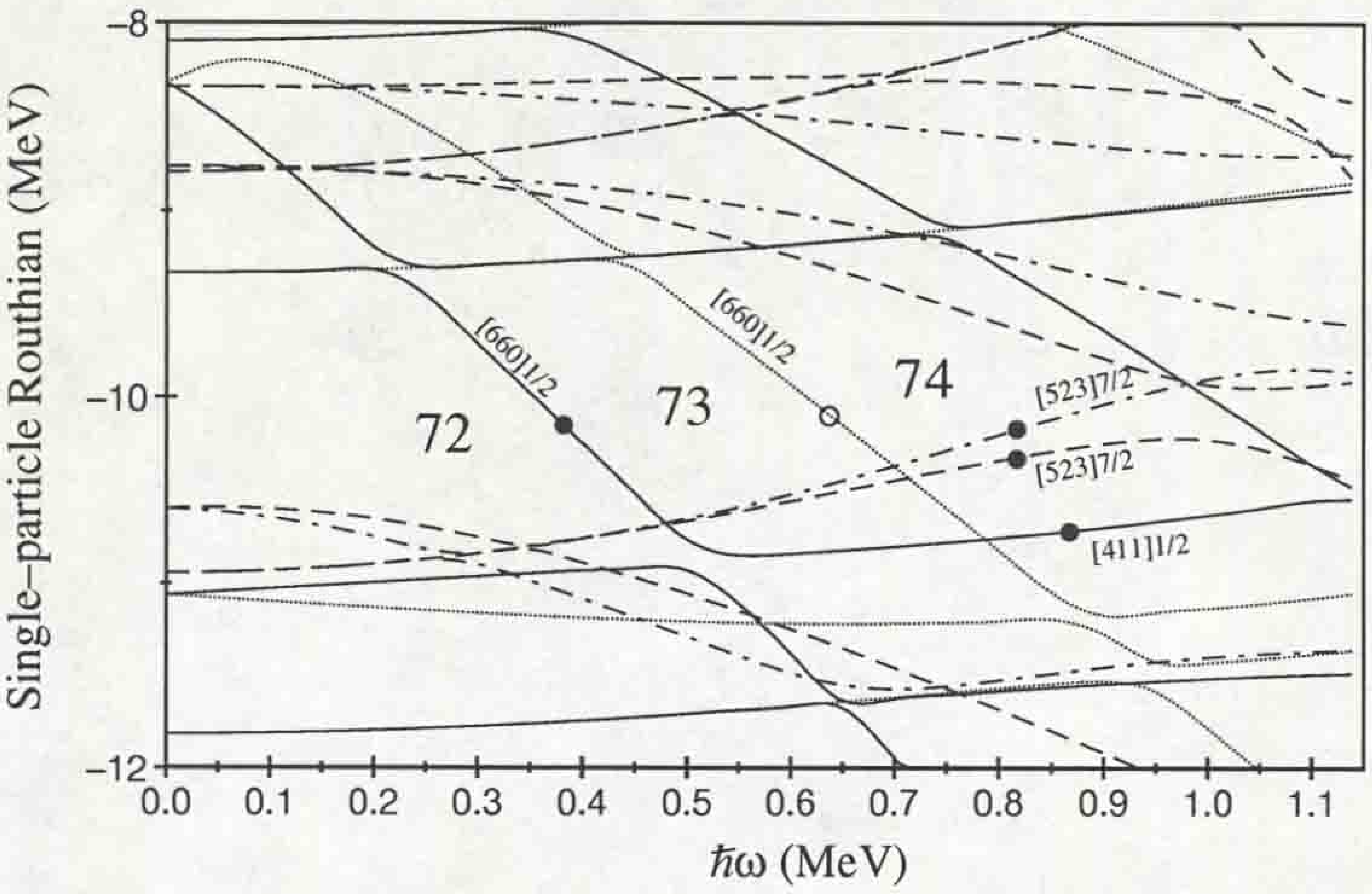

Figure 5.6: ^{131}Ce Band 1. Single-particle neutron calculations for β_2 = 0.35, β_4 = 0.014, γ=0° showing the suggested neutron configuration for ^{131}Ce Band 1 (73 neutrons). Filled circles indicate neutron occupation of outer orbitals, while open circles indicates a hole. Each orbital is referred to by its parity and signature (π, α) : Solid lines = (+,+1/2), dotted lines = (+,–1/2), dot–dash lines = (–,+1/2), dashed lines = (–,–1/2).

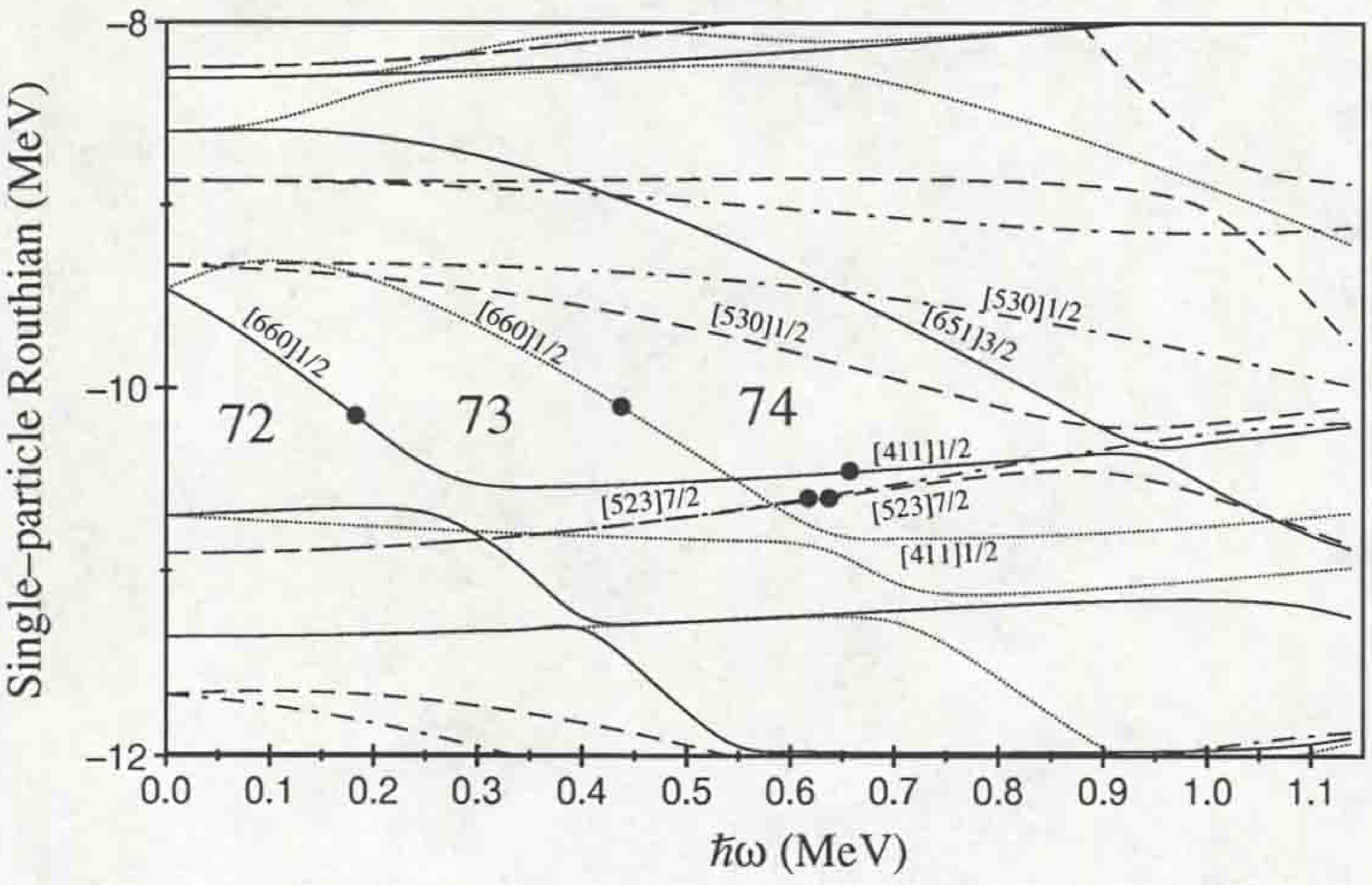

Figure 5.7: ^{132}Ce Band 1. Single-particle neutron calculations for β_2 = 0.43, β_4 = 0.014, γ=0° showing the suggested neutron configuration for ^{132}Ce Band 1 (74 neutrons). Filled circles indicate neutron occupation of outer orbitals. Each orbital is referred to by its parity and signature (π, α) : Solid lines = (+,+1/2), dotted lines = (+,–1/2), dot–dash lines = (–,+1/2), dashed lines = (–,–1/2).

small) and the consideration is limited to single neutron excitations, there are three possible excited bands in ^{131}Ce and twelve possible excited bands in ^{132}Ce.

When it is taken into account that there has only been one excited band observed in ^{131}Ce and two excited bands observed in ^{132}Ce, one can appreciate the difficult task that lies ahead in assigning a configuration to each band.

The approach employed in this discussion uses the large changes in the $\Im^{(2)}$ moment of inertia as an indication of band crossings.

5.5.1 ^{131}Ce Band 2

The single-particle routhians shown in Fig. 5.6 for ^{131}Ce Band 1 indicate that the lowest three neutron excitations are expected to have relatively similar probabilities. These correspond to excitations from one of the following orbitals:

1. [523]7/2$^-$ (α=+1/2)

2. [523]7/2$^-$ (α=–1/2)

3. [411]1/2$^+$ (α=+1/2)

and into the unoccupied [660]1/2$^+$ (α=–1/2) neutron orbital. The occupation of this orbital would agree with the experimentally deduced $\Im^{(2)}$ moment of inertia (Fig. 5.5), which indicated a sharp upbend at $\hbar\omega\approx$0.4 MeV. This feature is in common with ^{132}Ce Band 1, where the upbend in the $\Im^{(2)}$ was attributed to the alignment of $i_{13/2}$ neutrons. Therefore, for ^{131}Ce Band 1, it is assumed that both signatures of the [660]1/2$^+$ orbital must be occupied above $\hbar\omega\approx$0.4 MeV.

The problem remains however, in determining out of which of the three orbitals suggested above, the excitation would occur. The single-particle routhians for ^{131}Ce Band 1 would indicate that one of the [523]7/2$^-$ orbitals would be a likely choice. However, the occupation of the second [660]1/2$^+$ orbital would be expected to have a prolate-driving effect on the nucleus, and as a consequence the single-particle routhians shown in Fig. 5.6 may not be appropriate. Fig. 5.8 shows single-particle routhians

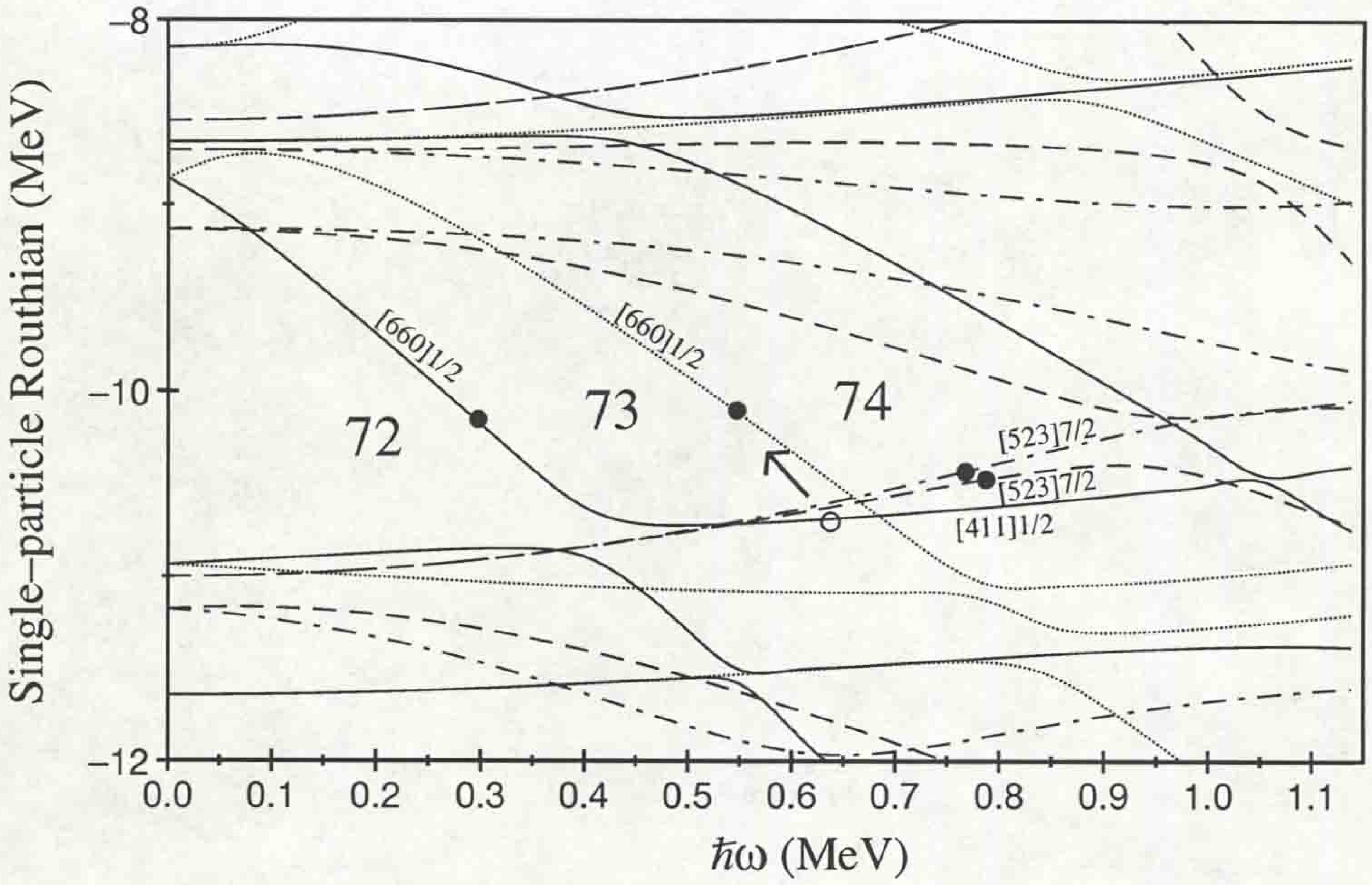

Figure 5.8: ^{131}Ce Band 2. Single-particle neutron calculations for $\beta_2 = 0.40$, $\beta_4 = 0.014$, γ=0° showing the suggested neutron configuration for ^{131}Ce Band 2 (73 neutrons). Black circles indicate neutron occupation of outer orbitals, while clear circles indicates a hole. Each orbital is referred to by its parity and signature (π, α) : Solid lines = (+,+1/2), dotted lines = (+,–1/2), dot–dash lines = (–,+1/2), dashed lines = (–,–1/2).

calculated for a larger deformation parameter of β_2=0.40 (as opposed to β_2=0.35 for ^{131}Ce Band 1).

The calculations show that although each of the three cases mentioned above have similar excitation energies, excitations from the [523]7/2$^-$ orbitals are slightly more favourable than for an excitation from the [411]1/2$^+$ (α=+1/2) neutron orbital. However, it would be expected that any excitation involving one of the [523]7/2$^-$ orbitals would be accompanied by a signature-partner band (the signature-splitting is small at low frequencies). Since only one excited band is observed in this nucleus, then the most likely excitation is considered to be from the [411]1/2$^+$ (α=+1/2) orbital into the [660]1/2$^+$ (α=–1/2) neutron orbital.

Although this argument favours the [411]1/2$^+$ (α=+1/2) orbital, it still does not exclude the [523]7/2$^-$ (α=±1/2) orbitals, and it is difficult to resolve the fact there are two missing excited bands. This is especially surprising in view of the close proximity of these orbitals to each other as indicated on Fig. 5.8.

5.5.2 ^{132}Ce Band 2

The single-particle routhians calculated for ^{132}Ce Band 1 (Fig. 5.7) indicate that many excitations are possible in order to produce an excited band. The most likely of these are:

1. [523]7/2$^-$ (α=+1/2)
2. [523]7/2$^-$ (α=–1/2)
3. [411]1/2$^+$ (α=+1/2)
4. [660]1/2$^+$ (α=–1/2)

and to the orbitals :

1. [530]1/2$^-$ (α=–1/2)
2. [530]1/2$^-$ (α=+1/2)
3. [651]3/2$^+$ (α=+1/2)

However, the $\Im^{(2)}$ moment of inertia for this band (Fig. 5.5) shows the sharp upbend at $\hbar\omega\approx0.4$ MeV which is characteristic of the $i_{13/2}$ neutron alignment. This suggests that the excitation producing this band must leave both [660]1/2$^+$ orbitals occupied, and this eliminates the [660]1/2$^+$ (α=–1/2) from the candidate orbitals suggested above.

The $\Im^{(2)}$ moment of inertia for ^{132}Ce Band 2 (Fig. 5.5) displays a second distinguishing feature. The $\Im^{(2)}$ is observed to rise gently for frequencies greater than $\hbar\omega\approx0.7$ MeV. This rise is indicative of a band crossing taking place over a wide frequency range, in contrast to the $i_{13/2}$ neutron alignment which occurs at $\hbar\omega\approx0.4$ MeV, which has a very sharp nature.

The single-particle routhians shown in Fig. 5.7 indicate that such a band crossing is predicted to occur in the frequency range $\hbar\omega\approx0.7$-1.1 MeV. This crossing is between the [530]1/2$^-$ (α=–1/2) and the [523]7/2$^-$ (α=–1/2) neutron orbitals. In order for the crossing to have an effect on the $\Im^{(2)}$ moment of inertia, the [530]1/2$^-$ (α=–1/2) orbital must remain unoccupied in the excitation producing the band, while the [523]7/2$^-$ (α=–1/2) orbital remains occupied. This enables the neutron occupying the [523]7/2$^-$ (α=–1/2) orbital to move into the unoccupied [530]1/2$^-$ (α=–1/2) orbital at the crossing frequency. This constitutes a change in structure of the nucleus, and therefore has a marked effect on the $\Im^{(2)}$.

These deductions have narrowed down the possible excitations for the band. The remaining candidates are from the orbitals :

1. [523]7/2$^-$ (α=+1/2)
2. [411]1/2$^+$ (α=+1/2)

and into the orbitals :

1. [530]1/2$^-$ (α=+1/2)
2. [651]3/2$^+$ (α=+1/2)

Fig. 5.7 indicates that the [411]1/2$^+$ (α=+1/2) neutron orbital is slightly more favourable for the excitation than the [523]7/2$^-$ (α=+1/2) orbital. This eliminates the requirement to observe a signature-partner band if the neutron occupying the [523]7/2$^-$ (α=+1/2) orbital had been excited. The figure also indicates that the [651]3/2$^+$ (α=+1/2) excitation is more favourable (lower in energy) than the [530]1/2$^-$ (α=+1/2) excitation.

It is therefore concluded that the most probable excitation producing ^{132}Ce Band 2 is from the [411]1/2$^+$ (α=+1/2) neutron orbital to the [651]3/2$^+$ (α=+1/2). The occupation of the [651]3/2$^+$ orbital would have a similar prolate-driving effect on the nucleus as the [660]1/2$^+$ orbitals. It is therefore expected, that the deformation of ^{132}Ce Band 2 should be slightly higher than that of ^{132}Ce Band 1.

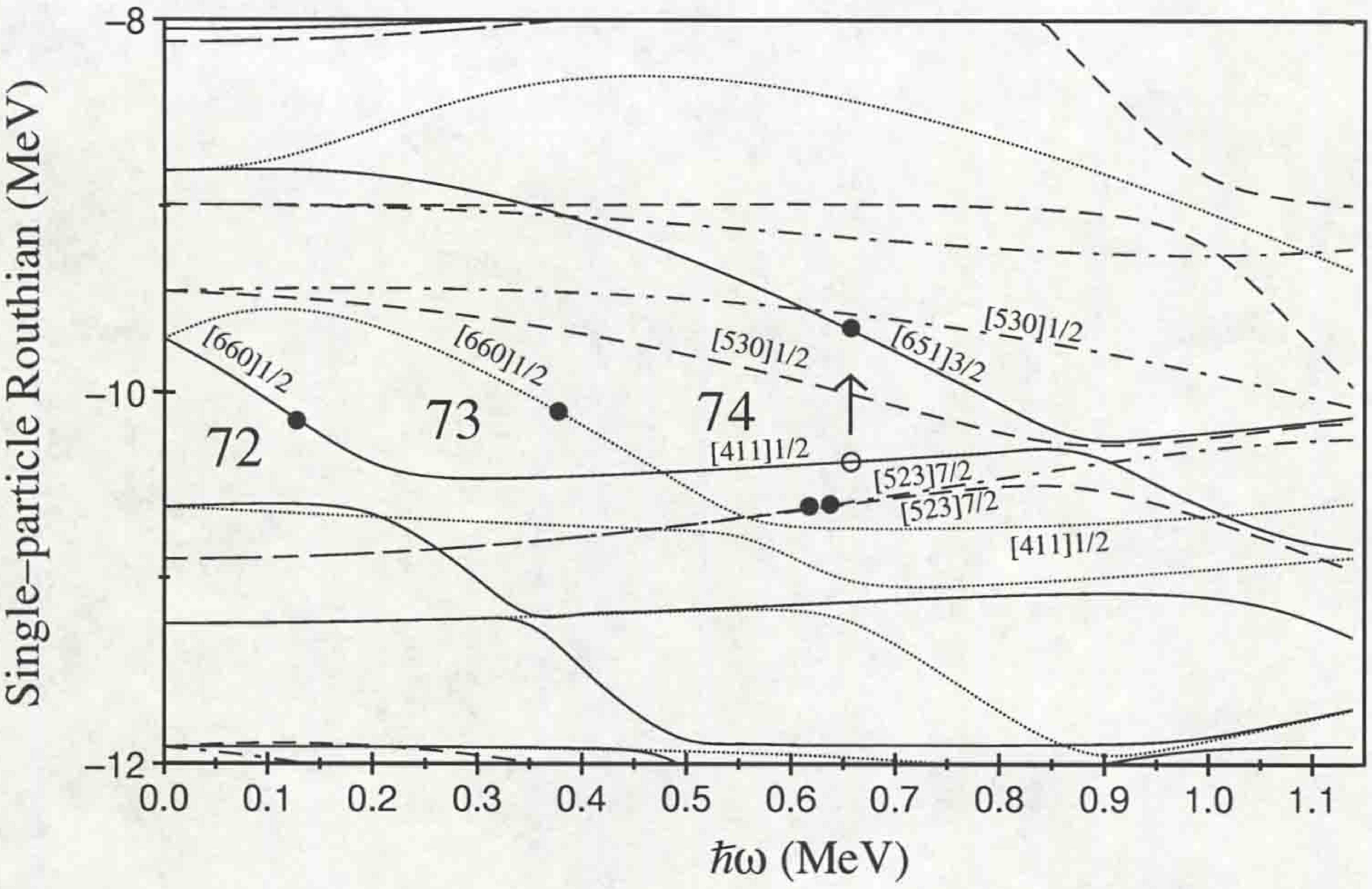

Figure 5.9: ^{132}Ce Band 2. Single-particle neutron calculations for $\beta_2 = 0.45$, $\beta_4 = 0.014$, γ=0° showing the suggested neutron configuration for ^{132}Ce Band 2 (74 neutrons). Filled circles indicate neutron occupation of outer orbitals, while open circles indicates a hole. Each orbital is referred to by its parity and signature (π, α) : Solid lines = (+,+1/2), dotted lines = (+,–1/2), dot–dash lines = (–,+1/2), dashed lines = (–,–1/2).

Single-particle routhians calculated with a deformation parameter of β_2=0.45 are shown in Fig. 5.9. Also indicated on the diagram is the structure of ^{132}Ce Band 2.

Although this configuration seems consistent with the measured $\Im^{(2)}$, there are clearly a number of bands missing that should have similar excitation energies. An excitation from the [411]$1/2^+$ (α=+1/2) to the [530]$1/2^-$ (α=–1/2) neutron orbital appears particularly favourable.

5.5.3 ^{132}Ce Band 3

The likely orbital candidates for ^{132}Ce Band 3 are the same as those for ^{132}Ce Band 2 (Sec. 5.5.2). The $\Im^{(2)}$ for ^{132}Ce Band 3 (Fig. 5.5) also shows the sharp upbend at $\hbar\omega\approx$0.4 MeV which is characteristic of the $i_{13/2}$ neutron crossing. The structure of this band is therefore assumed to have both [660]$1/2^+$ (α=$\pm$1/2) orbitals occupied above $\hbar\omega \approx 0.4$ MeV.

The $\Im^{(2)}$ moment of inertia (Fig. 5.5) for this band also shows a sharp increase at $\hbar\omega \approx 0.8$–0.9 MeV. This increase in $\Im^{(2)}$ is in contrast with the gradual change observed for ^{132}Ce Band 2 at a similar frequency, and implies that different orbitals must be responsible.

The routhians shown for ^{132}Ce Band 1 (Fig. 5.7) indicate that a sharp band crossing between the $[651]3/2^{+}$ (α=+1/2) and $[411]1/2^{+}$ (α=+1/2) orbitals takes place in the frequency range $\hbar\omega \approx 0.9$-1.0 MeV. The interaction between these two orbitals is a good candidate for the observed effect in the $\Im^{(2)}$ moment of inertia at high frequencies. In a similar manner for ^{132}Ce Band 2, for this crossing to have an effect on the $\Im^{(2)}$, the $[411]1/2^{+}$ (α=+1/2) must remain occupied in the excitation producing the band, while the $[651]3/2^{+}$ (α=+1/2) must remain unoccupied.

The most favourable orbital for the excited neutron to enter, is therefore the $[530]1/2^{-}$ (α=–1/2) (Fig. 5.7). The positive signature of the $[523]7/2^{-}$ orbital is considered more favourable for the excited neutron from the energy point of view.

It is therefore proposed, that the most probable excitation producing ^{132}Ce Band 3 is from the $[523]7/2^{-}$ (α=+1/2) to the $[530]1/2^{-}$ (α=–1/2) neutron orbital. This structure is shown on the single-particle routhians of Fig. 5.10. A deformation parameter of β_2=0.43 has been chosen based on the $i_{13/2}$ neutron configuration for this band (i.e the same as ^{132}Ce Band 1).

However, the problem remains of the unobserved bands corresponding to excitations from and to the orbitals detailed in Sec. 5.5.2, and in particular the signature-partner band corresponding to the $[523]7/2^{-}$ (α=–1/2) excitation.

5.6 Summary of Configurations

The most likely configurations for the superdeformed bands in ^{131}Ce and ^{132}Ce have been deduced in the preceding sections. The approach was to compare experimentally observed $\Im^{(2)}$ moment of inertia with theoretical cranked shell model predictions. In

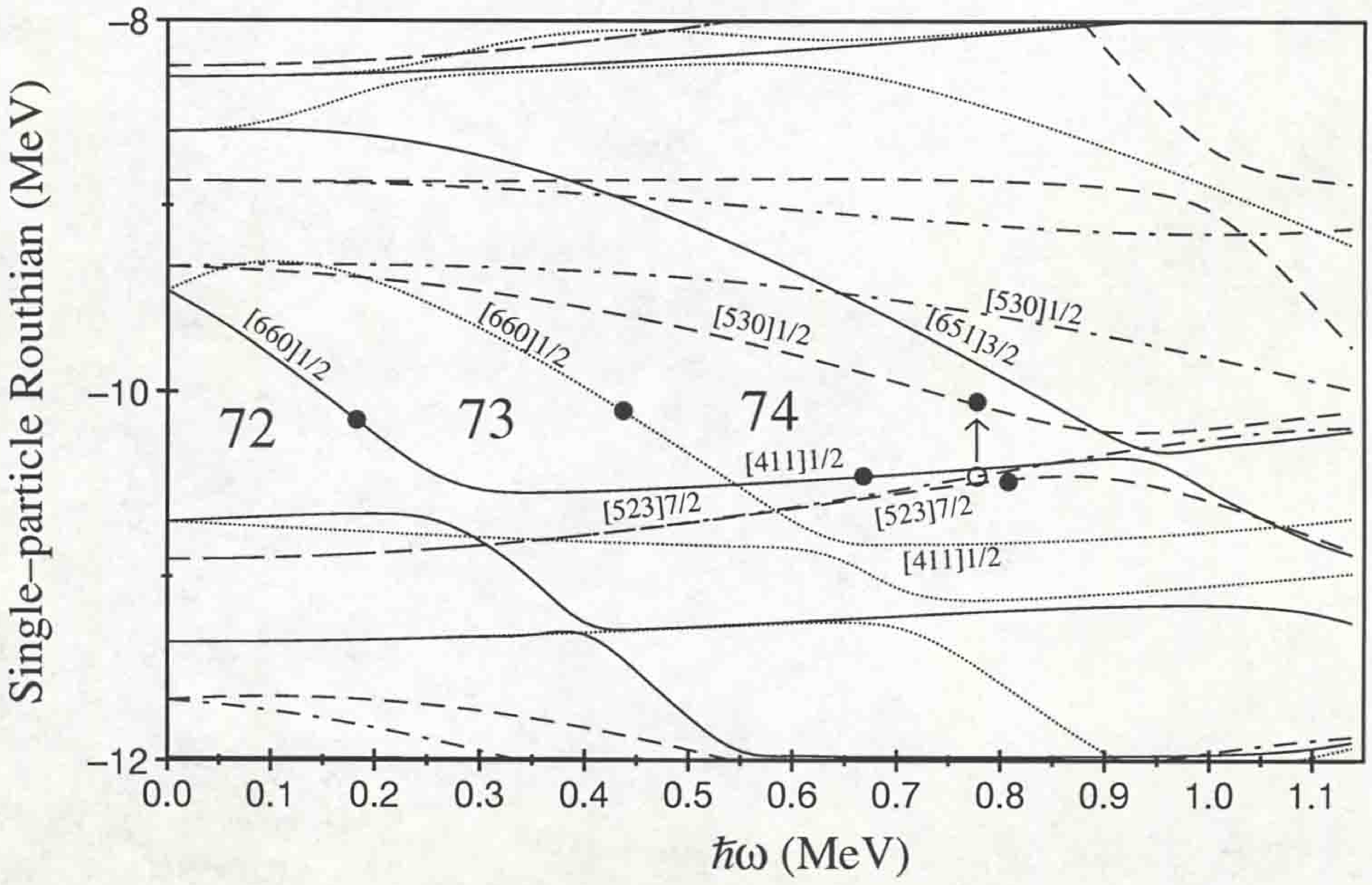

Figure 5.10: ^{132}Ce Band 3. Single-particle neutron calculations for $\beta_2 = 0.43$, $\beta_4 = 0.014$, γ=0° showing the suggested neutron configuration for ^{132}Ce Band 3 (74 neutrons). Filled circles indicate neutron occupation of outer orbitals, while open circles indicates a hole. Each orbital is referred to by its parity and signature (π, α) : Solid lines = (+,+1/2), dotted lines = (+,–1/2), dot–dash lines = (–,+1/2), dashed lines = (–,–1/2).

the following suggested configurations, ν^{-1} indicates a hole in that neutron orbital. e.g. ν^{-1} [411]1/2$^+$ (α=+1/2) indictates a hole in the [411]1/2$^+$ (α=+1/2) neutron orbital.

1. **^{131}Ce Band 1** $\pi 5^4 \nu 6^1$
2. **^{131}Ce Band 2** $\pi 5^4 \nu 6^2$ ν^{-1} [411]1/2$^+$ (α=+1/2)
3. **^{132}Ce Band 1** $\pi 5^4 \nu 6^2$
4. **^{132}Ce Band 2** $\pi 5^4 \nu 6^2$ ν [651]3/2$^+$ (α=+1/2) ν^{-1} [411]1/2$^+$ (α=+1/2)
5. **^{132}Ce Band 3** $\pi 5^4 \nu 6^2$ ν [530]1/2$^-$ (α=–1/2) ν^{-1} [523]7/2$^-$ (α=+1/2)

However, there remains the problem of a number of unobserved bands. These excited bands cannot be dismissed on the basis of higher excitation energies, as cranked shell model predictions indicate very similar excitation energies. This may suggest that the relative positions of orbitals are not produced correctly by the current calculations.

5.7 Identical Superdeformed Bands

It has been instructive in the preceding sections to treat each superdeformed band separately. However, it is by a comparison of superdeformed band properties that new and interesting phenomena are revealed. The concept of identical superdeformed bands was introduced in Sec. 2.6.2, where it was shown that superdeformed bands in one nucleus sometimes have 'identical' $\Im^{(2)}$ moments of inertia to superdeformed bands in a neighbouring nucleus. Fig. 5.11 shows the 'identical' $\Im^{(2)}$ relationships observed for the superdeformed bands in ^{131}Ce and ^{132}Ce. ^{131}Ce Band 2 and ^{132}Ce Band 1 are observed to follow each other very closely over the entire frequency range of the excited band. The excited bands in ^{132}Ce show 'identical' relationships with ^{131}Ce Band 1 and with each other.

Since the $\Im^{(2)}$ moment of inertia is similar for a pair of bands, this implies that a correlation exists between their transition energies (Sec. 2.6.2). The relationship between the transition energies E_γ in one nucleus, and those in another nucleus E_γ^{ref} (used as reference) may be expressed in the following equation [Szy90, San95] :

$$E_\gamma(I) = (1-x)E_\gamma^{ref}(I) + xE_\gamma^{ref}(I+2) \tag{5.1}$$

with x=0, 1/4, 1/2, 3/4, and the equation merely calculates the appropriate quarter-point energies (x) of the reference band. The correlations between the identical bands in ^{131}Ce and ^{132}Ce may now be calculated. Fig. 5.12 shows the energy differences (E-E_{ref}) between the transition energies in one band and those calculated from the reference band.

The results may be summarised :

(a) **^{131}Ce Band 2 and ^{132}Ce Band 1 (ref) x=1/4.** The Mean value of differences between γ-ray energies in ^{131}Ce Band 2 and the quarter-point energies of ^{132}Ce Band 1 is –1.9±1.1 keV in the 0.42 - 0.82 MeV rotational frequency range.

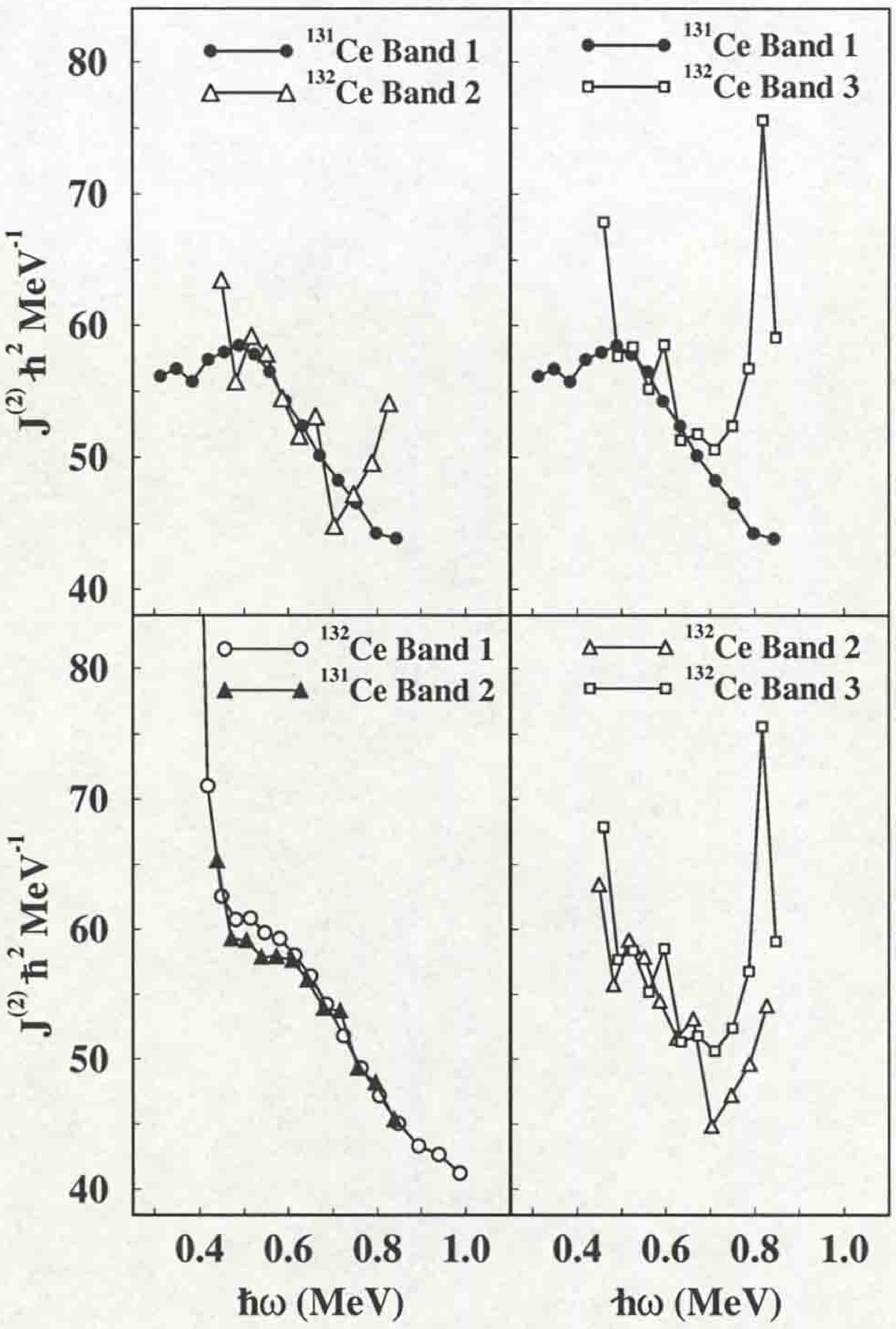

Figure 5.11: The Dynamic Moment of Inertia ($\Im^{(2)}$) for the five superdeformed bands discussed in this work, illustrating the 'identical' relationships between some bands.

(b) ^{132}Ce Band 2 and ^{131}Ce Band 1 (ref) x=3/4. The Mean value of differences between γ-ray energies in ^{132}Ce Band 2 and the quarter-point energies of ^{131}Ce Band 1 is 3.3±0.5 keV in the 0.46 - 0.68 MeV rotational frequency range.

(c) ^{132}Ce Band 3 and ^{131}Ce Band 1 (ref) x=0. The Mean value of differences between γ-ray energies in ^{132}Ce Band 3 and the quarter-point energies of ^{131}Ce Band 1 is 4.1±1.2 keV in the 0.48 - 0.73 MeV rotational frequency range.

(d) ^{132}Ce Band 3 and ^{132}Ce Band 2 (ref) x=1/4. The Mean value of differences between γ-ray energies in ^{132}Ce Band 3 and the quarter-point energies of ^{132}Ce Band 2 is 1.1±0.9 keV in the 0.47 - 0.69 MeV rotational frequency range. This

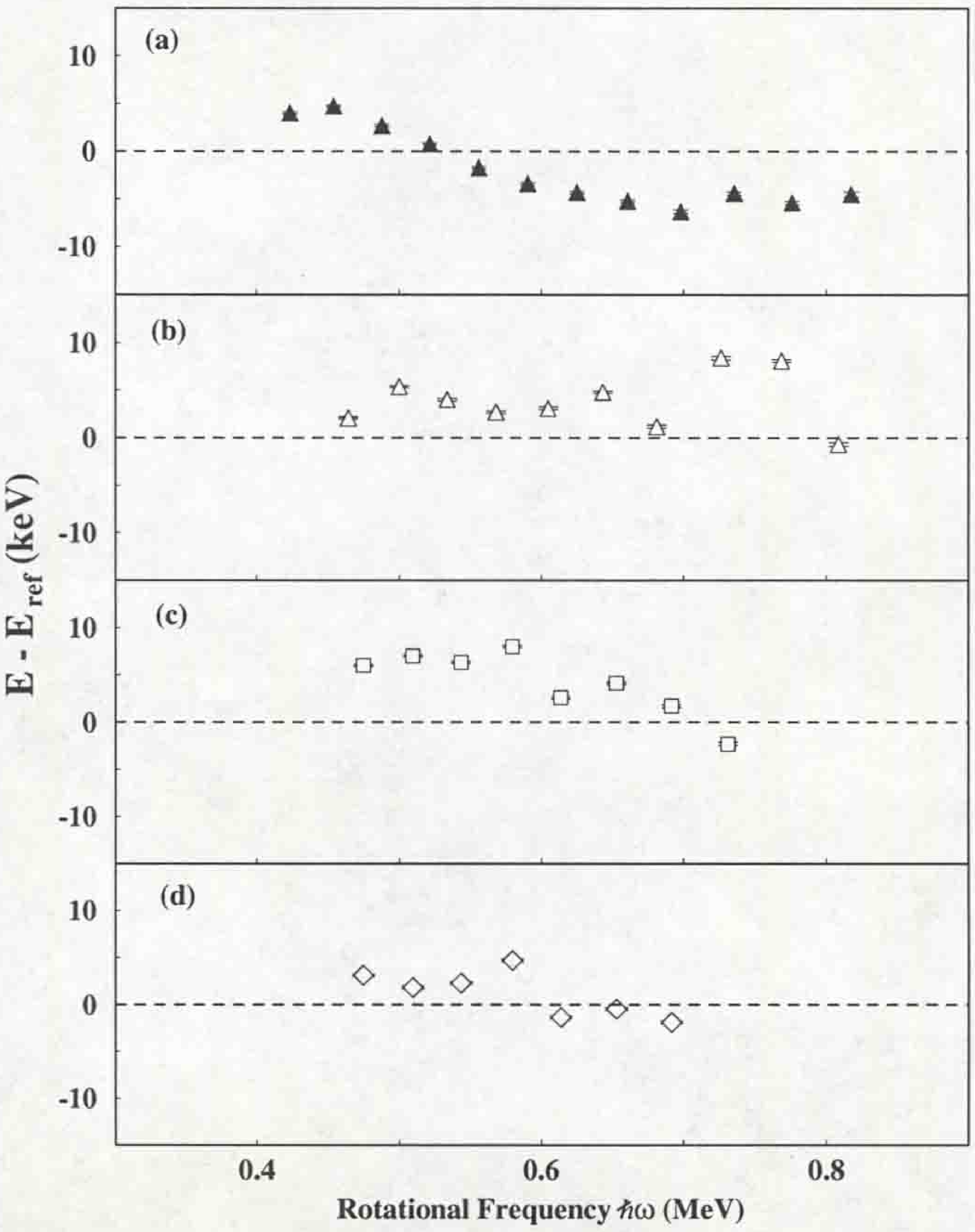

Figure 5.12: Energy differences (E-E_{ref}) between the transition energies in one band and those calculated from the reference band. (a) ^{131}Ce Band 2 and ^{132}Ce Band 1 (ref), x=1/4 (b) ^{132}Ce Band 2 and ^{131}Ce Band 1 (ref), x=3/4 (c) ^{132}Ce Band 3 and ^{131}Ce Band 1 (ref), x=0 (d) ^{132}Ce Band 3 and ^{132}Ce Band 2 (ref), x=1/4.

relationship is a consequence of (a) and (b).

The mean deviation of the γ-ray energies in the identical band to its x=0, 1/4, 1/2, 3/4 point reference is 2.6±0.7 keV, so that the degree of identicality for these bands is

$$\frac{E - E_{ref}}{E_\gamma} \approx \frac{2.6}{1200} \approx 2.1 \times 10^{-3} \tag{5.2}$$

which is incredibly small, and it is difficult to imagine that this could be purely accidental.

These identical bands provide a unique opportunity to identify properties of specific nuclear orbits and test their agreement with cranked shell model calculations. A useful quantity to consider is the alignment of a band relative to a reference band. The so-called 'relative alignment' is obtained by calculating the difference in spins between two bands at the same energy (Fig. 5.13). The quantity obtained is the contribution to the total spin of the nucleus by any additional particles (or holes) relative to the reference band. Fig. 5.14 shows the relative alignments of the identical bands in ^{131}Ce and ^{132}Ce. Each band is calculated relative to its identical yrast superdeformed band.

The fact that the identical bands have such similar $\Im^{(2)}$'s (Fig. 5.11) and transition energies which are closely correlated (Fig. 5.12) suggest that their structures should be very similar. Any differences in structure should be attributed to orbitals that only slightly modify the energy of the nucleus. The relative alignments of Fig. 5.14 therefore confirm the identical nature of these bands. For each band, the relative alignment is roughly constant (unless band crossings occur, Sec. 5.5) with respect to its reference band. This indicates that additional holes or particles in the excited bands are occupying flat orbitals - with very little curvature. Such orbitals have a nearly constant alignment in the frequency range $\hbar\omega \approx 0.4$-0.7 MeV, in accordance with eqn. 2.39. However, it is found that a quantitatve agreement is not observed between cranked shell model predictions and the observed relative alignments. Table. 5.1 shows cranked shell model predictions for the contribution to the alignment (negative the slope of the orbitals on single-particle routhians, Sec. 2.4.3) from specific orbitals.

The difference between the structures of ^{131}Ce Band 2 (filled triangles in Fig. 5.14) and its reference band ^{132}Ce Band 1 is a hole in the $[411]1/2^{+}$ (α=+1/2) neutron orbital (Sec. 5.5.1). The single-particle routhians in Fig. 5.8 indicates that this orbital is indeed relatively flat as a function of rotational frequency, and is therefore in good agreement with the observed alignment for ^{131}Ce Band 2 relative to ^{132}Ce Band 1. The contibution to the alignment of the $[411]1/2^{+}$ (α=+1/2) neutron orbital (Table. 5.1) is approximately $-0.5\hbar$. However, a hole in this orbital has a positive contribution, so the alignment of ^{131}Ce Band 2 relative to ^{132}Ce Band 1 should be approximately $0.5\hbar$, rather than consistent with $2\hbar$ as indicated on Fig. 5.14.

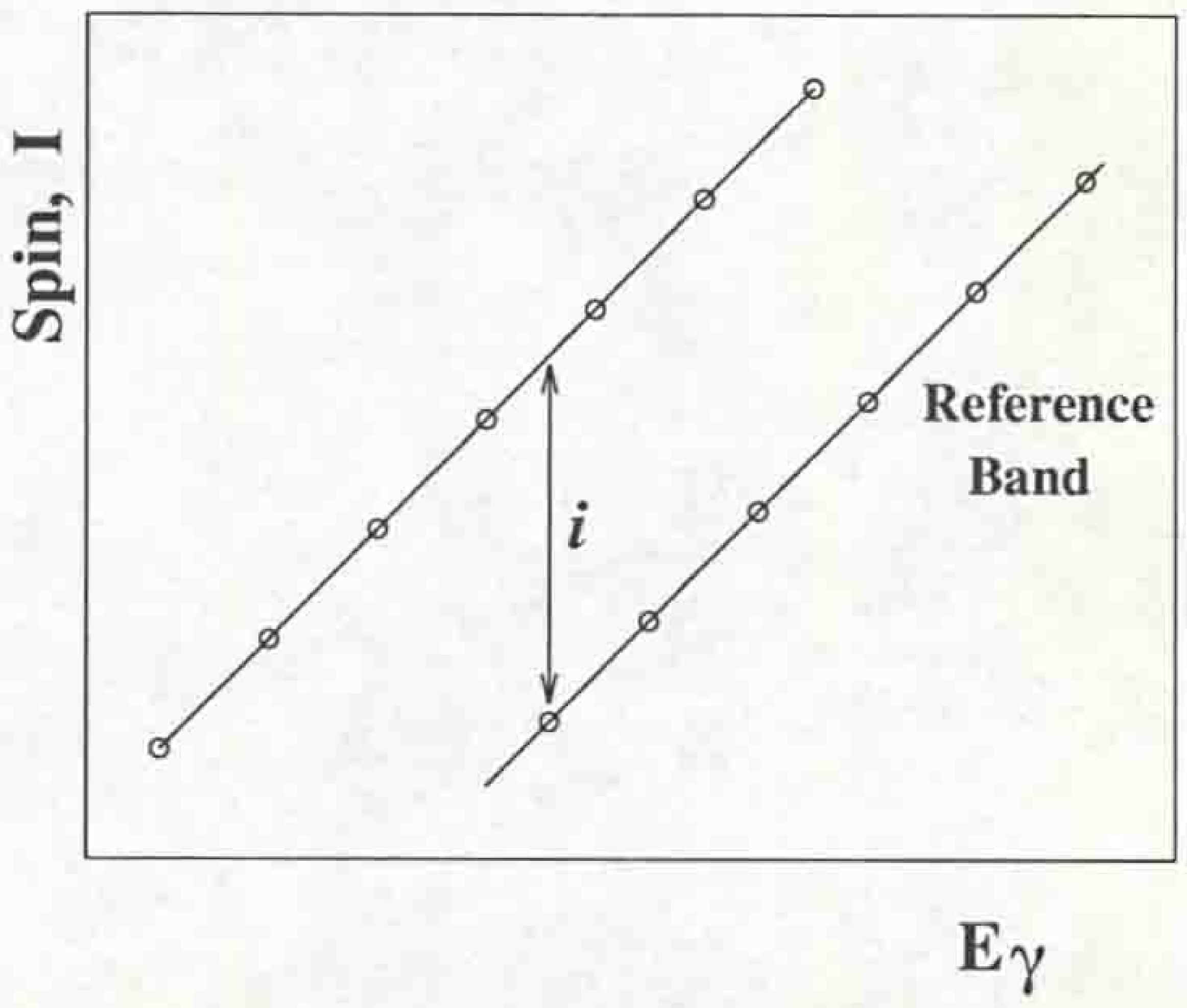

Figure 5.13: The difference between the spins of a superdeformed band, and the spins of a reference band is known as the relative alignment (i). It provides a way of measuring the contribution to the spin of the nucleus by an individual particle. In this way, the orbital that the particle is occupying may sometimes be deduced.

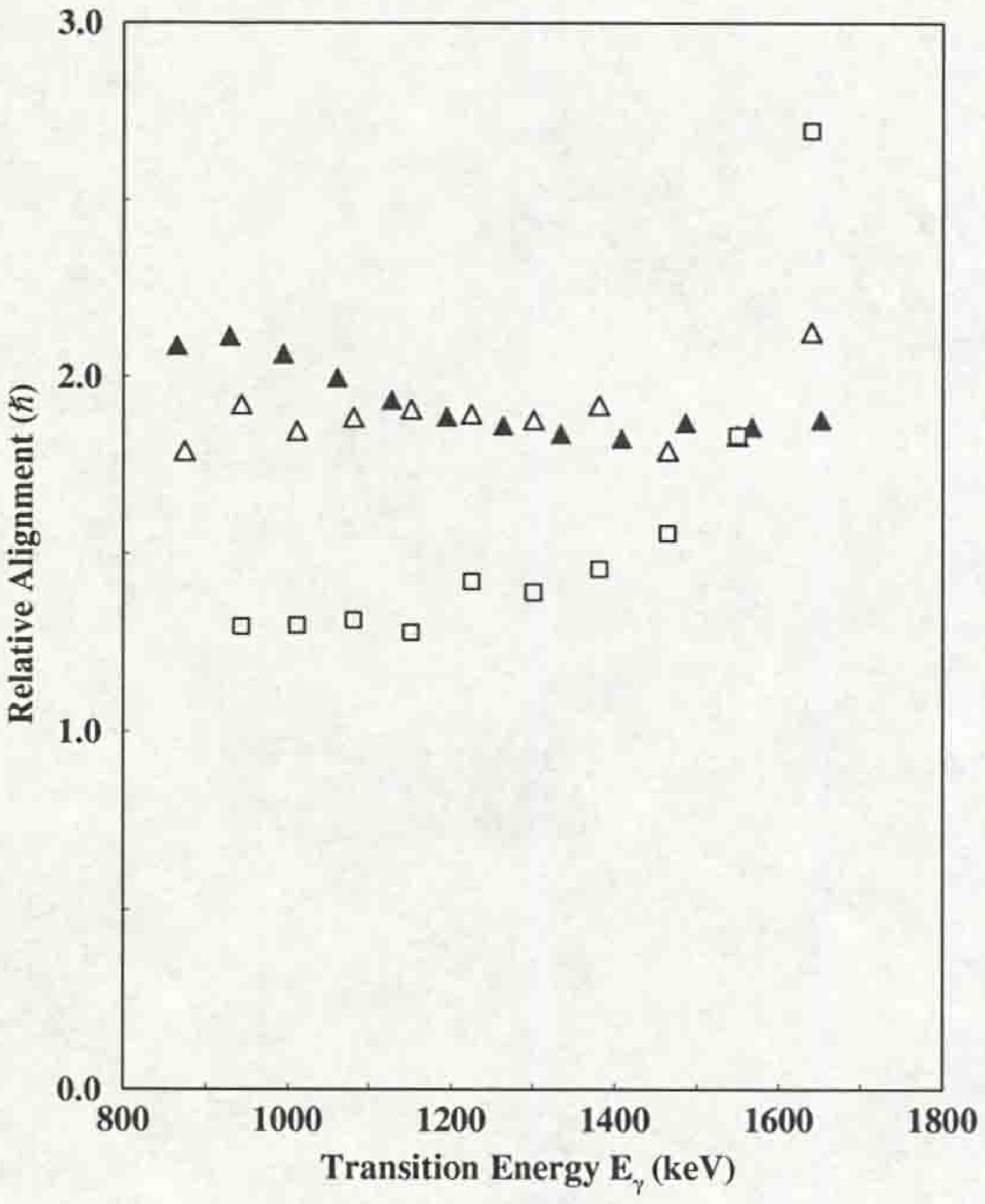

Figure 5.14: Relative alignments for the excited bands in ^{131,132}Ce, based on the Spin assignments made in Sec. 4.8. Each band is calculated relative to its identical yrast superdeformed band. The symbols are : ^{131}Ce Band 2 relative to ^{132}Ce Band 1 (Filled Triangles), ^{132}Ce Band 2 relative to ^{131}Ce Band 1 (Clear Triangles), ^{132}Ce Band 3 relative to ^{131}Ce Band 1 (Clear Squares).

Orbital	Alignment of orbital at $\hbar\omega\approx$0.6-0.8 MeV		
	^{131}Ce Band 2	^{132}Ce Band 2	^{132}Ce Band 3
[411]1/2$^+$ (α=+1/2)	**–0.47±0.05**	**–0.38±0.04**	–0.40±0.02
[411]1/2$^+$ (α=–1/2)	+0.40±0.03	+0.40±0.03	+0.43±0.02
[523]7/2$^-$ (α=+1/2)	–1.28±0.04	–0.90±0.02	**–0.92±0.02**
[523]7/2$^-$ (α=–1/2)	–1.00±0.02	–0.74±0.02	–0.75±0.02
[660]1/2$^+$ (α=+1/2)	+4.77±0.06	+3.54±0.07	+3.98±0.07
[660]1/2$^+$ (α=–1/2)	+3.90±0.07	**+3.28±0.04**	**+3.53±0.07**
[530]1/2$^-$ (α=+1/2)	+0.82±0.06	+0.73±0.02	+0.77±0.02
[530]1/2$^-$ (α=–1/2)	+1.55±0.03	+1.40±0.06	**+1.48±0.02**
[651]3/2$^+$ (α=+1/2)	+2.92±0.07	**+2.64±0.06**	+2.89±0.07

Table 5.1: Alignment contributions for orbitals predicted by cranked shell model calculations. Each alignment has been obtained from the slopes of single-particle routhians in the region $\hbar\omega\approx$0.5-0.9 MeV. The deformation parameters used for each band are those used in Sec. 5.5. Numbers in bold are those orbitals involved in the structure of a band.

The relative alignments are dependent on the experimentally deduced spins. Although a change in the spins will not alter the distribution of the relative alignmnents, it will vertically shift the alignments up and down the y-axis of Fig. 5.14. The apparent disagreement between experiment and cranked-shell model predictions may therefore indicate incorrect spin assignments. The alignment of 2$\hbar$ for ^{131}Ce Band 2 relative to ^{132}Ce Band 1, may be reduced to 0.5$\hbar$, by decreasing the spins of the excited band by 1.5$\hbar$ (thus moving the band down the y-axis by 1.5$\hbar$ on Fig. 5.13 and Fig. 5.14). However, this would make the spins for ^{131}Ce Band 2 integer values, rather than half integer (Sec. 4.8) which is not possible for an odd-mass nucleus. Conversely, an alignment of 0.5$\hbar$ may also be achieved by increasing the spins of ^{132}Ce Band 1 (the reference band) by 1.5$\hbar$. However, this would result in the spins of the even-even nucleus being half-integer values. The minimum discrepency between cranked shell model calculations and experiment is therefore $0.5\hbar$ (obtained by moving each of the bands by integer amounts on the spin axis). It is therefore not possible to account for $0.5\hbar$ within the confines of the cranked shell model. Of course, the relative alignments could indicate that the $[411]1/2^+$ (α=+1/2) neutron orbital is not involved at all in this band, and that the excitation is out of an orbital with zero slope. However, Table. 5.1 indicates that no such orbital is predicted to exist around the Fermi Surface. It is therefore not possible to explain the observed alignment of ^{131}Ce Band 2 relative to ^{132}Ce Band 1.

^{132}Ce Band 2 involves the $[660]1/2^+$ (α=–1/2), the $[411]1/2^+$ (α=+1/2) and the $[651]3/2^+$ (α=+1/2) neutron orbitals (Fig. 5.9, Sec. 5.5.2) outside the ^{131}Ce Band 1 core. Table. 5.1 indicates that these orbitals carry a total alignment of $6.3\pm0.1\ \hbar$. The alignment for ^{132}Ce Band 2 relative to ^{131}Ce Band 1 (clear triangles on Fig. 5.14) is experimentally $1.8\hbar$. To account for the discrepancy ($4.5\hbar$), the spins of ^{131}Ce Band 1 could be decreased by $2\hbar$ (bandhead spin would be $25/2\hbar$) and the spins of ^{132}Ce Band 2 increased by $2\hbar$ (bandhead spin would be $26\hbar$). The experimentally observed alignment of ^{132}Ce Band 2 relative to ^{131}Ce Band 1 would then be $5.8\hbar$, and is therefore still $\sim0.5\hbar$ less than cranked shell model predictions.

A similar problem arises for ^{132}Ce Band 3. This band involves the $[660]1/2^+$ (α=–1/2), the $[523]7/2^-$ (α=+1/2) and the $[530]1/2^-$ (α=–1/2) neutron orbitals (Fig. 5.10, Sec. 5.5.3) outside the ^{131}Ce Band 1 core. Cranked shell model calculations (Table. 5.1) therefore predict an alignment of $5.9\pm0.1\ \hbar$ for ^{132}Ce Band 3 relative to ^{131}Ce Band 1. Experimentally, this alignment is found to be $1.3\hbar$ (Fig. 5.14). The experimental value may be adjusted to $5.3\hbar$ (in a manner similar to above), but this still leaves a discrepancy of $\sim0.6\hbar$.

To summarise, alignments predicted by the cranked shell model do not agree with those obtained from experimental data. This is normally interpreted as incorrect spin assignments. However, even when the spins are adjusted within the experimental errors, a discrepancy of $\approx0.5\hbar$ remains in each case. When this is taken into context with the problem of a number of missing bands (Sec. 5.5), a serious question as to the reliability of the cranked shell model calculations in the Mass A≈130 region arises.

It should also be noted that the theoretical alignments calculated above assumed no pairing. The discrepancy may therefore also be an indication that pairing correlations still exist even at these high rotational frequencies.

5.8 ΔI=2 Energy Staggering

5.8.1 Introduction

It was shown in Sec. 4.9 that the γ-rays linking states in the yrast superdeformed bands of ^{131}Ce and ^{132}Ce are stretched electric quadrupole (E2) transitions. In fact, this is true for most rotational bands in which spin sequences with ΔI=2 are connected with E2 transitions. This implies that the intrinsic Hamiltonian is invariant under a rotation of 180° around an axis perpendicular to its symmetry axis (See Sec. 2.4.3).

The current generation of γ-ray detector arrays (Sec. 3.10) have enabled precise measurements of γ-ray transition energies. This is typified by the strongest superdeformed bands measured in this work, in which a typical uncertainty of ≈ 0.1 keV has been assigned to a γ-ray of ~ 1500 keV (Sec. 4.7.1).

Since the $\Im^{(2)}$ moment of inertia is related directly to experimentally measured γ-ray transition energies, small fluctuations in this quantity may now be identified. In December 1993, Flibotte *et al* [Fli93] reported that the $\Im^{(2)}$ moment of inertia in ^{149}Gd [Haa88, Haa90] exhibited a staggering. This staggering is now either referred to as ΔI=2 staggering, because states separated by ΔI=2 stagger in energy, or ΔI=4 bifurcation, because the bands divide into two sequences with levels differing in angular momentum by $4\hbar$.

To date, the only other reported case of ΔI=2 staggering is in three bands in ^{194}Hg [Ced94], and is therefore definitely not a common occurrence. However, in this work it has been observed that three superdeformed bands in ^{131,132}Ce exhibit the effect, in a way that is unique among all known cases.

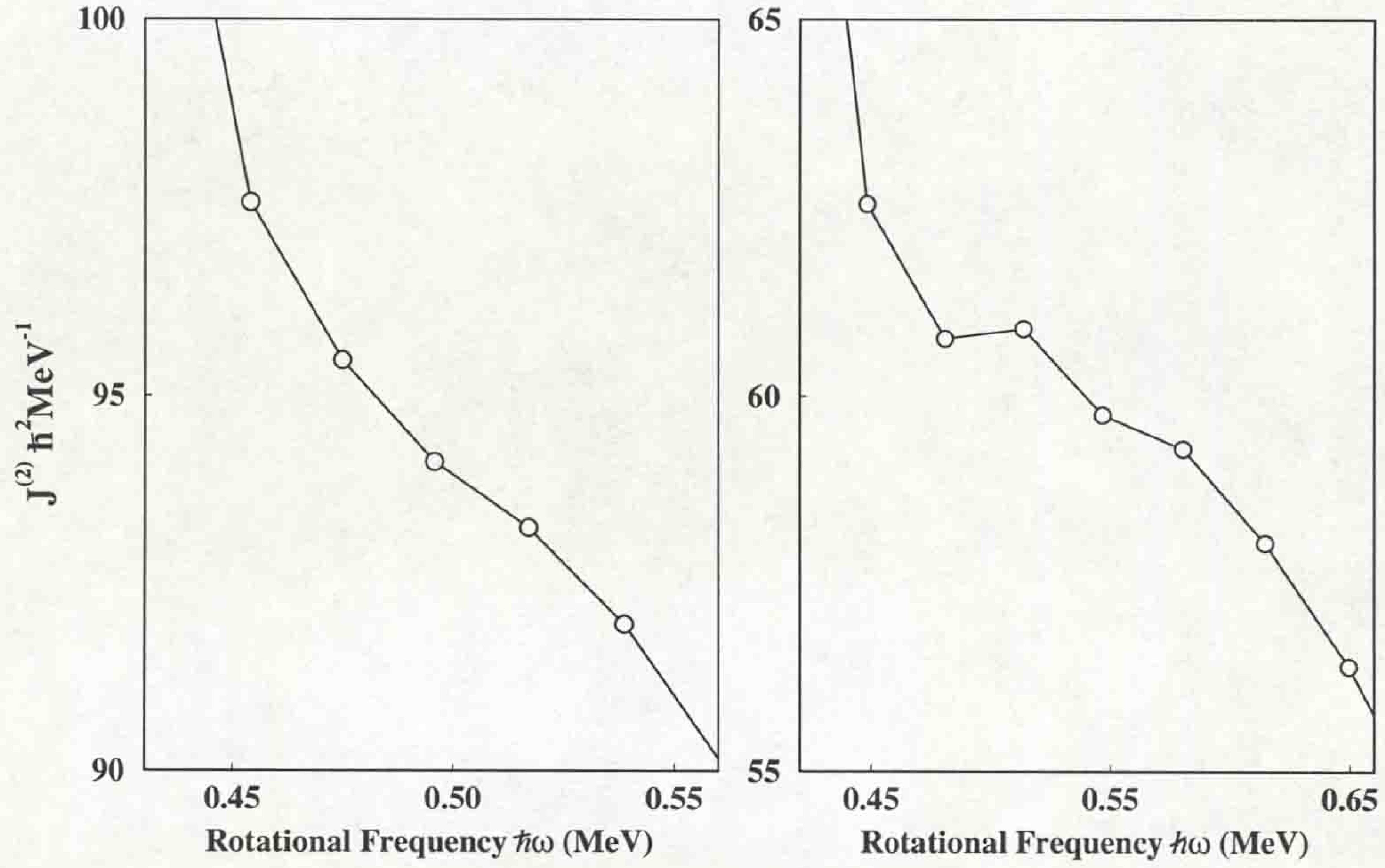

Figure 5.15: The low frequency region of the $\Im^{(2)}$ moment of inertia for (left) ^{150}Gd Band 1, and (right) ^{132}Ce Band 1. Both bands are characterised by a gradual drop in the $\Im^{(2)}$. However, ^{132}Ce Band 1 has states separated by $\Delta I=2$ alternately shifting up and down.

As this phenomenom has remained unknown until now, it is evident that it is a small effect. It is therefore not surprising that a staggering in the $\Im^{(2)}$ moment of inertia cannot be observed on the scale shown in Fig. 5.5. Fig. 5.15 shows the low frequency region of the $\Im^{(2)}$ moment of inertia for ^{150}Gd Band 1 [Fal89] and ^{132}Ce Band 1. Both bands show a $\Im^{(2)}$ characterised by a gradual drop with increasing rotational frequency (however, the magnitude of the $\Im^{(2)}$'s are different, and it is necessary to show the graphs on different scales). The difference between the bands at low rotational frequency, is a distinct staggering in the $\Im^{(2)}$ for ^{132}Ce Band 1, but in the case of ^{150}Gd Band 1, no staggering is observed. In an attempt to understand the process causing this effect in ^{132}Ce, a means of measurement must be devised.

5.8.2 Measuring the Degree of Staggering

Although the mechanism producing a $\Delta I=2$ staggering in the $\Im^{(2)}$ moment of inertia has no widely accepted explanation (current theories will be dealt with in Sec. 5.8.4), it's effects can be understood on the energy states in a superdeformed band. As shown in Sec. 1.3.6, the $\Im^{(2)}$ is directly related to the difference (ΔE_γ) between successive transition energies (E_γ) :

$$\Im^{(2)} = \frac{4\hbar^2}{\Delta E_\gamma} \tag{5.3}$$

Thus a staggering in the $\Im^{(2)}$ follows from a staggering in the ΔE_γ term of eqn. 5.3. The energy states E, with spins I, in a rotational band are governed by the relationship (Sec. 1.3.6)

$$E \propto I(I+1) \tag{5.4}$$

An oscillating $\Im^{(2)}$ is therefore a consequence of successive energy levels in the rotational band being perturbed in opposite directions.

In order to obtain a quantitative estimate for how much each state in the rotational band is shifted, some form of reference must be used. The relationship described above naturally leads to a fit of the E_γ versus spin (I). Fig. 5.16 shows a schematic of a perturbed band (in which alternate states are shifted up and down) and an unperturbed band (which closely follows the relationship of eqn. 5.4). The figure shows that a perturbed band oscillates about the curve made by the unperturbed band.

As it is a measure of the localised shift of each data point that is required, a quadratic fit is performed over four points only, rather than the entire curve of E_γ vs I. This also enables the method to accomodate a varying $\Im^{(2)}$ moment of inertia displayed by the bands in these nuclei. Below is a description of the fitting procedure devised in this work, the text refers to Fig. 5.17.

1. A quadratic fit is applied to the first four points (i.e. lowest energies) of E_γ v I experimental data. The degree of staggering is obtained for the middle two points by subtracting the fitted reference from the experimental data. The two end points are ignored for each fit to eliminate edge effects. See Fig. 5.17a.

2. The fit is then repeated for a further four points, using the second data point from the previous fit, as the first data point (effectively sliding the fit along the

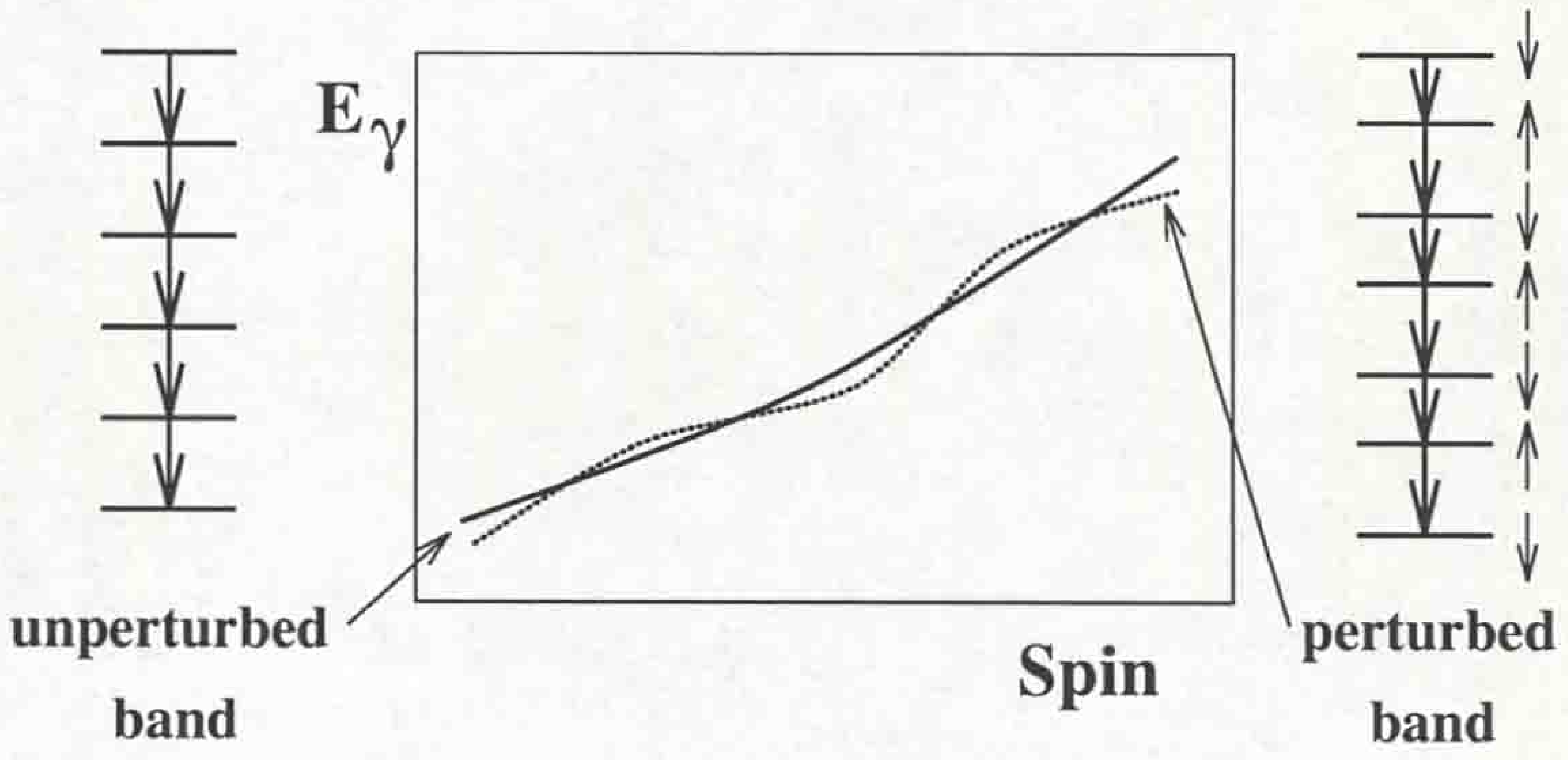

Figure 5.16: The variation of E_γ versus Spin (I) for a perturbed band (in which alternate states are shifted up and down (dotted line)) is expected to oscillate about the smooth variation for an unperturbed band (solid line).

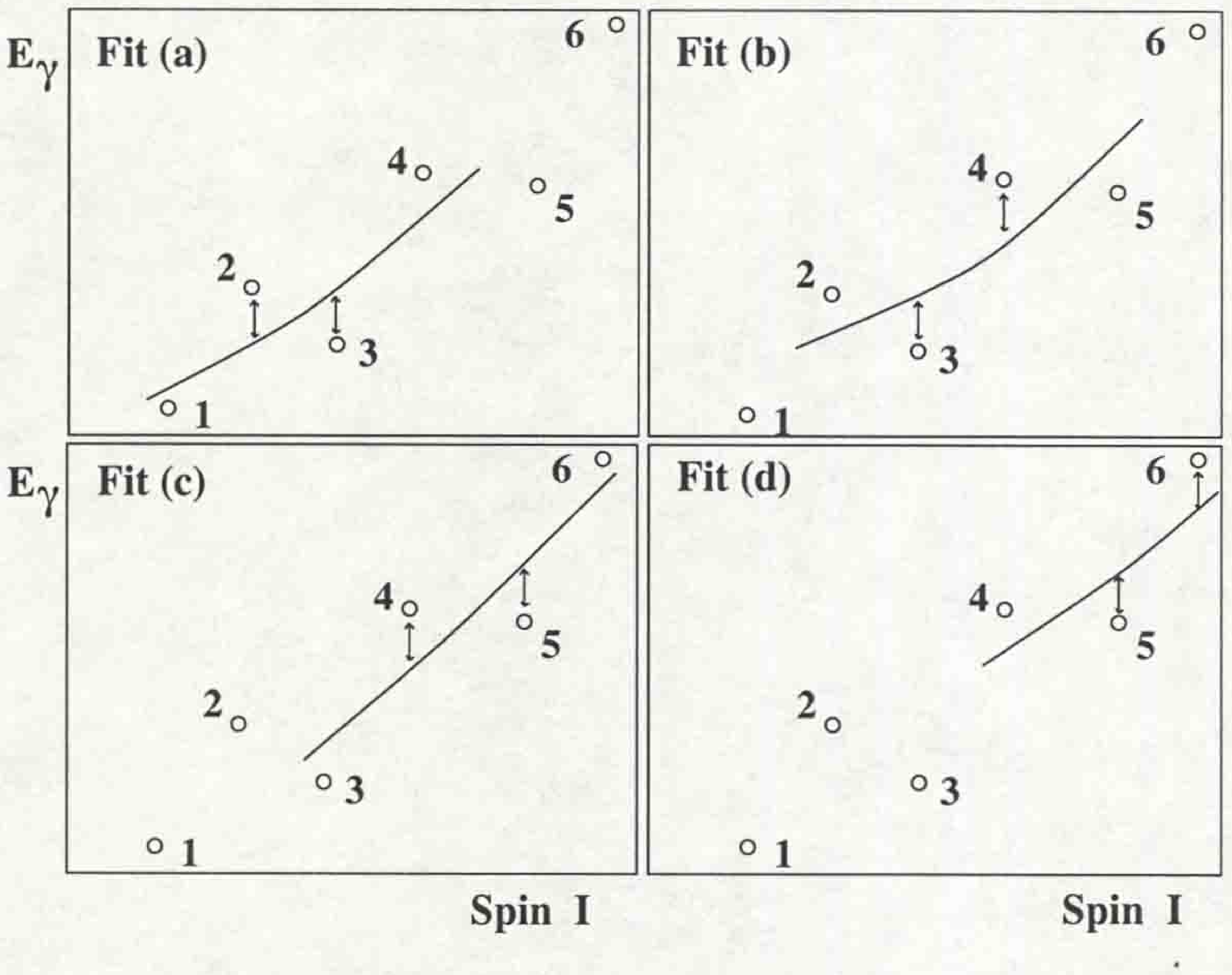

Figure 5.17: Schematic diagram illustrating the fitting procedure used in this work. (a) A quadratic fit is performed over four points, and shift values are obtained for points (2) and (3). (b) The fit is slid along the band by one transition, and shift values obtained for points (3) and (4). (c) and (d) continue the process. The final shift value is an average of the two obtained from two fits - e.g shift value for point (3) is an average of Fit (a) and Fit (b) values.

band by one transition). See Fig. 5.17b. The degree of staggering is obtained in the same way as above.

3. This process of fitting, obtaining the staggering, sliding along the band, and fitting again is repeated until the entire band has been covered. See Fig. 5.17c,d.

The result of this fitting procedure is that each data point is involved in four 'independent' fits. Two of the fits for each point are neglected because of edge effects as described in item (1) (the points were at the begining or end of the quadratic fit). An average is taken of the two 'usable' shift values for each point, and this is used as the final shift value for this data point. For example, the shift value for point (3) in Fig. 5.17, is obtained from an average shift value obtained from fit(a) and fit(b). The value from fit(c) cannot be used, as the data point was at the edge of the fit.

This procedure was also tried with a six-point fit. The results were similar, but not identical. However, it was decided that a four-point fit gave the best measure of a localised shift, and so this was used in the analysis. To take account of the fact that the choice of reference clearly does influence the degree of staggering, an error was assigned to each point to reflect this. This error was obtained by performing a six-point fit as well as the four-point fit, and a mean value for the shift, with a corresponding standard error on the mean (σ_m) was obtained for each point. The error assigned to the data point due to the fitting procedure is the value σ_m. This was added in quadrature to the total error obtained for the transition energy.

The other reported cases of ΔI=2 staggering in ^{149}Gd [Fli93] and ^{194}Hg [Ced94] use different fitting procedures to estimate the degree of staggering. In ^{149}Gd a linear fit over the variation of ΔE_γ with spin was used, whilst in ^{194}Hg, an interpolated quadratic fit over the variation of E_γ with spin was used. Fig. 5.18 shows the staggering results obtained for ^{149}Gd Band 1 using each of the three methods. The figure shows all three fitting procedures yield similar results, although the magnitude of the staggering obtained by the Flibotte method appears slightly larger than that obtained by the other two methods.

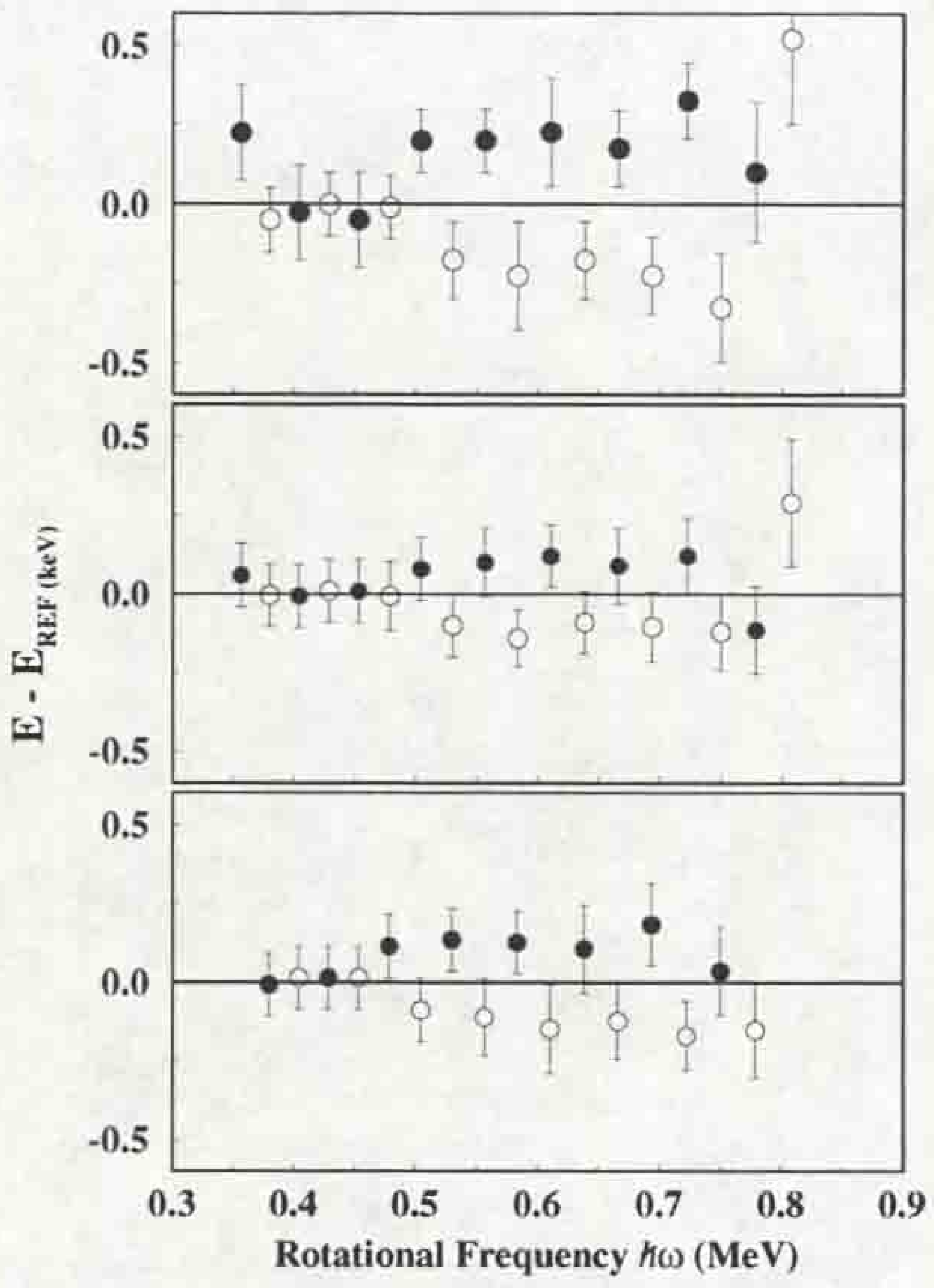

Figure 5.18: The amplitude of ΔI=2 Staggering obatined for ^{149}Gd Band 1 using the methods (Top) Flibotte *et al*, (Middle) Cederwall *et al.*, and (Bottom) the method devised in this work. All three methods are observed to give similar results. States separated by ΔI=4 have the same symbols.

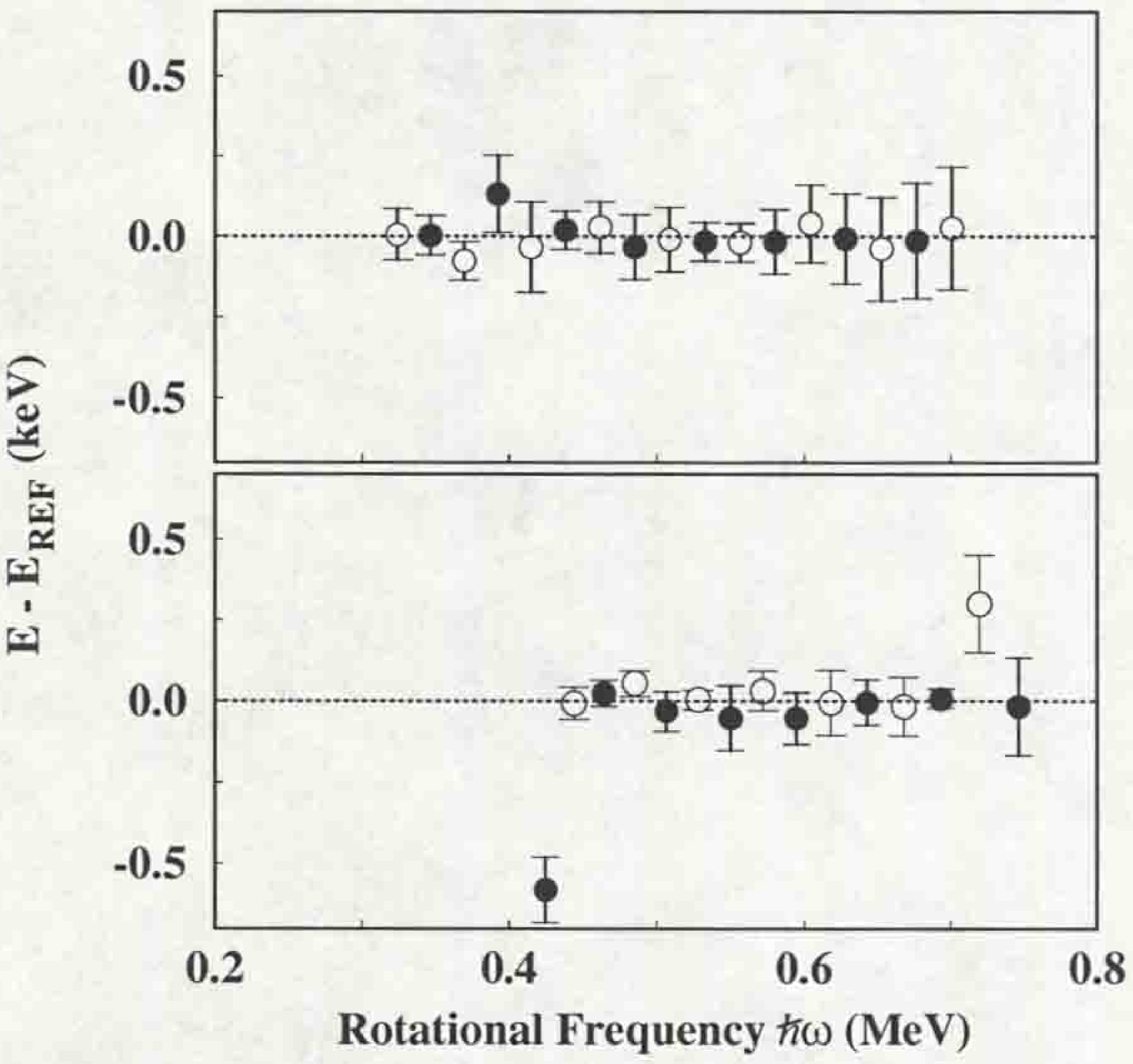

Figure 5.19: No staggering is observed in most Superdeformed Bands. Examples of ΔI=2 Staggering analysis performed on Superdeformed Bands, (Top) ^{152}Dy Band 1, and (Bottom) ^{150}Gd Band 1. States separated by ΔI=4 have the same symbols.

Having confirmed that the fitting procedure devised in this work yields similar results, a test was made to see if the staggering was a consequence of the fitting procedures themselves, and not a nuclear structure effect. The analysis was carried out on various superdeformed band energies, and in all cases, no staggering was observed. Fig. 5.19 shows examples of this analysis performed on ^{150}Gd Band 1 [Fal89] and on ^{152}Dy Band 1 [Dag94]. The figure clearly shows that no effect is present in these nuclei.

5.8.3 ΔI=2 Staggering in ^{131}Ce and ^{132}Ce

ΔI=2 staggering has been observed in ^{131}Ce Band 1, ^{131}Ce Band 2, and ^{132}Ce Band 1. It was not possible to determine if the effect was present in ^{132}Ce Bands 2 and 3, as these bands undergo many perturbations due to other effects (Sec. 5.3 and Sec. 5.5).

Fig. 5.20 shows the results obtained using the fitting procedure described in Sec. 5.8.2, where states separated by ΔI=4 have the same symbols. A number of features of the staggering are worth noting :

1. The energy staggering starts off large (≈0.3 keV) at low frequency in all cases. For ^{149}Gd [Fli93] and ^{194}Hg [Ced94], the bifurcation is small at low frequency and gradually rises to a maximum value of ≈0.2 keV.
2. The staggering reduces with frequency until $\hbar\omega\approx$0.6-0.7 MeV, where it disappears.
3. At higher frequency, the staggering reappears and continues at approximately the same magnitude as at low frequency for the yrast bands, but with a higher amplitude for ^{131}Ce Band 2.
4. A phase change in the staggering is observed for the yrast bands. No phase change is observed for ^{131}Ce Band 2.
5. The effect is much larger than the experimental errors.

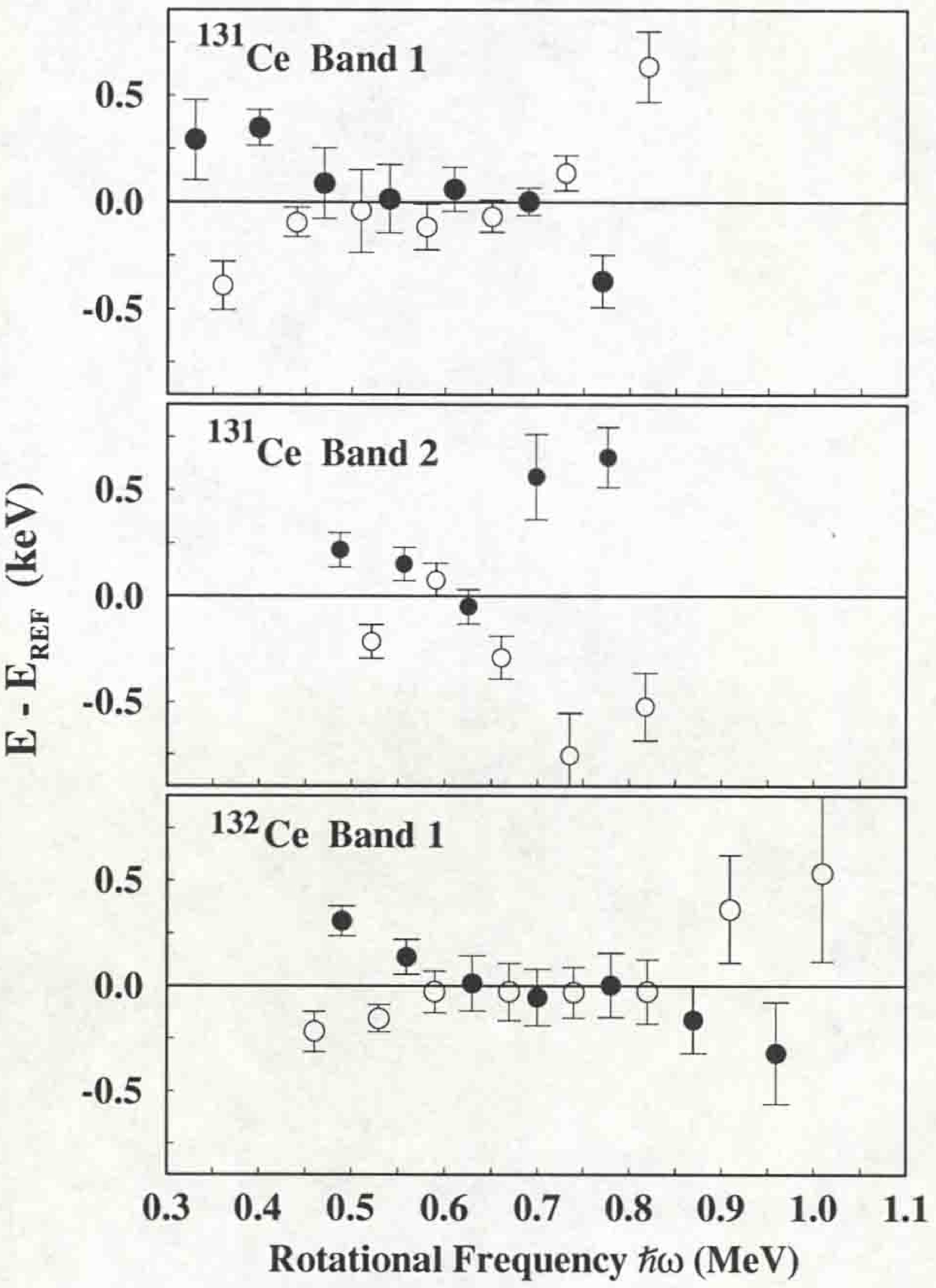

Figure 5.20: ΔI=2 Staggering distributions as a function of rotational frequency obtained for (Top) ^{131}Ce Band 1, (Middle) ^{131}Ce Band 2 and (Bottom) ^{132}Ce Band 1. States separated by ΔI=4 have the same symbols.

These results represent the first observations of ΔI=2 staggering in :

1. The mass A≈130 region.
2. Neighbouring nuclei (^{131}Ce and ^{132}Ce).
3. A pair of identical bands (^{131}Ce Band 2 and ^{132}Ce Band 1).
4. Bands exhibiting a midband disppearance.

As shown in Fig. 5.16, this staggering can be produced by alternately shifting up and down, energy states in the rotational band. The amount each state is shifted by may now be estimated.

The absolute value of the shifts in the transition energies for ^{131}Ce Band 1 is on average 282±65 eV at low frequency, while at high frequency it is 381±144 eV (Fig. 5.20). This corresponds to the states in the rotational band being shifted alternately up and down by 141±33 eV at low frequency and by 190±72 eV at high frequency. This is an incredibly small effect of

$$\frac{0.190}{800} \approx 0.02\% \tag{5.5}$$

relative to their unpertubed positions at ≈800 keV. Table. 5.2 summarises these results for all three bands which exhibit the effect.

Superdeformed Band	γ-ray transition energy shift (eV)		Energy Shift of state in band (eV)	
	low frequency	high frequency	low frequency	high frequency
^{131}Ce Band 1	282±65	381±144	141±33	190±72
^{131}Ce Band 2	195±21	581±96	97±11	290±48
^{132}Ce Band 1	204±38	345±77	102±19	172±38

Table 5.2: Summary of ΔI=2 staggering results for the ^{131}Ce and ^{132}Ce.

Because of the regularity of the effect in all three nuclei, the phenomenon causing it is unlikely to be chaotic in origin. This has led to many theories being proposed in an effort to try and explain the effect. Many of the approaches taken are rather complicated and are beyond the scope of this work. However, a brief discussion of the general principles involved in some of the theories is quite enlightening, and is discussed in the next section.

5.8.4 Current Theories

Most rotational bands have spin sequences with ΔI=2 that are connected by E2 transitions. This implies that the Hamiltonian is invariant under a rotation of 180° around the rotation axis - i.e. it represents a two-fold symmetry of the nucleus.

Flibotte *et al* [Fli93] suggests that the prescence of two ΔI=4 sequences in a rotational band implies a fourfold symmetry of the nucleus, corresponding to an invariance of the Hamiltonian under rotations of 90° around the rotation axis. By introducing a new quantum number α_4, they adapt the spin-signature relationship of eqn. 1.20 to be

$$I = \alpha_4 \bmod 4 \tag{5.6}$$

Excitations with the same α_4 are then expected to form one family of states.

Hamamoto and Mottelson [HM93] propose that the prescence of the four-fold symmetry suggested by Flibotte *et al*, implies that the strongly prolate spheroidal deformation of the superdeformed nucleus has been slightly perturbed.

They introduce parameters into the rotational Hamiltonian, which when adjusted, can produce various modes of ΔI=2 staggering. These modes can be either regular, irregular, or result in no oscillations at all. They also point out that if a small perturbation of the prolate deformation is a result of the rotation, then particles in high **j** orbitals must play a significant role. This is said to be particularly true for superdeformed nuclei, since other orbitals are less disturbed by the rotation.

Sun, Zhang and Guidry [SZG95] take a completely different approach to explain ΔI=2 staggering.

They propose that such staggering emerges naturally when rotational bands built upon particles close to the Fermi surface are mixed by ordinary two-body shell model interactions. It is also shown that if there are multiple band crossings in a particular region, the staggering effect can easily be washed out. However, they conclude by acknowledging that this theory does not rule out contributions to ΔI=4 sequences from other mechanisms.

Further theories on this phenomenon may be considered as variations on these themes. Details may be found in papers by Machiavelli *et al.* [Mac95], Pavlichenkov *et al.* [Pav94], and Burzynski *et al.* [Bur95].

5.8.5 The Midband Disappearance

The ΔI=2 staggering observed in ^{131}Ce and ^{132}Ce is characterised by a unique midband disappearance (Fig. 5.20). The degree of these 'damped oscillations' varies from band to band but always takes place within the same frequency region of $\hbar\omega \approx 0.5$-0.8 MeV.

^{132}Ce Band 1 is damped over 7 transitions in the frequency range of $\hbar\omega \approx 0.6$-0.8 MeV. ^{131}Ce Band 1 is also damped over 7 transitions, but occurs slightly lower in rotational frequency at $\hbar\omega \approx 0.5$-0.7 MeV. At high frequency, ^{131}Ce Band 2 has the largest amplitude of oscillations (Table. 5.2) and is only damped over 2 transitions in the frequency range of $\hbar\omega \approx 0.55$-0.65 MeV.

The question as to why all three bands should show this midband disappearance - but to varying degrees - should be addressed. This also provides an opportunity to test the band configurations proposed in Sec. 5.4 and Sec. 5.5, as differences in the staggering for each band may be indicative of differences in nuclear structure.

It has already been shown in Sec. 5.3 that four alignments are predicted to occur in the frequency region occupied by these bands (Fig. 5.2 and Fig. 5.3). Based on the configurations proposed in Sec. 5.4 and Sec. 5.5, the $h_{11/2}$ proton, the $h_{9/2}$ neutron, and the $h_{11/2}$ neutron alignments would all occur in all three cases exhibiting the ΔI=2 staggering. The $i_{13/2}$ neutron alignment would only occur ^{131}Ce Band 2 and ^{132}Ce Band 1, as it is blocked in ^{131}Ce Band 1.

Fig. 5.21 reproduces the ΔI=2 staggering distributions already presented in Fig. 5.20, with the positions of the above alignments also indicated on the figure. The $i_{13/2}$ neutron alignment takes place over a very narrow frequency range and is indicated by an arrow. The remaining alignments are more gradual and are indicated as a range of frequencies. Although the $h_{9/2}$ and $h_{11/2}$ neutron alignments probably continue to align upto $\approx$1.0 MeV, it is expected that they will be mostly aligned by $\approx$0.8 MeV.

An interesting pattern is seen to emerge. The $h_{11/2}$ proton alignment is accompanied by large staggering in ^{131}Ce Band 1. No data is available for the other two bands in this frequency region due to the $i_{13/2}$ neutron alignment. In all three cases however, the midband disappearance occurs in the frequency region of the $h_{9/2}$ and $h_{11/2}$ neutron alignments.

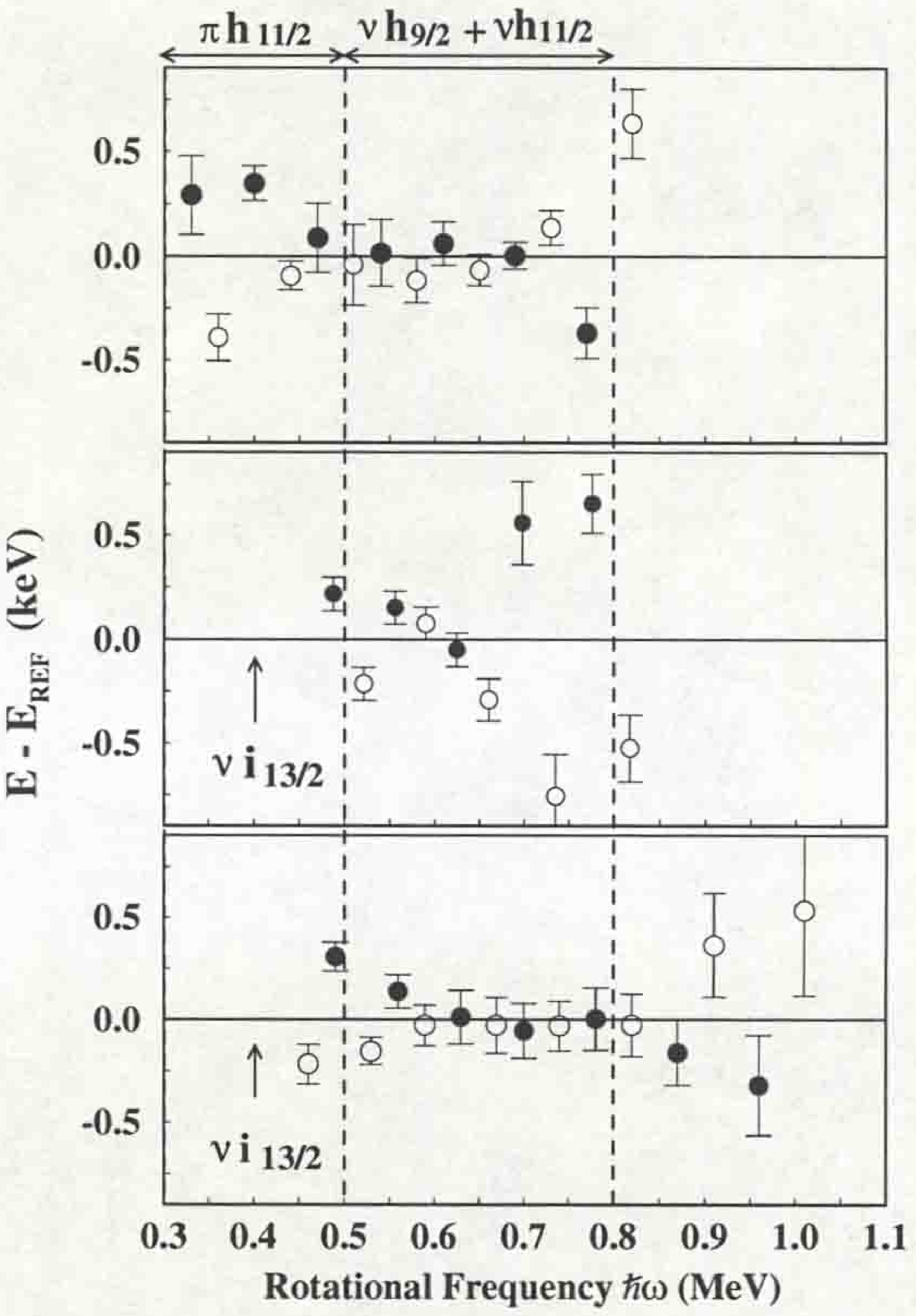

Figure 5.21: ΔI=2 staggering distributions as a function of rotational frequency obtained for (Top) ^{131}Ce Band 1, (Middle) ^{131}Ce Band 2 and (Bottom) ^{132}Ce Band 1. States separated by ΔI=4 have the same symbols. An $i_{13/2}$ neutron alignment is predicted to occur in ^{131}Ce Band 2 and ^{132}Ce Band 1 only (indicated by an arrow). Alignments of $h_{11/2}$ protons, $h_{9/2}$ neutrons and $h_{11/2}$ neutrons are predicted in all three cases in the regions indicated on the graphs.

A distinct difference is observed in the case of ^{131}Ce Band 2. Although the damped oscillations occurs within the same frequency range as the other two bands, it occurs over considerably fewer transitions. If the $h_{9/2}$ and $h_{11/2}$ neutron alignments are the cause of the midband disappearance, then this may indicate that one (or perhaps both) of the alignments is blocked for ^{131}Ce Band 2. This would require the excitation for this band occuring out of one of the [523]7/2$^-$ orbitals, rather than the [411]1/2$^+$ orbital as proposed in Sec. 5.5.1. Indeed, this structure was never completely ruled out in the discussion of this band, but was considered less likely due to a missing signature-partner band.

It is possible that this midband disappearance is the first observation of weak band crossings that have little effect on the $\Im^{(2)}$, being detected experimentally. One could speculate that the modulation of $\Delta I=2$ staggering in nuclei, could therefore be a sensitive probe of high-spin superdeformed band crossings.

5.9 Summary & Conclusions

A single experiment performed with the Eurogam γ-ray spectrometer to study the superdeformed nature of ^{131}Ce and ^{132}Ce has been very fruitful.

Prior to the experiment, each nucleus was known to exhibit a single superdeformed band. Both bands are of the order of five times more intense than most other known superdeformed bands. For this reason, it was surprising that no excited bands had been observed in these nuclei.

This work represents the first observation of excited superdeformed bands in the $A\approx130$ mass region. However, these bands are much weaker than their yrast counterparts, and have been estimated at only $\approx1\%$ the population of their respective main reaction channels. The high statistics obtained using the Eurogam array has made their discovery possible, and it was only by the study of higher-fold events that precise measurements of their properties could be made.

No transitions linking the superdeformed to normal-deformed states have been observed. These transitions are thought to be statistical with the intensity fragmented over many pathways. Thus, an exact spin assignment for the bands has not been possible. However, an observation of feeding into the normal-deformed states has enabled reasonable estimates to be made.

These bands have been interpreted using theoretical cranked-shell model predictions. However, the numerous orbitals predicted to be close to the Fermi surface for these bands has made nuclear structure assignments inconclusive. Structures have

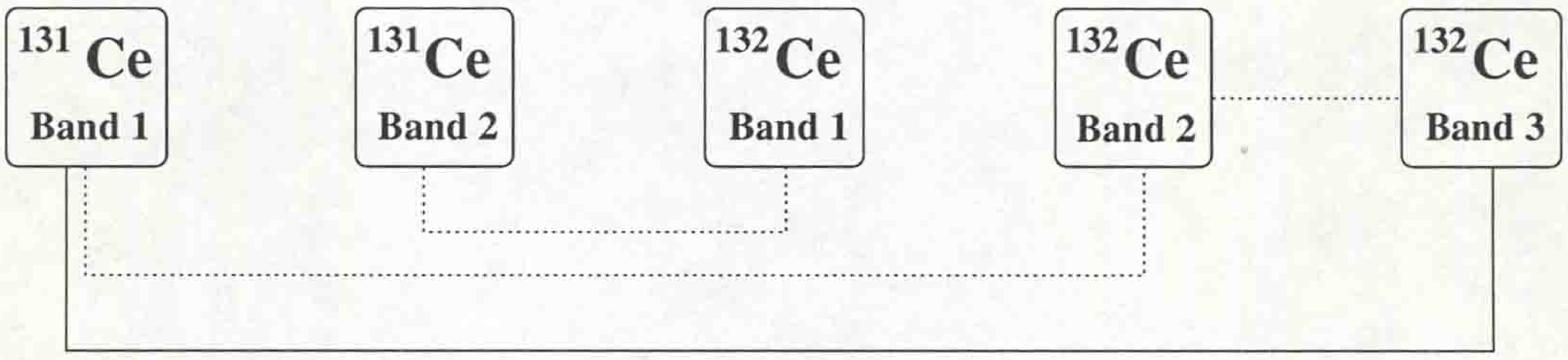

Figure 5.22: Identical band relationships for the nuclei studied in this work. Dotted line: the energies of the bands lie at the quarter-points of each other. Solid line: The energies of the bands are directly degenerate.

been proposed on the basis of the $\Im^{(2)}$ moment of inertia, but there are a number of bands that are predicted to occur, but have remained unobserved. This problem has remained unsolved.

Identical superdeformed bands have also been observed in the mass A≈130 region for the first time. The relationships between these bands are summarised in Fig. 5.22.

The average agreement between the energies of a pair of identical bands in these nuclei has been measured to be ≈0.2%. The identical nature of these bands were then confirmed by experimentally deduced relative alignments. However, a quantitative agreement between these alignments and cranked shell model predictions has been observed to be poor, with a minimum discrepency of $\approx 0.5\ \hbar$ always remaining.

This work has also reported for the first time, the relatively new observed phenomenon of ΔI=2 staggering in the mass A≈130 region. To date, there is no single universally accepted theoretical explanation for this effect. Most interpretations centre around a perturbation of the axially symmetric nucleus, such that it exhibits a four-fold rotational symmetry, rather than the 'more normal' two-fold symmetry.

The staggering observed in these nuclei also exhibit the unique property of a midband disappearance. The presence of these damped oscillations is not understood, but a relationship to nucleon alignments seems possible. It is suggested that the amplitude of ΔI=2 staggering may be a sensitive probe into superdeformed band crossings.

It is hoped that many of the problems encountered in these nuclei may be solved in the near future. At the time of writing, an experiment has been approved to revisit superdeformation in ^{131}Ce and ^{132}Ce using the Eurogam array in its second phase of operation. The apparent disagreement between experiment and cranked shell model calculations for these nuclei cannot remain unresolved. This study will no doubt pose as many new questions as it answers.

References

[Abe82] S.Åberg, Phys. Scr. **25** 23 (1982)

[And76] C.G. Andersson *et al*, Nucl. Phys. **A268** 205 (1976)

[Bak95] C. Baktash *et al*, Phys. Rev. Lett **74** 1946 (1995)

[BCS57] J.Bardeen, L.N.Cooper & J.R.Schreiffer, Phys. Rev. **108** 1175 (1957)

[Be85] T.Bengtsson and I. Ragnarsson, Nucl. Phys. **A436** 14 (1985)

[Bea92] C.W Beausang *et al*, Nucl. Instr. & Methods in Phys. Res. **A313** 37 (1992)

[Ben88] T.Bengtsson, I. Ragnarsson & S.Åberg, Phys. Lett. **B208** 39 (1988)

[Ben85] T. Bengtsson & I. Ragnarsson Nucl. Phys. **A436** 14 (1985)

[Ben87] M.A Bentley *et al*, Phys. Rev. Lett. **59** 2141 (1987)

[BF79] R.Bengstsson & S.Frauendorf, Nucl. Phys. **A327** 139 (1979)

[BM58] A.Bohr, B.R.Mottleson & D.Pines, Phys. Rev. **110** 936 (1958)

[BMR73] B.Banerjee, H.J.Mang & P.Ring, Nucl. Phys. **A215** 366 (1973)

[Boh36] N.Bohr, Nature **344** p137 (1936)

[BT73] P.Bhargava & D.J.Thousless Nucl. Phys. **A215** 515 (1973)

[Bur95] K.Burzynski *et al.*, Phys. Scr. **56** 228 (1995)

[BV78] Beranger & Vogt, Advances in Nuclear Physics, volume 10 (1978)

[Cas82] J.M.Cassels, Basic Quantum Mechanics, second edition, Macmillan Press, (1982)

[Ced94] B. Cederwall *et al.*, Phys. Rev. Lett. **72** 3150 (1994)

[Cla95] Sean Clarke, private communication, (1995)

[CPS74] S.Cohen, F.Plasil & W.J Swiatecki, Annu Phys. **82** 557 (1974)

[Dag94] P.J Dagnal *et al.*, Phys. Lett. B **335** 313 (1994)

[Deh74] W Dehnhardt *et al.*, Nucl. Phys. **A 225** 1 (1974)

[DW78] J.Dudek & T.Werner, J. Phys. G **4** 1543 (1978)

[Ehr59] H.F.Ehrenberg *et al.*, Phys. Rev. **113** 666 (1959)

[FAB79] F.A. Beck *et al.*, Phys. Rev. Lett. **42** 493 (1979)

[Fal89] P. Fallon *et al.*, Phys. Lett. B **218** 137 (1989)

[Fli93] S. Flibotte *et al.*, Phys. Rev. Lett. **71** 4299 (1993)

[Gar85] J.D.Garrett, Summer School on Frontiers in Nuclear Dynamics, (1985)

[Goo76] A.L.Goodman, Nucl. Phys. **A327** 113 (1976)

[Haa88] B.Haas *et al.* Phys. Rev. Lett. **60** 503 (1988)

[Haa90] B.Haas *et al.* Phys. Rev. **C42** R1817 (1990)

[He90] Y.He *et al.*, J. Phys. G **16** 657 (1990)

[Hil79] D.L Hillis *et al.*, Nucl. Phys. **A325** 216 (1979)

[HJS49] 0.Haxel, J.H.D. Jensen & H.E.Suess, Phys. Rev. **75** 1766 (1949)

[HM93] I. Hamamoto and B.R Mottelson, Phys. Lett. **B333** 284 (1994)

[Hus77] D. Husar *et al.*, Nucl. Phys. **A292** 267 (1977)

[HW53] D.L Hill & J.A Wheeler, Phys. Rev. **89** 1109 (1953)

[HW92] X.Han & C.Wu Atomic Data & Nuclear Data Tables **52** 43 (1992)

[Ing54] D.R Inglis, Phys. Rev. **96** 1059 (1954)

[Jam88] A.N James et al, Nucl. Instrum. and Methods **A267** 144 (1988)

[Kir87] A.J Kirwan *et al*, Phys. Rev. Lett. **58** 467 (1987)

[Kir87b] A.J Kirwan, Ph.D. thesis (1987)

[Kno89] Radiation Detection and Measurement. G.F.Knoll, Second Edition, Wiley (1989)

[Kra88] Intoductory Nuclear Physics. K.S.Krane, Second Edition, Wiley (1988)

[Lee94] I.Y. Lee *et al.*, Nucl. Phys. **A520** 641c (1994)

[Lil82] J.S Lilley, Phys. Scr. **25** 435 (1982)

[Luo87] Y.X Luo *et al.*, Z.Phys A **329** 125 (1988)

[Mac95] A.O Macchiavelli *et al.*, Phys. Rev. **C51** 1 (1995)

[Met80] V. Metag *et al.*, Phys. Reps. **65** 1 (1980)

[Mul93] S.M. Mullins *et al.* Phys. Lett. **312B** 272 (1993)

[New69] J.O. Newton *et al*, Nucl. Phys. **A141** 631 (1969)

[Nil55] S.G.Nilsson, Mat.Fys.Medd.Dan.Vid.Selsk. **29** No.16 (1955)

[Nil69] S.G.Nilsson *et al.*, Nucl. Phys. **A131** 1 (1969)

[Nol85] P.J Nolan *et al.*, J. Phys. G **11** L17 (1985)

[Nol92] P.J Nolan *et al.*, Nucl. Phys. **A520** 657c (1992)

[Nol93] P.J Nolan, Nucl. Phys. **A553** 107c (1993)

[Nol94] P.J Nolan, Annu. Rev. Nucl. Part. Sci. **45** 561 (1994)

[Pal91] M. Palacz *et al.*, Z. Phys. A **338** 467 (1991)

[Pav94] I.M Pavlichenkov and S.Flibotte 1994, Phys. Rev. C **51** 460 (1994)

[Pol62] S.M Polinkanov *et al.*, Sov Phys JETP **15** 1016 (1962)

[RS80] P.Ring & P.Schuck, The Nuclear Many-body Problem, Springer-Verlag, New York, (1980)

[San95] D.Santos *et al.*, Phys. Rev. Lett. **74** 1708 (1995)

[Sem95] A.T Semple *et al.*, Phys. Rev. Lett. to be submitted.

[Sha92] J.F Sharpey-Schafer, Prog. Part. Nucl. Phys. **28** 187 (1992)

[SRN72] R.K. Sheline, I. Ragnarsson and S.G Nilsson, Phys Lett **41B** 115 (1972)

[Str66] V.M Strutinsky, Sov. J. Nucl. Phys. **3** 449 (1966)

[Str67] V.M Strutinsky, Nucl. Phys **A95** 420 (1967)

[SW72] H.J Specht and J. Weber, Phys Lett **B41** 43 (1972)

[SZG95] Y.Sun, J.Zhang & M.Guidry, Preprint (1995)

[Szy90] Z.Szymanski, Nucl. Phys. **A520** 1c (1990)

[Twi86] P.J Twin *et al.*, Phys Rev Lett **57** 811 (1986)

[Twi83] P.J. Twin, *et al.*, Nucl. Phys **A409** 343c (1983)

[Twi93] P.J Twin, Nucl. Phys. **A557** 3c (1993)

[War68] D.Ward *et al* Nucl. Phys. **A117** 309 (1968)

[Wei35] C.F. von Weissacker, Z.Phys. **96** 431 (1935)

[WS54] R.D.Woods & D.S.Saxon, Phys Rev **95** 577 (1954)

[Wys88] R.Wyss *et al.*, Phys. Lett. **B215** 211 (1988)